Effects of parapets on the performance of unglazed solar collectors

Morkporkpor Delight Sedzro

A thesis submitted to

Auckland University of Technology

in fulfillment of the requirements for the degree of

Doctor of Philosophy (PhD)

2023

School of Engineering, Computer and Mathematical Sciences

Abstract

The useful energy output of a solar thermal collector is influenced by various factors, such as wind velocity. Elevated wind velocity results in substantial heat loss caused by wind, thereby affecting the performance of the collector. Solar thermal collectors that lack insulation or a glass covering (unglazed solar collectors) are especially susceptible. Considering the placement of these collectors on rooftops and their exposure to wind, it is imperative to examine methods for minimising this impact. Studies have demonstrated that perimetric parapets can modify wind loads on roofs and the structural support system of solar panels and collectors. Insufficient attention has been devoted to examining the influence of parapets on collector heat loss, as well as the optimal placement of collectors on roofs with respect to parapets and their effect on heat loss. Consequently, the focus of this study was directed towards examining the impact of parapets on the localised velocity surrounding roof-mounted unglazed solar collectors, as well as the subsequent heat loss.

The quantification of this effect was accomplished using Computational Fluid Dynamics (CFD) simulations validated through wind tunnel experiments. The aerodynamic properties of the roof were investigated across three distinct scenarios, namely those with high parapets, low parapets, and no parapets. The results of the study indicated that when perimetric parapets were not present, the vortex formed on the rooftop was located in closer proximity to both the leading edge and the surface of the roof. In contrast, the inclusion of parapets resulted in the elevation of the vortex above the surface of the roof. In each instance, the velocity at the central region of the roof exhibited higher velocities, while the velocity zones adjacent to the leading and trailing edges of the roof and parapets displayed lower velocities.

Measurements were taken at different roof mounting locations, representing 25%, 50%, and 75% of the roof length, for collector tilt angles of 5°, 20°, 40°, and 60° at different parapet heights and wind incidence angles (0°, 45°, 90°, 135°, 180°). The results of the simulations indicated that there was a direct correlation between the increase in tilt angle of unglazed solar thermal collectors and the corresponding increase in heat loss, irrespective of the height of the parapet. Additionally,

the study demonstrated that lower parapets led to higher levels of collector loss compared to parapets with greater perimetric height. The research revealed that increased collector tilt angles resulted in a decrease in heat loss for the following row of collectors, which were positioned further from the incoming flow in rooftop solar arrays. In all instances, it was observed that the leading row of collectors positioned at the edge of the roof experienced a greater heat loss compared to all subsequent rows of collectors.

In summary, the results of this study demonstrated the aerodynamic impacts of parapets on the heat loss of roof-mounted standalone and array unglazed solar thermal collectors. Based on the acquired insight, a set of correlations was formulated to enable designers and architects to consider the influence of parapets on the convective heat loss of unglazed solar thermal collectors. In a more comprehensive context, the study showcased the importance of mitigating the impact of velocity on unglazed solar collectors, thereby enabling its use in various solar thermal applications. This is particularly noteworthy given that unglazed solar collectors are cost-effectiveness.

Contents

List Of Figures

List Of Tables

Attestation Of Authorship

I hereby declare that this submission is my own work and that, to the best of my knowledge and belief, it contains no material previously published or written by another person nor material which to a substantial extent has been submitted for the award of any other degree or diploma of a university or other institution of higher learning.

Signature_____

Morkporkpor Delight Sedzro

Publications

The following publications have been derived in whole or in part from the work contained. within this thesis.

Conference Papers:

I. Sedzro, D. M., Anderson, T., & Nates, R. (2019). The Effect of Parapets on Roof Mounted Solar Collectors. *Proceedings of the Asia Pacific Solar Research Conference* 2019.

II. Sedzro, D. M., Anderson, T. N., & Nates, R. (2020). The Effect of Parapets on the Performance of Unglazed Solar Collectors. *The 54th International Conference of the Architectural Science Association (ANZAScA) 2020, Imaginable Futures*: Design Thinking, and the Scientific Method, 1095–1104.

III. Sedzro, D. M., Anderson, T., & Nates, R. (2020). Thermal performance of unglazed roof-mounted solar thermal collectors. *Proceedings of the Asia Pacific Solar Research Conference*, 2020.

Acknowledgment

If I were to list everyone who has provided me with intellectual, technical, and moral support, this thesis would require an additional chapter. Thus, while I cannot express my personal sincere gratitude to all those that helped me, the names that follow are the few that came to mind.

I would like to thank my supervisors, Associate Professors Tim Anderson and Roy Nates, for their technical support and direction. I would also like to thank Si Thu Paing, Sulaiman Fadlallah, Djamal Serradj, Lydia Damiloju, and Mehrdad Khamooshi for their constructive feedback and support. Additionally, I appreciate Josephine Prasad's prompt attention to all my administrative concerns. I am grateful to Professor Richard Flay, Dr. Li Fai, and Dr. Amir Safaei Pirooz of the University of Auckland for permitting me to conduct my experiments in the Wind Tunnel Hall. To Bernado Coehlo, Gutam , Mallick, Shilpa and Tahir, thank you too for all the technical guidance.

I will forever be grateful to Warner Brunton, Les Wilson, and the entire Mott MacDonald team for everything they have done for me throughout the years. Laura and Pauline, my sincere thanks to you for all your support during my time in New Zealand. To my new family at Arup (Ireland), especially John Bynum and Rubina Ramponi for their exceptional support and CFD insight, I am grateful. Also, to Dr Adeyina, I am indebted for your encouragement, support, and prayers. I am also grateful to Dr. Okai and Dr. Sarpong for always being there whenever I needed them. To Kiki and Kardi, time is the architect of everything and for the silence these years brought, thank you for being patient and supportive. Ivy and Cyril, your assistance and support are invaluable and I will continue to cherish that.

Finally, I would want to pay tribute to my mother, Beatrice Dzibgbordi Gadabor, who passed away six months into my studies, and my younger brother, Kwadwo Boateng, who died a year later. You are both missed a lot!

Nomenclature

A_C	Area of collector (m^2)
a	Solar altitude angle
B	Breadth (m)
b_s	Shading distance
b/a	Ratio of the row spacing and collector height
c_p	Specific heat capacity (J/kgK)
$C_{pi(t)}$	Specific tap location
C_L	Force coefficient
d	Diameter (m)
d_h	hydraulic diameter
F	Fin efficiency
F'	Corrected fin efficiency
F_L	Lift force
F_R	Collector heat removal factor
G	Incident solar radiation (W/m^2)
g	Gravitational acceleration (m/s^2)
H	Building height (m)
h_b	Height of base of roof to leading edge of parapet
hp	Parapet height
h_w	Wind induced heat transfer coefficient (W/m^2K)
h_c	Convective heat transfer (W/m^2K)
h_{nat}	Natural convective heat transfer
h_r	Heat loss due to radiation
k	Thermal conductivity (W/mK)
K_{abs}	Absorber conductivity (W/mK)
K	von Karman constant

L	Thickness (m)
L_c	Collector location
L_p	Length of the parapet
L_r	Length of the roof
$\dot{m}$	Mass flow rate (kg/s)
m	Thermal conductivity of the absorber
m	Thickness
N	Number of glazing covers
Nu	Nusselt number
Nu_{avg}	Average Nusselt number
P	Collector perimeter
P_∞	Static pressure at infinity
$P_{i(t)}$	Pressure measured at tap
PV/T	Photovoltaic Thermal
Q_u	Useful energy
$\dot{q}_{loss}$	Rate of heat loss (W)
$\dot{q}_{rad}$	Radiation heat transfer rate (W)
$\dot{q}_{useful}$	Collector useful energy gain (W)
R	Thermal resistance (M^2K/W)
R_e	Reynolds number
Ri	Richardson Number
T	Temperature (℃)
$\bar{T}$	Average temperature (℃)
T_a	Ambient temperature (℃)
T_{col}	Collector outlet water temperature (℃)
T_{in}	Collector inlet water temperature (℃)
T_{pm}	Collector mean plate temperature (℃)

T_s	Sky temperature (℃)
U	Velocity profile
U_L	Collector heat loss coefficient (W/mk)
U_{bottom}	Bottom heat loss coefficient
U_{edges}	Edge heat loss coefficient
U_{ref}	Reference velocity (m/s)
U_{top}	Top heat loss coefficient
u_τ	Friction velocity (m/s)
V	Wind velocity (m/s)
V_{loc}	Local velocity
w	Tube pitch
z	Solar azimuth angle
z_a	Solar azimuth angle
z_{ref}	Reference location
z_0	Surface roughness length
$(\tau\alpha)_T$	Transmittance–absorptance product of thermal collector
α	Thermal diffusivity (m^2/s)
β	Collector inclination angle
ε_g	Glass cover emittance
ε_p	Collector emittance
τ	Absorptance-transmittance product
η	Collector thermal efficiency
υ	Kinematic viscosity (m^2/s)
θ_s	Collector mounting angle (degrees)
θ	Wind Incidence angle
ρ	Air density (kg/m^3)
ϵ	Dissipation rate

π	Pi
δ	Stefan-Boltzman constant

Subscripts

a	Ambient
bottom	Bottom of the collector
col	Solar collector
edge	Collector edge
in	Collector inlet
ins	Insulation
p	Absorber plate
ref	Reference
s	Surface
top	Top of collector

Chapter 1

Introduction

1.1 Overview

The benefits of renewable energy sources such as wind, tidal, hydro, geothermal, and solar, along with the threat of climate change, continue to drive the targets and incentives for developing renewable energy technology (Menanteau *et al.*,2003). By 2050, renewable energy sources are expected to meet more than half of the world's total energy consumption (Lund, 2009; Luthra *et al.*, 2015; Sen and Ganguly, 2015; Yaqoot, *et al.*, 2016).

Of all the renewable energy sources available , solar energy technologies have proven to be particularly promising primarily, owing to their nonpolluting and abundant nature (Mohtasham, 2015). Solar energy has long been used in food preservation, textile drying, salt production, and, in some circumstances, for religious purposes (Anderson, 1977). Within the built environment, architectural designs that consider the orientation of buildings based on solar energy utilization as well as the integration of solar technologies to building facades continue to see marked growth (Zomer *et al.*, 2020). Accordingly, there is no doubt that solar technologies will continue to grow across several sectors of industry as research explores ways to improve performance, reduce costs, and increase market availability, just as with all other positive interventions aimed at reducing climate change. A detailed historical context on the evolution of solar energy use and its application is documented in literature (Kalogirou, 2004).

1.2 Solar Thermal Technologies

Solar photovoltaic (PV) and solar thermal energy conversion systems are the two types of solar energy conversion systems. Photovoltaic systems use direct conversion of solar radiation to electricity, whereas thermal systems use direct conversion of solar radiation to heat. The conversion efficiency of solar to thermal systems is typically much higher than that of solar to electrical systems. This is primarily due to the limitations of lower photon absorption and low photon conversion efficiency into electricity. There are many applications for heat energy that are preferred over electrical energy in many sectors. Due to this, solar thermal energy systems are

considered one of the most attractive options for producing thermal energy, offering a huge opportunity for replacing traditional energy sources.

Globally, solar thermal use is expanding, and this has grown from small-scale applications in homes to large-scale applications including space heating, cooling, water heating, heat for process industries, and power generation. A direct consequence of this growth, illustrated by Figure 1 , is the increase in global operating solar thermal collector capacity from 171 gigawatts thermal (GWth) in 2009 to 479 gigawatts thermal (GWth) in 2019, which corresponds to 244 and 684 million square meters (m2) of installed collectors (IRENA, OECD/IEA, REN21, 2020).

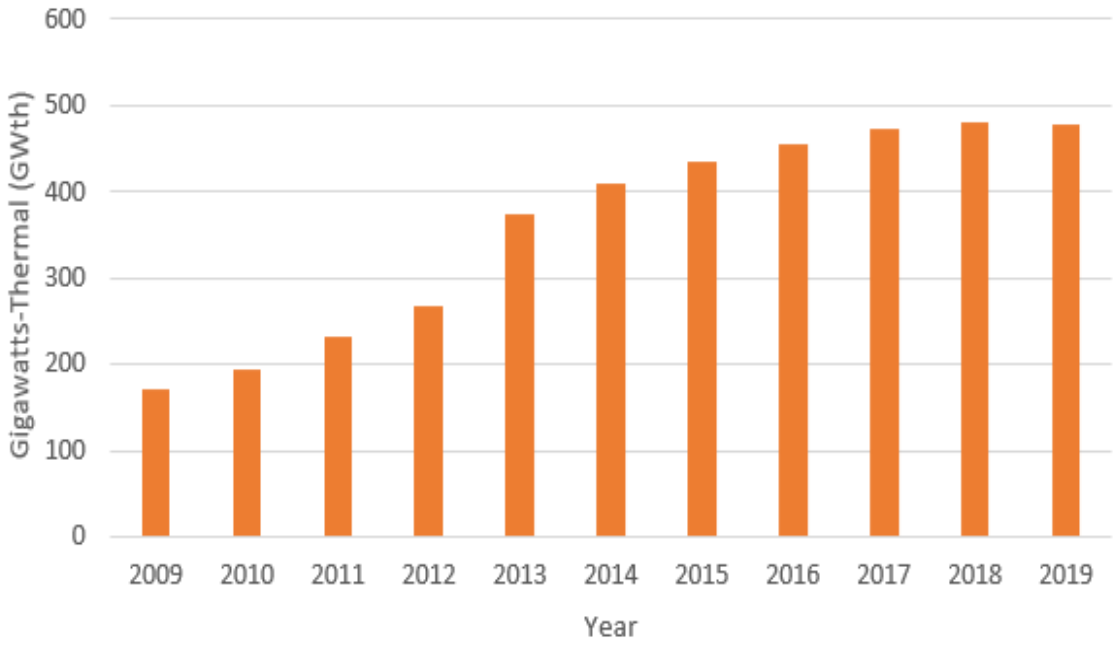

Figure 1: Global solar thermal capacity in operation, 2009-2019 (REN21, 2020)

Figure 2 depicts various types of solar thermal collectors which includes flat plates, evacuated tubes, thermosiphons, and concentrating collectors (SEIA,2019). Amongst these, flat plate solar collectors are one of the most widely used due to their low maintenance costs and ease of construction (Tyagi *et al.*, 2009; Chopra *et al.*, 2021). These consists of an absorber plate, absorber tubes, and a manifold; and are either glazed or unglazed. Glazed collectors have one or more layers of glass or clear polymer covers to minimize heat loss through convection and radiation while allowing solar radiation (Tian and Zhao, 2013). Unglazed collectors, on the other hand, are

made of metallic or polymer materials, and have no glazing, thus, making them less expensive (Klevinskis and Bučinskas, 2011; Pandey and Chaurasiya, 2017).

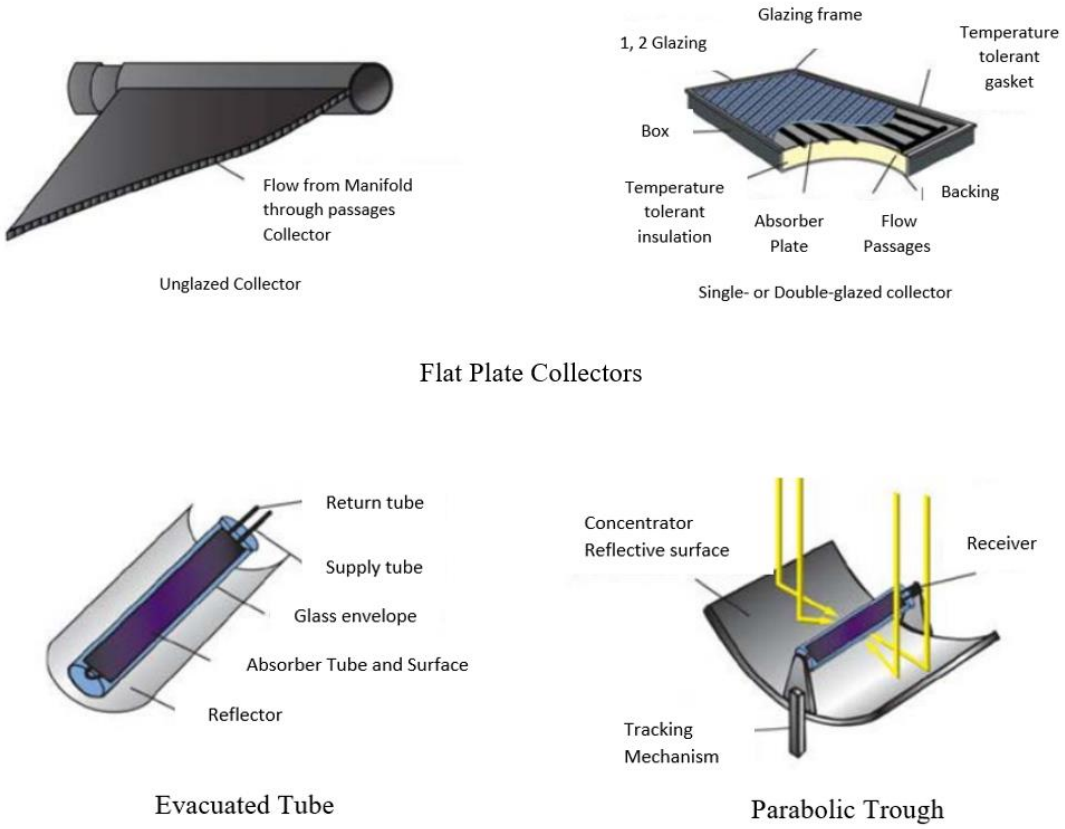

Figure 2: Solar thermal technologies, with unique characteristics shown (NREL, 2015)

Whereas solar thermal collectors can be used for a variety of applications such as space heating, solar water heating, and other industrial applications, one notable application that is growing in popularity is heating and cooling. As shown in Figure 3, millions of residential, commercial, and industrial clients in at least 134 countries used flat plate collectors for solar heating systems between 2010 and 2020. In particular, the marginal growth in the use of unglazed solar collectors, particularly those primarily used in pool heating and heat exchanger applications, provides the impetus for further research especially given its relative affordability when compared to other collectors (Mahesh *et al.,* 2013; Montoya-Marquez and Flores-Prieto, 2015)

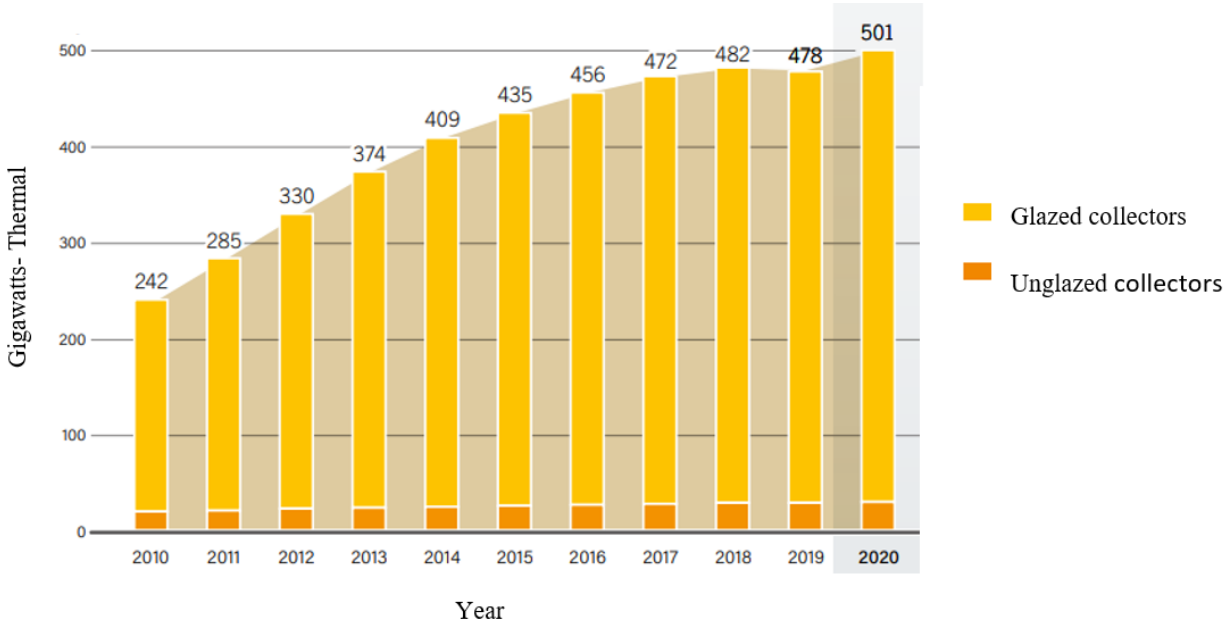

Figure 3: Solar Water Heating Collectors Global Capacity, 2010-2020 for glazed and unglazed collectors (REN21, 2021)

1.3 Unglazed Solar Collectors

Unglazed solar collectors (USC) are composed of absorbers (embedded channels through which fluid flows) that are devoid of any glazing or covering material. These collectors absorb a lot of solar radiation as no glazing or covering is present. However, the lack of insulation on their rear surfaces or glazing covering, allows most of the absorbed heat to escape, especially in windy conditions (Kalogirou, 2004). As a result of the high heat losses, unglazed solar collectors have low thermal performance compared to other types of solar collectors as depicted in Figure 4 and as such, have been relegated to low temperature applications.

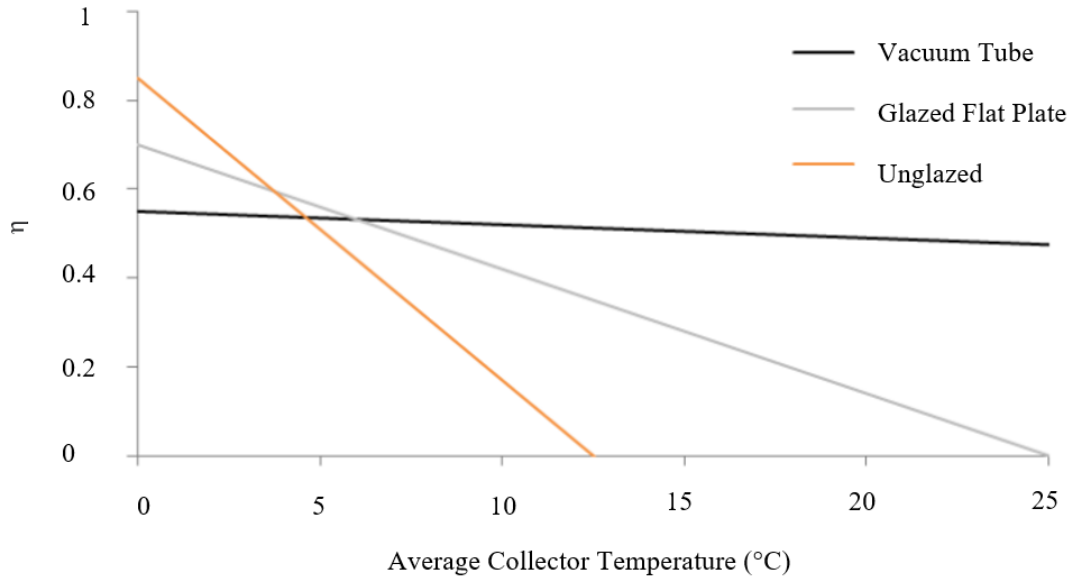

Figure 4: Efficiency of solar collectors depending on collector temperature for given ambient conditions (Martinez et al., 2017)

On the contrary, the absence of glazing and insulation has resulted in unglazed solar thermal collectors being less expensive due to glazing costs (Sopian *et al.,* 2004). Additionally, the establishment of renewable energy infrastructure necessitates a growing quantity of resources, including indium, gallium, and rare-earth metals. This transition poses the potential to shift environmental burdens rather than substantially alleviate them, as the unsustainable extraction of fossil fuels is replaced by the unsustainable extraction of materials essential for renewable energy (Vidal, 2013).

In this context, it is worth investigating technologies like USC that have low material requirements (owing to the lack of insulation and glazing). The increased adoption of such technologies has the potential to mitigate material consumption and its consequential long-term effects on carbon emissions through materiality. Moreover, as illustrated in Figure 5, the lack of glazing and insulation facilitates easy integration with architecture or façade cladding (Matsuka *et al.*, 2019), which makes a good case for the application of USC in the built environment.

a. Unglazed stainless steel flat plate collectors b. Façade cladding of unglazed collector

Figure 5: A roof-mounted unglazed solar collector (Photo Credit: Energie Solaire, 2020)

Combined with its cost advantages and architectural integration, USC has also seen its application to heat pumps expand rapidly in recent years. In this case, solar energy is used indirectly via the heat pump's evaporator not only to increase Coefficient of Performance (COP) but also to lower the operating temperature of the solar collectors below ambient conditions. The demand for this type of system has therefore forced manufacturers to consider the use of unglazed collectors compared to other types of solar collectors (Bunea *et al.*, 2015).

1.3.1 Thermal Performance of Unglazed Solar Collectors

The performance of solar thermal collectors and photovoltaic panels can be affected by convective heat loss caused by microclimatic factors such as wind velocity, humidity, and longwave irradiation. The impact of these microclimatic conditions, however, impact the two types of systems differently (Keller, 1985; Leon and Kumar, 2007; Li *et al.*, 2013).

For flat plate collectors (solar thermal), the main difference between glazed and unglazed solar collectors in terms of efficiency is that the performance of an unglazed collector depends primarily on four environmental factors, including shortwave radiation, longwave radiation, ambient temperature, and wind speed (Morrison, 1992). In contrast, glazed collectors are primarily affected by only two environmental factors, shortwave radiation, and ambient temperature. For both types of collectors however, there are several secondary factors such as diffuse radiation fractions and ground reflections which have an effect (Morrison, 1992).

In unglazed collectors, thermal performance is sensitive to wind velocity, which is driven by convective heat loss at both the rear and front of the collector as shown in Figure 6. As a result of the above, some national testing standards address wind speed as a primary factor in the performance of unglazed solar thermal collectors by specifying wind speeds to be maintained at a given value or by requiring testing at several wind speeds (ANSI/ASHRAE, 1986).

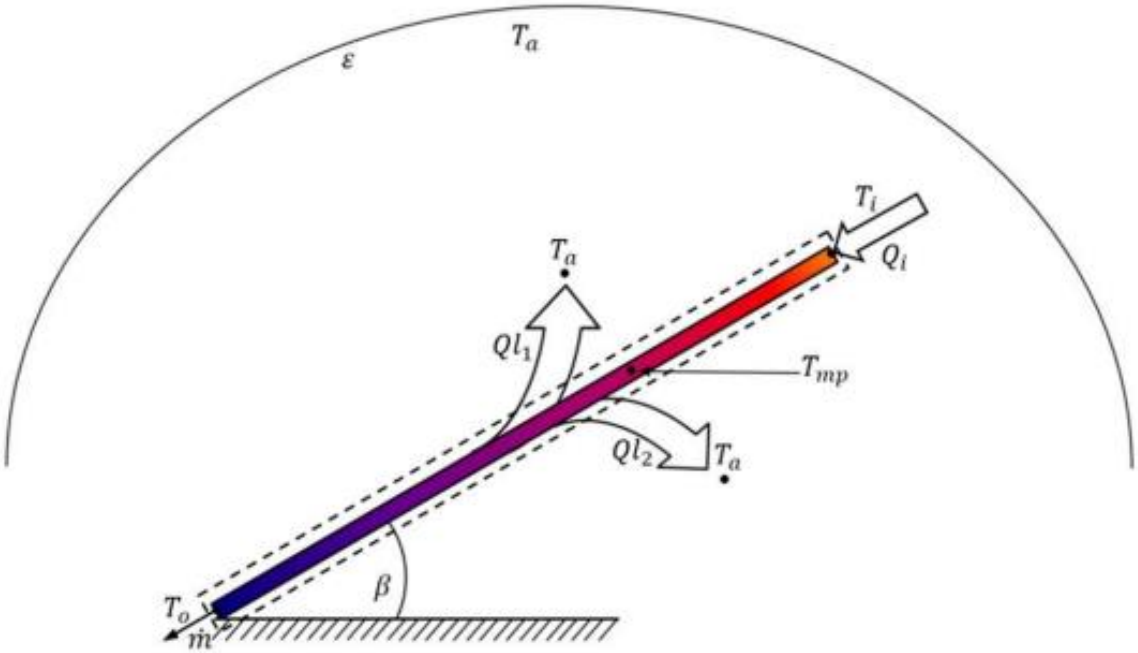

Figure 6: Schematic representation of heat flow rates on the front and rear surface of an unglazed solar thermal collector.

Literature documents the above, especially the effect of wind. For example, Keller (1985), experimentally examined plastic collectors under different meteorological factors in terms of the design and mounting. It was found that the solar thermal performance depended substantially on wind velocity, humidity, infrared sky radiation as well as solar irradiance. Similarly, Soltau (1992) assessed the thermal performance of several unglazed collector types, both indoors and outdoors. The wind speed varied between 1.0 m/s to 3.1 m/s for an outdoor small array area comprising of four unglazed solar collectors as shown in Figure 7.

Figure 7: Outdoor set up of roof mounted Solar thermal collector (Soltau,1992)

Thereafter, a more controlled test was conducted at the Canadian National Solar Test Facility's (NSTF) environmental chamber as reported in (Harrison, *et al.*, 1989) and cited in Soltau (1992a). For this, a wind generator system was used to create a flow field upstream, parallel to the collector surface with a stagnation line at its lower end. The average wind velocity in this case varied between 1.5 m/s to 3.5 m/s. For both the indoor and outdoor conditions, Soltau's (1992a) work demonstrated that the value of the heat loss coefficient recorded at zero wind speed was significant, thus, indicating that the heat loss coefficient at higher wind speeds could be increasingly significant. Figure 8 shows the results of the thermal performance of the collector under varying wind speeds.

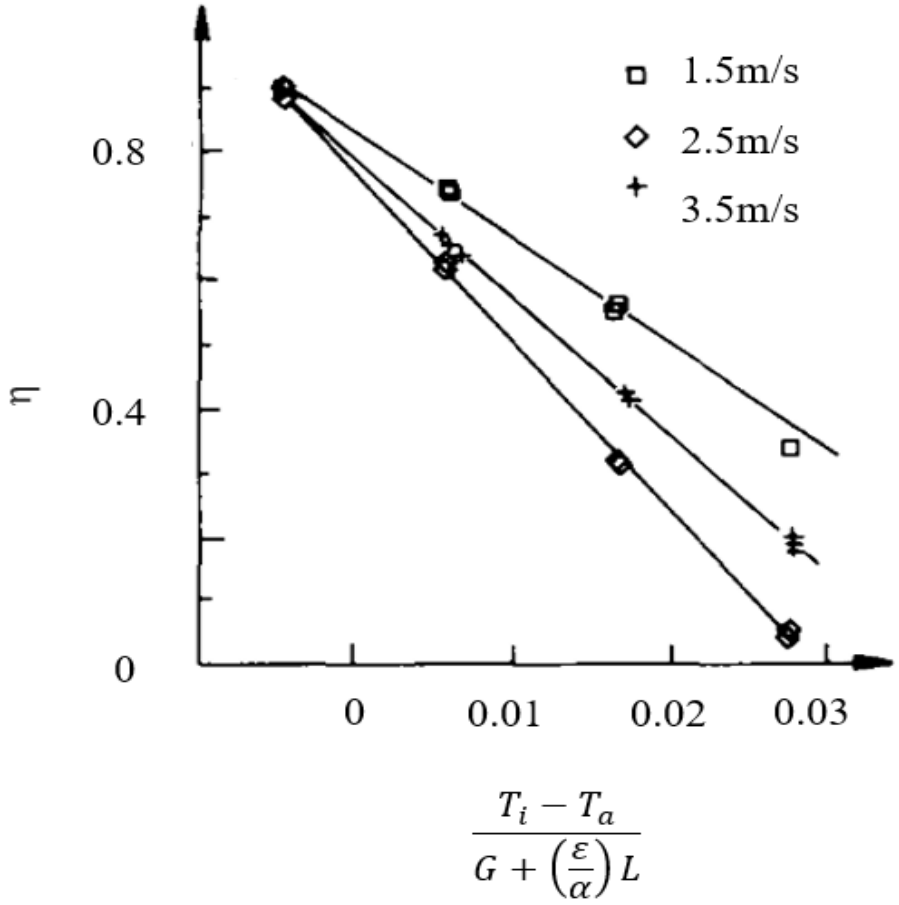

Figure 8: The efficiency of an unglazed solar collectors made of polypropylene (Soltau, 1992)

Also, Kumar and Mullick (2010), investigated the effect of wind velocity on the heat transfer coefficient on the surface of a solar a collector while estimating its upper surface heat losses. Experiments were carried out on the surface of the roof-mounted collector to quantify the wind-induced convective heat transfer coefficient, which was then associated with the wind speed over a two-year summer period and compared with the previous research. Similar to the observation made in Soltau (1992), Kumar and Mullick's (2010) work also demonstrated that an increase in wind velocity resulted in an increase in wind induced convection; leading to a decrease in the output of the solar collector.

While it is clear from the preceding that wind velocity has a significant impact on the performance of unglazed solar collectors (USC). Changing environmental factors such as wind can be challenging, especially on low-rise roofs, where the majority of solar collectors are installed. As

a result, more research is needed to better understand how wind velocity affects convective heat transfer on roof-mounted solar thermal collectors, as well as ways to mitigate this impact.

1.4 Wind effect on Convection Heat Transfer

Heat loss on the solar thermal collectors occurs due to natural convection (h_{nat}), but as velocity increases, this translates to forced convection, resulting in an increase in fluid bulk motion. This effect has been studied across extant literature, yet considerable variabilities exist in an accurate method of quantifying the forced convective heat loss coefficient (h_w), used in determining the wind induced convection heat loss.

Primarily, wind-induced convection contributes more to upward heat loss in single or double-glazed collectors. And for wind-sensitive collectors such as USCs, it is crucial to select acceptable values for convection-induced heat transfer coefficients to calculate both front and rear heat loss, given that both surfaces are exposed. At the same time, solar collectors are often mounted on low-rise buildings, where there are many obstructions on the roof surface along with adjacent buildings, parapets, or other bluff bodies. Accordingly, it is not practical to consider a common velocity since wind characteristics may differ from location to location on the roof. The above is highlighted in a wide range of literature.

For example, using Concordia University's boundary layer wind tunnel, Ladas *et al.*, (2017) measured the wind velocity on the surface of solar collectors in nine different mounting locations, three different wind directions, as well as on an isolated building and one surrounded by a variety of different environments. The study results found a 60 percent variation in the local velocities at different roof locations, which evidently translated into different performances. Moreover, the velocity distributions on the building roofs showed that the ratio between maximum and minimum local velocities could be high as 1.75 due to other phenomena such as building geometry and wind direction.

Also, it was shown that wind speed, turbulence intensity, obstacles, and building type could influence the wind velocity on an inclined windward roof of a low-rise building equipped with

solar collectors or panels in a study by Karava *et al.,* (2012). Having said that, it is equally important to note that other factors can also affect the convective heat transfer of solar collectors when considering the wind velocity relative to a mounting location. These factors include but are not limited to: the natural wind environment (Test *et al.,* 1981), plate characteristic length (Wattmuff, 1977; Sparrow *et al.,* 1979; Oosthuizen and Naylor, 1999), plate dimension (Sharples and Charlesworth, 1998) and air temperature (Sartori, 2006). When all of these factors are taken into account, the convective heat transfer coefficients have shown to be more variable.

Away from the above factors, as velocity markedly impacts USC's performance, it is imperative that different obstructions to the wind velocity and the location of the collector on the roof be considered when determining the collector's heat loss. Generally, most studies incorporate wind velocity as an assumed single velocity of a reference location rather than definite wind speeds (Ladas, *et al.,* 2017). Evidence of this can be drawn from other work (Sparrow and Tien, 1977; Sharples and Charlesworth, 1998), where it has been shown that the performance of collectors can vary at different locations on the roof surfaces.

For low rise buildings where collectors are often mounted, a distinct attribute that cannot be ignored is the presence of parapets on the roof. Particularly, the influence of parapets remains important, as low-rise buildings are subject to drastically fluctuating wind loads due to their location in the lowest region of the atmospheric boundary layer. This is because, in many circumstances, unfavorable pressure gradients downstream of low-rise building roof edges cause the boundary layer surrounding them to separate, as depicted in Figure 9. The resulting effect are vortex flows with significant suction loading in the separated flow zone. Thus, the roof of low-rise buildings, which account for a sizable proportion of all buildings worldwide, are more vulnerable to varying wind velocity and wind loads other than other elements of the building (Mooneghi and Kargarmoakhar, 2016)

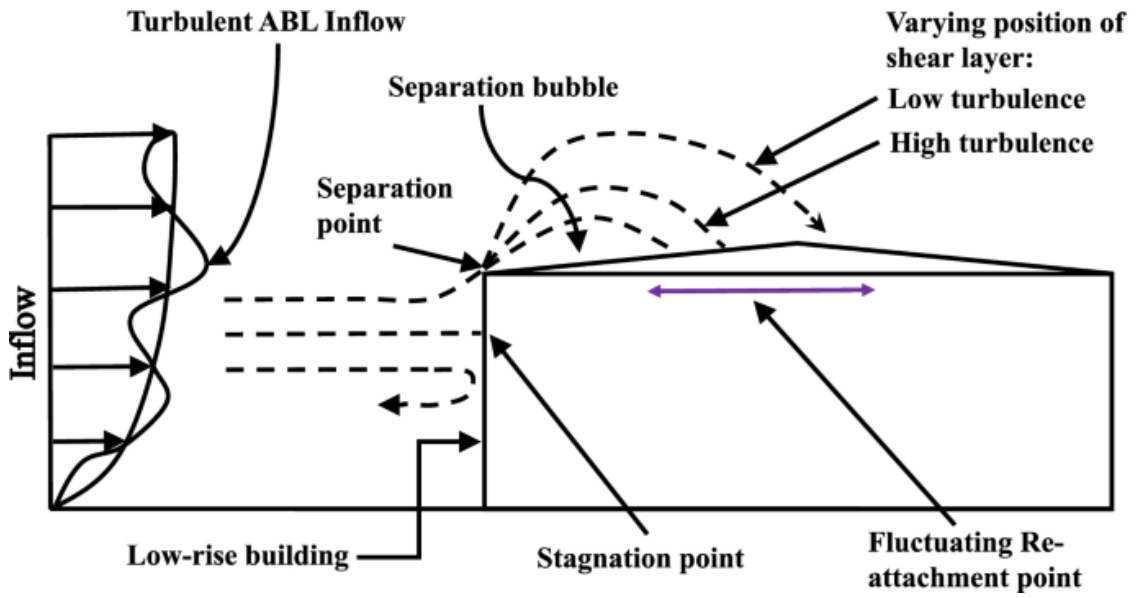

Figure 9: Schematic diagram of flow structure around low-rise building (Simui,2011)

Lastly, studies such as Palyvos (2008a), which have critically examined and reported on some of the noteworthy convective transfer coefficient correlations, argue that differences in convective heat transfer coefficient (h_w) values can be attributed to incompatibility between experimental studies and the reality of the field. Though Palyvos (2008a) does not define the reality on the field, these factors can be interpreted as including mounting location, obstructions to the coming flow, and so on. This may further explain why the relationship between local wind velocity and convective heat transfer coefficient (albeit linear) varies, as shown in Figure 10. The question arises, therefore, of how roof top collector mounting locations relative to the presence flow obstructions like parapets could impact heat transfer correlation and the heat loss of unglazed collectors.

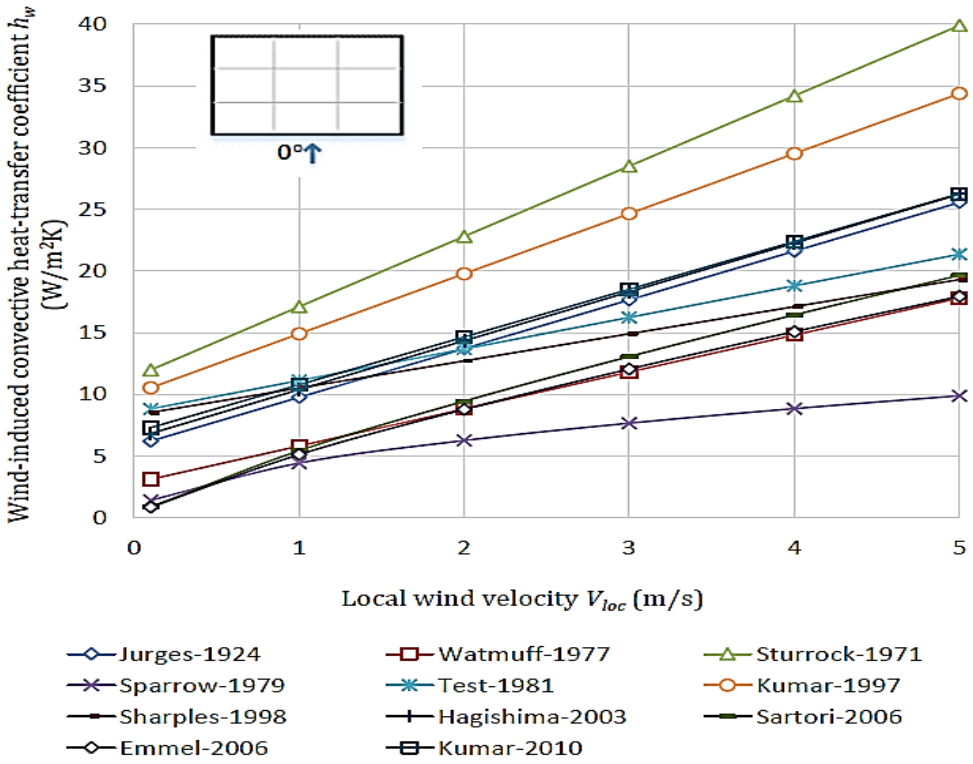

Figure 10: Comparison of h_w correlations of cited studies for 0° wind (Ladas et al., 2017)

1.5 Research Objective

Low-rise building roof systems are frequently subjected to higher winds than other sections of the building (Mooneghi and Kargarmoakhar, 2016). Because most solar technologies are installed on roofs, several studies have focused on how wind loads impact solar support structures rather than performance (Browne *et al.*, 2013; Cao *et al.*, 2013; Kopp, 2013; Mier-Torrecilla *et al.*, 2014).

Meanwhile, many solutions have been investigated in the past, such as parapets that disrupt and deflect the vortices from roof edges, in order to produce the "vortex suppression." Perimetric parapets have been found to minimize the wind loads by modulating the wind velocity at various heights and configurations (Lythe and Surry, 1983; Stathopoulos *et al.*, 1999; Cao *et al.*, 2013).

While parapets clearly influence wind loads, there is evidence that micro climatic factors, such as wind velocity, also influence collector performance. The two strands of research have however been treated as separate, yet equally important. Thus, despite the ability of parapets to reduce roof wind loads, their effect on varying the roof local velocity, particularly around roof mounted collectors, and how this translates to performance remains a research dearth. In the case of USC,

which is dependent on wind velocity for performance, this could be useful for market penetration. Especially as USC is less expensive to produce and can be easily integrated into architectural facades. This could lead to greater deployment of renewable energy, particularly in developing countries and low-income households.

Against this backdrop, this thesis questions: “Can the use of parapets reduce convective heat loss and thus improve the performance of an unglazed solar thermal collectors?”

Chapter 2

Aerodynamics on the roof of low-rise buildings with and without parapets.

2.1 Introduction

As discussed in the previous chapter, roof-mounted solar thermal collectors have been shown to be more sensitive to wind velocity than glazed collectors. In addition, although most solar collectors are mounted on low-rise buildings, studies on solar collectors on low-rise buildings are often skewed towards understanding wind loads on the collector support structure (Browne *et al.,* 2013; Akon and Kopp, 2016b; Wang *et al.,* 2018). Parapets on the other hand have been shown to reduce roof wind loads (Lythe and Surry, 1983), however, it remains to be investigated how the roof aerodynamics, result in changes in wind velocity that could impact the heat loss of roof mounted collectors.

Considering the foregoing, it is necessary to understand the roof aerodynamics with and without parapets. To do this, bluff body aerodynamics, which has proven to be extremely useful in the fields of urban planning, structural, and architectural design can be useful. Such analysis, however, necessitates in-depth research that approaches reality using in-situ measurements, wind tunnel tests, or computational fluid dynamics (CFD) simulations. CFD simulations provide quick and relatively low-cost data collection amongst these methods (Stankovic *et al.,* 2009).

Regarding parapets, research has demonstrated the classification of parapet heights into two categories: parapets representing higher perimetric heights $\boldsymbol{h_p}/(H + \boldsymbol{h_p}) \geq 0.23$ or $\boldsymbol{h_p} \geq 0.9\text{m}$ and parapets representing lower perimetric heights $\boldsymbol{h_p}/(H + \boldsymbol{h_p}) \leq 0.17$ *or* $\boldsymbol{h_p} \leq 0.9\text{m}$ (Kopp *et al.,* 2005; Mans *et al.,* 2005).The parapet height and eaves height in this scenario are denoted as $\boldsymbol{h_p}$ and H, respectively, as illustrated in Figure 11. In line with this categorisation, it has also been found that various parapet configurations, as depicted in Figure 12, can result in different outcomes in terms of reducing wind loads on roof corners (Huang *et al.,* 2017). However, these studies are skewed towards the understanding of wind loads only. Thus, since parapets are

commonly used on roof edges and corners, having a better understanding of how parapets affect aerodynamics around buildings, specifically on the roof, could help identify the probable mounting location of a solar collector, given that, this can influence the local wind velocity and thus heat loss

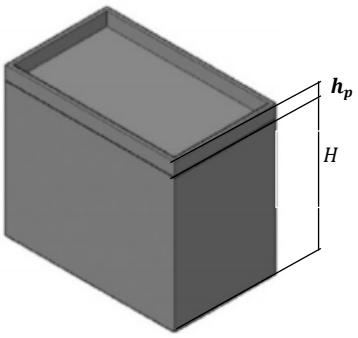

Figure 11: Classification of parapet height (Solid parapets)

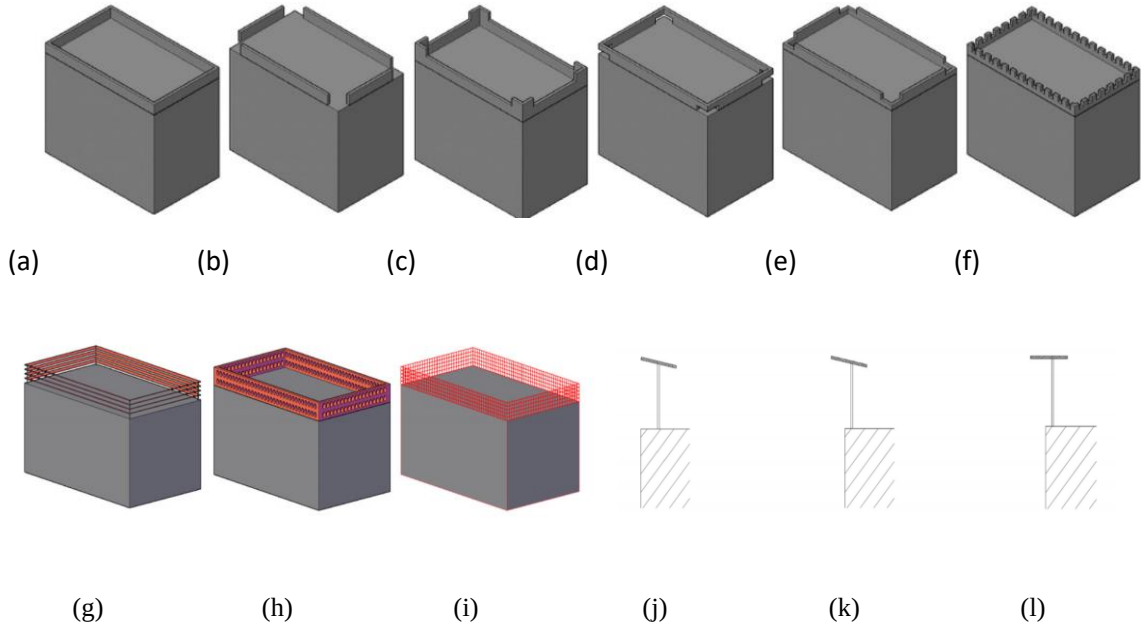

Figure 12: Configuration of different partial parapets (a-f) and parapets configurations (h-m). (a) solid, (b) isolated, (c) corner-raised, (d) bottom-slotted, (e) top-slotted, and (f) castellated, (h) slatted fence, (i) porous (circular hole), (j) screen mesh, (k) inclined spoiler, (l) overhanging inclined spoiler, and (m) overhanging horizontal spoiler. (Huang et al., 2017)

2.2. Method

Because of the interest in the influence of wind on low-rise buildings in the lower portion of the atmospheric boundary layer, a square shape was chosen to represent a low-rise building with a flat roof. For the first part of this investigation, a 3D building of dimensions 16 m (length) × 16

m (width) × 4 m (height) was developed using the commercial software Ansys: Space Claim. This was followed by the same geometry with a low and high parapet built onto it. Accordingly, the parapet heights were chosen to be 0 m, 0.4 m, and 1.2 m, respectively, corresponding to no parapet, low, and high perimetric parapets. For the low and high parapets, this corresponded to $\boldsymbol{h_p}/(H + \boldsymbol{h_p}) =$ 0.09 and 0.23. Parapet heights above 1.2 m are uncommon in low-rise buildings. However, for the purposes of this study, 1.2 m was chosen to represent the highest likely parapet height in this instance. Also, the thickness of the parapet was not taken into consideration given its marginal effect reported in the work of Kramer *et al.,* (1978) ; Baskaran and Stathopoulos (1988). The dimension of the modelled building is shown in Figure 13.

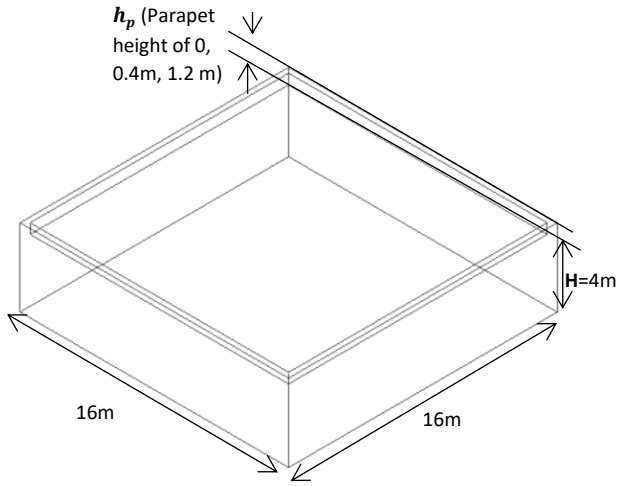

Figure 13:Model of low-rise building (Not drawn to scale)

Next, the computational domain was modeled following the European best practices recommendation in COST Action 732 (Franke *et al.,* 2007). To allow for the difference in geometric configurations, the computational domain in this case was modeled as a cylinder while conforming to the dimensions and standards indicated in the best practice guidelines. The use of cylindrical domains for investigating aerodynamics around bluff bodies has been previously reported elsewhere (Lu *et al.,* 2014; Gimenez *et al.,* 2018). As a result, a 176m diameter cylindrical computational domain was modeled with the building at its center (representing 44H, where H is the height of the building).

As can be seen in Figure 14, the computational domain had upstream and downstream fetches of 20H to facilitate the redevelopment of the boundary layer downstream of the wake as recommended in the best practice guidelines and to satisfy a blockage ratio of <3 percent (Franke *et al.*, 2007). Also, in accordance with the best practice guidelines, a domain height of 40m was applied (representing 10H).

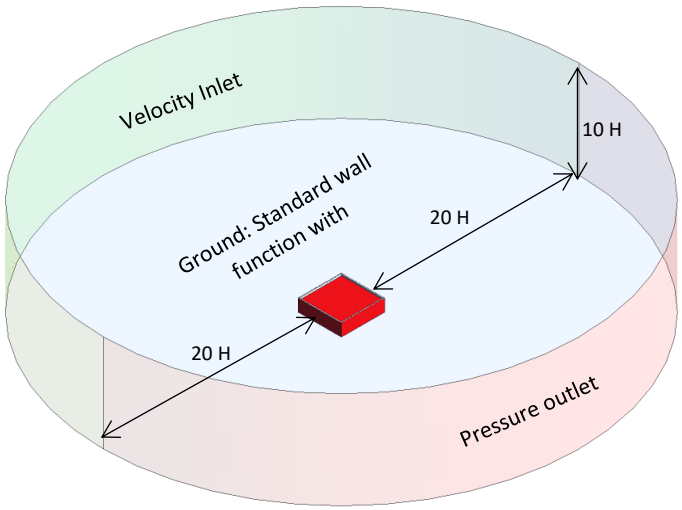

Figure 14: Computational domain and boundary conditions (Not to scale)

The mesh generation software Pointwise (now Cadence), (2019), was used for the meshing. A hybrid O-H meshing scheme was applied. According to Schlipf et al. (2016), a hybrid O-H type mesh composed of hexahedrons and tetrahedrons can capture complex geometries and provide good convergence. Thus, the computational domain was divided into five major blocks, each with a central body of influence as shown in Figure 15. While the core cube (body of influence) was discretized as a tetrahedral cell, the domain's outer edges were divided into hexahedral cells. To report grid-convergence studies uniformly, the concept of the grid-convergence index (GCI), proposed by Roache (1994, 1997), was applied. Further details of the mesh sensitivity study are outlined in Appendix A.

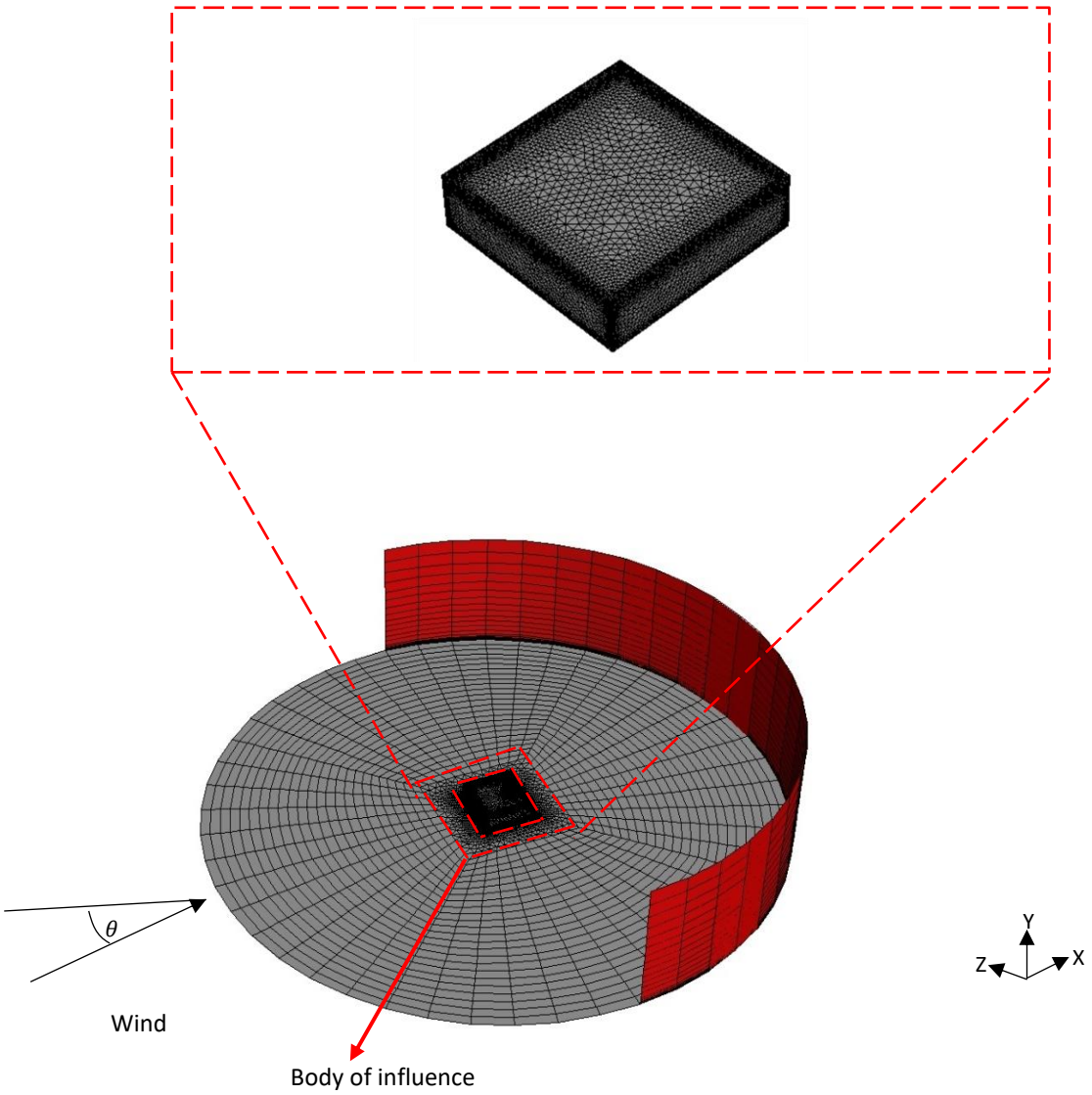

Figure 15: Perspective view of computational grid at bottom, side and back face of the computational domain for flat roof model

For the turbulence modeling, a Reynolds-Averaged Navier-Stokes (RANS) approach (ANSYS Fluent v19.2) was used. Specifically, the realizable k-epsilon ($k-\varepsilon$) model was applied. Developed by Shih *et al.*, (1995), the realizable k-epsilon ($k-\varepsilon$) is described as 'realistic' since it satisfies certain mathematical constraints in contrast to the standard $k-\varepsilon$ model reported in Jones & Launder, (1972). Also, the realizable k-epsilon (k) was chosen since it had previously been investigated along with other turbulence models for a similar computational domain by Gimenez and Bre (2019).

Given the nature of the computational domain, it is essential that the approaching flow is homogeneous. In reality, the computational domain truncates the real world, and so the boundary

conditions must be assigned correctly to reflect the problem as documented in Blazek, (2005). Further, empirical equations, such as power laws for velocity, can result in the inlet flow changing rapidly (Mathew, 1987). Near the surface, the flow can accelerate significantly before being slowed by the building. A modified velocity and turbulence profile associated with the turbulence model proposed by Richards and Hoxey (1993), and later Richard and Norris (2015), was thus required. It must be noted that using modified polynomial coefficients to modify (Richards and Hoxey, 1993) equation results in velocity gradients changing by less than 4% across the entire boundary layer (Richard and Norris, 2015).

The representation of the Atmospheric Boundary Layer (ABL) was achieved by implementing User-Defined Functions (UDFs) within the ANSYS Fluent solver. These UDFs were formulated to describe the velocity profile (U), turbulent kinetic energy (k), and the dissipation rate (ϵ). As demonstrated in prior research conducted by Heargraves and Wright (2007), a wall function that is compatible with the ground, along with a symmetry condition applied to the top boundary of the domain, was employed to maintain the inflow profile's consistency along the fetch, regardless of the distance between the inlet and the building. Figure 16 illustrates the reference coordinates, heights, and velocities. With respect to the boundary conditions, the outlet was designated as pressure outlets. The utilisation of the wall functions suggested by Launder and Spalding (1974), which integrate the adjustment of roughness by Cebeci and Bradshaw (1977), is implemented for the purpose of modelling the surface of the ground. The determination of the roughness parameters, specifically the sand-grain roughness height k_s and the constant c_s, was conducted by establishing their consistency relationship with the aerodynamic roughness length Y_o as derived by Blocken *et al.* (2007b). The domain was regarded as isothermal with no-slip conditions applied to the building and roof surface. A comprehensive description of the boundary conditions can be found in Appendix B.

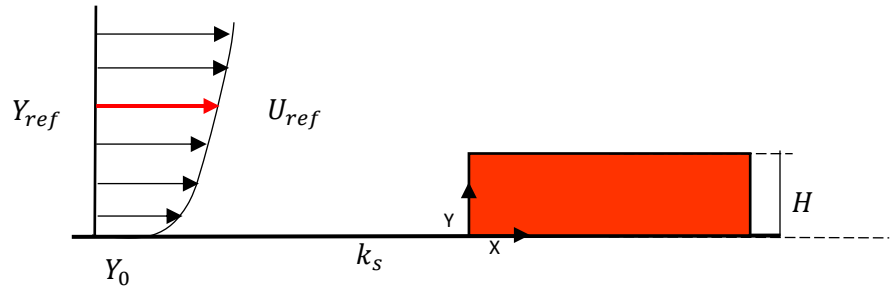

Figure 16: Reference coordinates, heights, and velocities (Not drawn to scale). H is the height of the building (4m), $U_{ref=}$ 2.5, 5 m/s is the velocity at the reference height $Y_{ref} = 3.5\mathrm{m}$, $k_s = 0.028$ the sand-grain roughness height. Y is the vertical coordinate, Y_0 the surface roughness height.

For the solver settings, the SIMPLE algorithm scheme was used as the pressure velocity coupling. Pressure interpolation in second order and second-order discretization schemes were specified for both the convection and viscous terms of the governing equations. The solution was initialized by the values of the inlet boundary conditions, termed as velocity inlet. The chosen convergence criterion was specified so that the residuals for the velocity components, turbulent fields, and continuity have decreased to 10^{-5} as recommended in European best practice guidelines of COST Action 732 (Franke *et al.*, 2007; Gimenez and Bre, 2019)

2.3 Validation

To assess the validity of the method and numerical setup applied, the simulation results were compared with other experimental results. This was done to assess the accuracy of the CFD simulation, the significance of which is documented elsewhere (Ferziger & Perić, 1996; Roache, 1997; AIAA, 1998; Celik *et al.*,2008). To do this, experimental data from wind tunnel measurements performed by the Wind Engineering Information Center of Tokyo Polytechnic University (TPU), (Tamura, 2012) was used. The database was primarily considered for its isolated low-rise buildings. Three types of roof models are represented in the database: flat-roof, gable-roof, and hip-roof, each containing statistical values of average wind pressure coefficients on roof and wall surfaces.

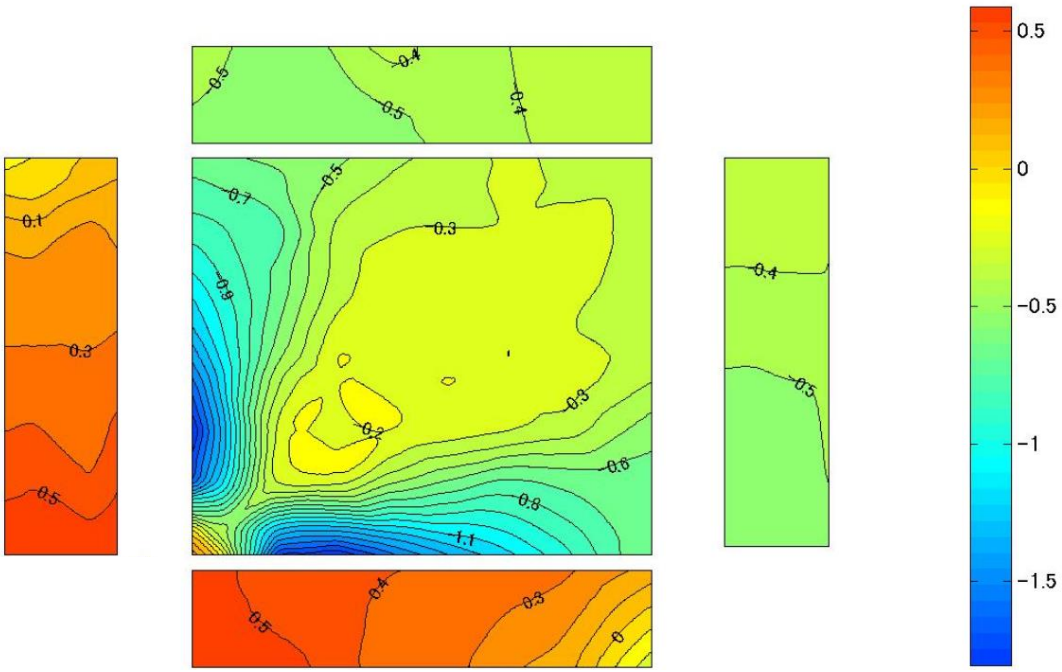

Mean wind pressure coefficients on a flat roof of a low-rise building (TPU). θ=45°

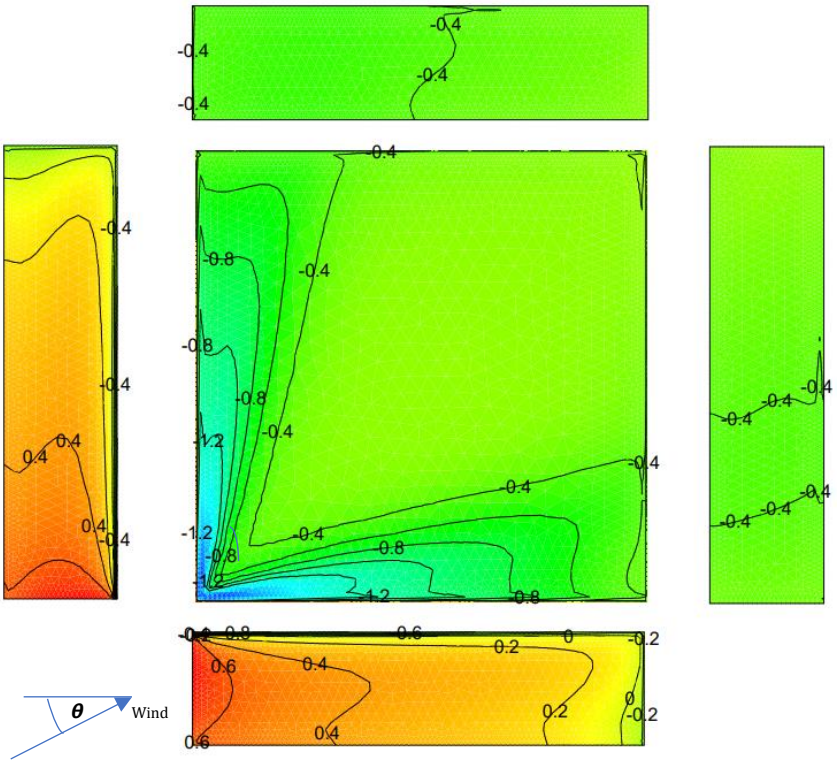

Mean wind pressure coefficients on a flat roof of a low-rise building (CFD simulation). θ=45°

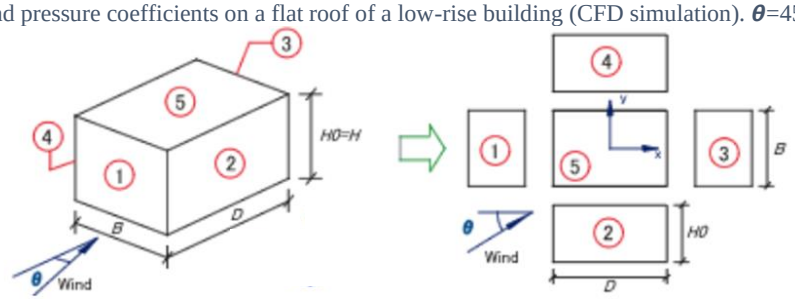

Figure 17: Results of mean pressure contour plots at wind angle of 45 a. TPU Experimental data b. CFD Simulation

For the prediction of averaged pressure coefficients on the building surfaces, the geometric parameters in the database for B/D/H=16:16:4 (the same as that in this study) were chosen for wind incidence angles of 0° and 45°. The contour plots of mean pressure are shown in Figure 17 for wind incidence angles of 45°. Additional information on this validation can be found in Appendix C.1. Largely, it was found that both the wind incidence angles considered in the simulation and the TPU database result have similar vortical "footprints" on the surface, as well as similar pressure magnitudes and distributions as shown in Figure 17. Discrepancies observed from the comparison results is primarily from simulated wind fields (e.g., terrain and length scale) as well as the level of detail in meshing.

In addition, given the interest in aerodynamics around the building and on the roof, and particularly the need to understand how aerodynamics impacts collector heat loss, it was determined to qualitatively compare the flow around the building. This was carried out by comparing the velocity streamlines from the work of Martinuzzi and Tropea's (1993) and the CFD simulations. In Martinuzzi and Tropea (1993), tracer particles were used for the laser light sheet visualization experiments with smoke generated from a commercially available fog-generator. The study conducted by Martinuzzi and Tropea (1993) continues to be highly referenced in the literature, as evidenced by Abohela's (2012) documentation and the findings of the present study. This research is particularly notable for its investigation of flow behaviour around cube models that simulate low-rise buildings. Here, the velocity streamlines along the building's center plane were extracted in 2D from the CFD simulation for wind incidence angle normal to the building where ($\theta = 0^{o}$). Figure 18 shows a comparison of this study's CFD results and the experimental data obtained by Martinuzzi and Tropea (1993). As can be seen, the result provides a good qualitative agreement between the CFD simulations and Martinuzzi and Tropea (1993)’s results.

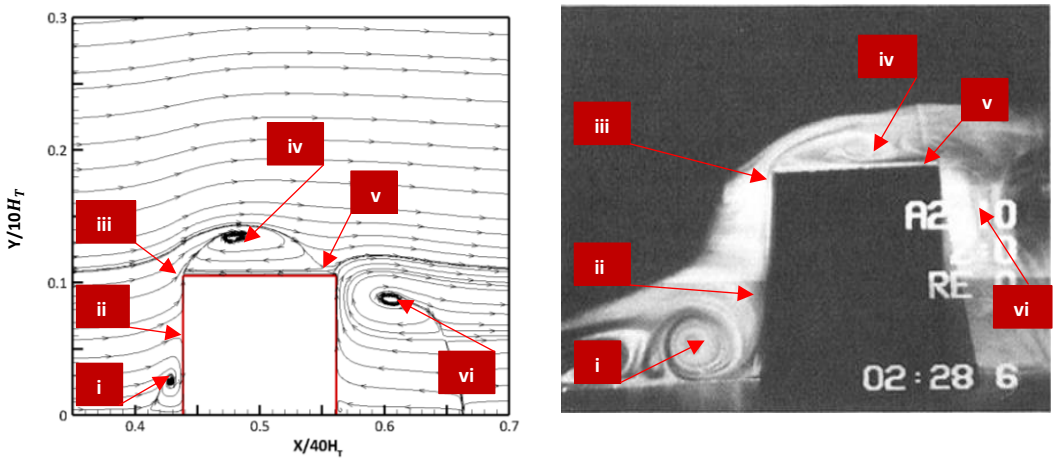

a. CFD simulation at center plane of domain Operating conditions v=10m/s, wind incidence angle of 0°)

b. Laser sheet visualization of the flow in front of a cube (Martinuzzi and Tropea, 1993)

i	Standing vortex
ii	Stagnation point
iii	Flow separation
iv	Vortex (roof top)
v	Re-attachment point
vi	Leeward vortex

Figure 18: Comparison between the CFD results and experimental results.

2.4 Results and Discussion

Having validated the numerical method, it was decided to investigate the CFD findings in greater detail, first to gain an understanding of the overall flow structure and velocity on the roof and around the building when parapet heights are varied, and secondly, to determine whether based on the above, a variation in collector location across the roof, with or without parapet would likely impact the collector heat loss.

2.4.1 Aerodynamics on roof of low-rise buildings without parapets

For building without perimetric parapets, Figure 19 depicts the generation of three vortices, occurring both upstream and downstream of the domain, as well as on the rooftop of the structure. As the oncoming flow approaches building, it deflects along its sides resulting in the creation of

a point of maximum pressure, commonly referred to as the stagnation point. Likewise, the windward side of the building generates a downwash flow, which opposes the incoming airflow and results in the development of a standing vortex at the base of the building. According to Reiter (2010), the height of the building has an impact on the characteristic length of the vortex and wind speed within this area. Moreover, it is apparent that the positioning of the downwash is impacted by two key variables: the direction and intensity of the incoming wind, as well as the vertical dimension of the windward surface of the building's exterior. This suggests that the inclusion of parapets is expected to have an impact on both the location of the stagnation point and the characteristics of the downwash phenomenon.

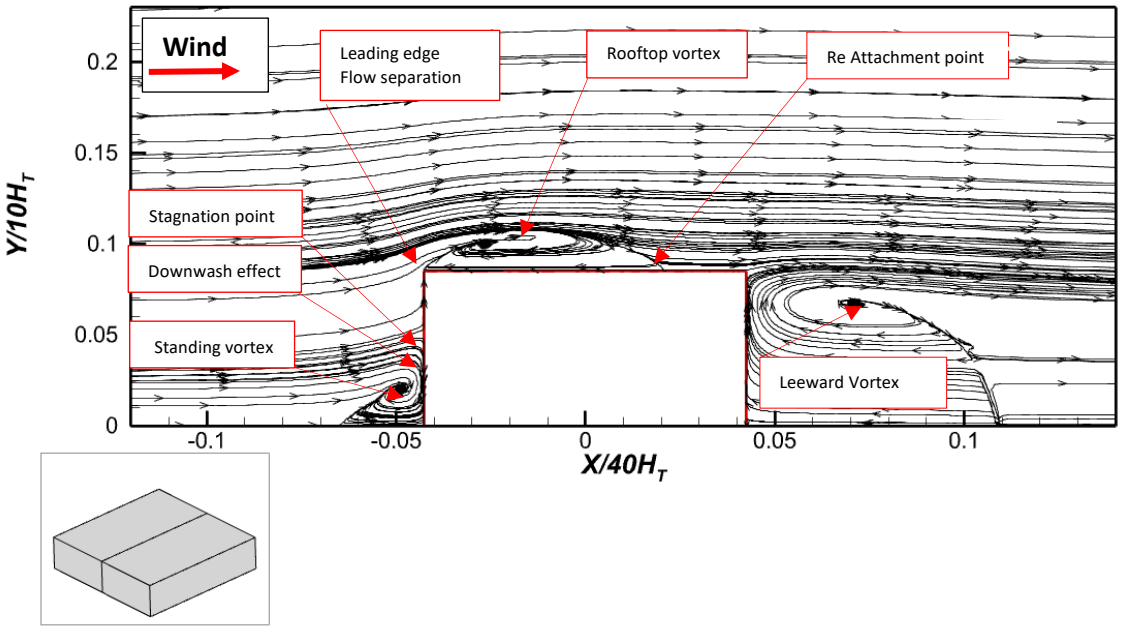

Figure 19: Velocity streamlines on center plane of the domain without perimetric parapets (Operating condition of wind velocity V=10m/s, wind incidence angle 0°)

At the roof, a flow separation can be seen on the building's leading edge, where it abruptly separates from oncoming flow. The separated flow is displaced above the roof, and a vortex forms beneath it due to reattachment on the roof surface. When the flow field changes direction from reverse to forward, reattachment points form near the roof surface, causing a separation bubble to form. The roof vortex is close to the roof surface, as seen in Figure 19. The nature of the vortex formed on the roof, which is separated by the flow separation at the leading edge of the building, and the reattachment point suggests a parapet and collector will alter the vortex formation. As

depicted, the vortex expands across the roof, which suggests that placing a collector above the roof will displace the vortex. Further, when the roof area is examined in terms of velocity, Figure 20, it is visible that lower velocity is formed at the leading and trailing edges of the roof; areas where the vortex does not extend. At the center of the roof, where the roof vortex depicted in Figure 19 is present, velocity appears to be higher but diminishes above the roof.

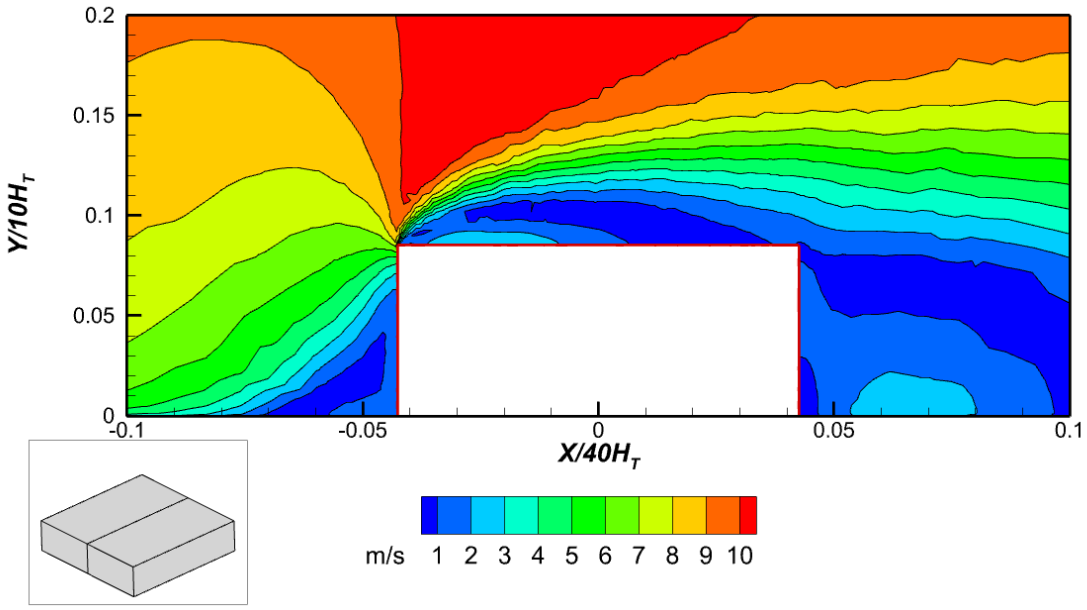

Figure 20: Mean Velocity contours on center plane of the domain without perimetric parapets (Operating condition of wind velocity V=10m/s, wind incidence angle 0°)

The aforementioned observation implies that unglazed collectors, being sensitive to wind, may experience reduced heat loss if positioned with a lower tilt angle near the leading edge of a roof without a parapet. This is attributed to the presence of a lower velocity in those specific areas. On the other hand, positioning a collector at the centre of a roof without a parapet is expected to lead to significant heat dissipation, particularly due to the observed expansion of the high-velocity region. It is imperative to acknowledge that the above is also contingent upon the tilt angle of the collector. This phenomenon occurs due to the inclination of the collector, whereby a higher tilt angle results in the trailing edge of the collector extending beyond the roof surface, thereby encountering flow separation and vortex effects.

2.4.2 Aerodynamics on roof of low-rise buildings with low perimetric parapets

Figure 21 depicts the aerodynamics with a low perimetric parapet present. Similarly, the building is surrounded by three vortices, one on each side and one on the roof. The flow forms a maximum

pressure at the stagnation point along the windward façade, with a standing vortex formed upstream of the building due to the downwash effect and the flow opposing the oncoming flow. In comparison to a scenario without a parapet, it is observed that the aerodynamics on the roof is different.

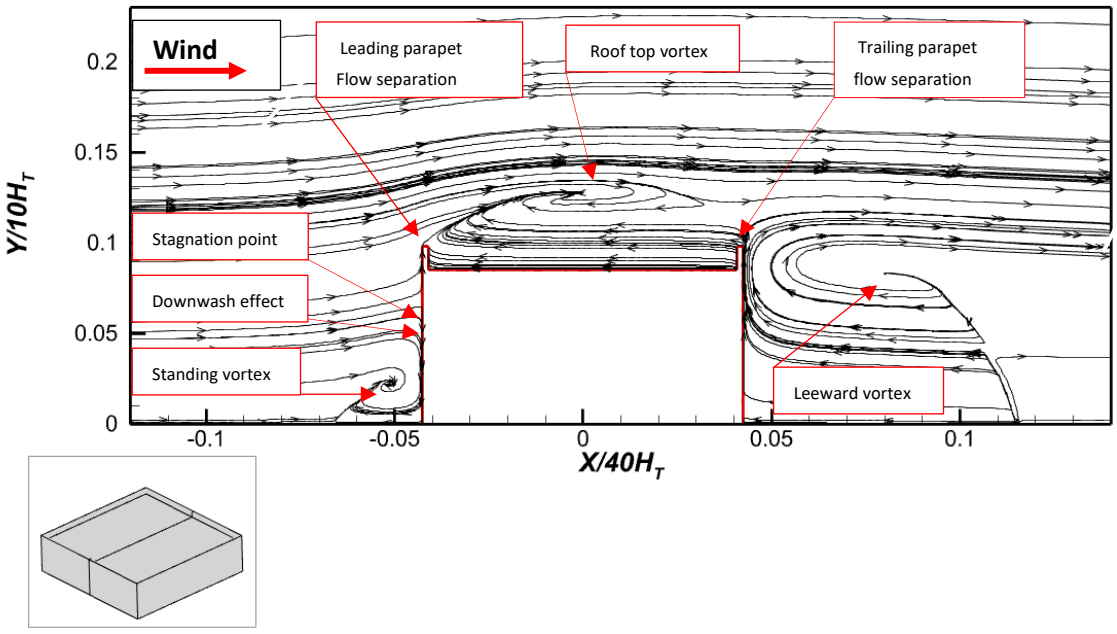

Figure 21: Velocity streamlines on center plane of the domain with low perimetric parapets (Operating condition of wind velocity V=10m/s, wind incidence angle 0°)

Parapets, as shown in Figure 21 above, displace the roof vortex higher above it. In this case, the pattern of the vortex is determined by the interaction between the backward-facing step flow from the leeward vortex (downstream of the domain), and the flow separation at both the trailing and leading parapet. Also, considering the backward-facing step flow from the edge of the trailing parapet in Figure 21, it is apparent that mounting the collector toward the trailing edge will result in down washing of its rear due to the aerodynamics in that region.

When examined in terms of velocity, Figure 22, the center of the roof has a higher velocity area. And this extends above the parapet. Particularly, this is more dominant at the center of the roof which suggests that mounting wind-sensitive collectors along the roof surface at any point on a roof with a low parapet could result in significant heat loss, given the predominant presence of high-velocity winds shown.

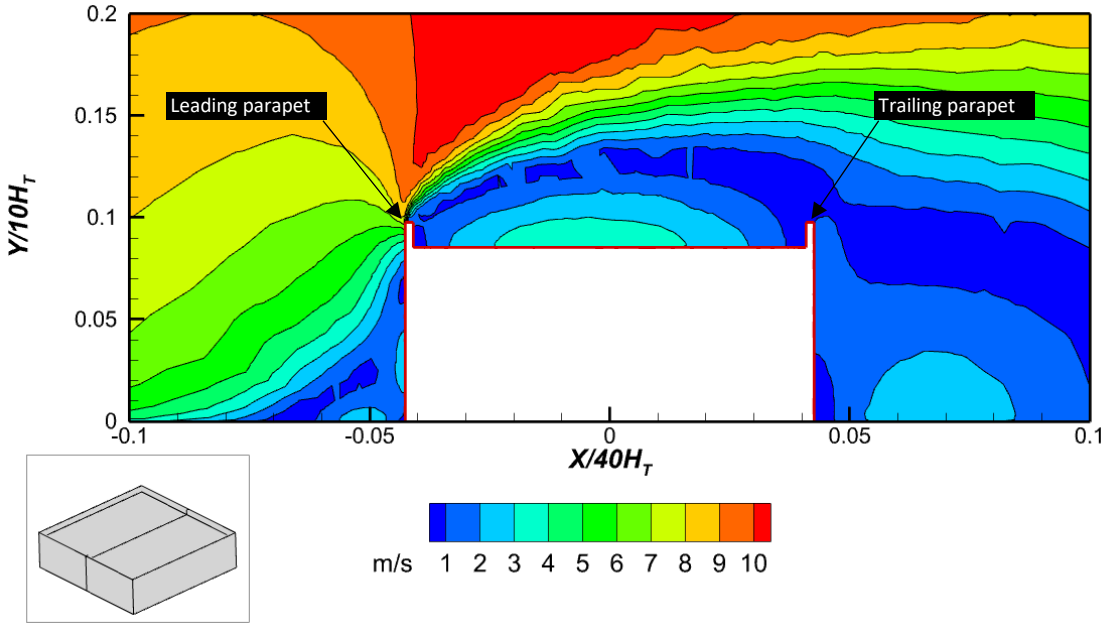

Figure 22: Mean Velocity contours on center plane of the domain with low perimetric parapets (Operating condition of wind velocity V=10m/s, wind incidence angle 0°)

On the contrary, the regions closer to both the leading and trailing parapets show lesser velocity. Accordingly, mounting collectors so close to the parapet edge has the obvious drawback of causing shading from the parapet, which has been shown to negatively impact collector performance (Applebaum and Bany, 1979).

2.4.3 Aerodynamics on roof low rise buildings with high perimetric parapets

An aerodynamic analysis of a roof with higher perimetric parapets can be seen in Figure 23. As in the previous two cases, there are three vortices present with a stagnation point forming on the windward façade (upstream of the domain). On the windward surface, the point of downwash and stagnation is higher than that in the case of no and lower parapets.

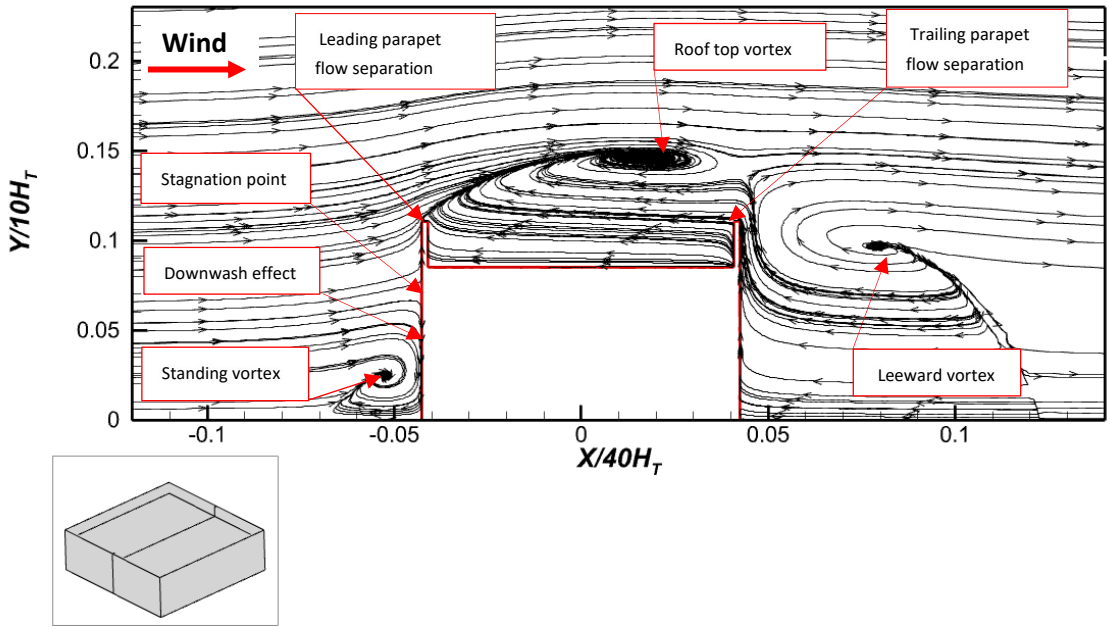

Figure 23: Velocity streamlines on center plane of the domain with high perimetric parapets (Operating condition of wind velocity V=10m/s, wind incidence angle 0°)

Unlike the low and no parapet cases, the vortex formation at the roof top is displaced closer to the trailing parapet than at the center of the roof. Similar to that observed for the low parapet, the backward stepping flow and the separation of flow at the leading and trailing parapet determine the formation of the vortex on the roof. In this case, the eye of the vortex is displaced higher above the roof surface which is as a result of height of the parapet. In comparison with earlier cases (no and low parapet), a region of higher velocity is more prominent across the roof as depicted in Figure 24. Particularly, higher velocities are formed at the roof's center. The regions near the parapets show lower velocity than at the roof center, which is due to the obstructing effect of the parapets to the oncoming and back stepping flows.

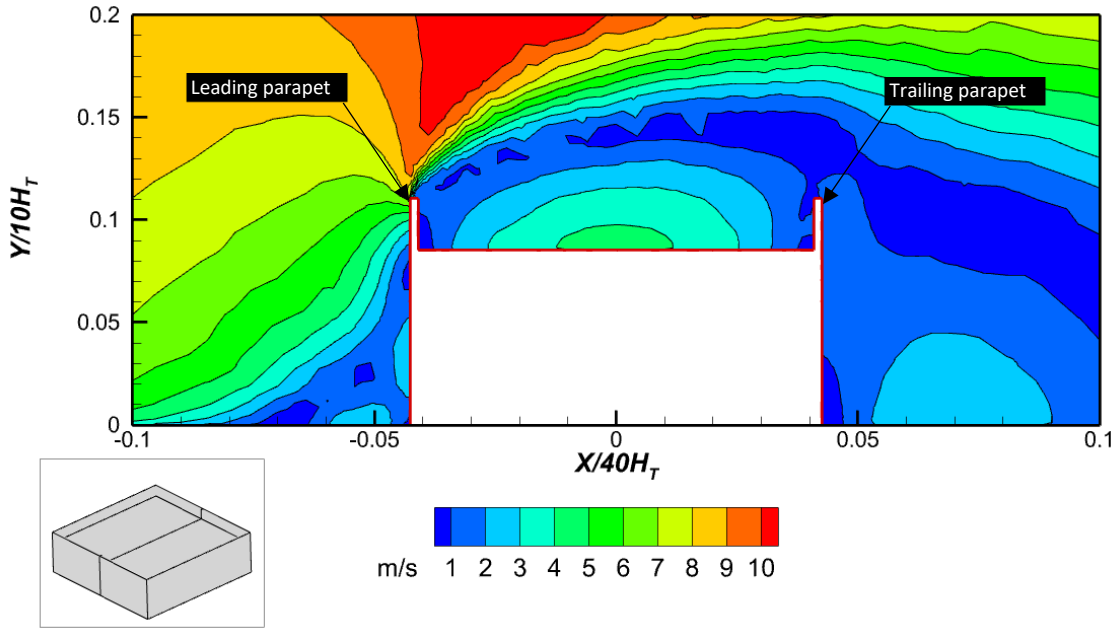

Figure 24: Mean Velocity contours on center plane of the domain with high perimetric parapets (Operating condition of wind velocity V=10m/s, wind incidence angle 0°)

Based on the aforementioned observations, it can be deduced that the installation of a wind-sensitive collector on a roof featuring higher parapets, particularly at its central location, will result in a more significant dissipation of heat. This assertion remains valid even when considering higher collector tilt angles, as the elevated velocity zone persists beyond the roof and surpasses the parapet height. On the contrary, the presence of a lower velocity zone in the vicinity of the parapet indicates a reduced rate of heat dissipation. However, it is important to acknowledge that this observation may be influenced by potential shading effects on the collectors.

2.4.4 Characteristics of flow features

To further elaborate on the effect of the parapet and how that translates to a change in the roof aerodynamics, the characteristic length of the recirculation upstream of building, Length of the recirculation on roof of the building, Length of the recirculation downstream of building and height of the stagnation point is reported. As can be seen in Table 1, an increase in the parapet height leads to a corresponding increase in all the parameters assessed, thereby establishing the assertion that the existence of the parapet exerts a substantial influence on the aerodynamics of the roof.

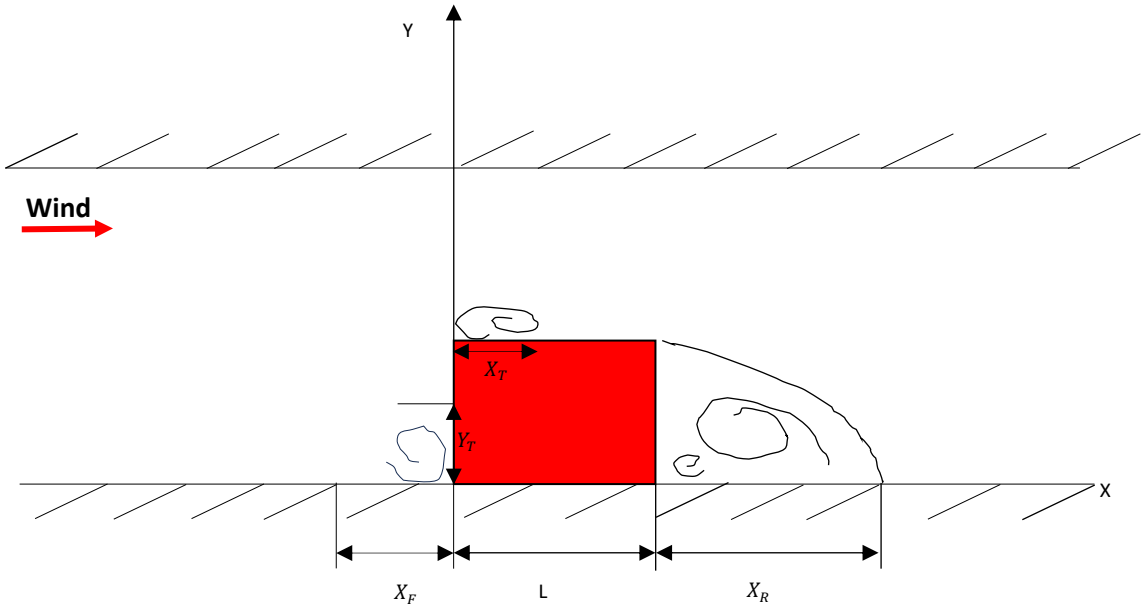

Figure 25: Sketch of the model in domain

Based on Figure 19,Figure 21 and Figure 23, upwind of the domain, X_F is the length of the recirculation, X_T is the length of the reattachment length on the roof, X_R is the recirculation length downstream of the domain, L is the length of the building while Y_T length of the stagnation point.

Table 1 Summary of flow reattachments and stagnation of different building with and without parapets

	Length of the recirculation upstream of building [X_F]	Length of the recirculation on roof of the building [X_T]	Length of the recirculation downstream of building [X_R]	Length of the stagnation point [Y_T]
No Parapet	0.0234	0.0642	0.06767	0.0475
Low Parapet	0.0236	0.0751	0.0731	0.0663
High Parapet	0.0236	0.0861	0.0812	0.0678

2.5 Chapter Conclusion

In this chapter, an analysis was conducted to investigate the impact of parapets on the aerodynamics and velocity of a low-rise building. The results indicate that substantial heat losses may occur when wind-sensitive collectors are installed at a distance from parapets, as evidenced by roof velocity and aerodynamics. In instances where parapets are absent or of limited height, it has been observed that the velocity of airflow is diminished in proximity to both the leading and trailing edges of the roof, while it is heightened at the central region of the roof.

Increasing the height of parapets offers the opportunity to place wind-sensitive collectors in closer proximity to both the leading and trailing edge. This is due to the parapet's ability to reduce velocity in its immediate vicinity. Nevertheless, the positioning of the collectors is limited by the factor of shading, which possesses the capability to influence their performance. The results also indicate that the inclusion of parapets has a notable influence on the length of recirculation on the roof, as well as the formation of vortices both upstream and downstream of the building, including the elevation of the stagnation point.

Also, the results show that that the rooftop vortex exhibits a significant vertical extension beyond the roof surface, particularly in the case of higher parapets. Based on the preceding observation, it is evident that the inclination angle of the collector holds significance, particularly in the case of roofs featuring parapets. Additionally, the findings indicate that the rooftop vortex demonstrates a substantial vertical expansion beyond the roof's surface, particularly when higher parapets are present. The preceding observation indicates that the inclination angle of the collector is of importance, especially when considering roofs with parapets.

The investigation of the effects of different mounting locations and tilt angles on wind-sensitive solar collectors, in the presence of parapets, is motivated by the potential modification of roof top aerodynamics and wind velocity resulting from the installation of these collectors on the roof. The exploration of this topic is discussed in Chapter 3.

Chapter 3

Study of wind-induced convection heat transfer on a standalone, unglazed solar thermal collector mounted on a roof with perimetric parapets.

3.1 Introduction

Chapter 2 of this study demonstrated that in the case of low-rise buildings featuring perimetric parapets, there exists a notable variation in aerodynamics and velocity on the roof. A significant number of low-rise buildings, specifically those of industrial or residential nature, experience constraints in terms of roof space availability, primarily due to the presence of service equipment or other architectural components. Thus, due to various operational factors such as wind incidence angle, collector tilt, and others, it is not feasible to install solar collectors at predetermined locations. The incorporation of solar collectors on rooftops, commonly equipped with parapets, requires a recognition of the influence exerted by these parapets and other operational factors on roof aerodynamics and velocity. These factors can subsequently affect the rate at which heat is lost by the collector.

The convective heat transfer coefficient (CHTC) plays a crucial role in the assessment of heat transfer through convection from the collector. Its value is directly influenced by the wind velocity, as indicated by various equations employed in the calculation of useful energy from solar collectors. Therefore, given the observed variability in aerodynamics and local velocity on the roof, as discussed in the preceding chapter and supported by existing research, it is crucial to conduct a more thorough investigation. This is because convective heat transfer coefficients have been found to differ for bodies experiencing different flow patterns and velocities.

Meinders *et al.* (1999) conducted a study to investigate the occurrence of local convective heat transfer within a cube situated in a turbulent channel flow characterised by low Reynolds numbers. A notable discrepancy in convective heat transfer, amounting to a maximum of 100 percent, was observed among the five surfaces of the cube. The observed discrepancy can be ascribed to the inherent characteristics of the flow field and the turbulent velocity field. In a

similar way, Defraeye *et al.* (2011) evaluated a cube put in a turbulent channel flow of low and high Reynolds number using a steady Reynolds-Averaged Navier–Stokes application. The study revealed a significant variation in the convective heat transfer coefficient (CHTC) across the windward surface of the cube. This variation can be attributed to the distinct flow characteristics that were examined.

Kahsay *et al.* (2017) employed numerical simulations to assess the forced convection heat transfer coefficients on the facades of low and high-rise buildings. The Convective Heat Transfer Coefficient (CHTC) was observed to exhibit a positive correlation with the height of the building, which aligns with the alterations in flow patterns and the subsequent rise in wind velocity within the atmospheric boundary layer. In their study, Karava *et al.* (2012) conducted an investigation on the convective heat transfer characteristics of roof mounted solar collectors. Specifically, they examined a 30° slanted building roof utilising a PV-thermal system. The researchers discovered that a comprehensive analysis of convective heat transfer on inclined roof surfaces necessitates the meticulous consideration of various factors, including the turbulence characteristics of the natural wind and the topography upstream.

Numerous studies have provided evidence indicating that the flow characteristics in the vicinity of an object significantly influence convective heat transfer, resulting in varying heat loss. Therefore, given the significant influence of parapets on the flow dynamics of roofs, as evidenced in chapter 2, it is crucial to investigate the potential ramifications of other parameters alongside parapets in relation to the aerodynamics of roofs, particularly in terms of heat loss from collectors.

3.2 Method

To address the issues described above, a low-rise 3D building measuring 16 m in length, 16 m in width, and 4 m in height was modelled using CFD, see Figure 26 . On the roof, two Unglazed Solar Collectors (USC) were mounted side by side. Each had dimension 2m (length), 1m (width) 0.07m (thickness). Moreover, the model integrated perimetric parapets, which were derived from the categorisation of low and high parapets that were previously investigated in this study. Subsequently, the heat loss of the collector was examined under different operating conditions, as illustrated in Figure 27.

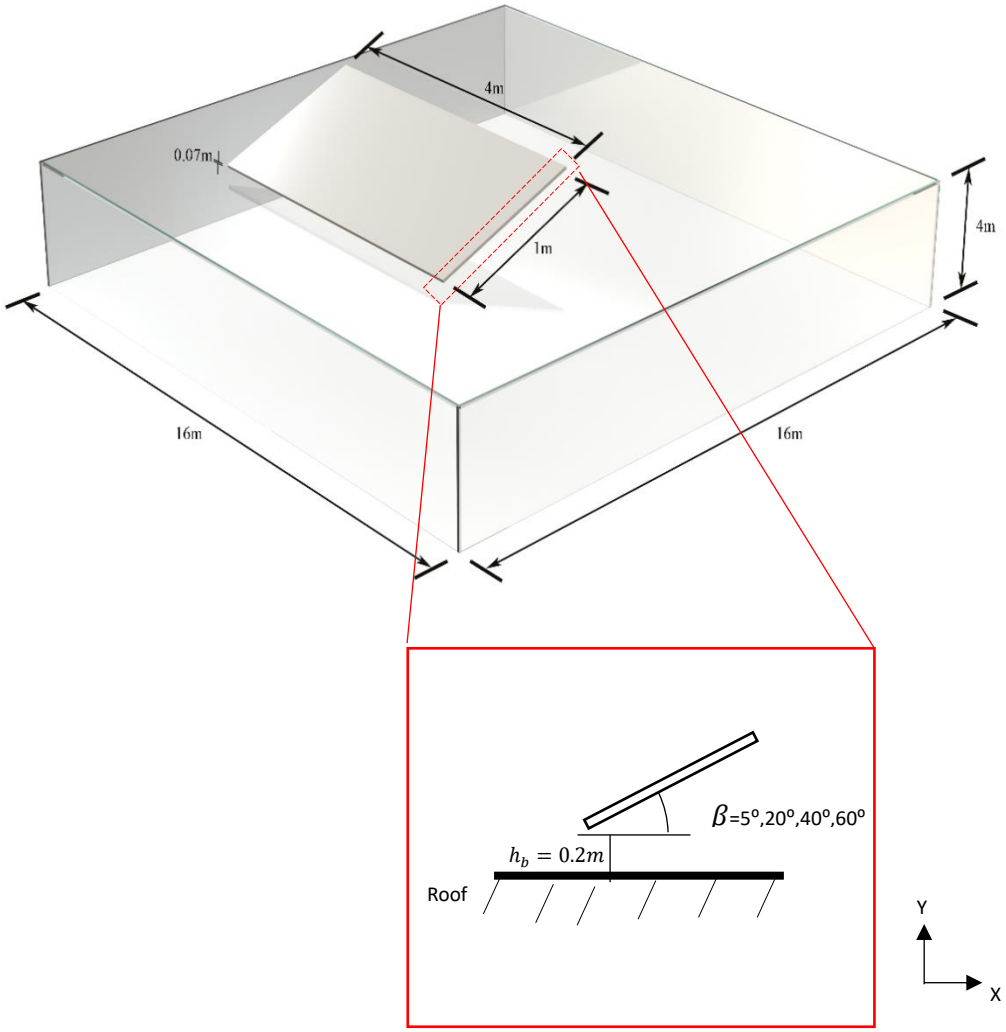

Figure 26: Geometry of model with standalone collector for the case of no parapet (Not drawn to scale)

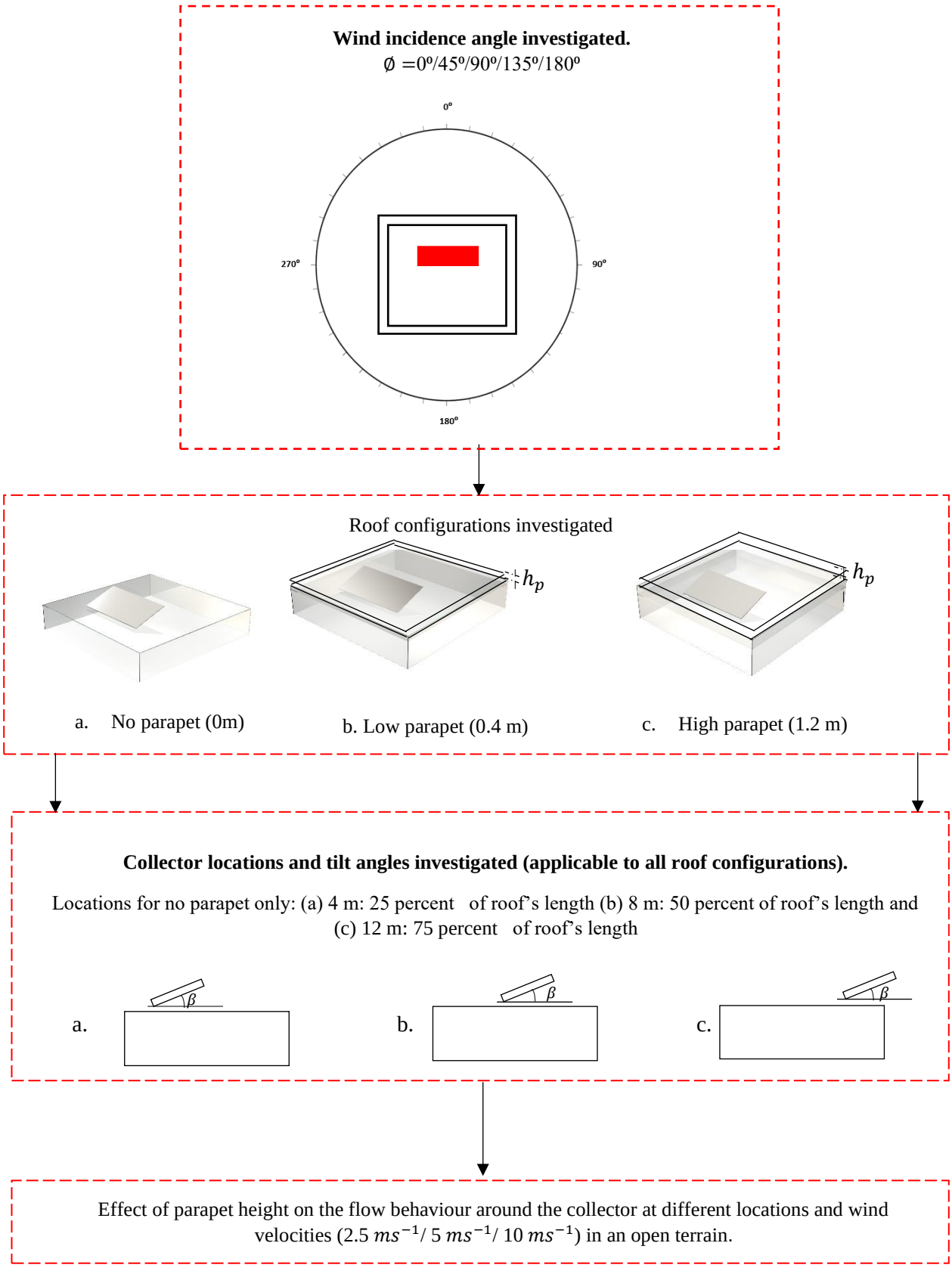

Figure 27: Flow diagram of investigation sequence.

As shown in Figure 27, the collector was installed in three different positions on the roof, each representing 25, 50, and 75 percent of the roof's total length. To account for the presence of structural support systems commonly found in roof-mounted solar collectors, the leading edge of each collector was positioned at 0.2 metres from the roof surface. As demonstrated, the inclination angle of the collector in relation to the plane of the roof was adjusted to 5°, 20°, 40°, and 60° for each scenario involving the absence, presence of a low parapet, and presence of a high parapet. In order to achieve precise simulation of various flow conditions while accounting for slight variations in factors such as the mounting location of the collector, tilt angle, and parapet height, the computational domain was maintained in a circular shape, as outlined in section 2.2 of this study (see Figure 14).

The selection of a computational domain with a height of 10H, as per the recommendations of COST Action 732 (Franke et al., 2007), ensures that the model maintains a maximum blockage of less than 3 percent across all aspects. To ensure the redevelopment of flow, a value of 20H was employed in order to position the outflow boundary at a sufficient distance behind the wake region. Subsequently, the process of meshing the domain was undertaken.

The flow domain was meshed using a hybrid O-H mesh, while the computational domain was discretised into five hexahedral blocks, see Figure 28. The body of influence and the building, except for the computational domain, were discretised into hexahedral cells. However, the inner cube, also known as the body of influence, was discretised into tetrahedral cells. The grid-convergence index (GCI) developed by Roache (1994, 1997) was employed in the computation of mesh sensitivity. The detailed outline of the mesh sensitivity analysis can be found in Appendix A.

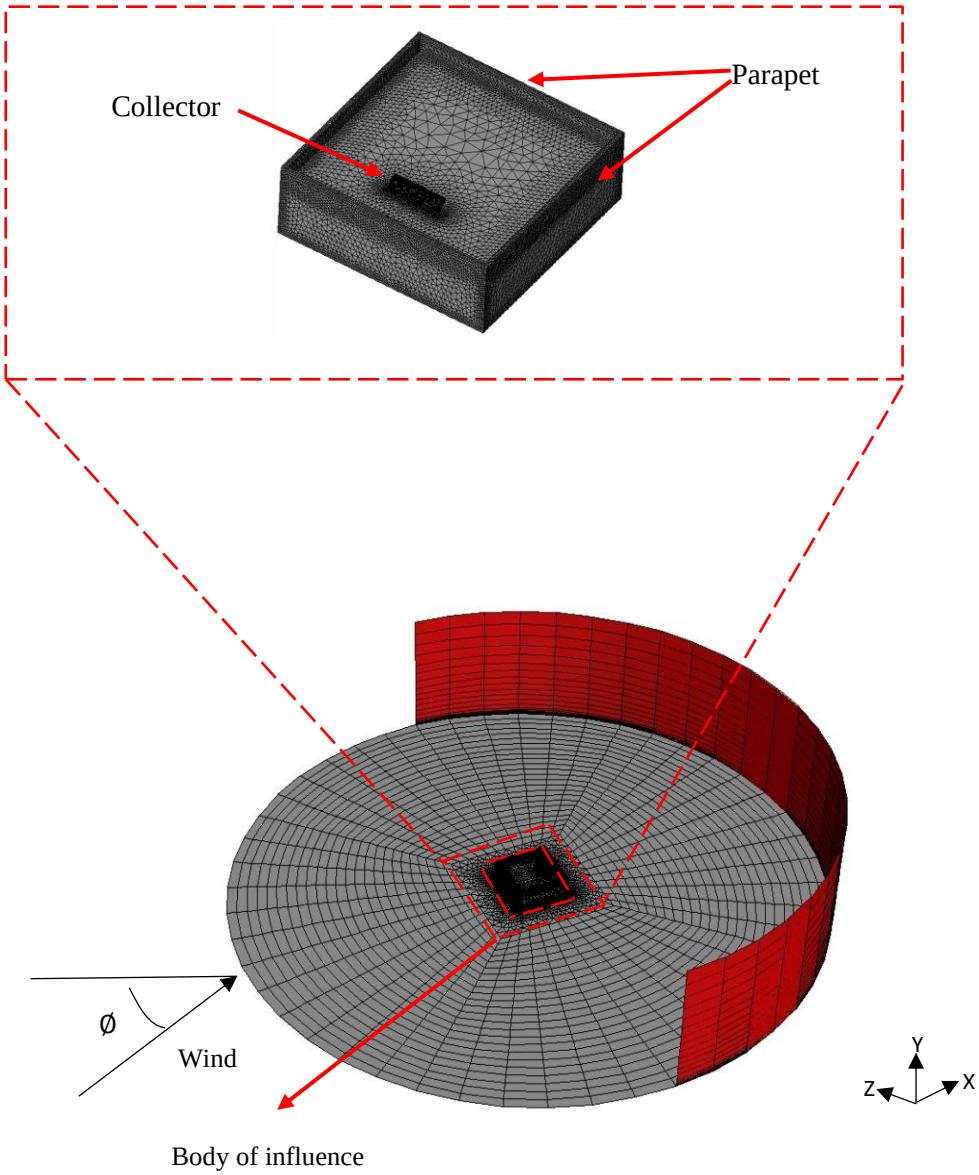

Figure 28: Perspective view of computational grid at bottom, side, and back face of the computational domain for model with parapet

User-Defined Functions (UDFs) were used in the ANSYS Fluent solver to achieve homogeneity of the approaching flow based on Richard and Norris (2015). The boundary conditions were specified as pressure outlets for outlet, standard wall function with sand grain roughness at the bottom, and symmetry at top. A no-slip condition was applied to the building, collector and roof surface. This is elaborated in detail in appendix B and section 2.2. For closing the transport equation, the $k-\varepsilon$ turbulence model-realizable was applied, the SIMPLE algorithm was used for pressure velocity coupling and pressure interpolation at the second order. Second-order discretization techniques were used to solve the viscosity and convection equations.

Due to the interest in the effects of parapets on wind velocity and how that affects roof mounted wind sensitive solar collectors, variable wind velocities were investigated. Three wind velocities of 2.5, 5, and 10 m/s were used, representing the Reynolds number range of $1.646x10^6$ to $6.586x10^6$. This velocity range was determined using the Richardson number for thermal convection, Ri, a nondimensional parameter used to estimate the relative contribution of forced and natural convection in a given scenario. Natural convection becomes insignificant when the Richardson number (Ri) is less than 0.1, while forced convection becomes insignificant when Ri exceeds 10. However, when the Richardson number falls within the range of 0.1 to 10, neither natural nor forced convection can be considered negligible. Appendix D describes in detail how to calculate velocity using the Richardson number.

Furthermore, a decision was made to maintain the temperature difference between the ambient and collector at 298 K and 328 K respectively to enhance conciseness and reduce the number of parameters currently under investigation. Following this, an evaluation was conducted to determine the wind speed in relation to different angles of wind incidence towards the structure. These angles included 0°, 45°, 90°, 135°, and 180°, as illustrated in Figure 27.

3.3 Validation

The validation of the numerical method was conducted by utilising pressure coefficient values. This approach was chosen due to the well-established inverse correlation between velocity and pressure, as well as the recognition that parapets have an impact on velocity, which subsequently influences the heat loss of the collector. Consequently, two distinct validations were conducted: initially for a freestanding collector mounted on the roof, and subsequently for a freestanding collector mounted on the roof with a perimetric parapet.

In the initial phase, the outcomes obtained from the computational fluid dynamics (CFD) simulations were juxtaposed with the empirical investigations conducted by Stathopoulos *et al.* (2014) and Xypnitou (2012). This comparison was carried out for a Standalone collector, adhering to a 1:200 geometric scale, which was affixed to a level rooftop lacking perimetric parapets. The

findings of the computational fluid dynamics (CFD) simulation were observed to align with the reported results, as illustrated in Figure 29 and further outlined in Appendix C.2.

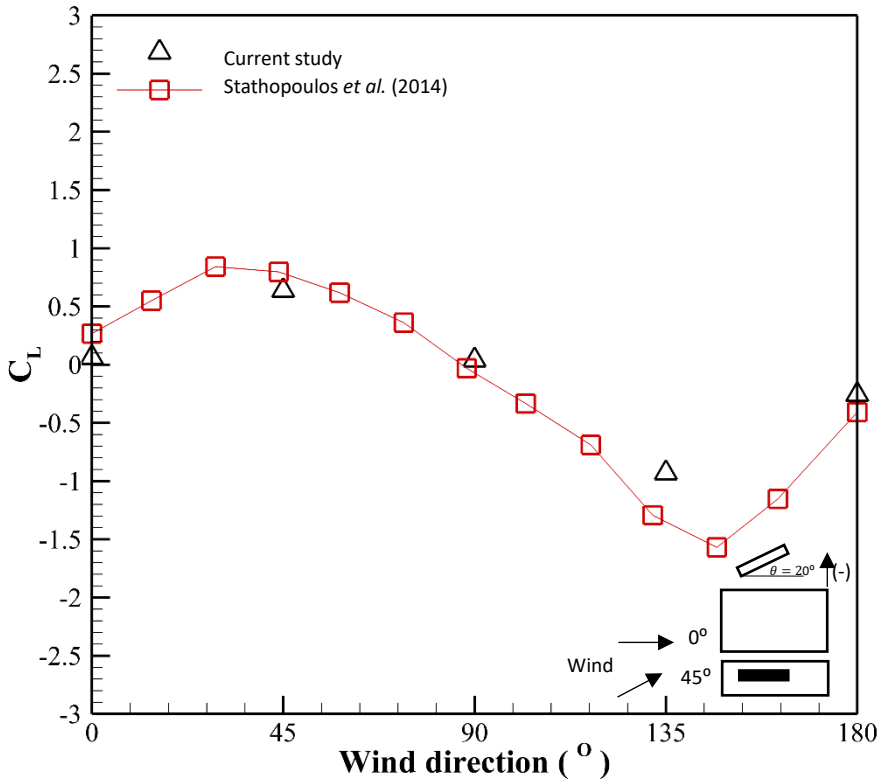

Figure 29: Comparison of Lift coefficient (C_L) for panels inclined at 20° at varying wind incidence angle located at 25 percent of roof length.

Subsequently, the numerical method for a standalone collector with perimetric parapets was validated. This was undertaken through a wind tunnel study at the University of Auckland's ABL wind tunnel. The wind tunnel is closed-circuit, with a cross-section of 3.6 m (width) 2.5 m (height) and a test section of 20 m. To generate the required wind profile, the tunnel is equipped with two fans as well as a combination of roughness elements such as spires and trips.

To undertake the wind tunnel study, a model made of polymethyl methacrylate (PMMA) sheet at a length scale of 1:20 was constructed. Dimensions of the model were 0.8 m (D) by 0.8 m (B) by 0.2 m (H), with a ratio of height (H) to breadth (B) of 1:4 and breadth to depth (D) of 1:1. These dimensions were taken into account because they closely matched those of the models used in the Aerodynamic database of low-rise buildings at the Tokyo Polytechnic University (Tamura, 2012).

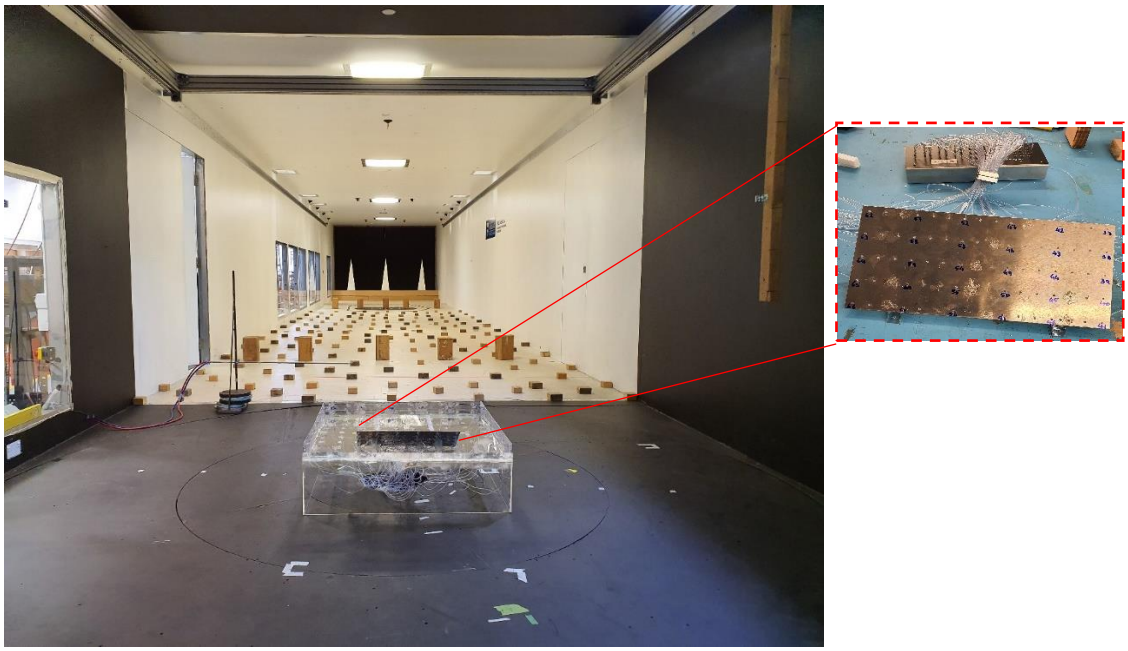

Figure 30: Photograph of model of the low rise building with standalone collector and perimetric parapet in the UoA wind tunnel.

As shown in Figure 30, an aluminum plate measuring 0.4 m (H) by 0.2 m (B) and 0.03 m thick was mounted on the flat roof. A larger collector size than 1:20 scale (1: 10 scale) was considered in this instance to allow for a wider distribution of pressure taps. Thereafter, two sets of no slip wedges made from PMMA sheet were installed with the collector's leading edge off the roof surface. Only the high perimetric parapet configuration of 0.06 m, which represents 1.2 m in full scale, was considered for this validation phase. On the roof, collector, and parapet surfaces, 86 pressure taps were mounted: 5 on each parapet, 36 on the roof, and 30 on the collector surface. A diagram of the model's tap distribution is shown in Figure 31.

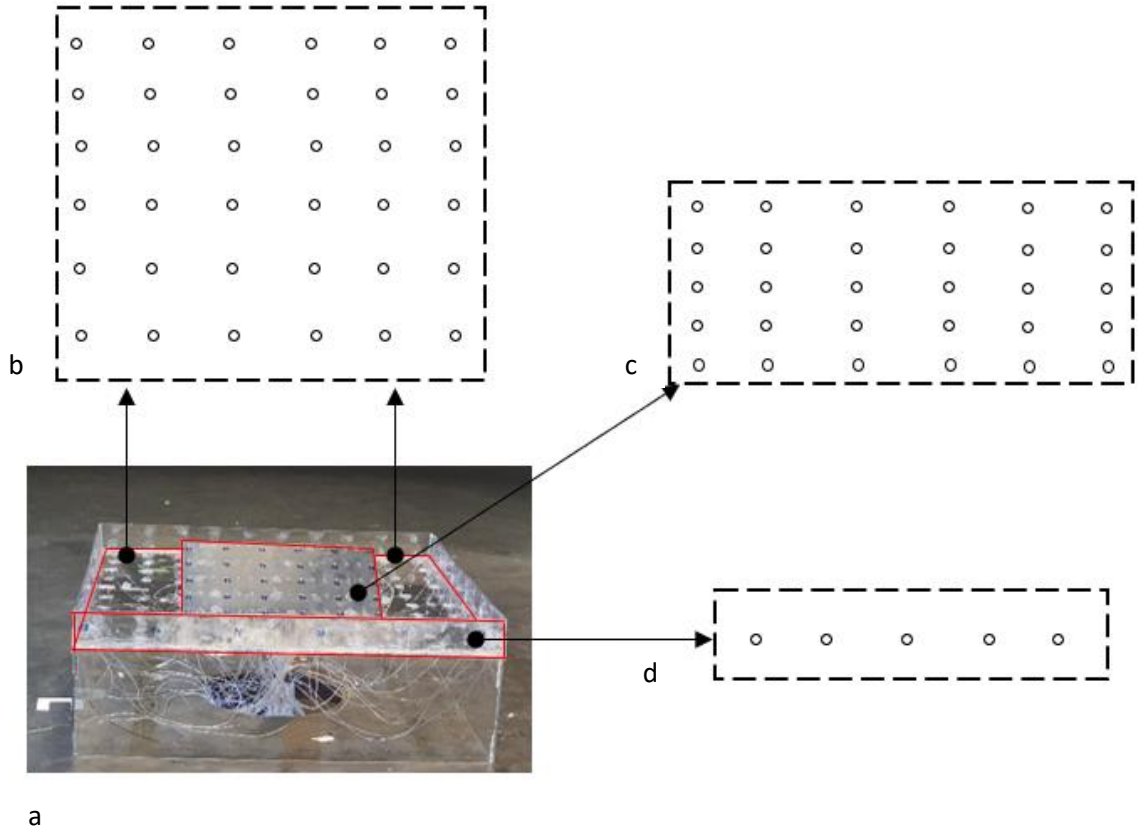

Figure 31: (a) 1:20 wind tunnel test model (b) building plan view (c) collector plan view (d) parapet Plan view with respective tap layout.

Pressure measurements were taken for the operational condition of 0° wind incidence angle. A terrain category-2 ground roughness with 0.02 effective roughness was used for the target profile. This was based on AS/NZS1170.2 (2011). Several other studies have been conducted in the Auckland University wind tunnel (Richards and Hoxey, 1992, 1993, 2006, 2008; Richards, Fong and Hoxey, 1997; Richards *et al.*, 2007). As a result, the velocity profile of the numerical simulation was compared with different roughness values from the wind database. Wind pressure in the wind tunnel was measured at 0.26 m above the floor of the wind tunnel using Pitot tube pressure data. Details of the validation approach can be found in Appendix C.3.

3.3.1 Comparison between wind tunnel experiment and numerical simulation

Following the wind tunnel experiment, the non-dimensional pressure coefficient, $C_{pi(t)}$, at the specific tap location was determined from the pressure taps fitted across the surfaces based on equation 1. $P_{i(t)}$ represents the pressure measured at tap. P_{∞} is the static pressure at infinity. The air density is denoted by ρ, and U_{ref} is the wind velocity of the approaching flow to the model which is measured at a reference height of 0.6m. For the same location in the experiment and

numerical simulation, the mean pressure coefficient, C_p, distribution on the collector, the parapet, and the roof surface is shown in Figure 32 to Figure 34 to (marked as red). Compared to the experimental model, no structural support was modeled at the back of the collector. To account for the scaling difference between the CFD simulation (Full Scale) and the experiment (1:20), all x-axis values were calculated as dimensionless.

$$C_{pi(t)}=\frac{P_{i(t)}-P_{\infty}}{0.5\rho {U_{ref}}^2} \qquad 1$$

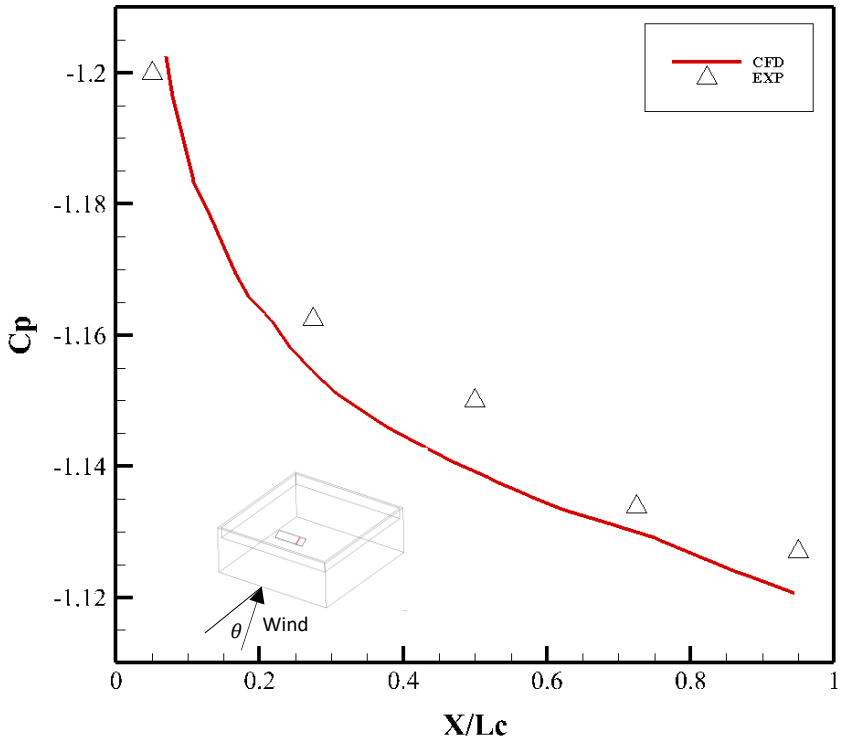

Figure 32: Comparison of C_p prediction of CFD simulation and experimental data on collector upper surface. L_c is the length of the collector. Here C_p plots are along the length of the collector where the leading edge (LE = 0) is 0 and the trailing edge (TE = 1). The wind is normal to the front of the building where (θ= 0º).

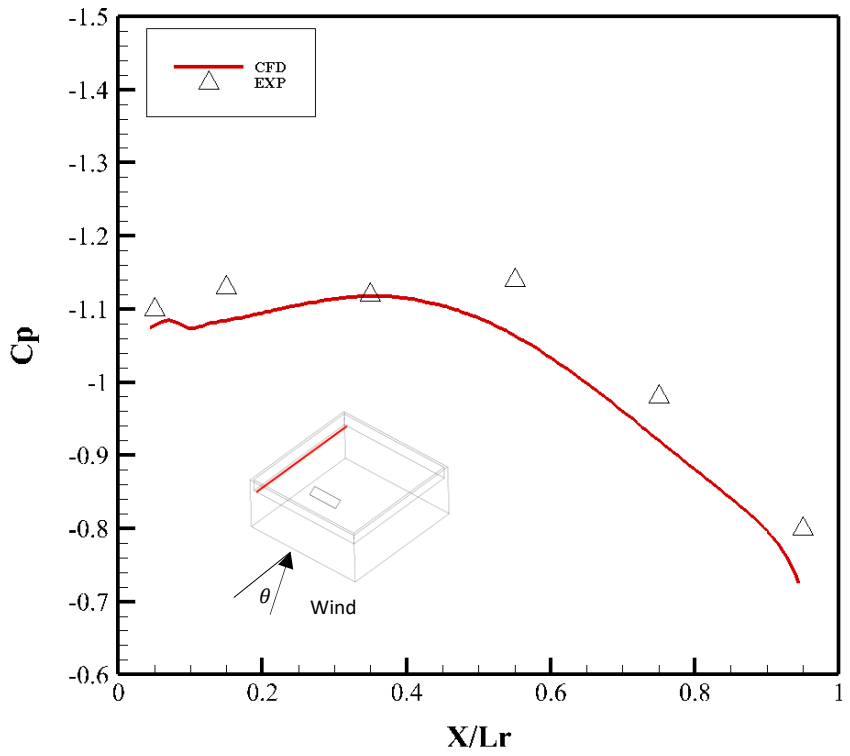

Figure 33: Comparison of C_p prediction of CFD simulation and experimental data on roof surface. L_r is the length of the roof. Here C_p plots are along the length of the roof where the leading edge of the roof (LE = 0) is 0 and the trailing edge (TE = 1). The wind is normal to the front of the building where ($\theta=0^o$)

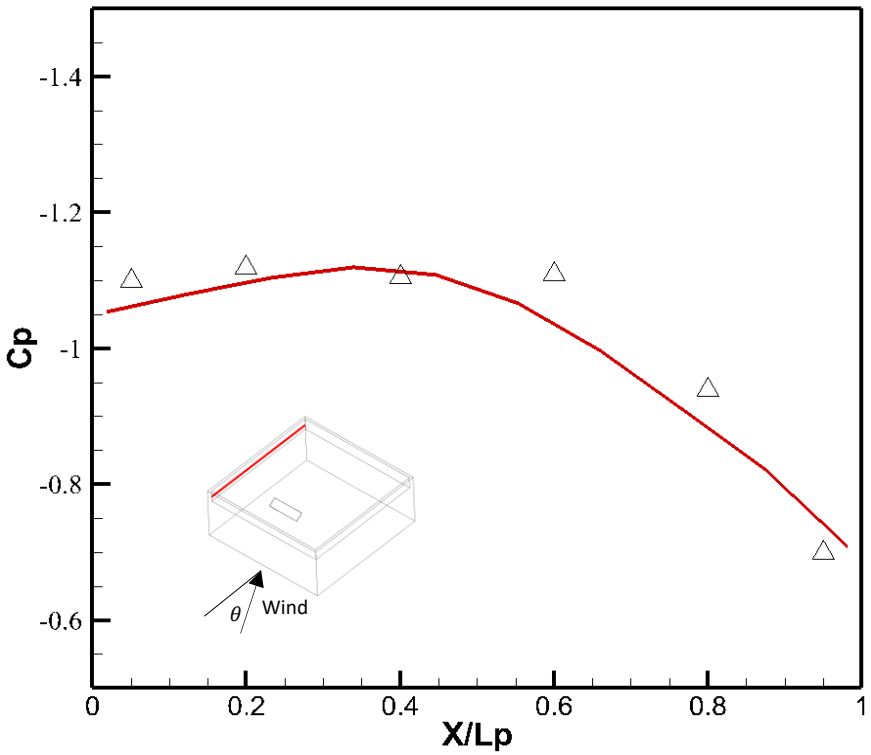

Figure 34: Comparison of C_p prediction of CFD simulation and experimental data on parapet surface. L_p is the length of the parapet. Here C_p plots are along the length of the parapet where the leading edge of the roof (LE = 0) is 0 and the trailing edge (TE = 1). Experimental data are measured from inner tapings on the parapet. The wind is normal to the front of the building where ($\theta=0^o$)

Based on the data presented in Figure 32, it can be observed that the distribution of C_p, at both the leading and trailing edges of the collector exhibits similarities. Negative mean pressure coefficients tend to be higher in proximity to the leading edge of the collector compared to the subsequent edge. In addition to the presence of flow turbulence, the observed increase in C_p, can be ascribed to the positioning of the collector and other geometric characteristics in relation to the parapet, as documented by Browne *et al.* (2013) in their study on rooftop solar arrays. Moreover, it can be observed from Figure 33 and Figure 34 that the mean C_p, values for both the roof and parapet exhibit a decreasing trend from the front edge to the rear edge.

In both instances, there is a notable variation in the average C_p, as the distance from the roof edge changes. The observation regarding the impact of parapet height on pressure coefficients aligns with the findings reported by Stathopoulos *et al.* (2002). The mean pressures at the roof and parapet, with respect to the specified wind direction, exhibit a high degree of similarity. Additionally, this observation bears resemblance to the findings of Stathopoulos *et al.* (2002), as they also noted that the average pressure gradient near the edge of a 1-metre-tall parapet is not significant. Therefore, it is evident that the model accurately reproduces the experimental findings.

3.4 Results and discussion

After validating the numerical method, the subsequent phase involved examining the convective heat loss in a steady-state scenario for a standalone unglazed collector mounted on a roof. This investigation encompassed diverse operating conditions, including variations in wind incidence angle, collector mounting location, tilt angle, and parapet heights. In each instance, a single operating condition was altered while keeping all other conditions unchanged to observe its impact on convection heat loss. Before examining the heat loss, it was determined that an initial investigation should be conducted to analyse the variation in velocity on the roof based on the wind incidence angle and the height of the perimetric parapet. The objective of this, in the context of this study, was to reduce the extensive and potentially repetitive reporting of the impact of each wind incidence angle examined.

3.4.1 Wind velocity on the roof of low-rise buildings with single roof-mounted collectors and perimetric parapets

Chapter 1 demonstrated that wind velocity exerts a substantial impact on the heat loss experienced by wind sensitive collectors. Chapter 2 demonstrated that perimetric parapets have an impact on wind velocity on a low-rise roof. Nevertheless, it is important to acknowledge that the deduction made in Chapter 2 was established under the assumption of a wind incidence angle of 0° towards the building, without the presence of a collector.

Due to the influence of various factors such as geographical location and building orientation, it is imperative to conduct an initial evaluation of wind velocities on low-rise building roofs at different wind incidence angles. Based on the insights acquired in Chapter 2, the subsequent procedure assumes paramount importance as it aims to ascertain whether parapets exert a consistent influence on roof velocity under different wind incidence angles in the presence of collectors.

To accomplish this, a decision was made to conduct an investigation on the wind velocity experienced by the roof for the different wind directions illustrated in Figure 35. This section does not discuss the results of wind direction for 135° and 180°. The aerodynamic properties and velocity associated with these angles will exhibit variations when reversed. However, due to the symmetrical nature of the building, it can be inferred that an angle of 45° is equivalent to 135°, and an angle of 180° is equivalent to 0°. The detailed impact of the parapet on roof velocity, for all wind directions examined, is presented in Appendix E.

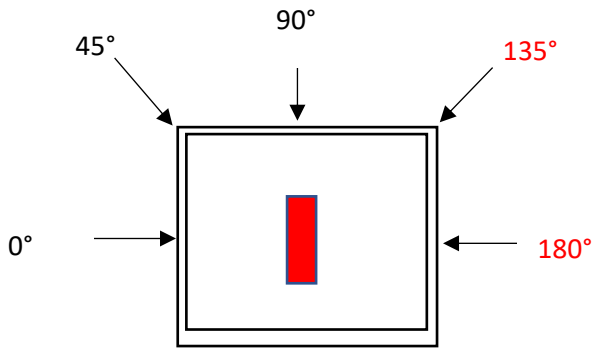

Figure 35: Wind incidence angle to building with standalone roof mounted solar thermal collector.

To present the findings, an analysis was conducted on a specific plane located at Y=4.3 on the roof surface. In this instance, the analysis focused on the distribution of velocity zones under operational conditions characterised by a velocity of v=10m/s, a collector mounting location that covers 50 percent of the roof, and a collector tilt angle of 20°. Figure 36 illustrates the reference plane denoted by Y=4.3, which signifies a plane and position that is equidistant from the leading and trailing edge of collector at a tilt angle of 20°.

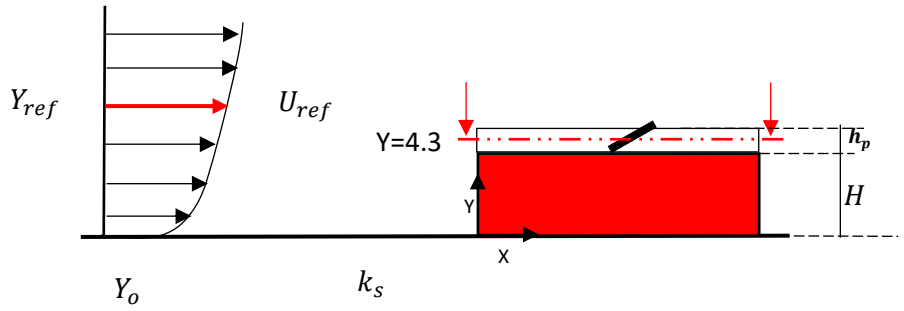

Figure 36: Reference coordinates and plane of assessment (Not drawn to scale). Reference coordinates, heights, and velocities (Not drawn to scale). H is the height of the building,$U_{ref=}2.5, 5, 10\ m/s$ is the velocity at the reference height $Y_{ref} = 4\ m$, $k_s = 0.028$ the sand-grain roughness height. Y is the vertical coordinate, Y_0 the surface roughness height.

Figure 37 (a to c) depicts the velocity on the roof in the presence of a collector and perimetric parapet, specifically at a wind incidence angle of 0°. The absence of a parapet results in a discernibly reduced velocity on the roof, which can be attributed to the presence of a recirculation bubble at the leading edge of the roof, as previously discussed in the preceding chapter. On the other hand, the presence of low perimetric parapets leads to increased velocity on both the front and rear of the collector. The change in parapet height results in elevated velocities in the rear section of the roof. This phenomenon, as discussed in the previous chapter, is influenced by the flow generated by the backward-facing step from the leeward vortex.

The above observation indicates that the presence of perimetric parapets can result in a notable heat loss for collectors that are sensitive to wind, particularly when the collector is positioned at the center of the roof. On the contrary, when a parapet is not present, there is a minimal wind velocity, indicating a reduced amount of heat loss.

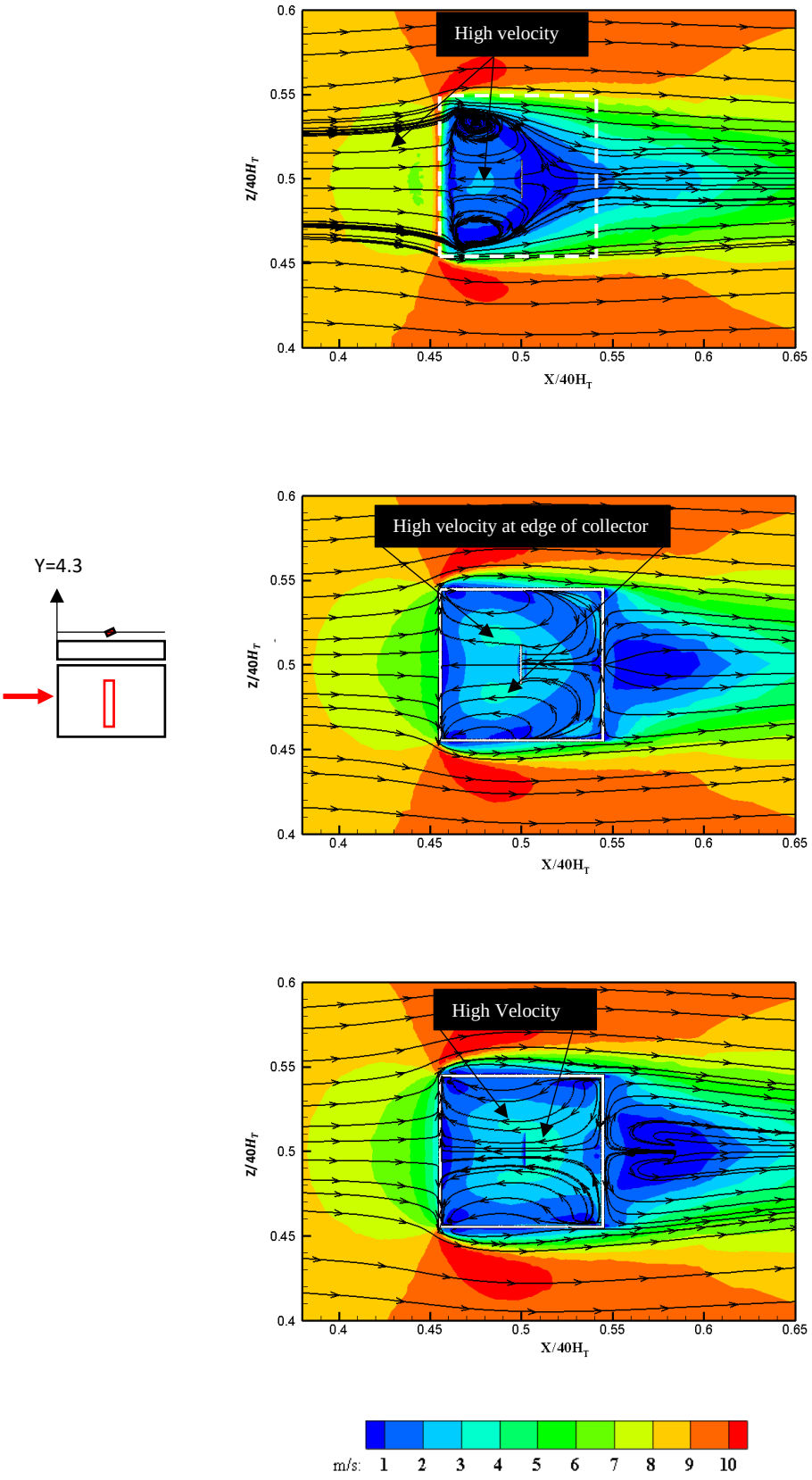

Figure 37: Flow behavior on roof surface at wind incidence angle of 0°. (Operational conditions of V = 10 m/s, β = 20°, Lc = 50 percent of the roof's length) a. No Perimetric parapets b. Low perimetric parapets c. High perimetric parapets.

Figure 38 (a to c) depicts the velocity on the roof at a 45° wind incidence angle. When there are no parapets, the velocity is higher on the roof near the separation point. In this instance, there is no obstruction to the oncoming flow at the roof's leading edge. On the other hand, at low parapets, there is a decrease in velocity on the roof beyond the point of separation from the oncoming flow. Consequently, there is a decrease in velocity, particularly near the front of the collector. This suggests that at 45° wind incidence angles and low perimetric parapets, the heat loss for roof-mounted collectors would be less than the heat loss for roofs without perimetric parapets.

On roofs with high perimetric parapets, Figure 38c, the velocity is significantly reduced. Typical of buildings facing oblique wind directions, the high parapet displays a spreading vortex at the roof's edges. The high parapet, which acts as an obstruction due to its height, results in a lower velocity zone on the roof. On the basis of the preceding, it is likely that the heat loss of the collector on roofs with higher parapet and oblique wind angles will be lower compared to that with no and low parapet.

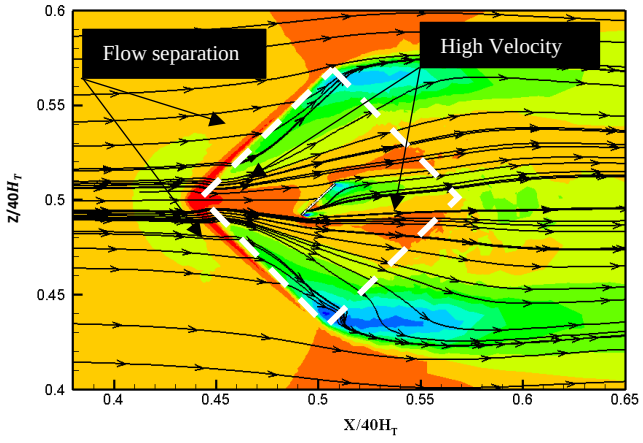

[a]

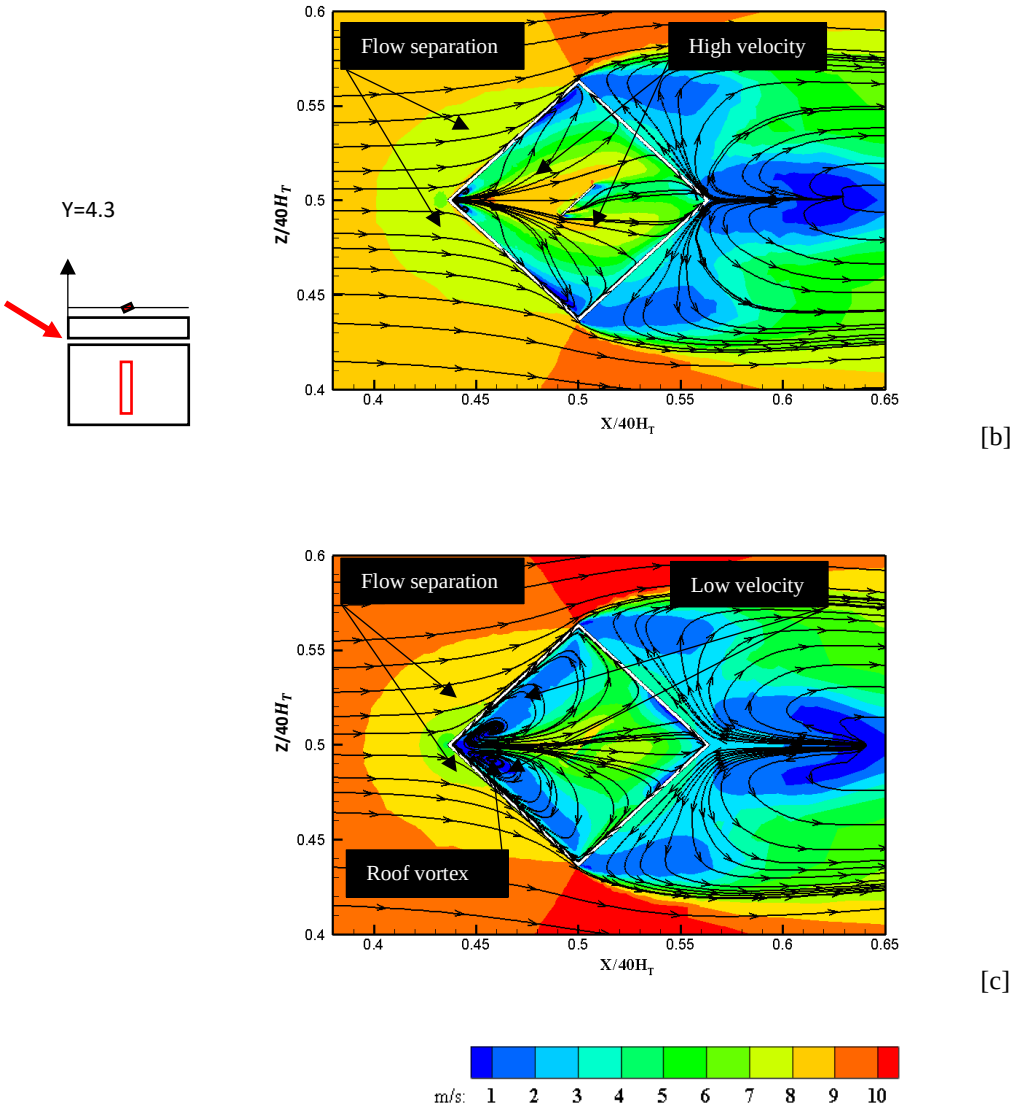

Figure 38: Flow behavior on roof surface at wind incidence angle of 45° (Operational conditions of V = 10 m/s, β = 20°, Lc = 50 percent of the roof's length) a. No Perimetric parapets b. Low perimetric parapets c. High perimetric parapets.

Wind incidence of 90 degrees is shown in Figure 39 (a to c). In the absence of parapets, a roof vortex forms at the leading edge of the roof, similar to when the wind incidence is 0°. As a result, the oncoming flow separates along the collector in this case, especially at the edge, which results in high velocity at the collector's edge that faces the approaching flow. In the presence of low perimetric parapets, it is noticeable that the velocity around collectors becomes more dominant on the roof. The main cause of this is the separation that occurs at the edge of the parapets, described in Chapter 2. There is a noticeable increase in velocity around the collector which is located mostly at the center of the roof at higher parapets. Thus, for buildings with dominant 90-

degree wind incidence angles, this suggests that higher parapets will lead to greater heat loss from collectors than lower or no parapets.

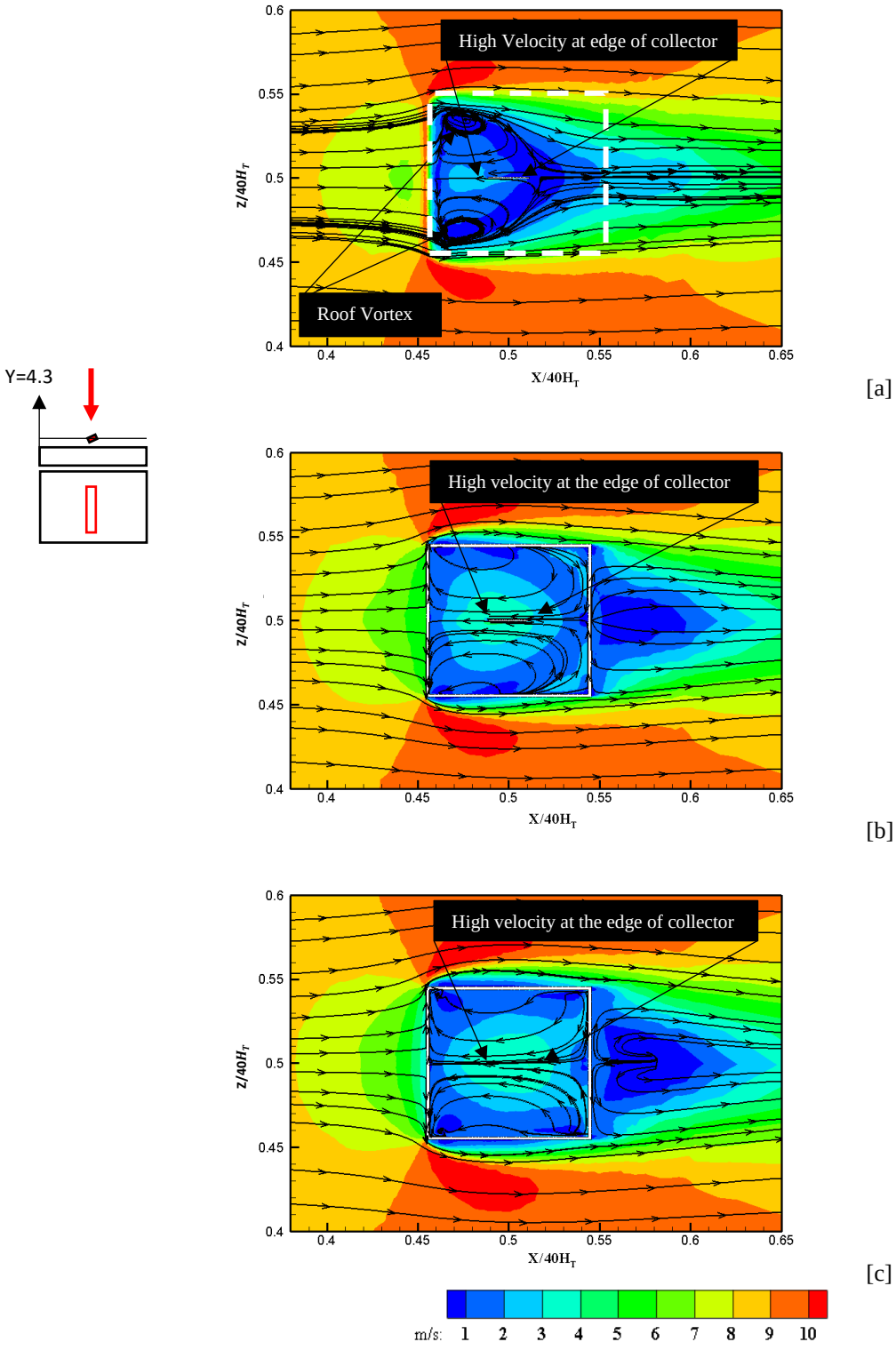

Figure 39: Flow behavior on roof surface at wind incidence angle of 90° (Operational conditions of V = 10 m/s, β = 20°, Lc = 50 percent of the roof's length) a. No Perimetric parapets b. Low perimetric parapets c. High perimetric parapets.

In general, upon comparing the aerodynamics of the room across three scenarios with wind angles of 0°, 45°, and 90°, it becomes evident that there is a noticeable separation of airflow along the front edge of the building in the case of a 45° wind incidence. This separation is attributed to the pointed edge of the building facing the incoming flow. The outcome of this phenomenon is a decrease in surface velocity on the roof when compared to scenarios where wind incidence angles are either 0 °or 90° where the building acts as a bluff body to the oncoming flow.

3.4.2 Combined effect of perimetric parapet and collector mounting location on collector heat loss.

The preceding analysis showed that wind velocity changes as parapet height and wind incidence angle change. And since wind velocity affects heat loss, it follows that roof-mounted collectors would experience convective heat loss varyingly at different angles of wind incidence. Now, while other wind incidence angles for varying operating conditions were studied, the section that follow only reports on the wind incidence angle of 0° for the sake of brevity.

A steady-state heat loss analysis for the collector was performed at various mounting locations representing 25, 50, and 75 percent of the roof length while varying the parapet height. The reasons for this, is discussed in Chapter 2, where velocity zones were shown to vary along the roof at different perimetric parapet heights. Furthermore, by combining the aerodynamics of the roof due to the presence of parapets and a general understanding of aerodynamics around inclined bodies, it is possible to hypothesise that the aerodynamics on the roof could vary significantly in each instance, thus affecting the local velocity hence heat loss. Moreover, the collectors' position relative to the parapet may have an effect on the roof's aerodynamics which could aid in understanding how its positioning affects local velocity and consequently its heat loss.

To assess the effect of varying the above parameters on the collector heat loss, the collector's average Nusselt number, Nu_{avg}, was determined. Given that the collector is an unglazed collector, both front and rear surfaces were considered. Also, the Nu_{avg} was chosen as the output parameter because, in addition to quantifying the relative contributions of conduction and convection, it is an efficient method of calculating overall heat transfer over time as the collector's length or tilt angle changes.

Generally, the local convective heat transfer coefficient h_x can be determined from equations 2.

$$h_x = \frac{q_x}{T_c - T_\infty} \qquad 2$$

Where in the above equation, q_x is the local heat flux, T_c temperature of the collector and T_∞ the ambient temperature. The convective heat transfer coefficient is normalised using the characteristic length of the collector ($L_c = 1m$) and the thermal conductivity of the ambient air k_{air} to give the non dimensionless local Nusselt number Nu_x provided in equation 3 below. x is the distance along the plate from the leading edge, depicted in Figure 40. h_b is the gap between the roof surface and the leading edge of the collector, θ is the collector tilt angle, and g is the acceleration due to gravity.

$$Nu_x = \frac{h_x x}{k_{air}} \qquad 3$$

The average Nusselt number can be evaluated from the following expression:

$$Nu_{avg} = \frac{h_{avg} L_c}{k_{air}} \qquad 4$$

Where the average convective heat transfer of the plate h_{avg} can be evaluated from the expression along the plate in the direction of x, see equation 5.

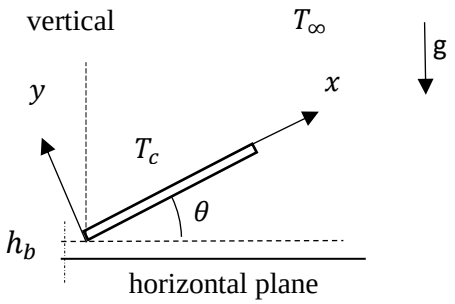

Figure 40: Schematic of Inclined plate

$$h_{avg} = \frac{1}{L_c} \int_0^{L_c} h_x dx \qquad 5$$

It is worth noting that the above methodology for calculating the average Nusselt number Nu_{avg} pertains to two-dimensional scenarios. In this study, which is three dimensional, the convective heat transfer coefficient was determined using the heat flux obtained from the simulation results. Subsequently, the average Nusselt number $Nu_{avg}$was calculated by incorporating the

characteristic length and thermal conductivity of the ambient air as per equation 4. Also, to show the aerodynamics on the roof and around the collector, the results of mean velocity flow stream traces at the building's and collector's center planes were analyzed. Figure 41, demonstrates the region on the roof for which the results are presented.

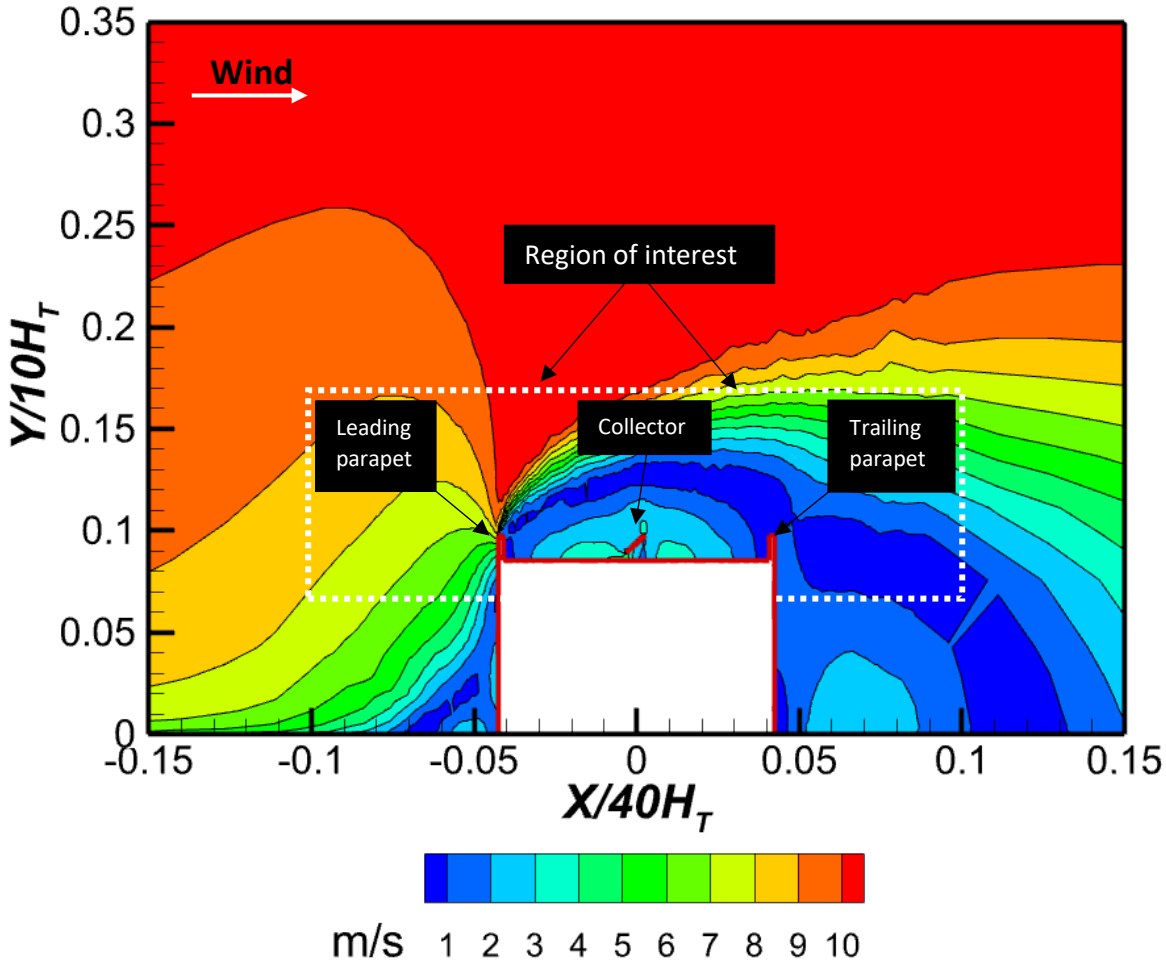

Figure 41: Zone of aerodynamics analysis presentation

3.4.2.1 The combined effect of a perimetric parapet and a mounting location representing 25 percent of the roof on collector heat loss.

Following the section above, an analysis of steady state heat loss at a mounting position closer to a parapet in the path of an oncoming flow, which represents 25 percent of the roof's length, was conducted. The collector inclination angle was maintained at 20 ° while the parapet height was varied based on the height classification discussed in section 2.2 of this study. Figure 49 depicts the Nu_{avg}, for the three cases of varying parapet height.

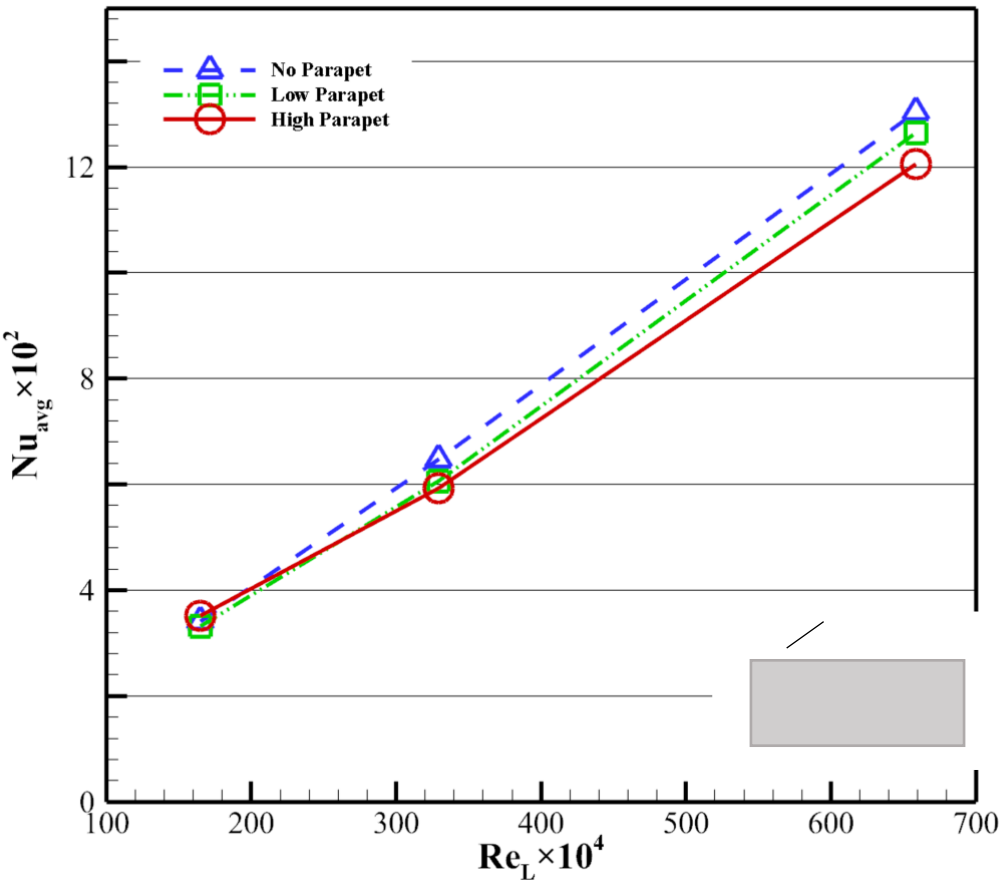

Figure 42: Nu_{avg} for collector at different parapet heights and Reynolds number (Operational condition: Characteristic length= 1m, β = 20°, Collector location 25 percent of roof's length)

Figure 43 illustrates the flow characteristics observed when the collector is situated at a distance equivalent to 25 percent of the roof's length, in the absence of a parapet. It is evident that flow separation occurring at the leading edge of the roof results in the generation of a vortex on the rooftop. The formation of a recirculation bubble occurs due to the positioning of the collector relative to the edge of the roof. The downward curvature of the shear layer causes the reattachment points to come into contact with the roof surface, resulting in a constraint on the extent of the recirculation bubble where the collector is situated.

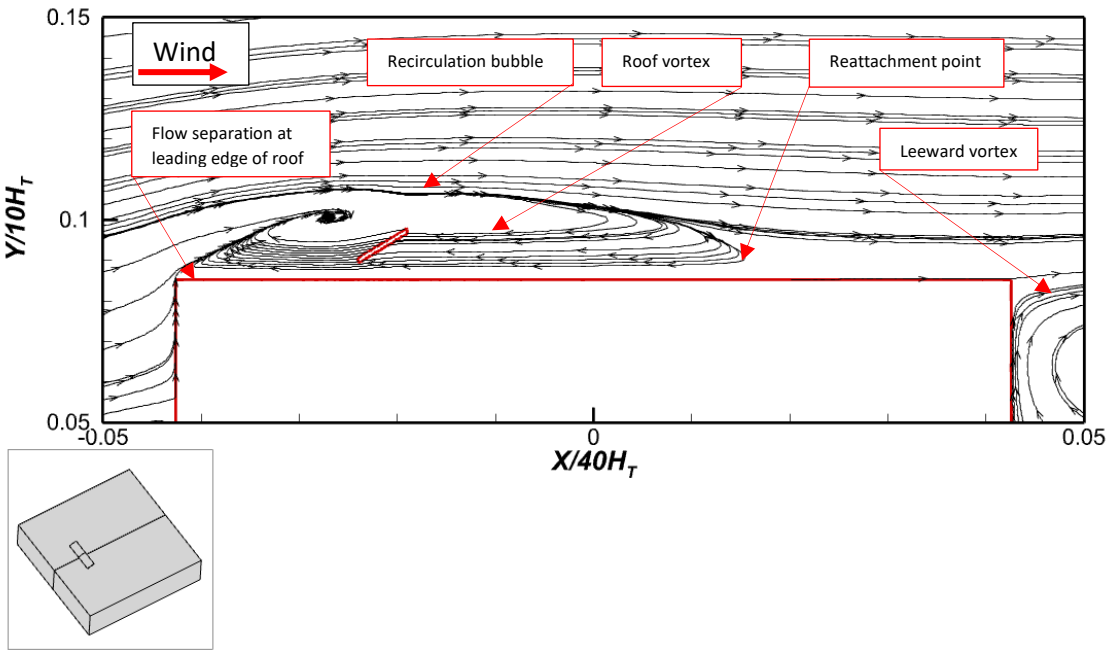

Figure 43: Mean stream traces on the center plane for flow behavior with no perimetric parapet present (Operational condition V= 10 m/s, β = 20°, Collector location 25 percent of roof's length)

Upon examination of velocity, it is evident that a region of reduced velocity is present above the collector, as depicted in Figure 44. This reduction in velocity is particularly noticeable at the trailing edge of the collector, suggesting a decrease in the rate of heat loss in the vicinity of said trailing edge. Furthermore, the proximity of the collector to the roof edge, coupled with the intentional inclusion of a gap between the collector and the roof surface to accommodate the support structure of the USC, gives rise to the creation of a flow path. The effect of the fore going is the presence of heightened velocity observed in a specific area near the leading edge of the collector, as illustrated in the local velocity plots depicted in Figure 45.

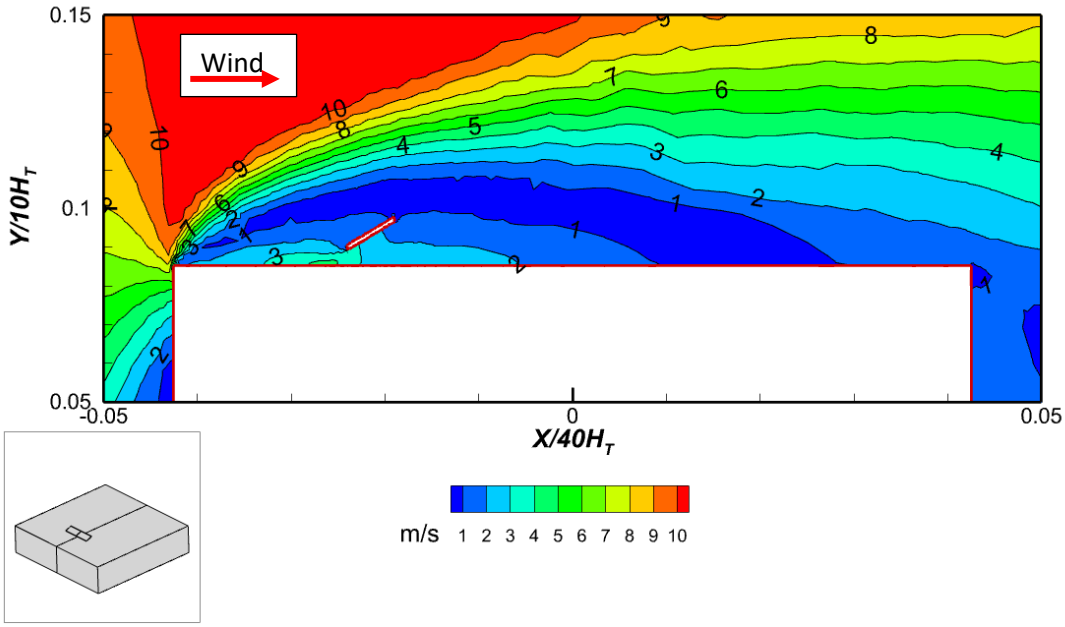

Figure 44: Mean velocity contours on the center plane for flow behavior with no perimetric parapet present (Operational condition V = 10 m/s, β = 20°, Collector location 25 percent of roof's length.

Based on the analysis above, it can be deduced that the primary determinant of heat loss in cases where collectors are located near the front edge of a roof without parapets is the vortex, which is situated in closer proximity to the surface of the roof. Moreover, when taking into account the collector's close proximity to the leading edge of the roofs, it becomes evident that the gap between the collector's edge and the roof surface plays a pivotal role in determining the extent of heat loss experienced by the collector.

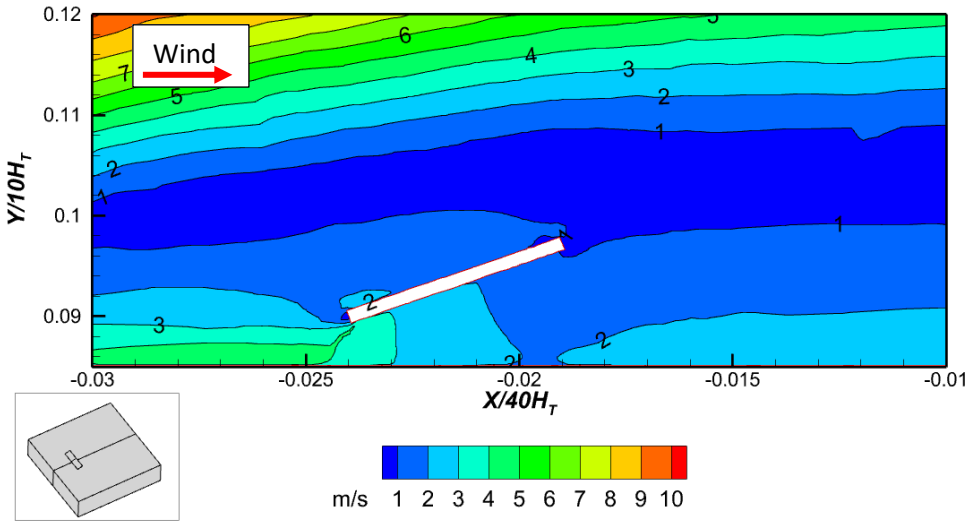

Figure 45: Local velocity (V_l) around collector for collectors located at 25 percent of roof's length with no parapet present

Figure 46 illustrates the aerodynamic characteristics of a roof featuring a lower perimetric parapet, while maintaining consistent operational parameters and mounting location. It is evident that a vortex is generated above the roof due to the phenomenon of flow separation taking place at both the leading and trailing parapets. Moreover, the displacement of the vortex above the roof can be attributed to the collector's close proximity to the roof edge, as well as the prevailing influence of the oncoming flow and its interaction with the backward stepping flow emanating from the flow separation at the trailing parapet.

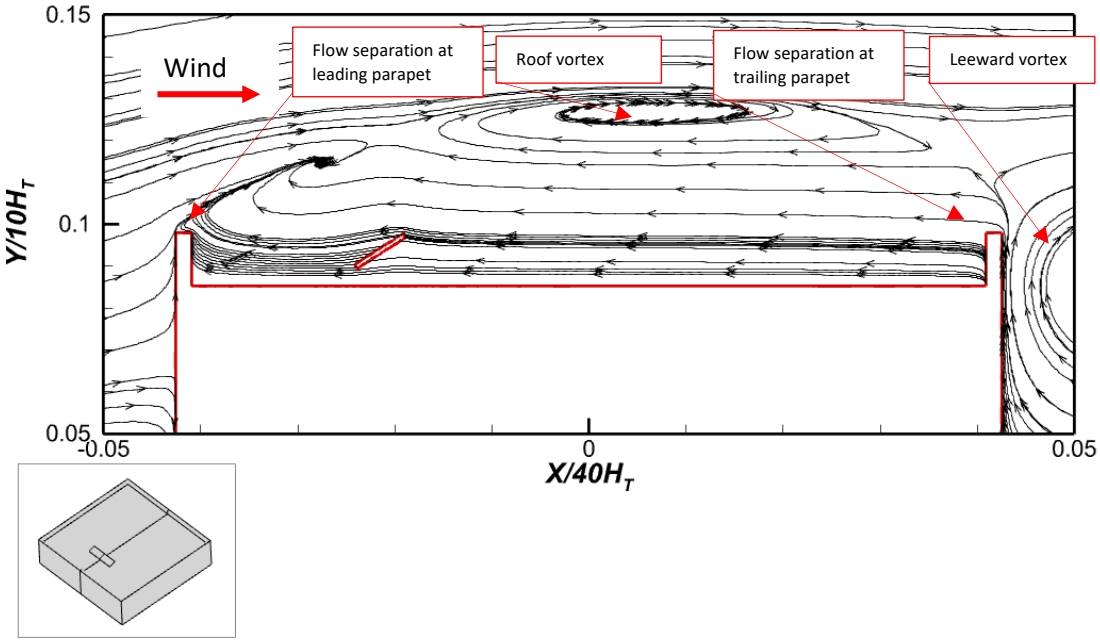

Figure 46: Mean velocity flow stream traces on the center plane for flow behavior with low perimetric parapet present (Operational condition V = 10 m/s, β = 20, Collector location 25 percent of roof's length)

Upon analysis of velocity, it is evident that the central region of the roof displays a higher magnitude of velocity as depicted in Figure 47. This can be attributed to the flow that moves in a backward direction from the trailing parapet, as depicted in Figure 46. Upon a more comprehensive analysis of the aerodynamics pertaining to the roof, it is also observed that there exists a downward flow at the rear of the collector. The downwash phenomenon, as illustrated by the local velocity depicted in Figure 48 leads to the formation of a region with high velocity at the rear of the collector indicating the likely occurrence of substantial heat loss.

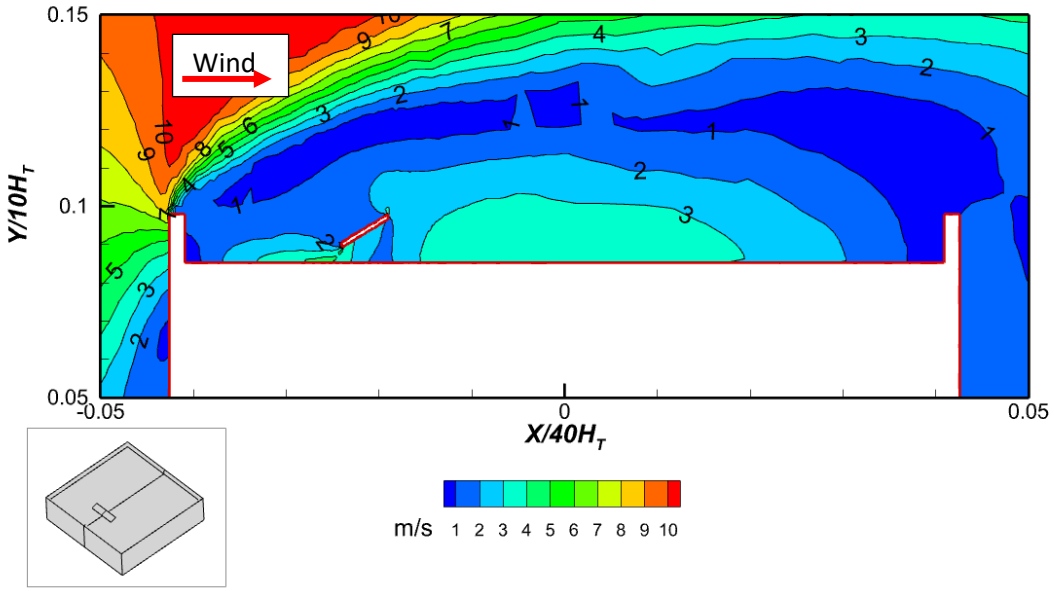

Figure 47: Mean velocity contours on the center plane for flow behavior with low perimetric parapet present (Operational condition V= 10 m/s, β = 20°, Collector location 25 percent of roof's length.

A decrease in velocity is observed at the front of the collector, indicating a reduction in heat loss. The observed decrease in velocity can be attributed to two factors: firstly, the presence of a backward stepping flow, and secondly, the formation of a vortex along the roof that separates at the trailing edge of the collector as depicted in Figure 46.

Additionally, a "shallow cavity" is formed between the parapet and the collector, leading to the generation of a semi-recirculation bubble in front of the collector. Hence, it is apparent that the proximity of the collector to a lower perimetric parapet influences the heat loss predominantly through the downwash at the rear of the collector rather than its front.

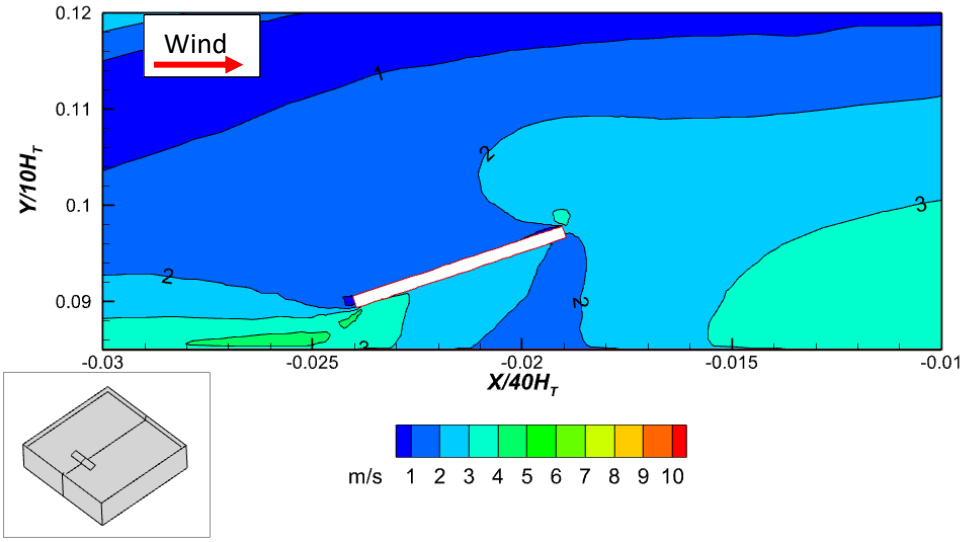

Figure 48: Local velocity (V_l) around collector for collectors located at 25 percent of roof's length with low parapet present

Figure 49 depicts the presence of a higher parapet under the same operating conditions. When the aerodynamics is examined in this case, it is noticeable that the roof has a similar flow structure to that reported for low parapets. The flow separates both the trailing and leading parapets edges. In this case, however, the parapet height causes the roof vortex to extend higher above the roof.

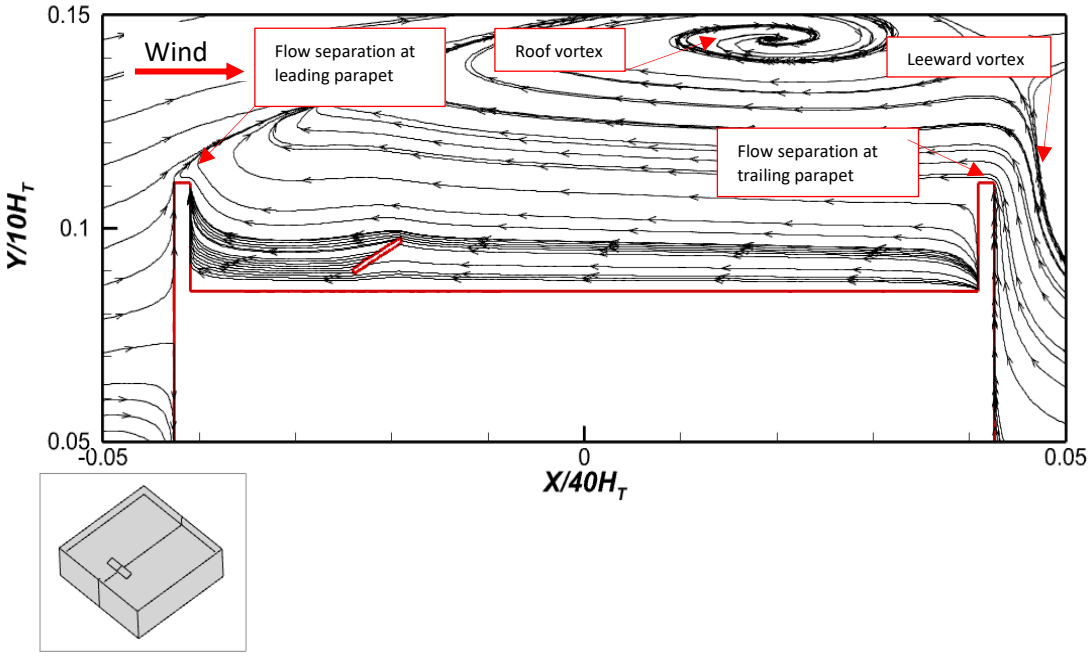

Figure 49: Mean velocity flow stream traces on the center plane for flow behavior with high perimetric parapet present (Operational condition V = 10 m/s, β = 20°, Collector location 25 percent of roof)

Like the lower parapets, a region of increased velocity can be observed at the central portion of the roof, propelled by the vortex, as depicted in Figure 50. Likewise, an observation of the local velocity at the rear of the collector, as depicted in Figure 51, reveals the presence of a downwash phenomenon. This downwash generates a region of elevated velocity, thereby indicating the occurrence of significant heat loss. Conversely, a reduced velocity can be observed towards the leading edge of the collector. This phenomenon, as previously explained in the context of a lower parapet, is attributed to the creation of a shallow cavity in front of the collector. However, in this case, due to the increased height of the parapet, there is a more noticeable region of lower velocity closer to the parapet which explains why the heat loss is lower at higher parapets when the collector is places at 25 percent of the roof.

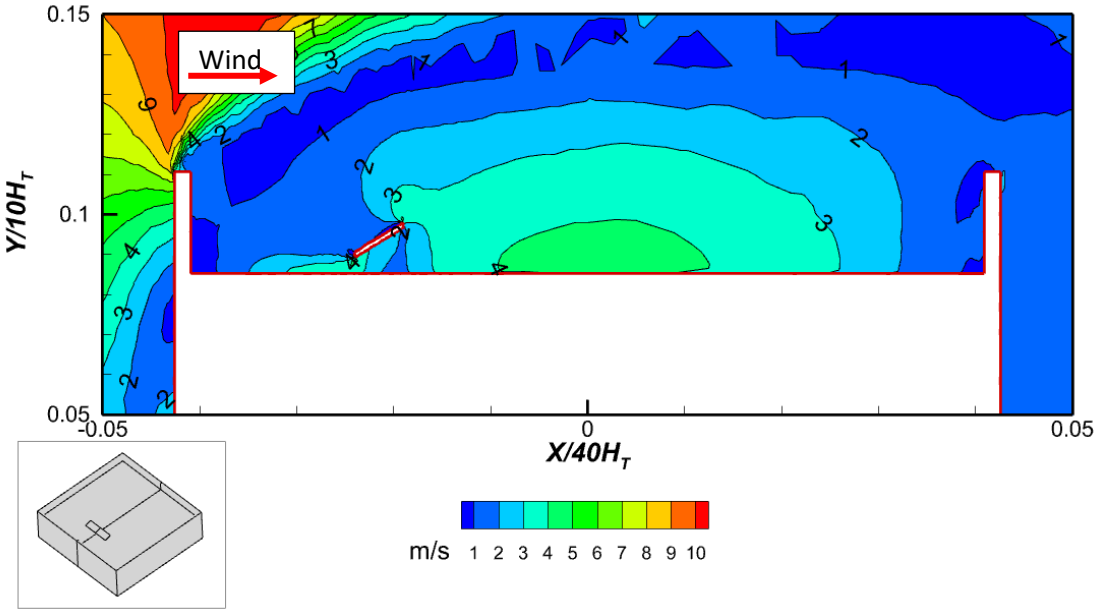

Figure 50: Mean velocity contours on the center plane for flow behavior with low perimetric parapet present (Operational condition V = 10 m/s, β = 20°, Collector location 25 percent of roof's length).

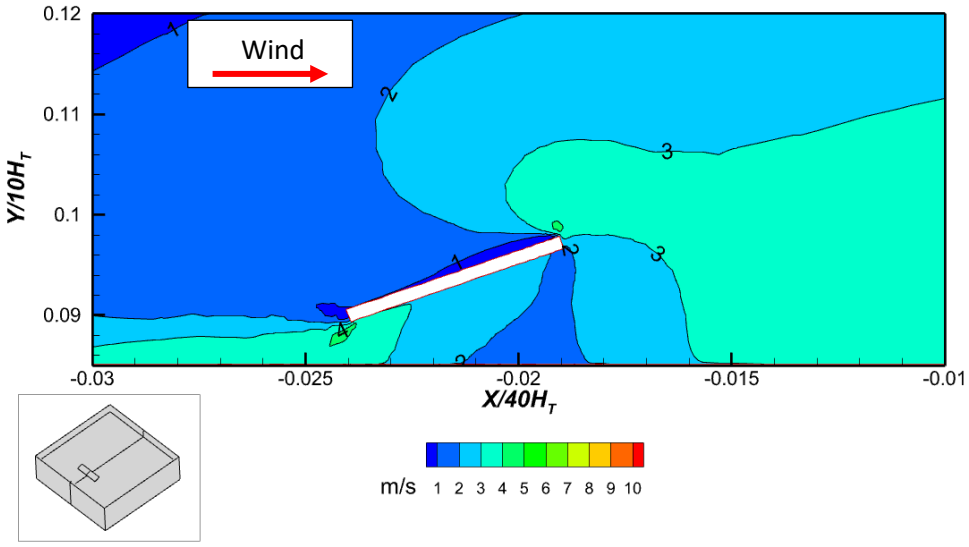

Figure 51: Local velocity (V_l) around collector for collectors located at 25 percent of roof's length with high parapets present.

Based on the comparable aerodynamic characteristics of the low and high parapets on the roof, it can be inferred that the collector featuring a low parapet on the roof will experience greater heat loss compared to the collector featuring a high parapet, considering the observed local velocity. Therefore, it can be inferred that the proximity of single roof-mounted collectors to the building's edge is inversely related to heat loss, with a higher parapet height resulting in decreased heat loss. Roofs without parapets will result in more pronounced heat loss given the surface of the collector is exposed to the flow separation from the oncoming flow.

3.4.2.2 The combined effect of a perimetric parapet and a mounting location representing 50 percent of the roof on collector heat loss.

After conducting an investigation on the impact of collector proximity to parapets and its influence on collector heat loss, the subsequent phase involved an examination of the potential aerodynamic effects on the roof when a collector is positioned at its centre. Figure 52 illustrates the heat loss of the collector, denoted as Nu_{avg}, under different operating conditions. The collector is positioned at the centre of the roof, representing 50 percent of the roof's length, while the parapet height and Reynolds number are varied. Specifically, a tilt angle of 20° is considered.

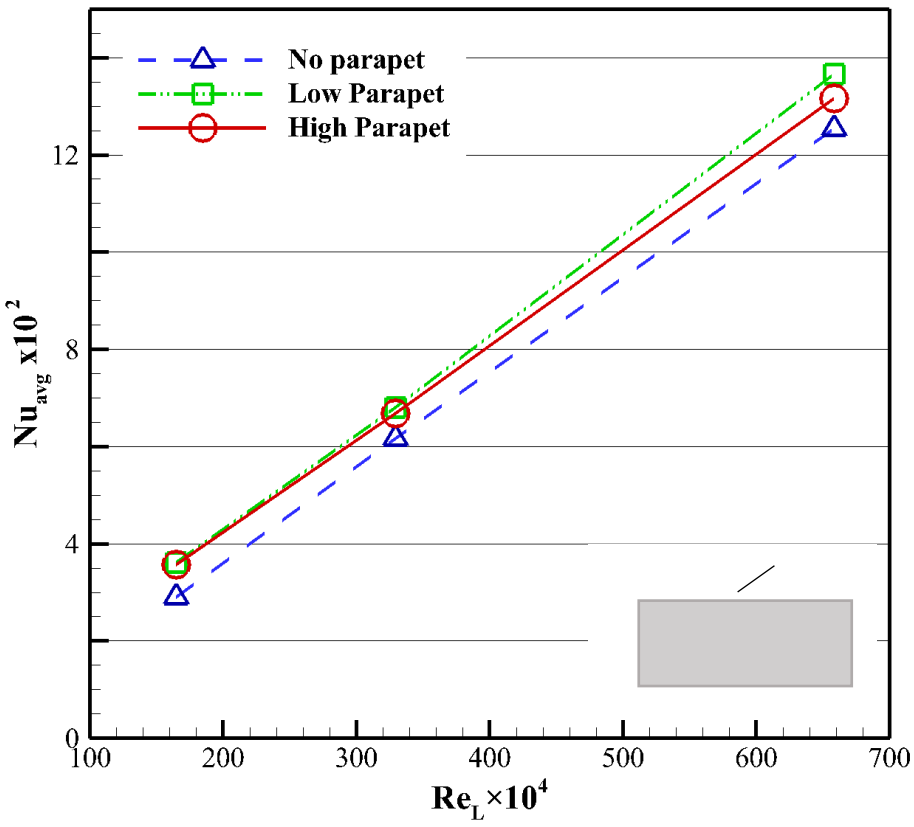

Figure 52: Nu_{avg} for collector at different parapet heights and Reynolds number (Operational condition: β = 20°, Characteristic length= 1m, Collector location 50 percent of roof's length)

Without a perimetric parapet, as shown in Figure 54, a flow separation occurs at the leading edge of the roof, resulting in a vortex between the leading edge of the roof and the collector's surface. A recirculation bubble forms in front of the collector as a result of the interaction between the flow separation and the shear layer, which causes the vortex to expand.

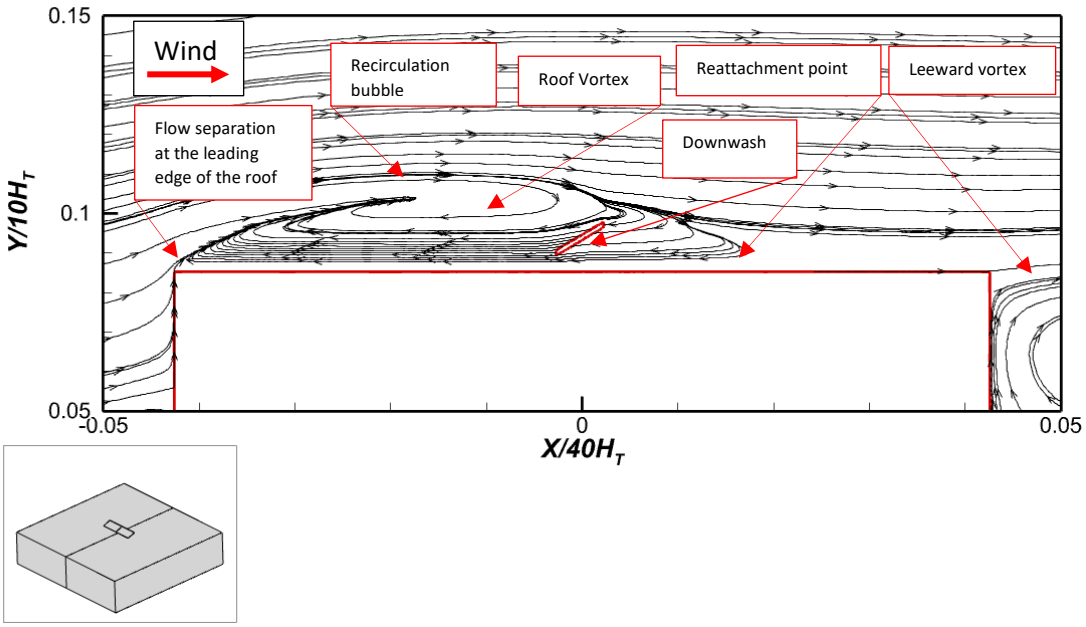

Figure 53: Mean velocity flow stream traces on the center plane for flow behavior on roof at no parapet (Operational condition V = 10 m/s, β = 20°, Collector location 50 percent of roof's length)

Because the collector is immersed in the vortex, this results in a low velocity zone at its front surface as depicted in Figure 54. At the leading edge of the roof and collector, however, the velocity is marginally higher due to two factors: first, the gap between the leading edge of the collector and the roof surface, and second, the downwash effect at the rear of the collector's leading edge, shown in Figure 53.

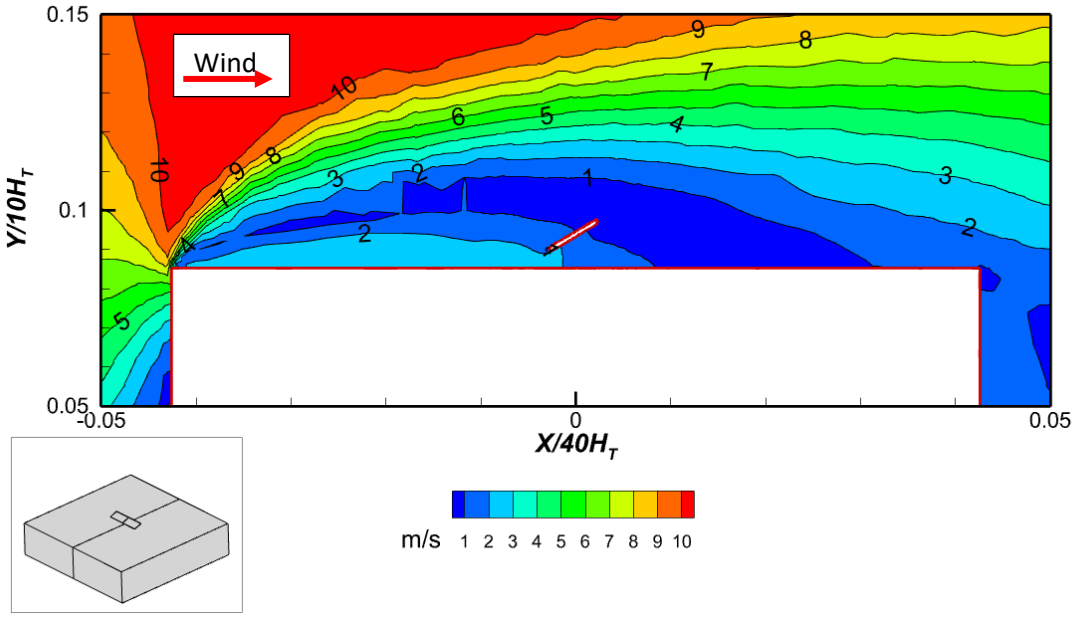

Figure 54 : Mean velocity contours on the center plane for flow behavior with no perimetric parapet present (Operational condition V= 10 m/s, β = 20°, Collector location 50 percent of roof's length.

Upon close examination of the local velocity, as depicted in Figure 55, it becomes evident that the upper surface of the collector generally exhibits lower velocity, except for its leading edge. The inverse phenomenon takes place at the trailing edge, indicating a reduction in heat loss. Based on these observations, it is evident that the heat loss from the collector will be relatively negligible at its front surface in comparison to its rear surface. Conversely, the lower surface of the collector's leading edge would experience a more rapid heat loss. In this instance, given that both the front and rear surfaces of the collector are exposed, it can be inferred that the average heat loss of the collector would be low. This therefore suggests that collectors positioned at the central area of roofs lacking parapets will experience flow separation at the roof's leading edge which create a recirculation bubble around the collector, resulting in a region of reduced velocity and subsequent heat loss.

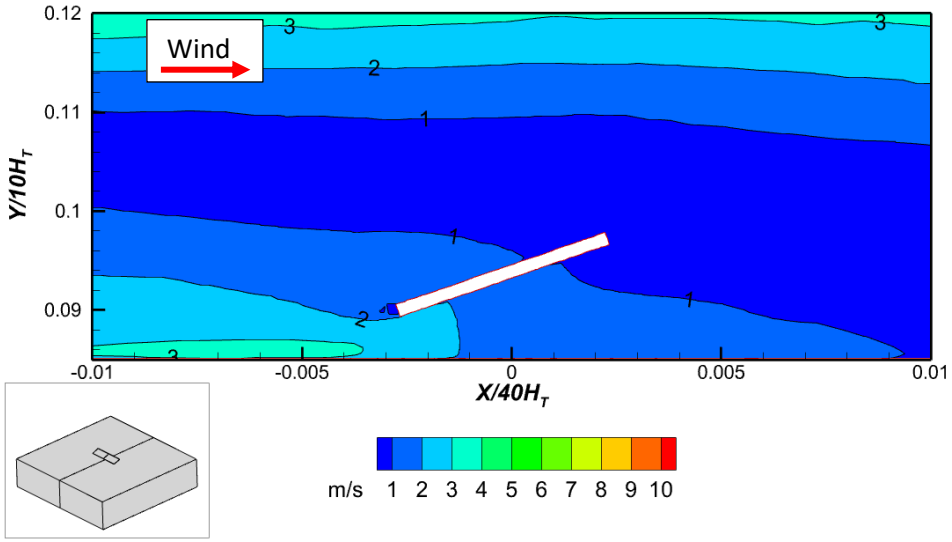

Figure 55: Local velocity (V_l) around collector for collectors located at 50 percent of roof's length with no parapet present

Figure 56 illustrates the aerodynamic characteristics of a roof featuring a perimetric parapet with a low height, under identical operating conditions. Evidently, a flow separation phenomenon manifests itself at both the leading and trailing edges of the parapet. The convergence of the two streams on the rooftop results in the formation of a vortex. Nevertheless, as a result of the increased parapet height and the position of the collector, the vortex is positioned at a greater distance above the surface of the roof.

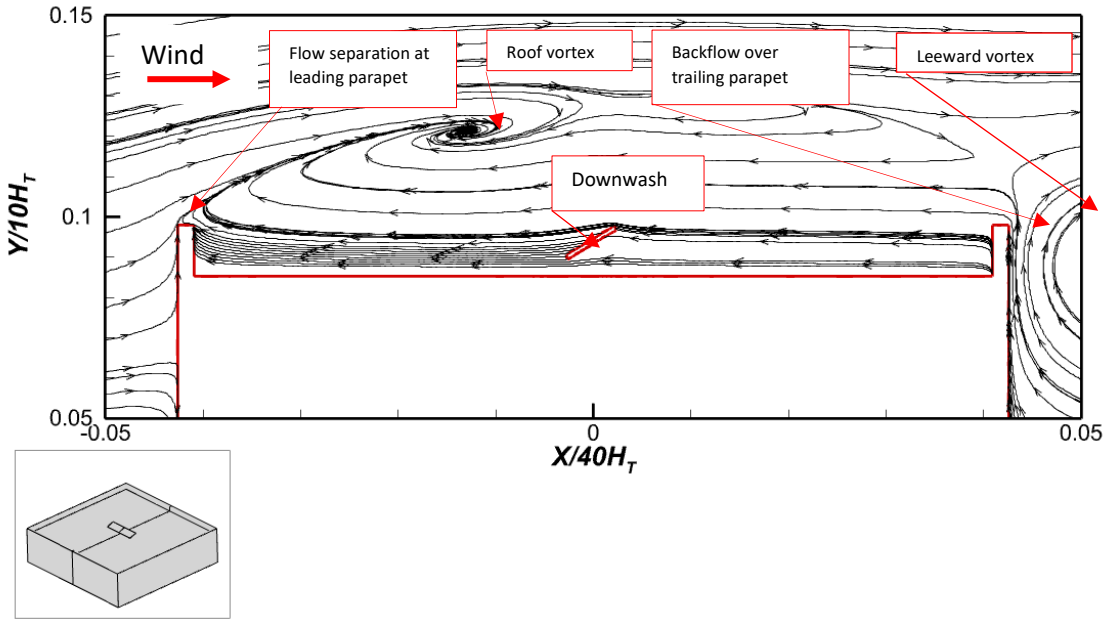

Figure 56: Mean velocity flow stream traces on the center plane for flow behavior on roof at low parapet (Operational condition V= 10 m/s, β = 20°, Collector location 50 percent of roof's length)

When examined in terms of velocity as depicted in Figure 57 it is observed that a higher velocity occurs at the front surface of the collector which as shown in Figure 69 is driven by the downwash on the collector's surface. Similarly, at the collector's rear, see Figure 58, the backward stepping flow from the trailing parapets shown in Figure 56 creates a zone of higher velocity. Thus, Given the relationship between wind velocity and convective heat loss, the noticeable high velocity at both the rear and front surface of the collector account for the greater Nu_{avg} reported in Figure 52. From the foregoing, it is reasonable to conclude that when the collector is placed at the roof centre with low parapets present the average collector's heat loss is primarily determined by downwash at the surface and rear.

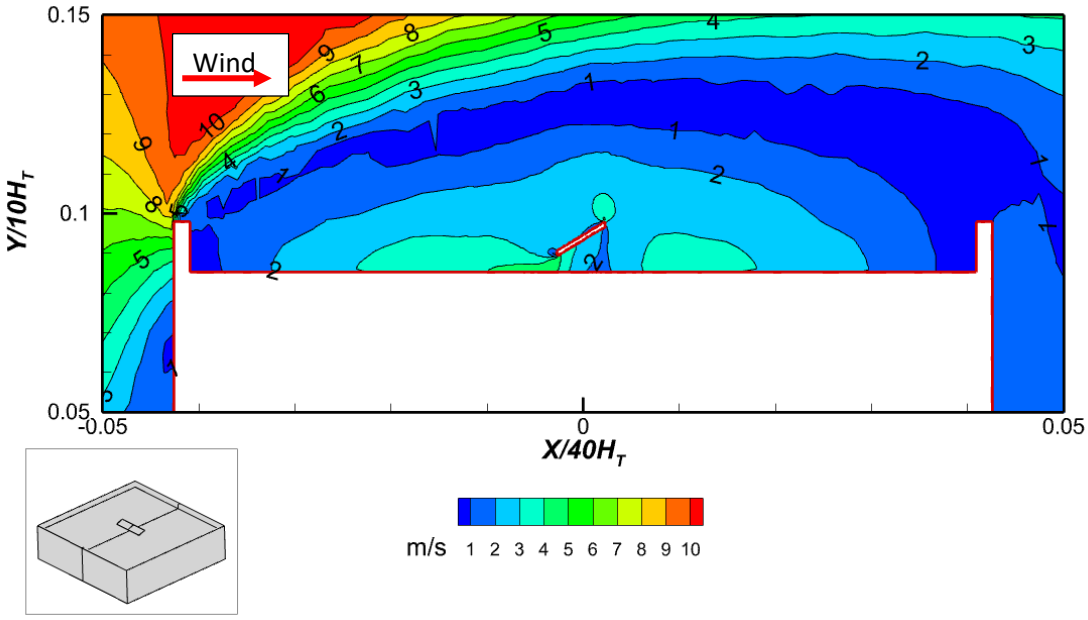

Figure 57: Mean velocity contours on the center plane for flow behavior at low perimetric parapet present (Operational condition V = 10 m/s, β = 20°, Collector location 50 percent of roof's length.

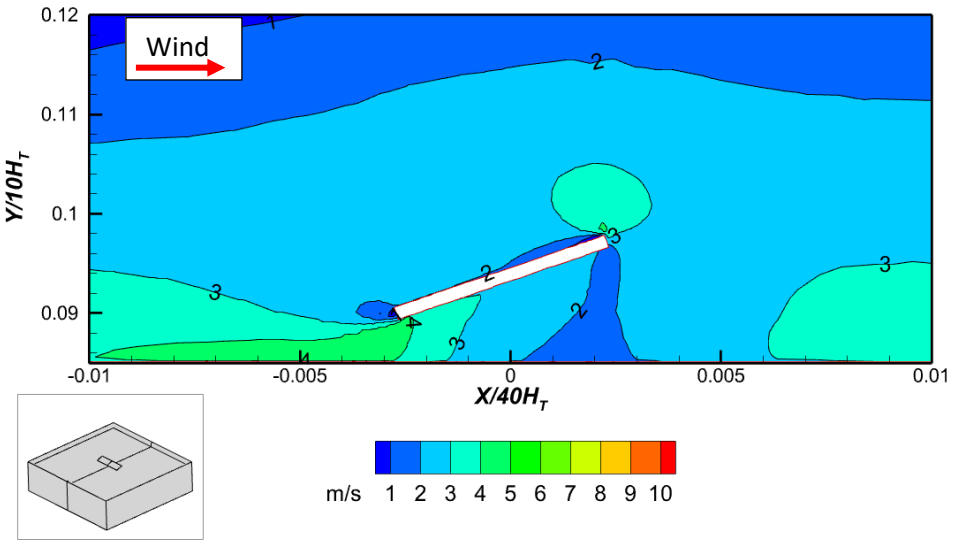

Figure 58: Local velocity (V_l) around collector for collectors located at 50 percent of roof's length with low parapet present

Figure 59 depicts an increased height of the perimetric parapet under the same operating conditions as described above. Flow separation at both the leading and trailing edges causes vortices to form. However, because of the height of the parapet, the vortex is located higher above the roof. A backward stepping flow from the leeward vortex causes a flow separation at the trailing parapet. Because this flow occurs higher above the roof, the roof vortex is noticeably closer to the trailing parapet.

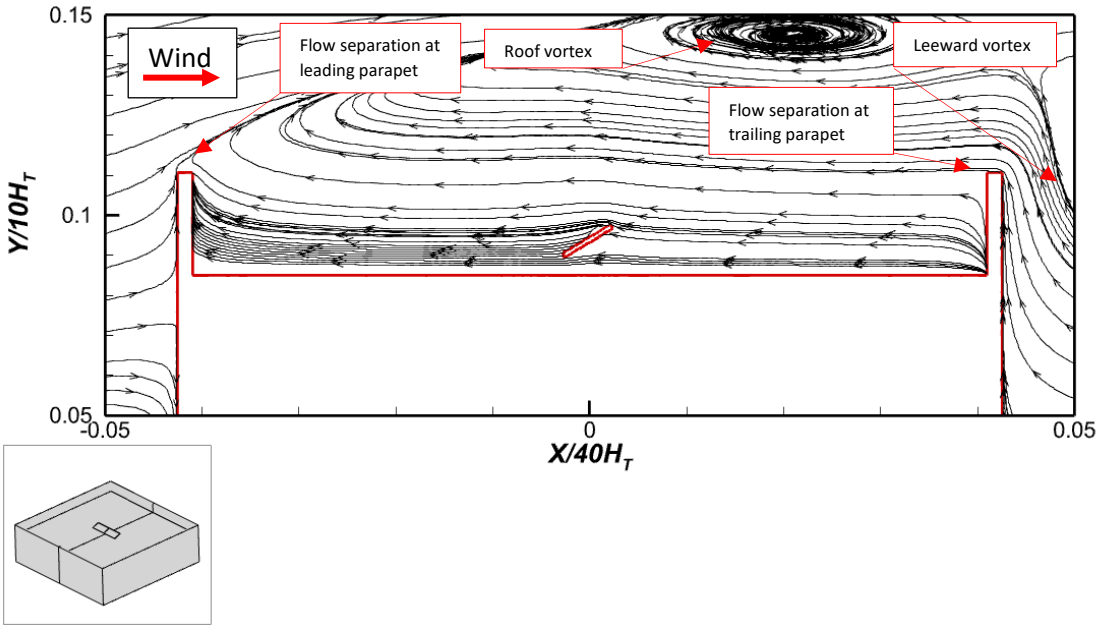

Figure 59: Mean velocity flow stream traces on the center plane for flow behavior on roof at high parapet (Operational condition V = 10 m/s, β = 20°, Collector location 50 percent of roof's length)

Upon analysis of Figure 60, it becomes evident that there exists a greater velocity at the trailing edge of the collector, which can be attributed to the gap between the collector and the roof surface. The analysis becomes more intricate when the local velocity is examined closely, see Figure 61. In contrast to the lower parapet, where the vortex induces substantial downwash affecting both the rear and surface of the collector, the vortex in this scenario is positioned away from the collector. As a result, the collector surface experiences a slightly reduced velocity, leading to a decrease in heat loss. The reason for this occurrence can be attributed to the fact that the trailing edge of the collector is positioned below the parapet height, thereby placing it directly in the path of the oncoming flow and vortex.

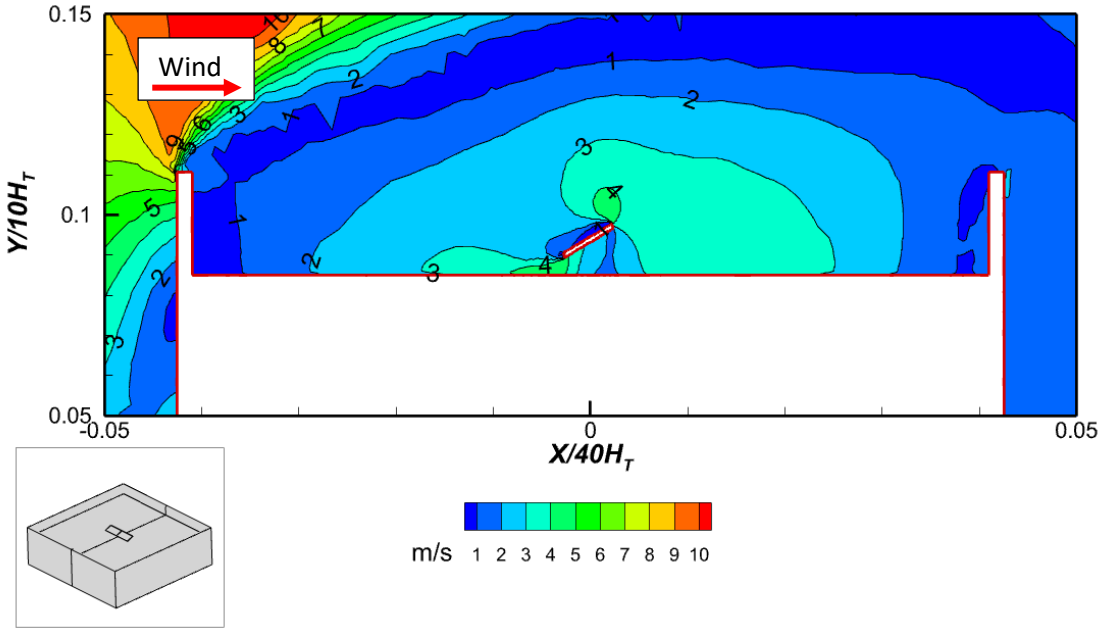

Figure 60 : Mean velocity contours on the center plane for flow behavior with high perimetric parapet present (Operational condition V = 10 m/s, β = 20°, Collector location 50 percent of roof's length.

From the above, it follows that when higher parapets are present, the average heat loss of the collector would be determined by the heat loss at its rear and not its surface. Based on the preceding discussion, it is evident that parapets would result in greater heat loss when a collector is mounted in the middle of the roof. In particular, this would be more prominent at lower perimetric parapets as demonstrated in the Nu_{avg} plots, given the velocity on the surface of and rear of the collector.

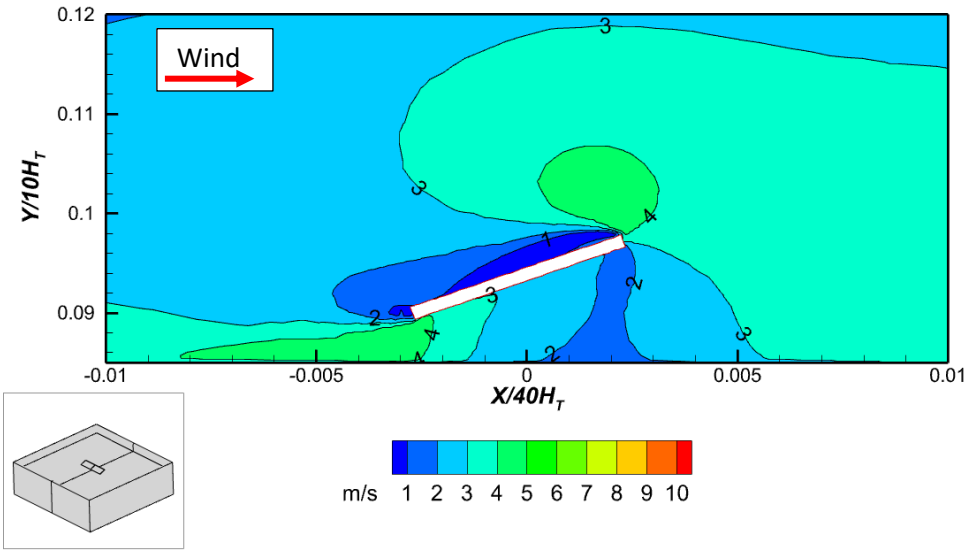

Figure 61: Local velocity (V_l) around collector for collectors located at 50 percent of roof's length with low parapet present

3.4.2.3 The combined effect of a perimetric parapet and a mounting location representing 75 percent of the roof on collector heat loss.

Following the investigation of the heat loss of a collector in the path of an incoming flow and at the center of the roof, the next step was to investigate the heat loss of a collector mounted away from an approaching flow at varying perimetric parapet heights. Again, the collector inclination angle was maintained at 20 ° while the parapet height was varied. Depicted in Figure 62 is the Nu_{avg}, of the unglazed collector for the three scenarios where parapet height is varied.

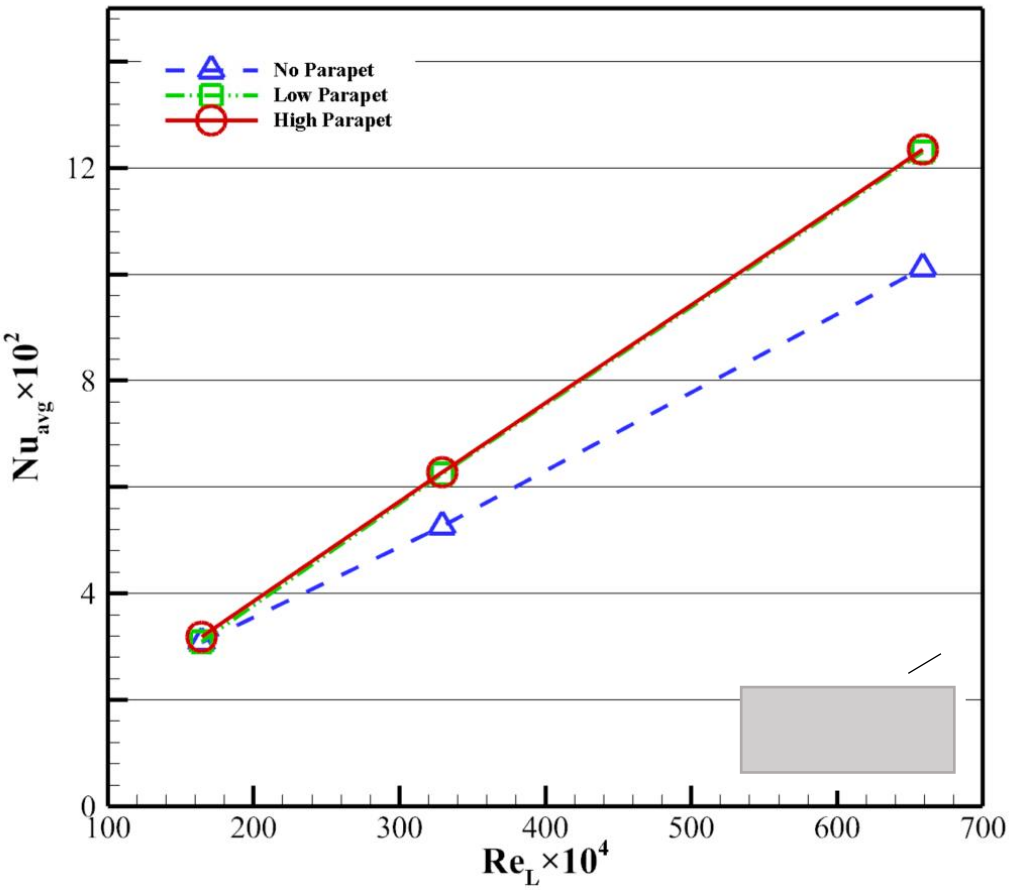

Figure 62: Nu_{avg} for collector at different parapet heights and Reynolds number (Operational condition β = 20°, Collector location 75 percent of roof's length)

To explain the above graph in Figure 62, Figure 63 depicts the roof aerodynamics when no parapet is present. As can be seen, the separation of flow at the leading edge of the roof produces a vortex close to the roof surface. A reattachment of the vortex to the roof creates a recirculation bubble that expands towards the roof's trailing edge.

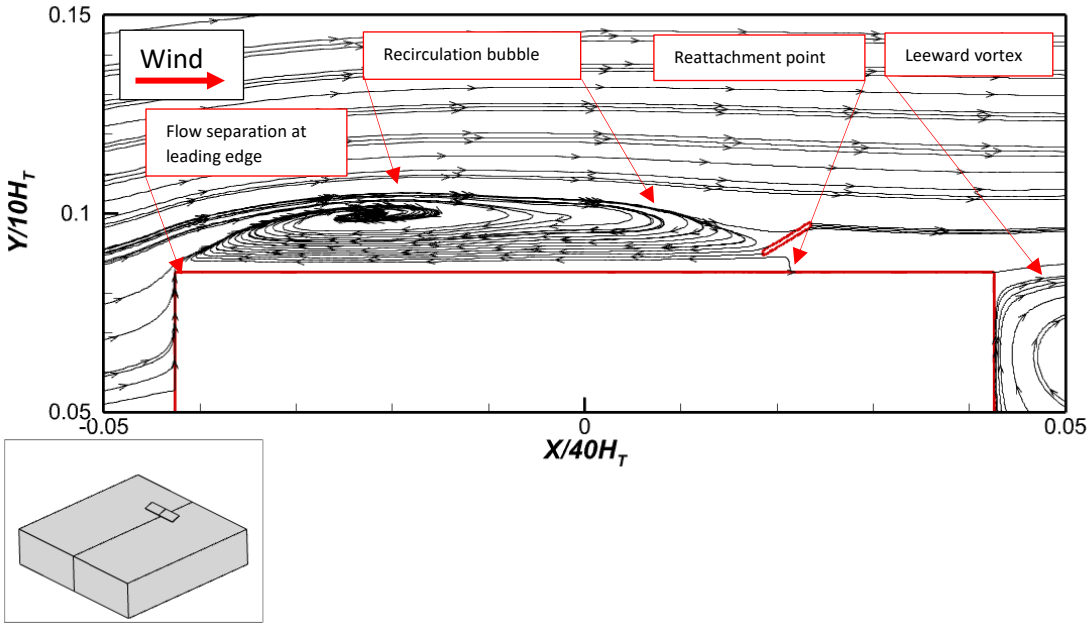

Figure 63: Mean velocity flow stream traces on the center plane with no perimetric parapet (Operational condition V = 10 m/s, β = 20°, Collector location 75 percent of roof's length)

By positioning the collector at a distance from the approaching flow and submerging it within the recirculation bubble, the velocity surrounding the collector is reduced. This reduction in velocity occurs because the collector is immersed within the recirculation bubble, as depicted in Figure 63 and Figure 64. Upon a more detailed analysis of the local velocity, as depicted in Figure 90, it becomes evident that the local velocity at both the surface and rear of the collector is low. This observed occurrence can be attributed to the collector's placement at a distance from the incoming flow, which diminishes its vulnerability to the impact of the oncoming wind. From this, it can be inferred collectors mounted on roofs without parapets would have minimal heat loss if the collector were placed away from the incoming flow.

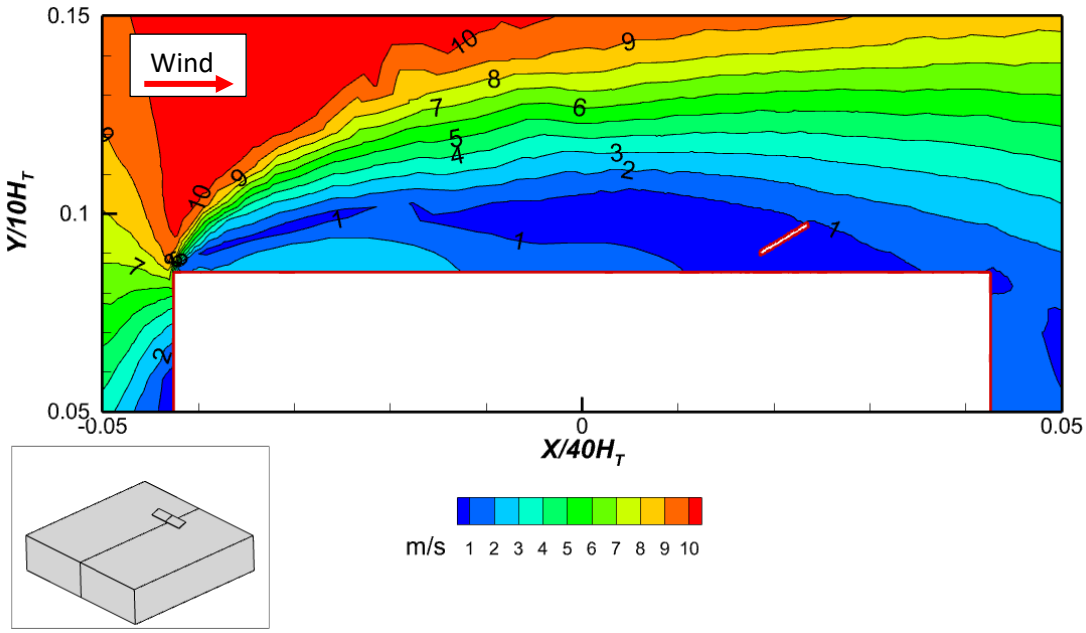

Figure 64: Mean velocity contours on the center plane for flow behavior with no perimetric parapet present (Operational condition V = 10 m/s, β = 20°, Collector location 75 percent of roof's length)

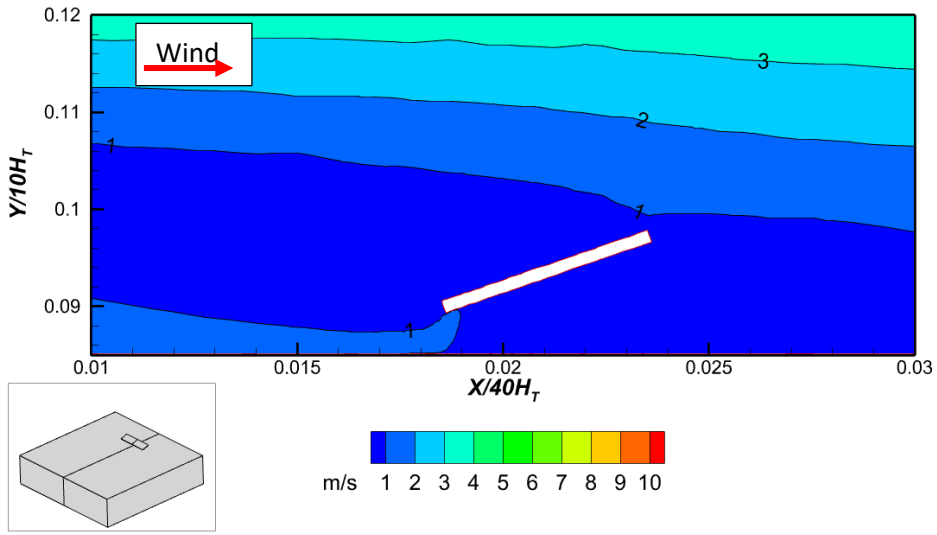

Figure 65: Local velocity (V_l) around collector for collectors located at 75 percent of roof's length with no parapet present

Figure 66 shows the aerodynamics of a low perimetric parapet roof with the collector mounted away farther away from the approaching flow. A vortex forms in front of the collector due to flow separation at the trailing and leading parapets and the collector's position relative to the flow interaction. However, due to the collector's proximity to the backward stepping flow, the vortex extends to the collector's surface, causing downwash at the surface as well as parts of its rear.

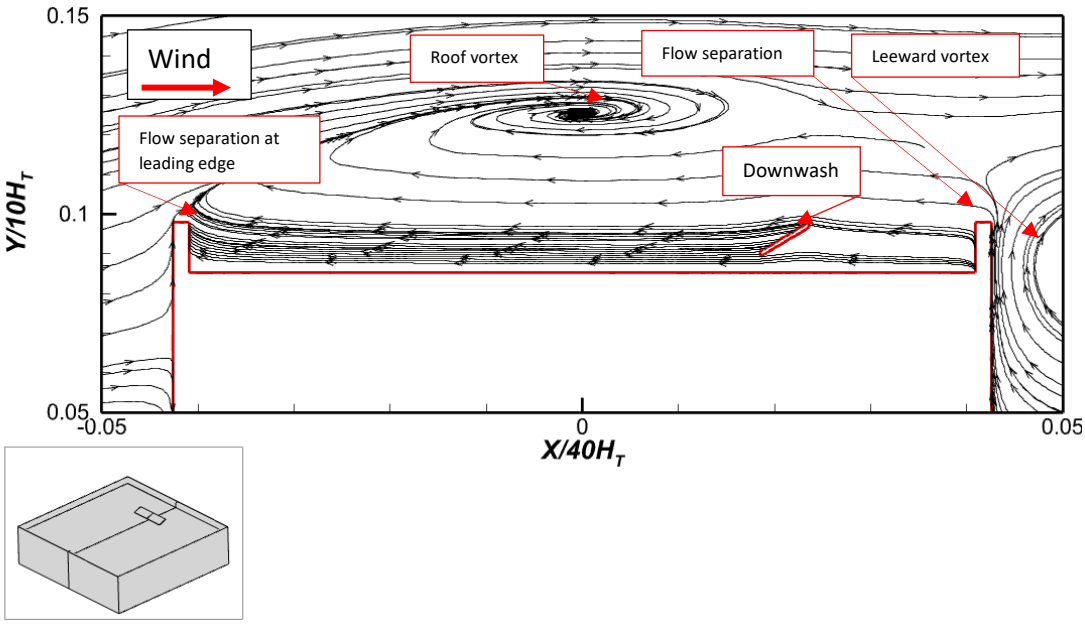

Figure 66: Mean velocity flow stream traces on the center plane with low perimetric parapet (Operational condition V = 10 m/s, β = 20°, Collector location 75 percent of roof's length)

As illustrated in Figure 67, this phenomenon results in alterations in velocity occurring at both the anterior and posterior surfaces of the collector. Upon closer scrutiny, two observations become apparent: firstly, there is a significant disparity in velocity between the leading edge and the trailing edge of the collector, as depicted in Figure 67 and Figure 68. The reason for this can be ascribed to the flow that takes place in the space between the front edge of the collectors and the roof surface. Furthermore, the velocity at the surface of the collector is reduced due to the flow that moves backward from the trailing parapet, which separates the trailing edge of the collector. This decrease in velocity is a result of the collector's close proximity to the trailing parapet, as depicted in Figure 68.

Drawing from the above, it can be inferred that the primary factors influencing the heat loss of the collector are the backward stepping flow originating from the trailing parapet. This is particularly evident when the perimetric parapet heights are lower and the collector is positioned at a greater distance from the oncoming flow.

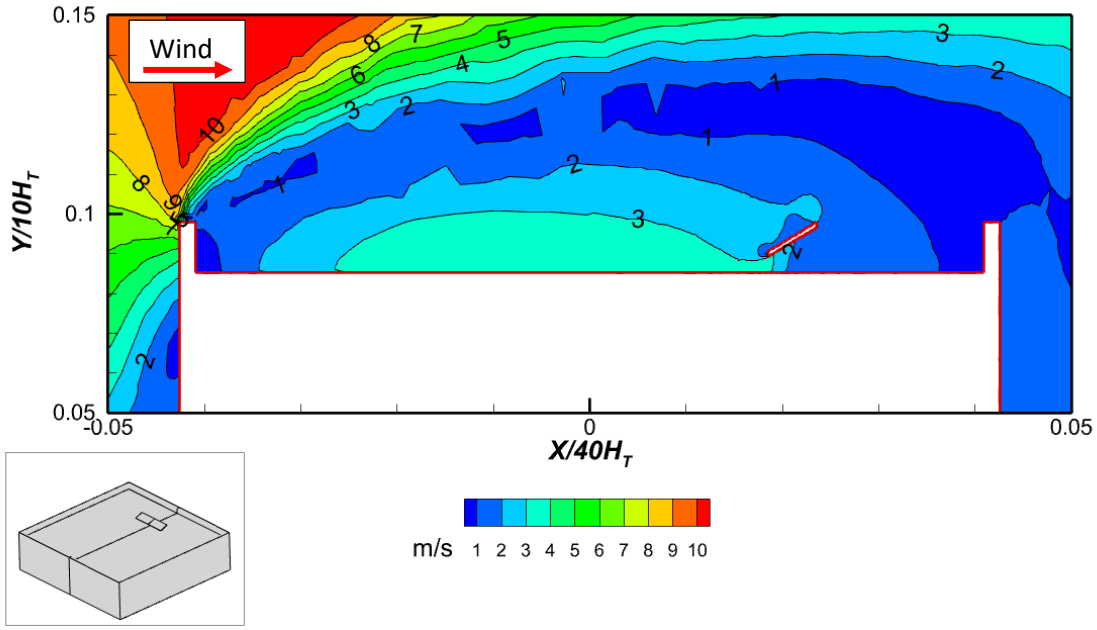

Figure 67: Mean velocity contours on the center plane for flow behavior with low perimetric parapet present (Operational condition V = 10 m/s, β = 20°, Collector location 75 percent of roof's length.

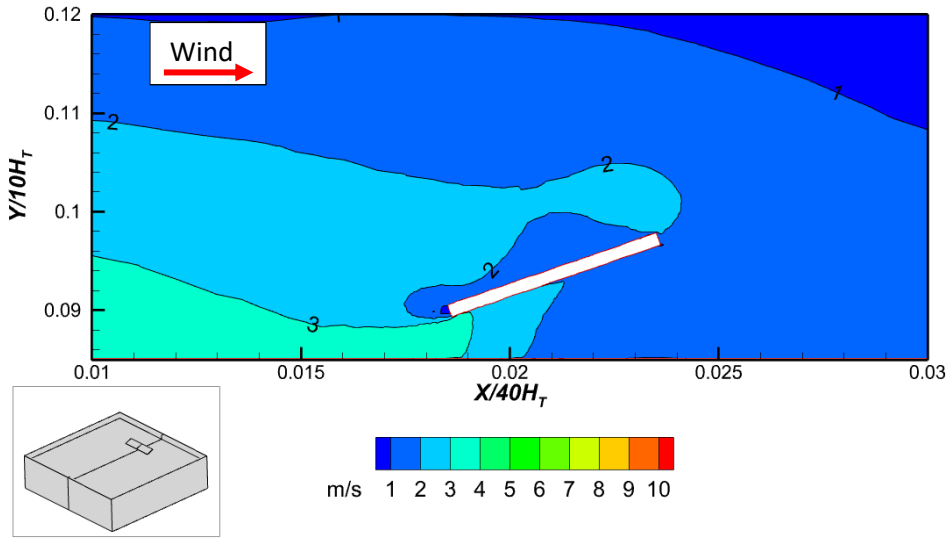

Figure 68: Local velocity (V_l) around collector for collectors located at 75 percent of roof's length with low parapet present

Figure 69 depicts the roof's aerodynamics when the collector is positioned away from the incoming flow with a high parametric parapet present. Similar to the presence of a low perimetric parapet, a vortex forms above the roof due to the separation of flow at the leading and trailing parapets edges and the mounting position of the collector.

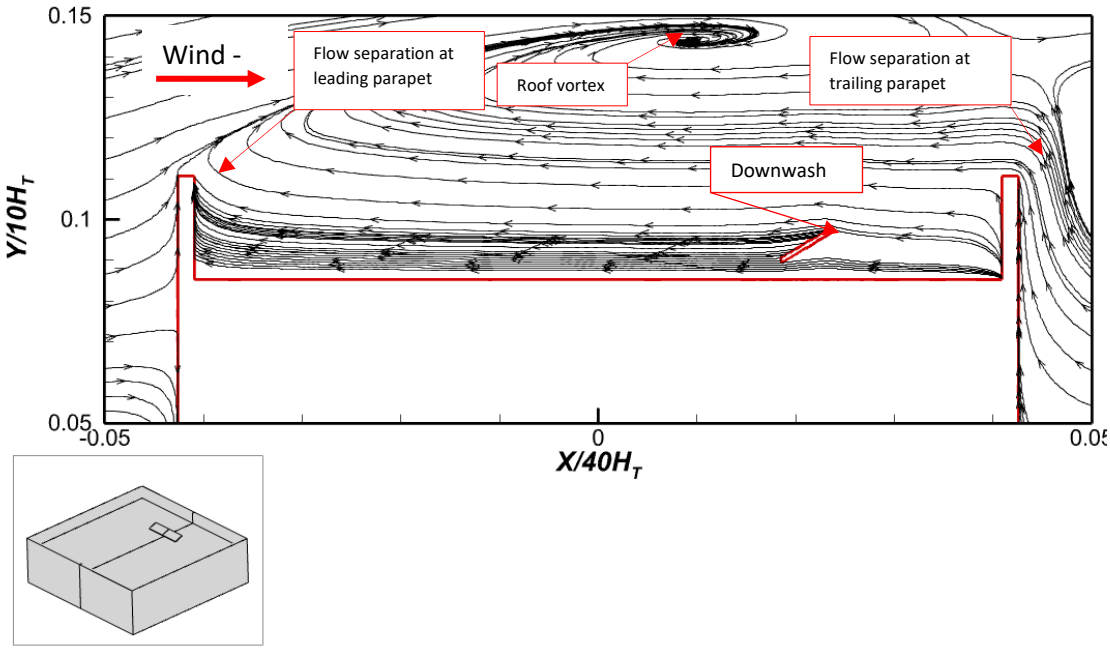

Figure 69: Mean velocity flow stream traces on the center plane for flow behavior for varying location of collector with high perimetric parapet (Operational condition V = 10 m/s, β = 20°, Collector location 75 percent of roof's length)

Similar to what was observed in the case of the low parapet, the presence of a high parapet leads to the displacement of the vortex at an increased height above the roof. Moreover, the velocity distribution surrounding the collector is subject to the influence of flow separation originating from the trailing parapet. This phenomenon is observed on both the front and rear surfaces of the collector, as illustrated in Figure 70, due to the collector's positioning.

Like the case of low parapet, it can be noted that the velocity at the leading edge of the collector is higher, while simultaneously experiencing a decrease in velocity along the surface of the collector. This previously discussed phenomenon provides clarification on the influence of collector heat loss, as demonstrated by the average Nusselt number Nu_{avg} values presented in Figure 62. The examination of the low parapet and higher parapet demonstrates that, although there are some differences, both scenarios exhibit a more significant heat loss as a result of the presence of back stepping flow.

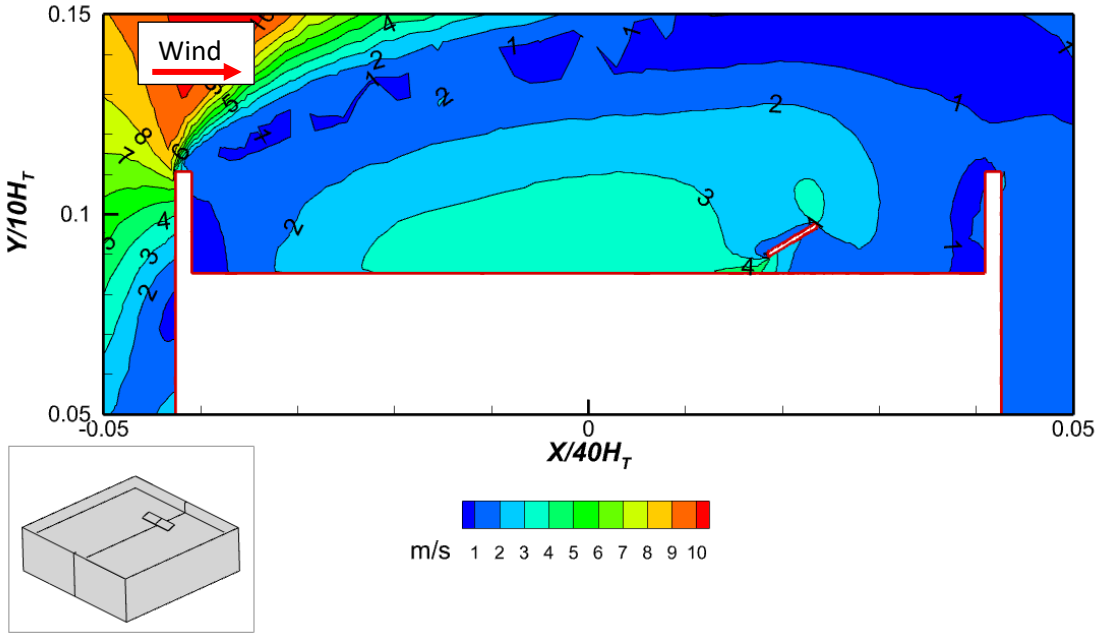

Figure 70: Mean velocity contours on the center plane for flow behavior with high perimetric parapet present (Operational condition V = 10 m/s, β = 20°, Collector location 75 percent of roof's length.

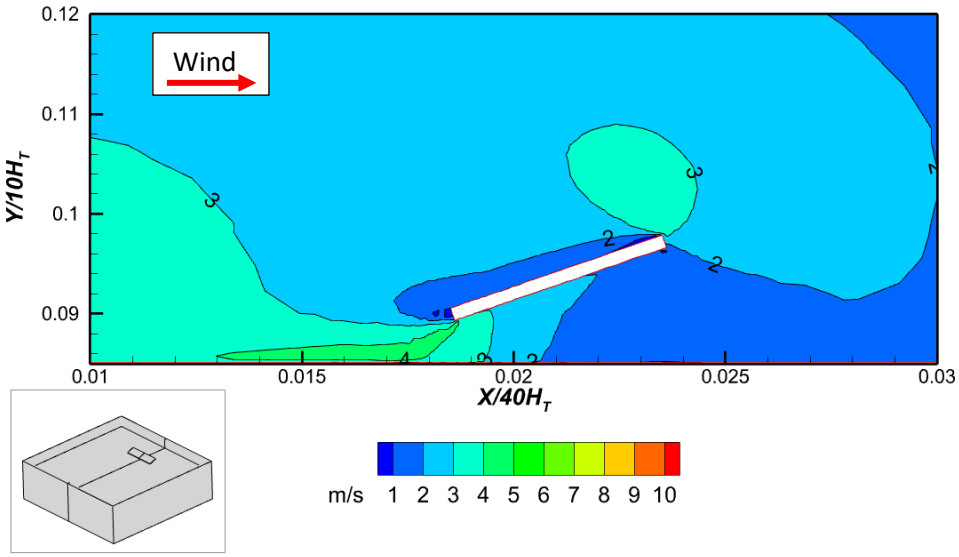

Figure 71: Local velocity (V_l) around collector for collectors located at 75 percent of roof's length with high parapet present

3.4.2.4 The effect of collector mounting location on heat loss.

The heat loss of the collector was shown in the preceding sections to vary with changes in perimetric parapet height. By using the dataset above, it follows that the heat loss of the collector can be examined for different mounting location across the same roof.

Figure 72 shows that for a roof without a parapet, the collector loses more heat if it is located close to the roof's leading edge. This is due to the collector's exposure to the oncoming flow and the flow path between the roof surface and the leading edge, as explained in the previous section. In contrast, by positioning the collector far from the oncoming flow, the rate of heat loss is significantly reduced, owing to the oncoming flow's limited effect.

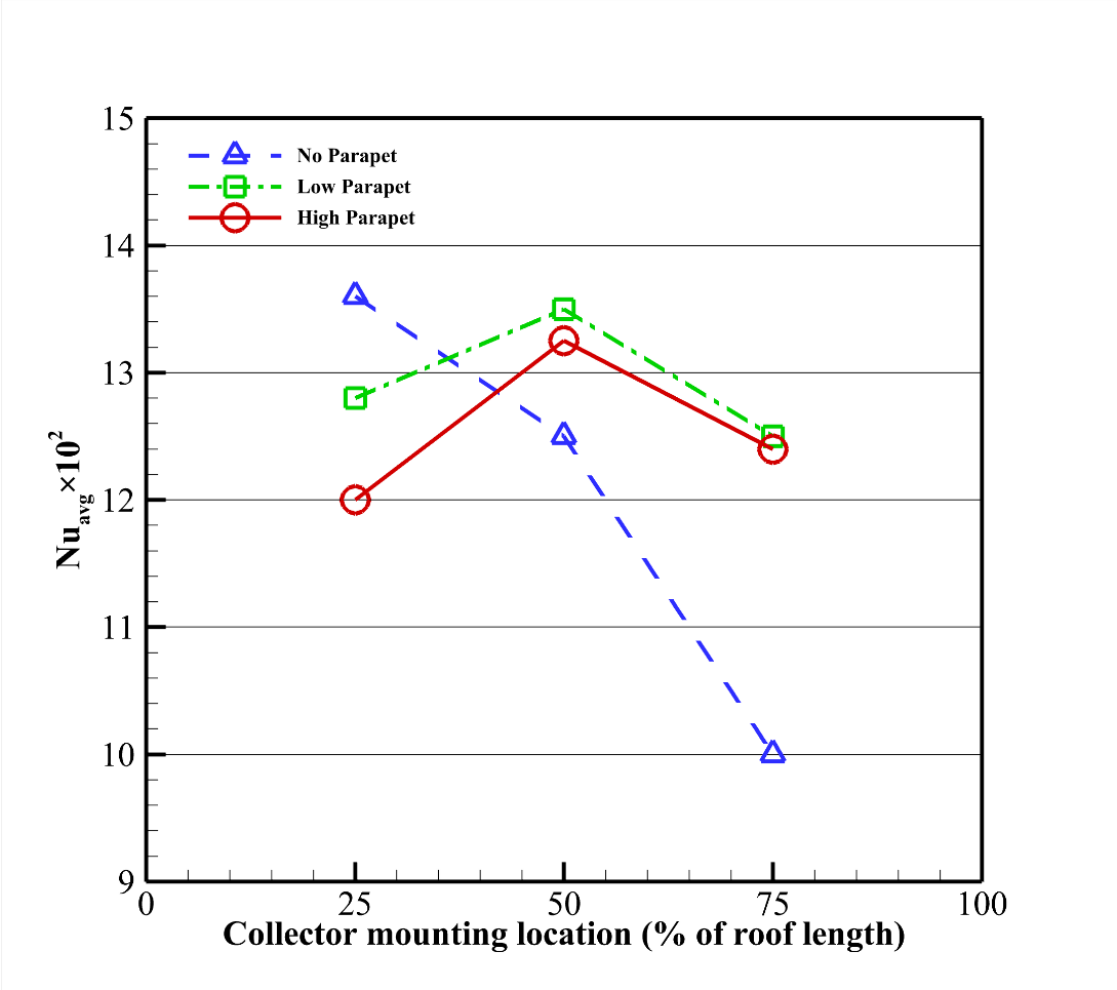

Figure 72: Nu_{avg} for collector at different parapet heights and Reynolds number (Operational condition β = 20°, Varying roof mounting location)

In the case of roofs featuring low perimetric parapets, it becomes apparent that the extent of heat loss is heightened when the collector is positioned at the roof's centre. This is due to the collector surface being exposed to the flow separation that takes place at the edges of the leading and trailing parapets, as well as the location of the roof vortex. The aforementioned phenomena hold true for roofs featuring low perimetric parapets, where the heat loss becomes more pronounced when the collector is positioned at the roof's centre. Comparatively, it is evident that the heat loss on the collector is generally more pronounced in roofs with low perimetric parapets, except for cases where the collector is positioned at the leading edge of the roof where no parapets are present.

Finally, due to the absence of glazing on the collector, the flow structure on each surface of the collector will invariably lead to disparate heat losses at the front and rear of the collector. A significant amount of heat is loss at the surface of the collector in closest proximity to the incoming flow. Likewise, the presence of a downwash at the posterior region of the collector results in a significant increase in heat loss. Parapets, on the other hand, result in increased downwash when they are present. A comprehensive analysis of the heat loss at the front and rear surfaces of the collector is provided in the next section.

3.5 Convective heat transfer coefficient (CHTC)

Considering the unglazed nature of the collector, it is crucial to assess the influence of roof aerodynamics on the heat loss at the front and rear surfaces of the collector. In order to accomplish this, graphical representations of the average convective heat transfer coefficient are provided for the front and rear surfaces of the collector.

When the collector is positioned at a distance of 25 percent of the roof length, and the parapet height is varied, it becomes evident, as depicted in

Figure 73, that there is a noticeable disparity in heat loss between the front and rear surfaces of the collector. The previous discussion on the decrease in velocity at the rear of the collectors serves as the foundation for understanding why the convective heat transfer coefficient (CHTC) is lower at the rear of the collector. Thus, regardless of the parapet height, the heat loss for an

unglazed collector positioned nearer to the leading edge of a collector is more prominent on the front surface of the collector due to its proximity to the incoming flow. There exists a disparity of 29.4% between the front and rear portions of the collector for a roof with no parapet. Similarly, a lower parapet exhibits a discrepancy of 13.5%, while a roof featuring high perimetric parapets results in difference of 5.1% on the front and rear surface of the collector. This suggests that for a high parapet, there is not much of a difference in terms of heat loss at the front and rear and front of the collector. The basis for this foregoing observation is the height of the parapet which acts as an obstruction to the oncoming flow.

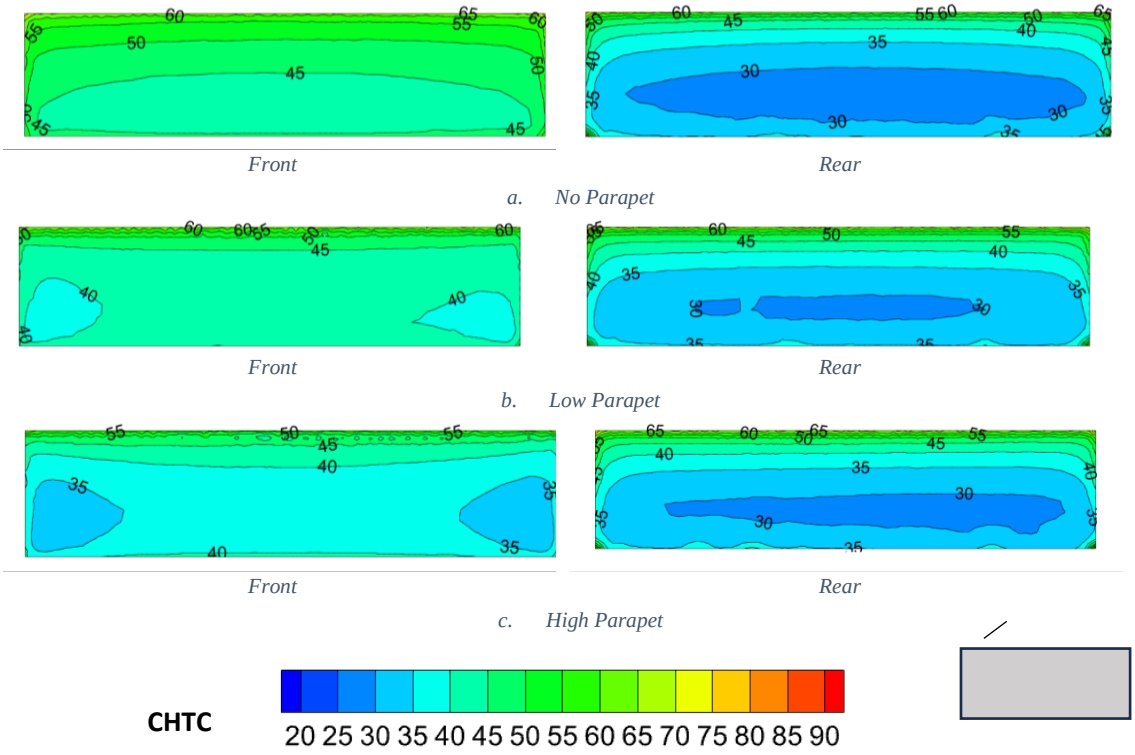

Figure 73: CHTC contours on the front and rear surfaces of the collector positioned at 25% of the roof (Operational condition V = 10 m/s, β = 20°, Collector location 25 percent of roof's length. 0° wind)

In a similar vein, when the collector is positioned at the central location on the roof, there is a discernible increase in heat loss at the front of the collector in comparison to its rear. In the comparative scenario where no parapets are present, the findings depicted in Figure 74 indicate that the heat loss at the rear of the collector is lower when compared to the collector positioned in closer proximity to the leading edge of the roof (25% of the roof's length), shown in

Figure 73. In the context of a roof lacking a parapet, it is observed that there is a notable discrepancy of 30.6% between the front and rear sections of the collector when the collector is positioned at the midpoint of the roof. The presence of a lower parapet demonstrates a disparity of 21.5%, whereas a roof incorporating elevated perimetric parapets yields a discrepancy of 5.2% on both the front and rear surfaces of the collector. The above supports the inference drawn in the preceding section that the heat loss is more pronounced at lower parapets. Moreover, the heat is noticeably higher at the front of the collector compared to its rear.

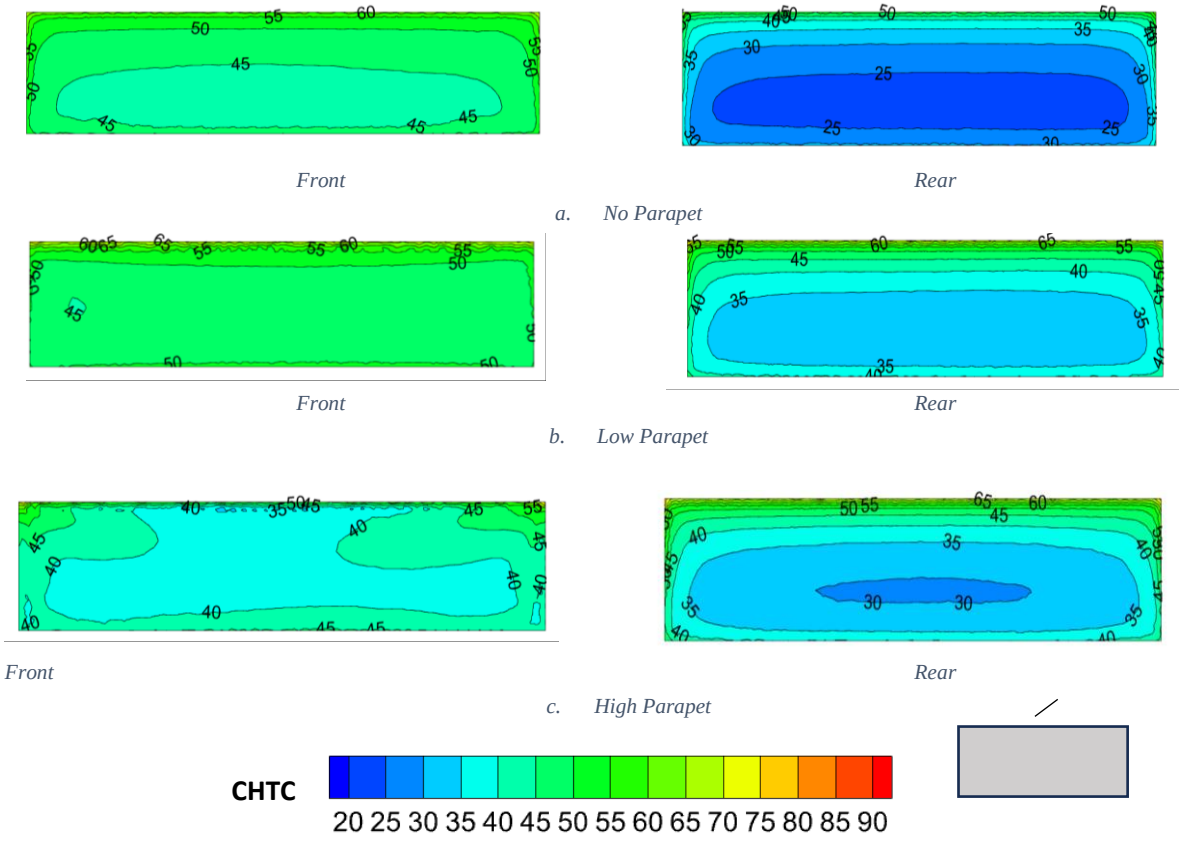

Figure 74: CHTC contours on the front and rear surfaces of the collector positioned at 50% of the roof (Operational condition V = 10 m/s, β = 20°, Collector location 50 percent of roof's length. 0° wind)

The findings depicted in

Figure 75 indicate that positioning the collector at a greater distance from the approaching flow, leads to a reduction in heat loss at the rear of the collector. The lack of a parapet contributes to a lower heat loss at the rear of the collector, which can be attributed to the distance between the collector and the oncoming flow. However, when perimetric parapets are present, the collector in this case becomes fully exposed to the back stepping flow from the trailing parapet which

consequently leads to the observed marginal heat loss at the rear of the collector. Between the lower and higher parapets, it is observed that the heat loss is slightly greater at the rear of the collector for lower parapets. The findings indicate that in the absence of parapets, there is a notable disparity of 71.72% between the frontal and rear surfaces of the collector. The presence of a lower parapet demonstrates a variation of 33.62%, whereas a roof featuring perimetric parapets show a discrepancy of 19% on both the front and rear aspects of the collector.

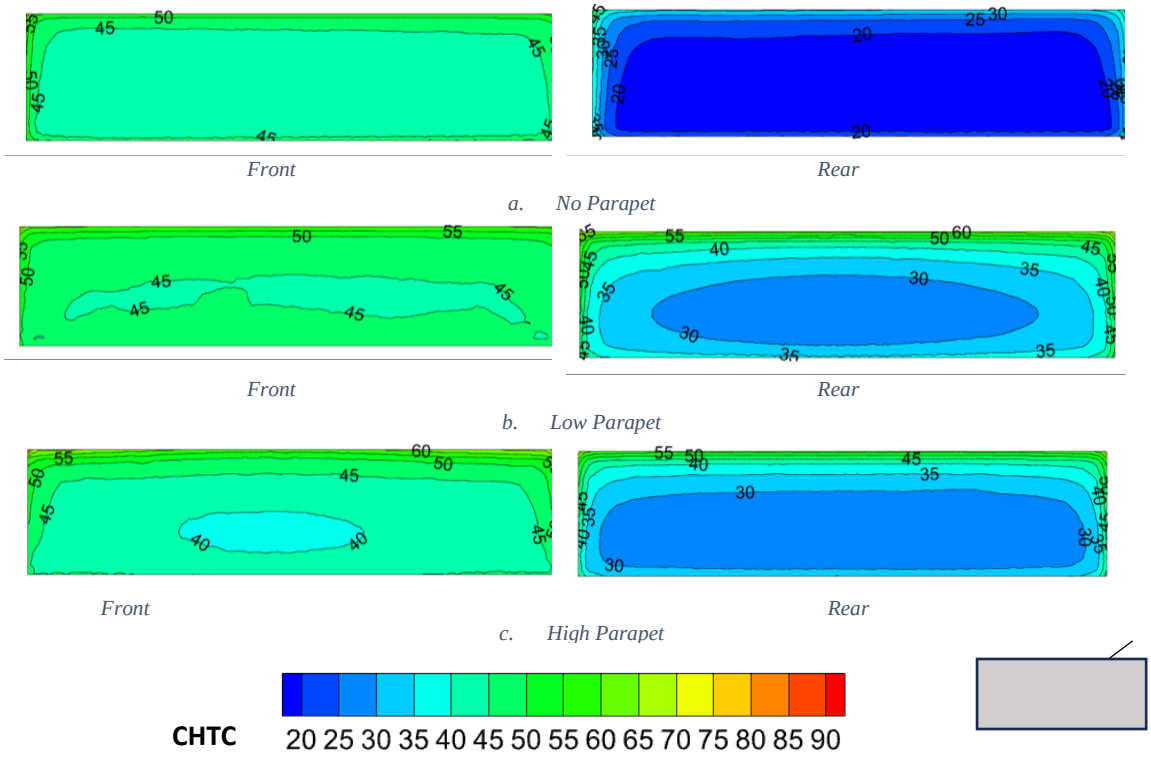

Figure 75: CHTC contours on the front and rear surfaces of the collector positioned at 75% of the roof (Operational condition V = 10 m/s, β = 20°, Collector location 75 percent of roof's length. 0° wind)

3.6 The effect of collector tilt angle on roof aerodynamics and heat loss on roofs with perimetric parapet.

The preceding section has shown that the heat loss from a collector inclined at a tilt angle of 20° varies with collector mounting location and parapet height. Given that the tilt angle of the collector's surface with respect to the horizontal has a significant impact on its performance (Chang, 2010), the next step was to investigate the above effect at varying collector tilt angles.

To do this, collector tilt angles of 5°, 40°, and 60° were considered. Including the tilt angle of 20°, these angles were chosen as they apply to a reasonable range of latitudes for different geographical locations. Now, even though the heat loss analysis was conducted for each tilt angle at different collector mounting locations and perimetric parapet heights, the results presented in this section are only for the collector located at the center of the roof.

Figure 76 depicts the Nu_{avg} for an unglazed collector mounted at the center of a roof at an inclination angle of 5° for the three parapet height scenarios considered.

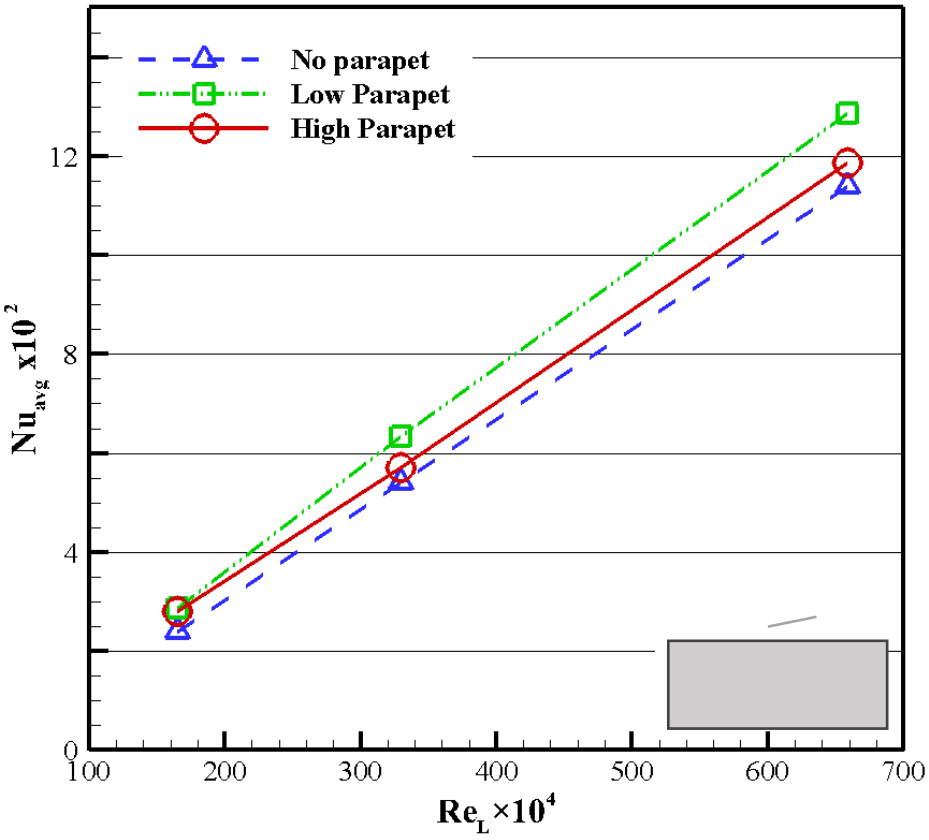

Figure 76: Nu_{avg} for collector at different parapet heights and Reynolds number (Operational conditions β =5°, Collector location 50 percent of roof's length)

In order to explain the average Nusselt number Nu_{avg} depicted in Figure 76, it is evident from Figure 77 that in the absence of parapets, a recirculation bubble forms on the roof, similar to the observations made in the preceding sections. In this particular scenario, the collector's tilt angle is relatively low, causing its surface to be submerged within the recirculation bubble.

Consequently, this leads to a decrease in velocity at the front surface of the collector, as illustrated in Figure 78.

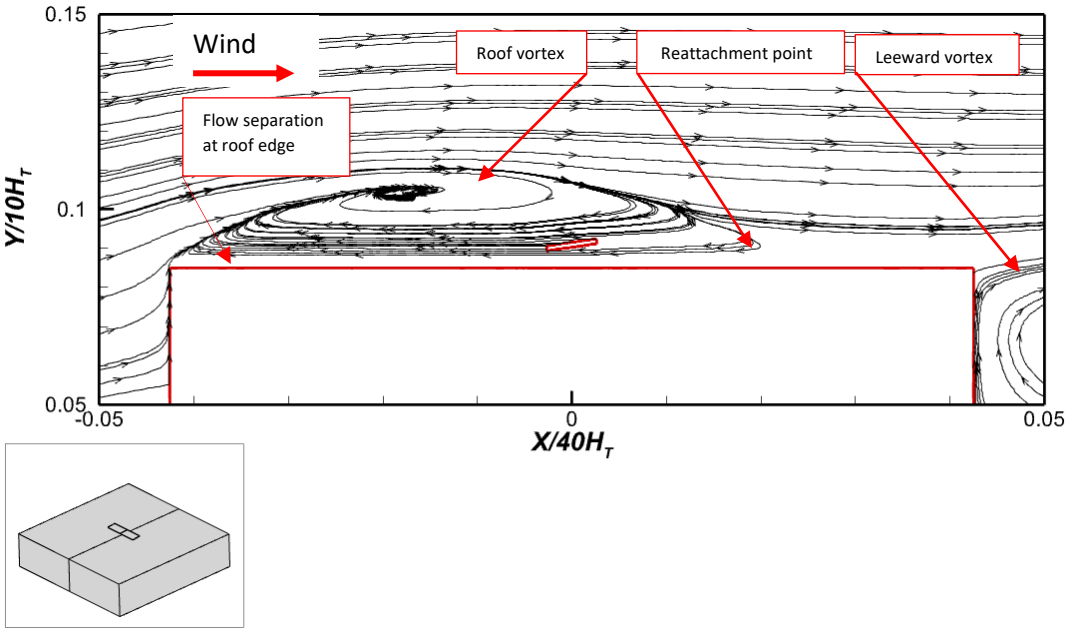

Figure 77: Mean velocity flow stream traces on the center plane with no perimetric parapet (Operational condition V = 10 m/s, β = 5°, Collector location 75 percent of roof's length)

Upon close examination, as depicted in Figure 79, it becomes evident that the presence of a flow path surrounding the leading edge of the collector and the roof surface results in the manifestation of a heightened velocity in the vicinity of the leading edge of the collector. Although the aforementioned factors contribute to heat loss, it is apparent that the net heat loss of the collector in this scenario is primarily influenced by the low velocity at its surface.

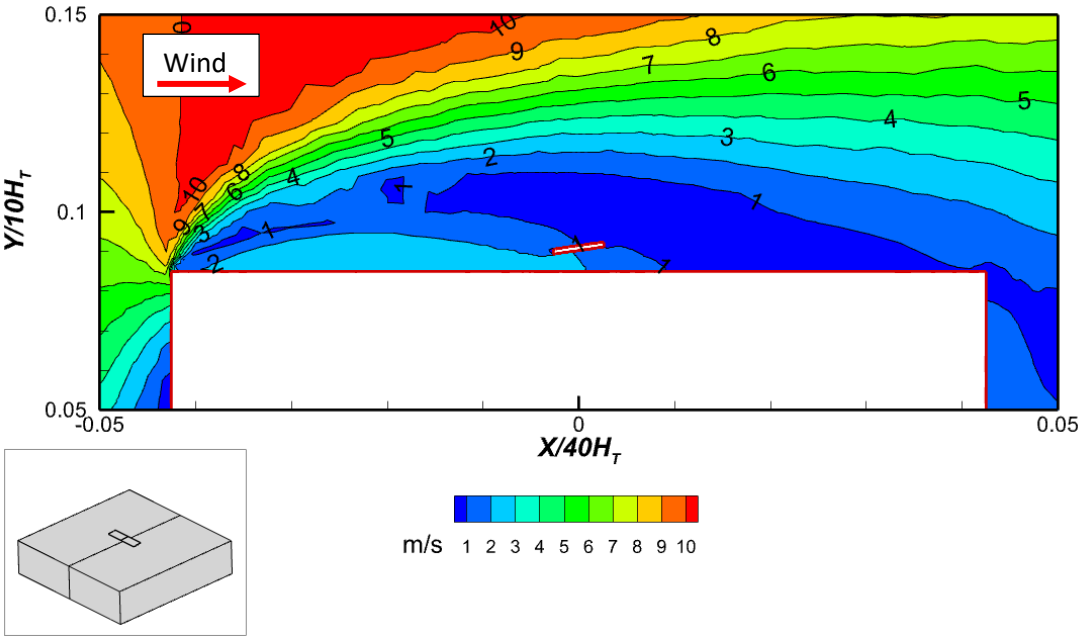

Figure 78: Mean velocity contours on the center plane for flow behavior with no perimetric parapet present (Operational condition V = 10 m/s, β = 5°, Collector location 50 percent of roof's length.

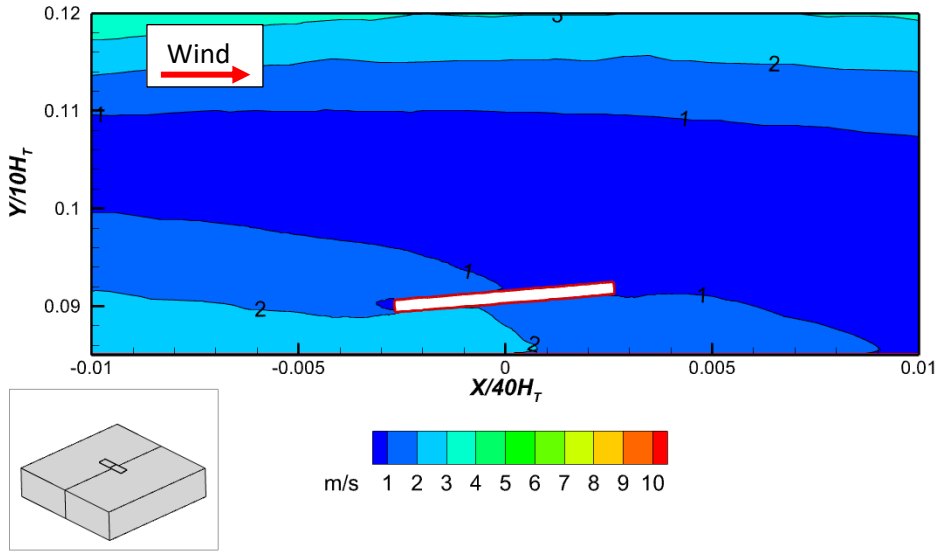

Figure 79: Local velocity (V_l) around collector for collectors located at 50 percent of roof's length with no parapet present

In instances where a parapet with a low perimeter is present, it is noticeable that the vortex is positioned at a higher level above the roof as shown Figure 80. Also, the central region of the roof exhibits an elevated velocity, as depicted in Figure 117. This observed increase in velocity can be ascribed to two phenomena, firstly, the existence of a vortex situated above the roof, and secondly, the flow separations originating from the leading and trailing parapets.

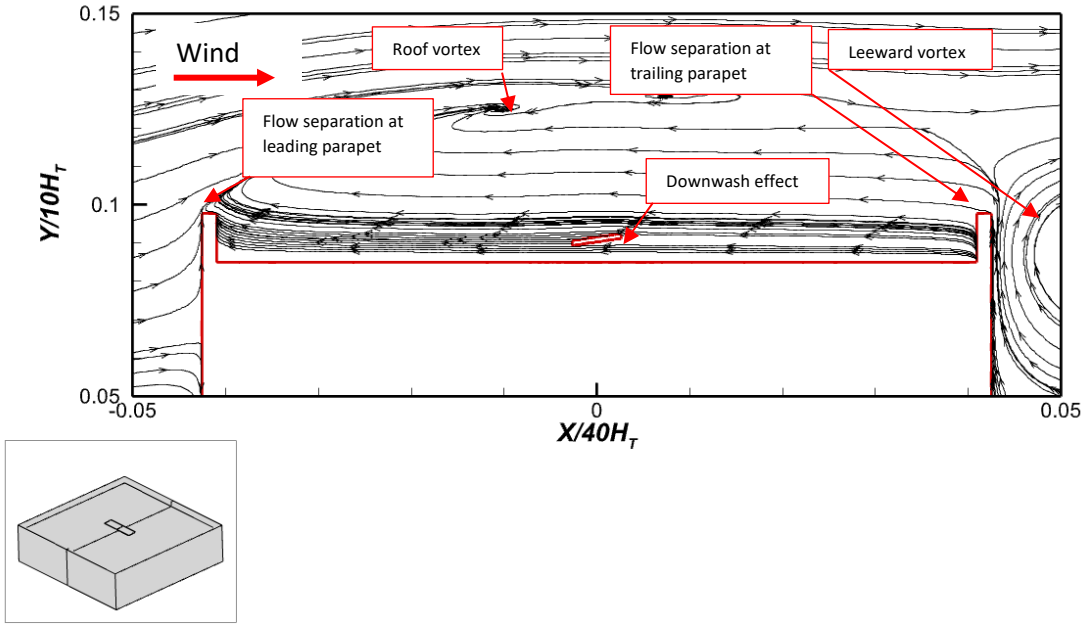

Figure 80: Mean velocity flow stream traces on the center plane for flow behavior with low parapets present (Operational condition V = 10 m/s, β = 5°, Collector location 50 percent of the roof's length)

As a result of the collector's low tilt angle, both its front and rear surfaces are fully immersed within the flow, leading to heightened velocity observed. Furthermore, the gap between the leading edge of the collector and the upper surface of the roof results in an increase in velocity, particularly at the rear surface of the collector, as illustrated in Figure 82. This phenomenon forms the basis for the notable heat loss observed in situations involving the presence of low perimetric parapets, in contrast to scenarios where no parapets are present, as illustrated in Figure 76.

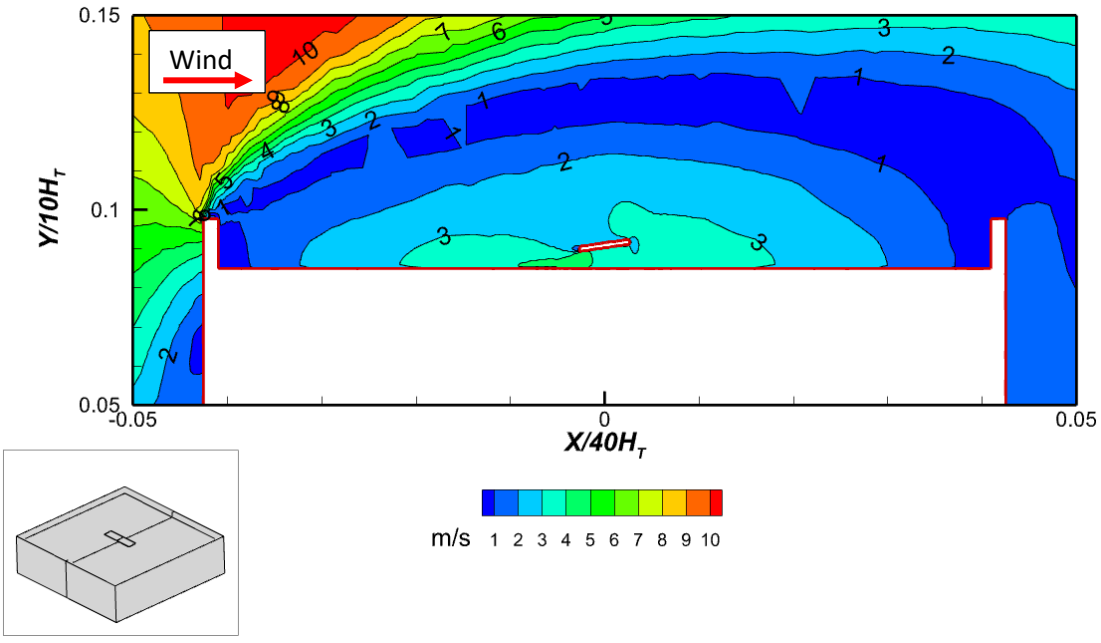

Figure 81: Mean velocity contours on the center plane for flow behavior with low perimetric parapet present (Operational condition V = 10 m/s, β = 5°, Collector location 50 percent of roof's length)

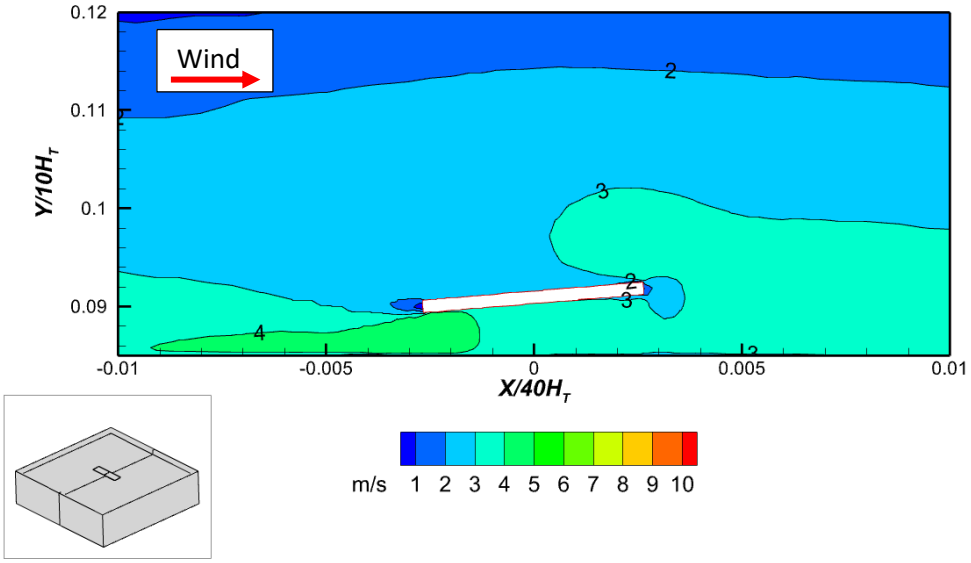

Figure 82: Local velocity (V_l) around collector for collectors located at 50 percent of roof's length with no parapet present

Figure 83 illustrates the displacement of the vortex above the roof, a phenomenon observed in the presence of a lower parapet. Like the situation observed in the low parapet scenario, an increase velocity is generated at the midpoint of the roof, Figure 84. This occurrence is attributed to the vortex and flow separation, causing the collector to be fully enveloped within the high velocity, as illustrated in Figure 85.

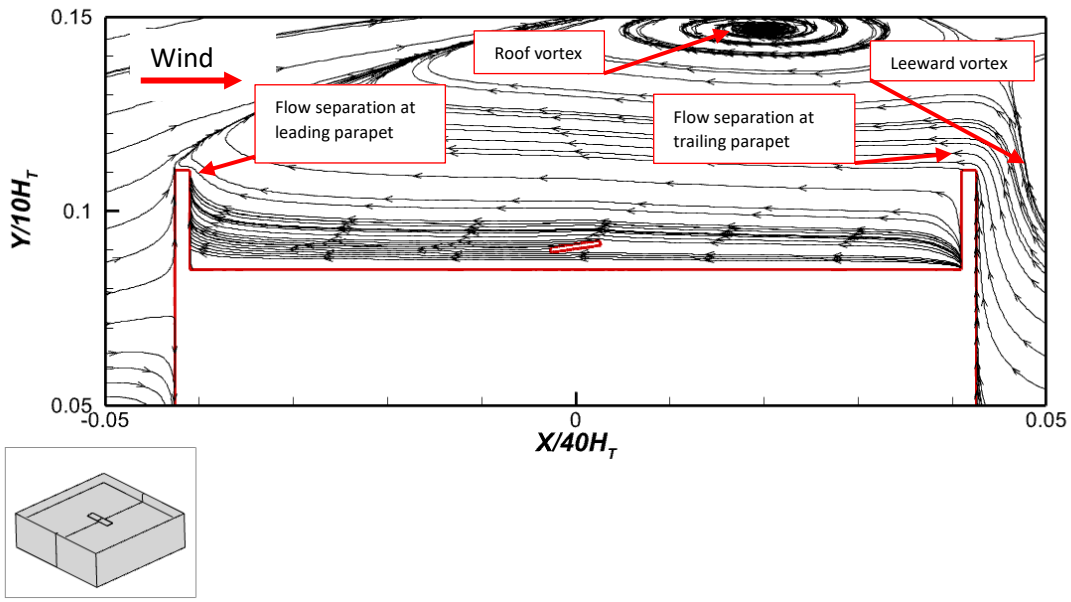

Figure 83: Mean velocity flow stream traces on the central plane for flow behavior with high parapets present (Operational condition V = 10 m/s, β = 5°, Collector location 50 percent of the roof's length)

However, in this scenario the collector's low tilt and its placement in relation to the parapet's height necessitate a more detailed analysis of the local velocity, shown Figure 84. The examination reveals that the flow separates at the trailing edge of the collector, leading to a relatively low velocity at the surface of the collector. However, the rear of the collector is exposed to higher velocities due to the presence of a gap between its leading edge and the surface of the roof, as previously discussed. In comparison to the low parapet, where the velocity zone is correspondingly higher, it can be deduced that the heat loss at the higher parapet will be relatively lower due to the reduced velocity experienced at the surface of the collectors.

Nonetheless, it is apparent that there will be a significant heat loss at the rear of the collector in both scenarios. Based on the preceding discourse, it can be inferred that when collectors are positioned at low tilt angles, the collector surface experiences elevated airflow velocities near low parapets, leading to significant heat loss. Conversely, low velocity zones at the roof center when no parapets are present results in less heat loss for the collector.

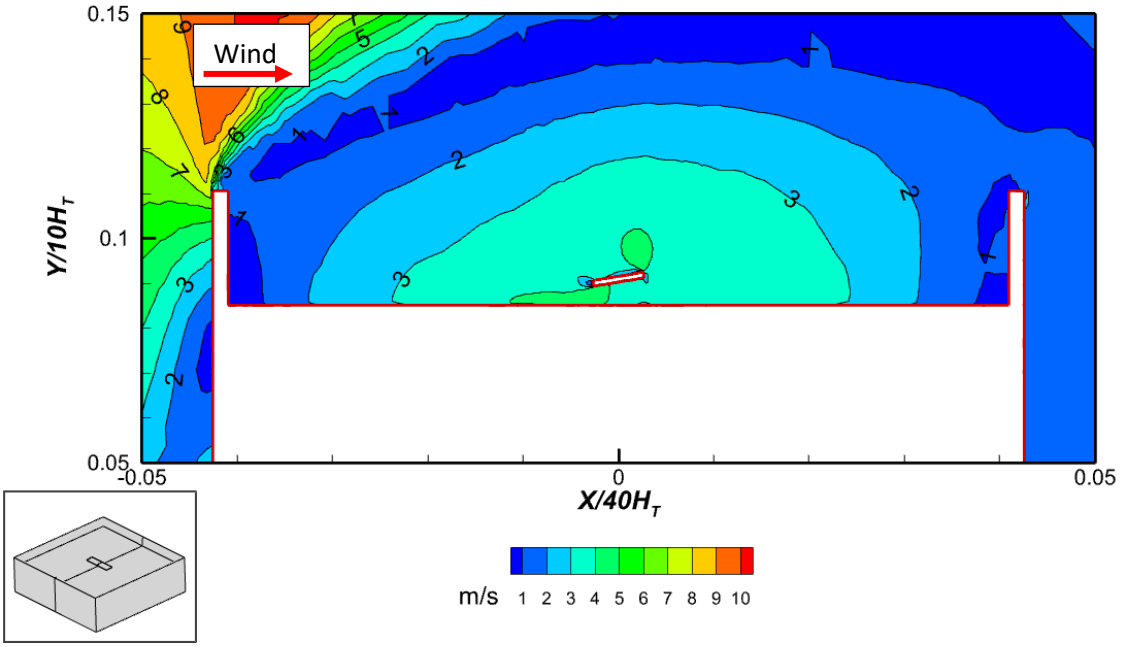

Figure 84: Mean velocity contours on the center plane for flow behavior with high perimetric parapet present (Operational condition V = 10 m/s, β = 5°, Collector location 50 percent of roof's length)

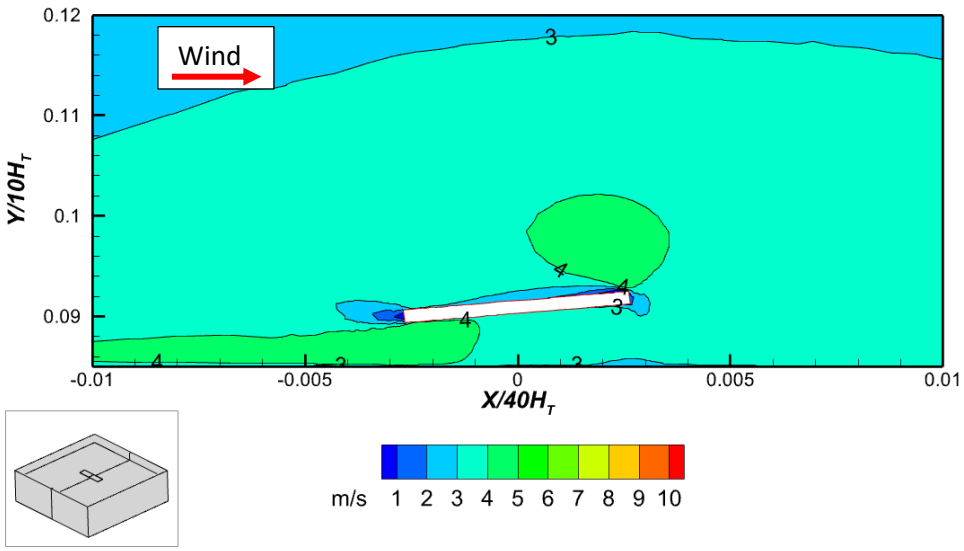

Figure 85: Local velocity (V_l) around collector for collectors located at 50 percent of roof's length with no parapet present

The Nu_{avg} under fixed operating conditions for a collector tilted at 40° is shown in Figure 86. Again, the collector is maintained at the center of the roof representing 50 percent, whereas the parapet height varies. As can be seen, the heat losses for a collector with a low perimetric parapet is more pronounced than those for a collector without or with a high perimetric parapet.

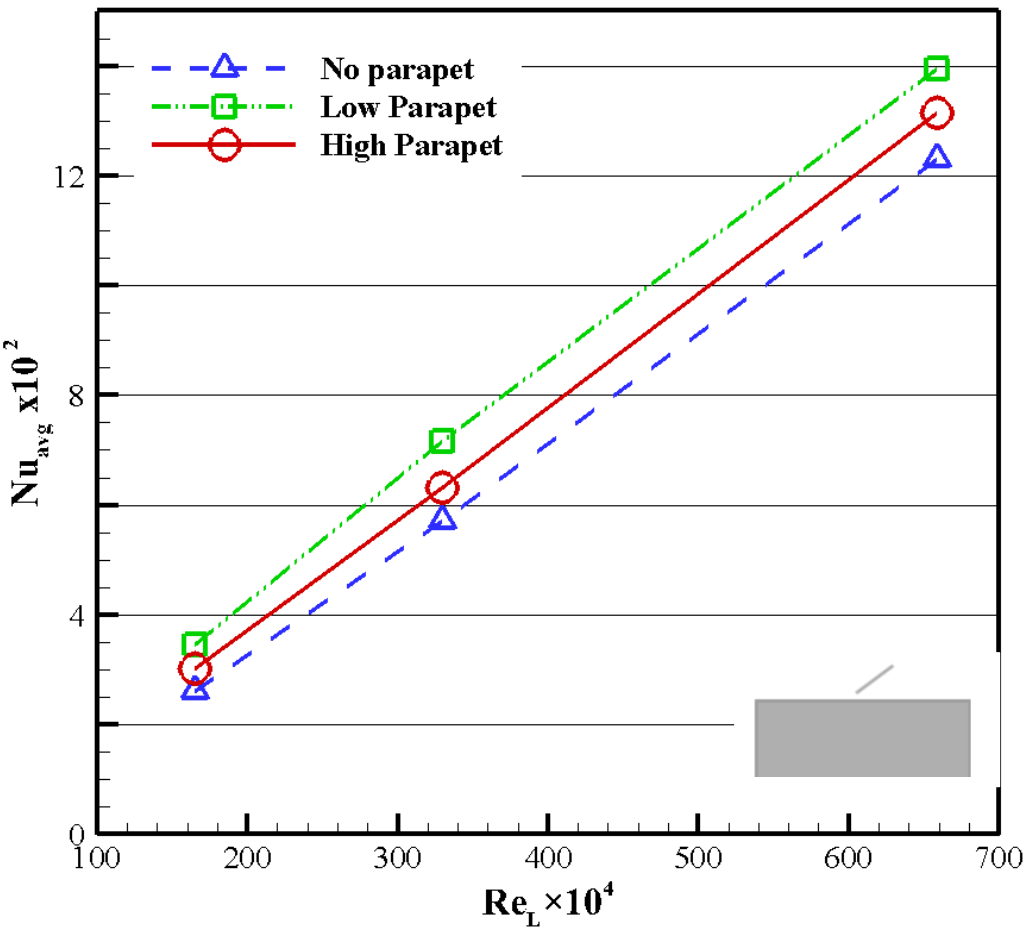

Figure 86: Nu_{avg} for collector at different parapet heights and Reynolds number (Operational condition β =40°, Collector location 50 percent of roof's length)

As depicted in Figure 87, without a parapet, a recirculation bubble forms around the collector, similar to that observed at collector tilt angle of 20°. A low velocity is seen at both the front and back of the collector as shown in Figure 88 , indicating minimal heat loss. When examined in terms of the local velocity as depicted in Figure 89, it is noticeable that the velocity at the front of the collector is lower. At the collector's leading edge however, it can be seen that both the front and rear of the leading edge of the collector gets exposed to the marginally higher velocity. This thus suggests that the heat loss for a collector tilted at 40 on a roof with no parapets present will be lower.

As illustrated in Figure 87, the absence of a parapet results in the formation of a recirculation bubble around the collector, which bears resemblance to the phenomenon observed at a collector tilt angle of 20°. Figure 88 illustrates that there is a low velocity observed at both the front and

rear of the collector, suggesting that there is minimal heat loss. Upon analysis of the local velocity, as illustrated in Figure 89, it becomes evident that the velocity at the leading edge of the collector is comparatively higher. Both the front and rear surfaces of the leading edge are subjected to slightly elevated velocities. The above provides the basis for why the heat loss for a solar collector inclined at a 40-degree angle on a roof lacking parapets is lower.

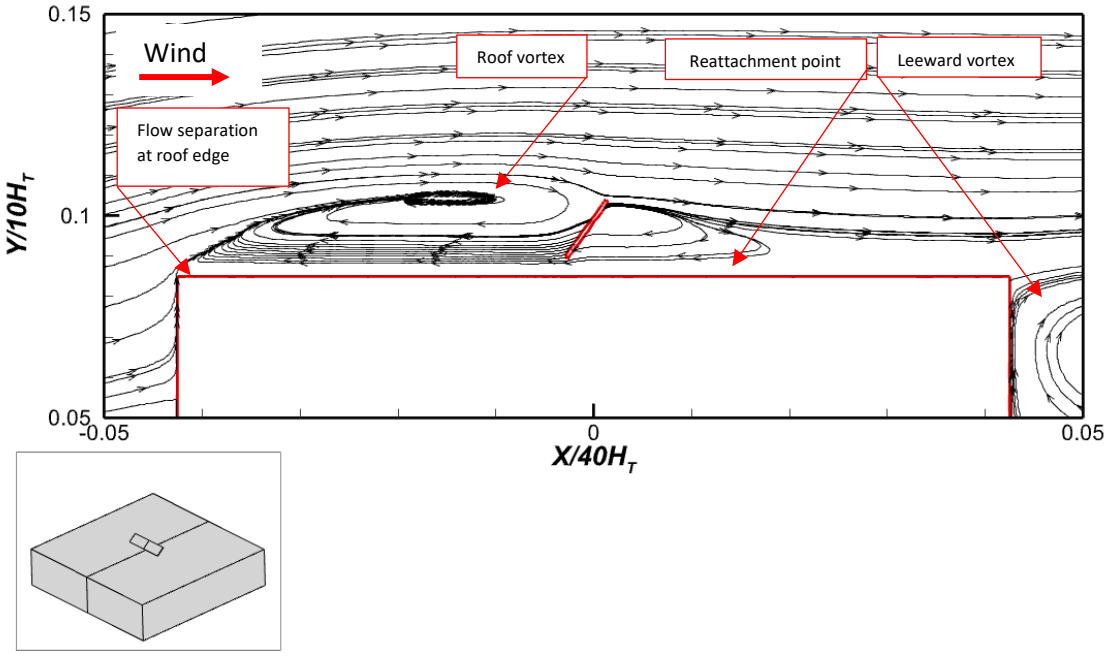

Figure 87: Mean velocity flow stream traces on the center plane for flow behavior with no parapets present (Operational condition V = 10 m/s, β = 40°, Collector location 50 percent of the roof's length)

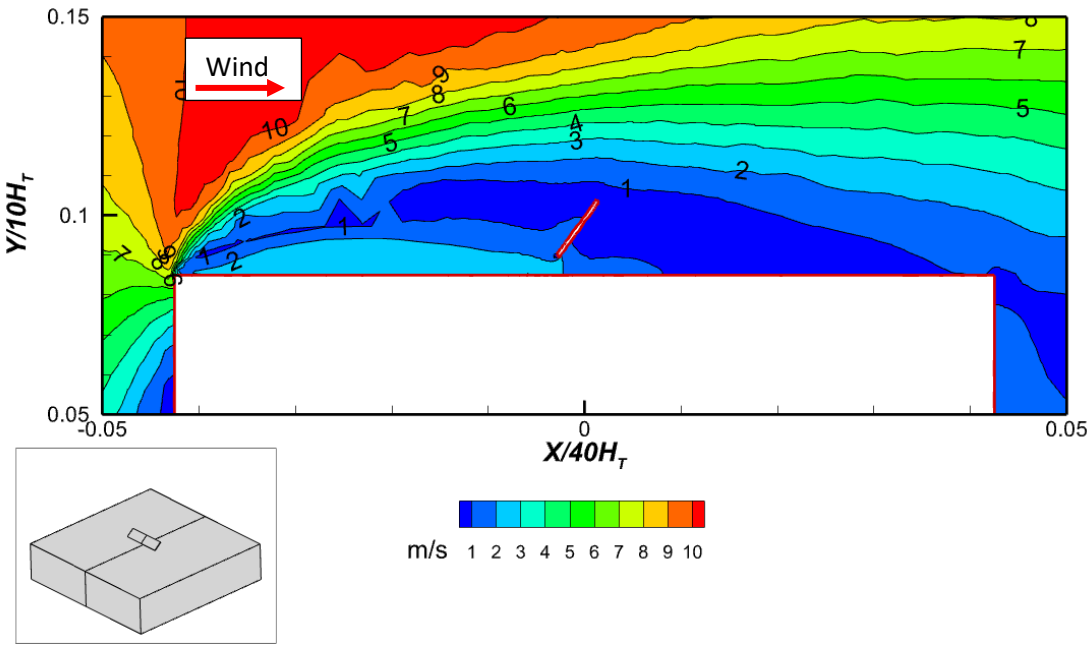

Figure 88: Mean velocity contours on the center plane for flow behavior with high perimetric parapet present (Operational condition v = 10 m/s, β = 40°, Collector location 50 percent of roof's length)

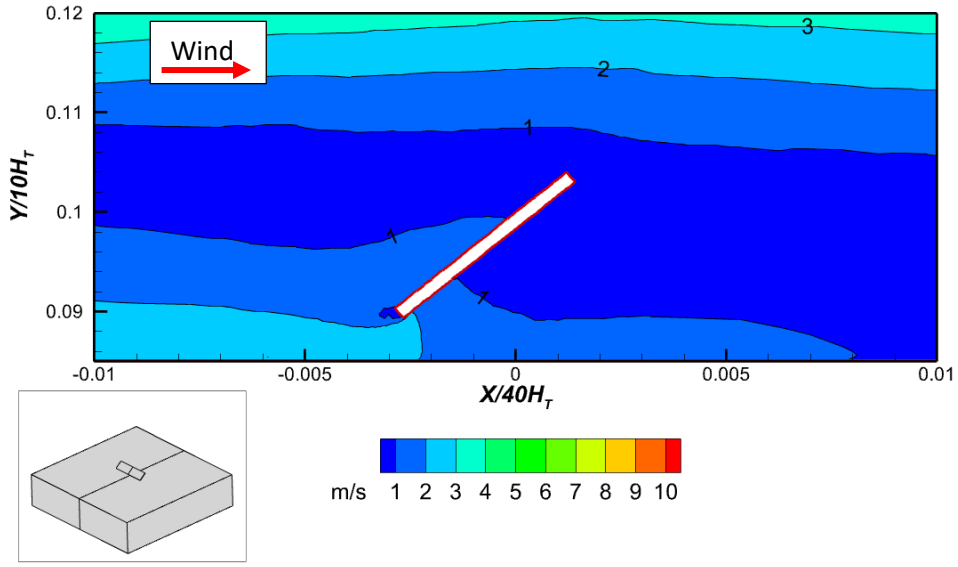

Figure 89: Local velocity (V_l) around collector for collectors located at 50 percent of roof's length with no parapet present

The presence of a low perimetric parapet, as shown in Figure 90, divides the roof vortex into parts, each with its own vortex eye above the roof. With the collector's upward tilt, it distorts the roof vortex created by flow interactions resulting from leading and trailing parapet flow separations. As a result, the collector's rear surface is also down washed as shown in Figure 91 and Figure 92 resulting in a high velocity which suggests a pronounced heat loss.

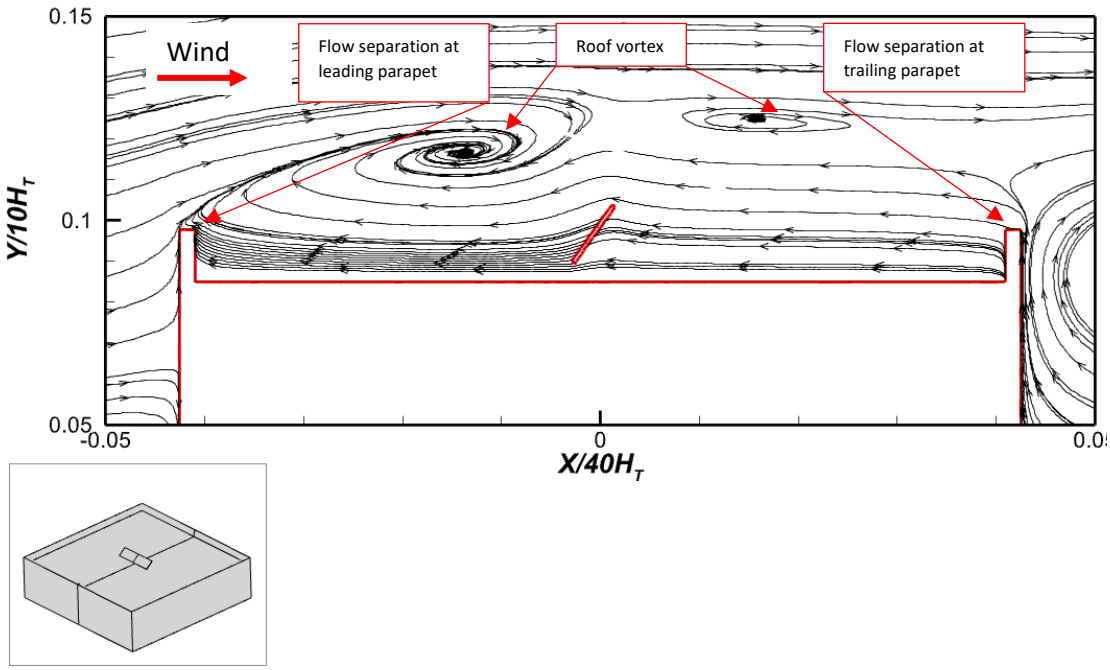

Figure 90: Mean velocity flow stream traces on the center plane for flow behavior with low parapets present (Operational condition v = 10 m/s, B = 40°, Collector location 50 percent of the roof's length)

Additionally, it is noticeable that due to the collector tilt angle being above the parapet, its surface is directly positioned in the path of the oncoming flow and the roof vortex. Thus, the net heat loss of the collector would be higher in comparison to situations without parapets as illustrated using Nu_{avg} in Figure 86.

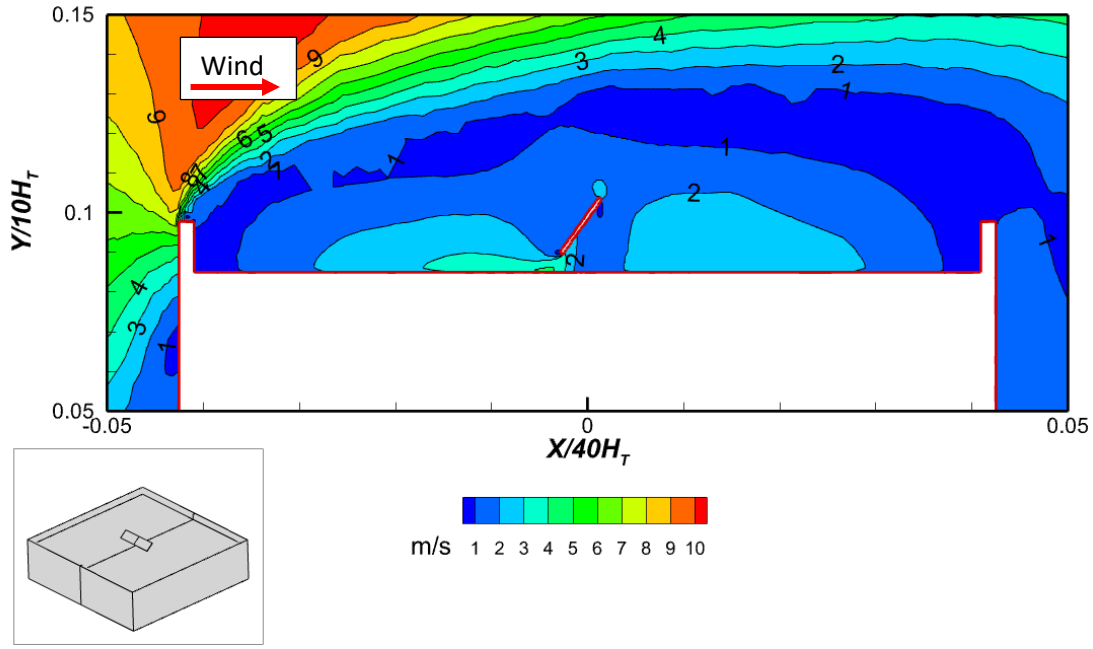

Figure 91: Mean velocity contours on the center plane for flow behavior with high perimetric parapet present (Operational condition V = 10 m/s, β = 40°, Collector location 50 percent of roof's length)

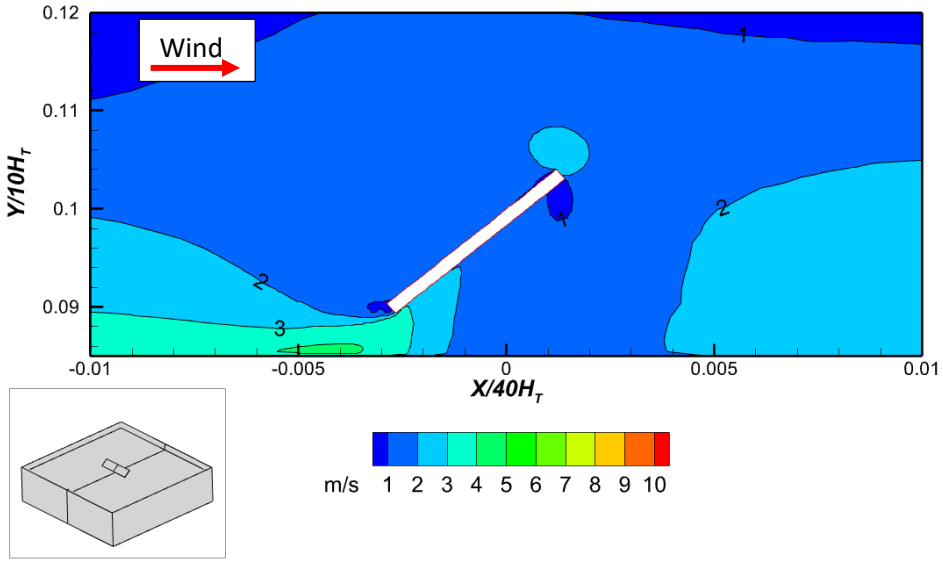

Figure 92: Local velocity (V_l) around collector for collectors located at 50 percent of roof's length with no parapet present

Figure 93 shows that higher parapets cause the same flow distortion as lower parapets. Here, the flow separation at the parapets occurs above the roof due to the height of the parapets, while the flow path emanating from the backward stepping flow results in a higher velocity around the collector's rear as shown in Figure 94. It does, however, cause a flow separation at the collector's trailing edge, resulting in a low-velocity area at the collector's front due to the lack of downwash. This suggests that the collector's front surface would lose less heat.

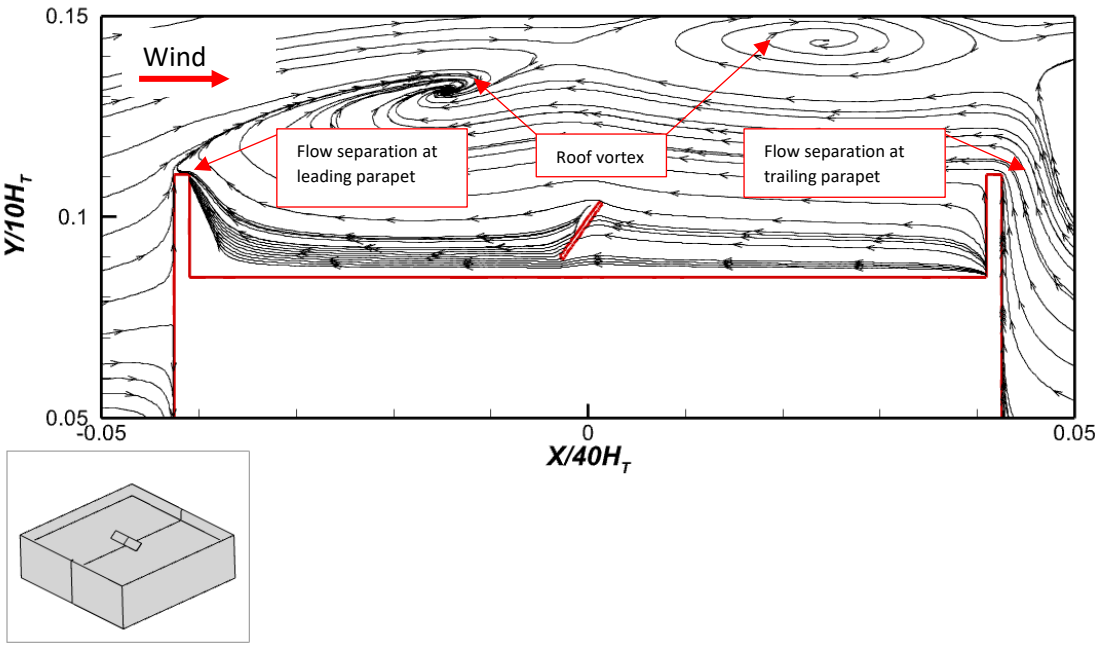

Figure 93: Mean velocity flow stream traces on the center plane for flow behavior with high parapet present (Operational condition v = 10 m/s, β= 40°, Collector location 50 percent of the roof's length)

As depicted Figure 95, the velocity at the rear of the collector is marginally higher, especially near the rear of the leading edge, indicating greater heat loss. Based on the low velocity at the collector's surface, it can be concluded that the collector's heat loss would be lower at higher parapets than at lower parapets on average for the collector. The trailing edge of the collector is also not above the parapet in this case, as it is with a lower parapet, which explains why its front surface has a lower velocity. Based on the above, it can be inferred that with parapets present, collectors tilted at a higher angle, such as 40°, are clearly exposed to greater velocity, resulting in greater heat loss. This is especially noticeable at low parapets where high-velocity winds are present.

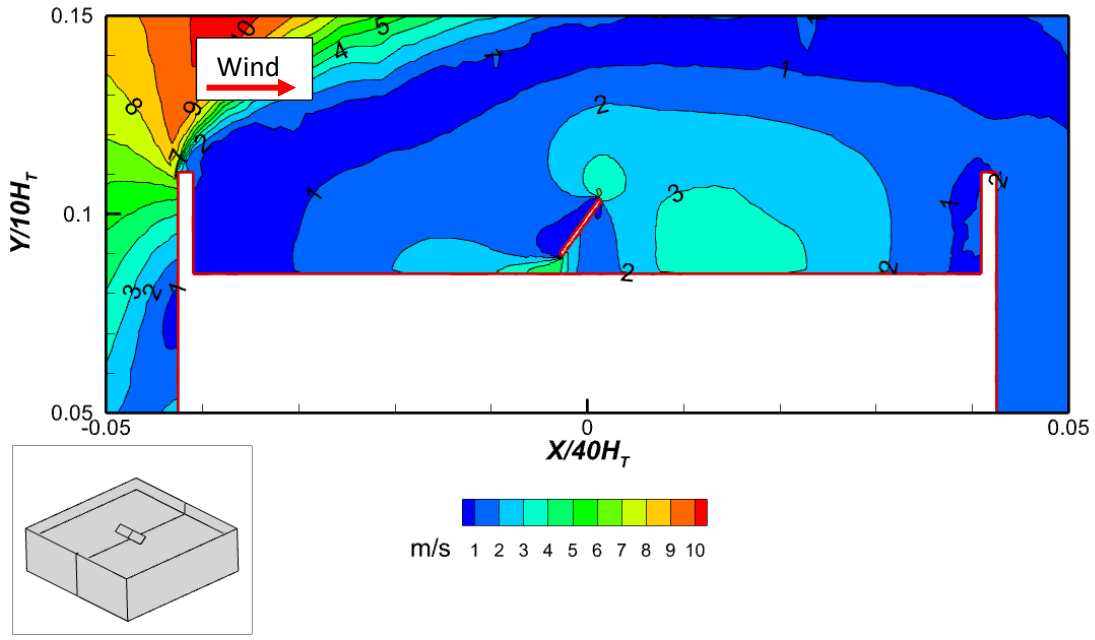

Figure 94: Mean velocity contours on the center plane for flow behavior with high perimetric parapet present (Operational condition V = 10 m/s, β = 40°, Collector location 50 percent of roof's length)

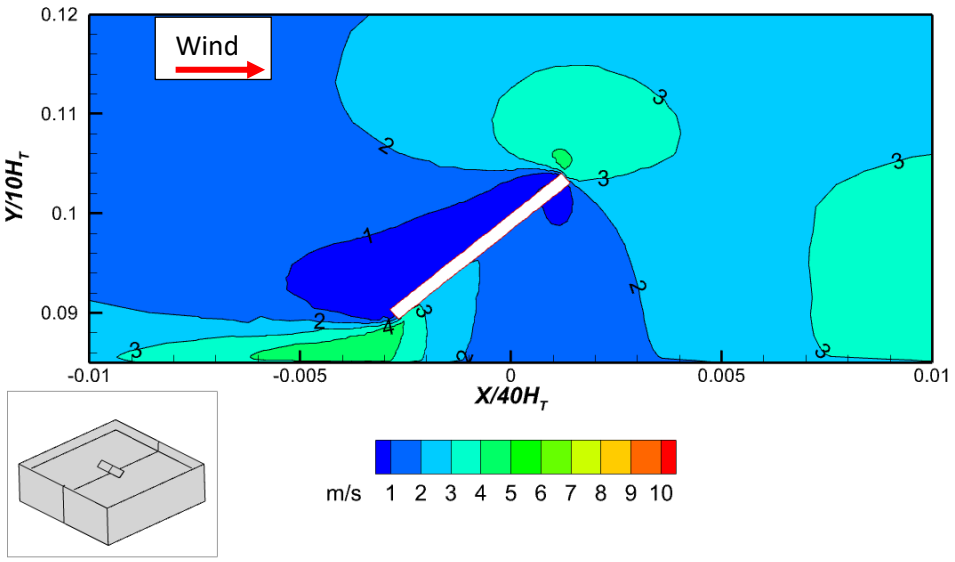

Figure 95: Local velocity (V_l) around collector for collectors located at 50 percent of roof's length with no parapet present

Figure 137 depicts the heat loss associated with a collector tilt angle of 60°. It is evident that the average value of Nu_{avg} is higher in the presence of low perimetric parapets. In a similar vein, the placement of the collector is consistently maintained at the central position of the roof, while the height of the perimetric parapet is altered. The findings indicate that there is a greater degree of heat loss observed in lower perimetric parapets compared to the other scenarios examined.

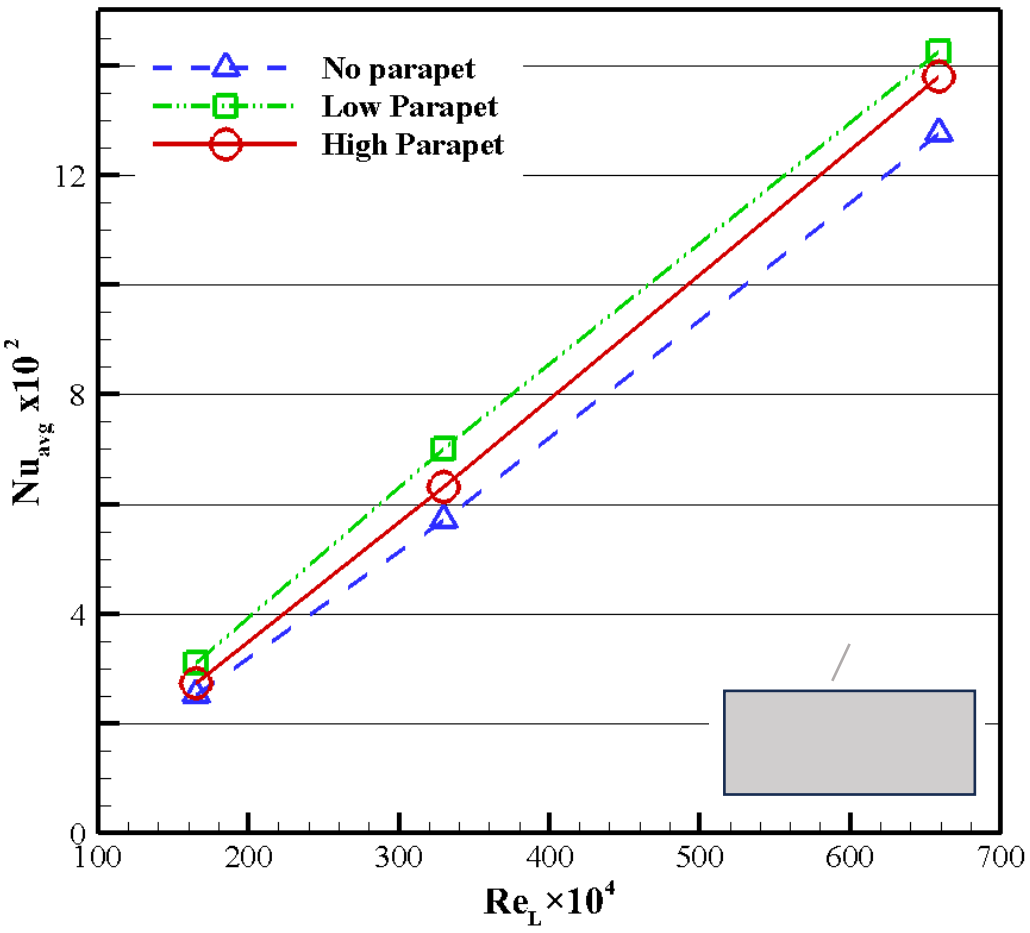

Figure 96: Nu_{avg} for collector at different parapet heights and Reynolds number (Operational condition β =60°, Collector location 50 percent of roof's length)

The absence of a perimetric parapet, as illustrated in Figure 97, causes the collector's tilt to obstruct the flow directly from the leading edge of the roof. The presence of recirculation bubbles is evident on both the front and rear surfaces of the collector. The observed phenomenon indicates a decrease in velocity at the front and rear of the collectors, implying minimal heat loss at the front of the collectors (Figure 98).

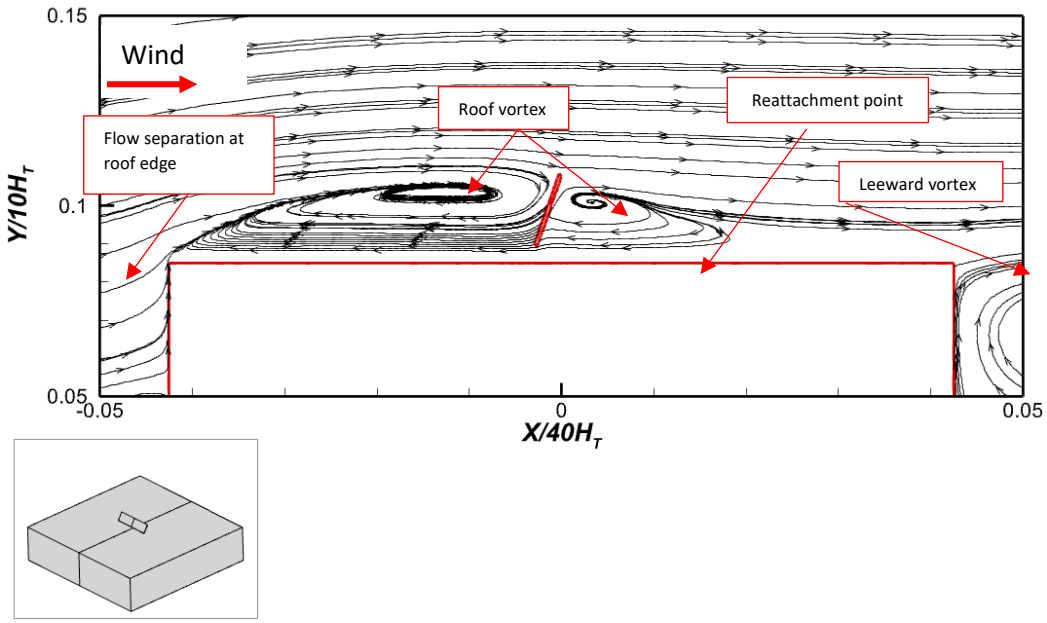

Figure 97: Mean velocity flow stream traces on the center plane for flow behavior with no parapet present (Operational condition V = 10 m/s, β = 60°, Collector location 50 percent of the roof's length)

Due to the flow path between the leading edge and roof of the building, the velocity is noticeably higher at the front of the collector compared to the rear of the collectors (Figure 99). This suggests that heat loss will be more pronounced at the front of the collectors. Evidently, the presence of the collector tilt results in the distribution of higher velocities across the collector's surface, which occurs when the collector is oriented almost perpendicular to the oncoming flow.

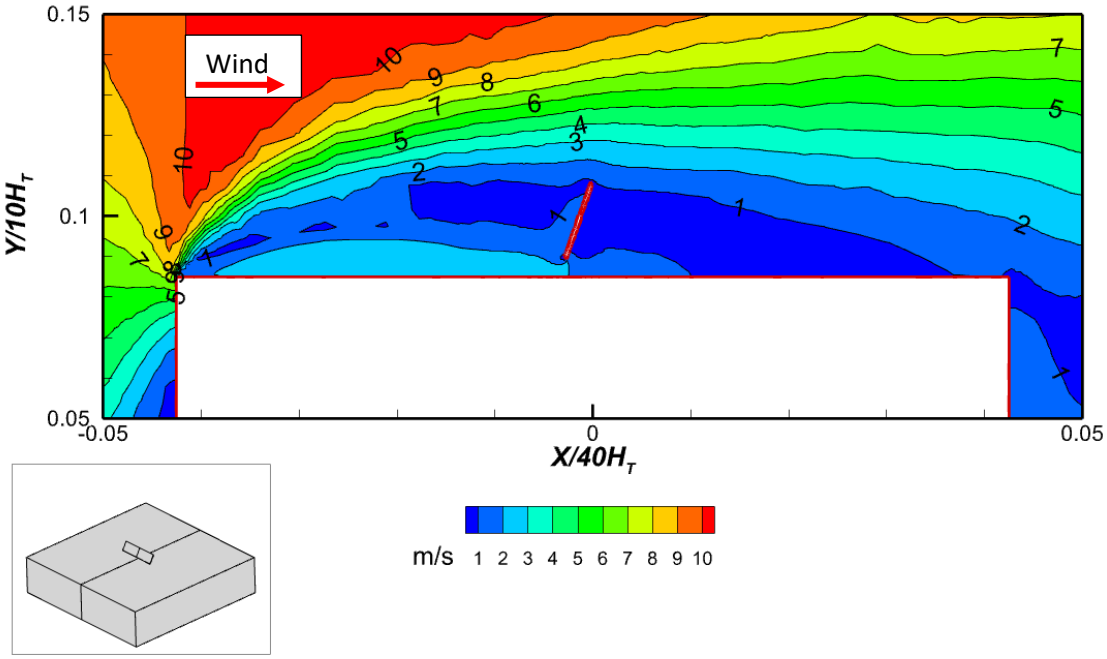

Figure 98: Mean velocity contours on the center plane for flow behavior with high perimetric parapet present (Operational condition v = 10 m/s, β = 60°, Collector location 50 percent of roof's length)

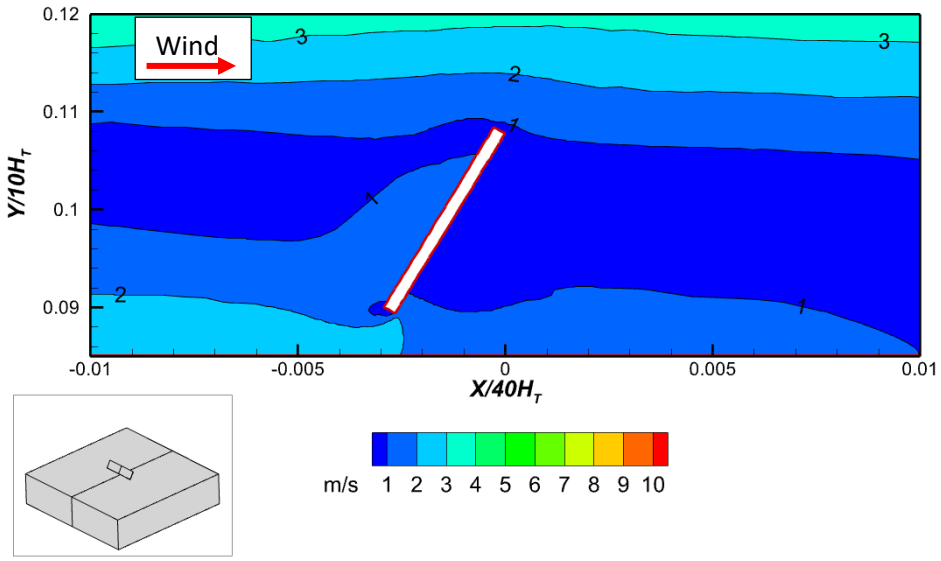

Figure 99: Local velocity (V_l) around collector for collectors located at 50 percent of roof's length with no parapet present

Figure 100 depicts the phenomenon wherein the presence of a low perimetric parapet and a higher tilt angle of the collector lead to the formation of a vortex in front of the collector. The presence of the collector's trailing edge projection above the parapet, as depicted in Figure 101, indicates that it is positioned directly in the trajectory of the separating flow originating from the leading parapet. Consequently, this arrangement leads to the observation of higher velocity at the surface of the collector as shown in Figure 101.

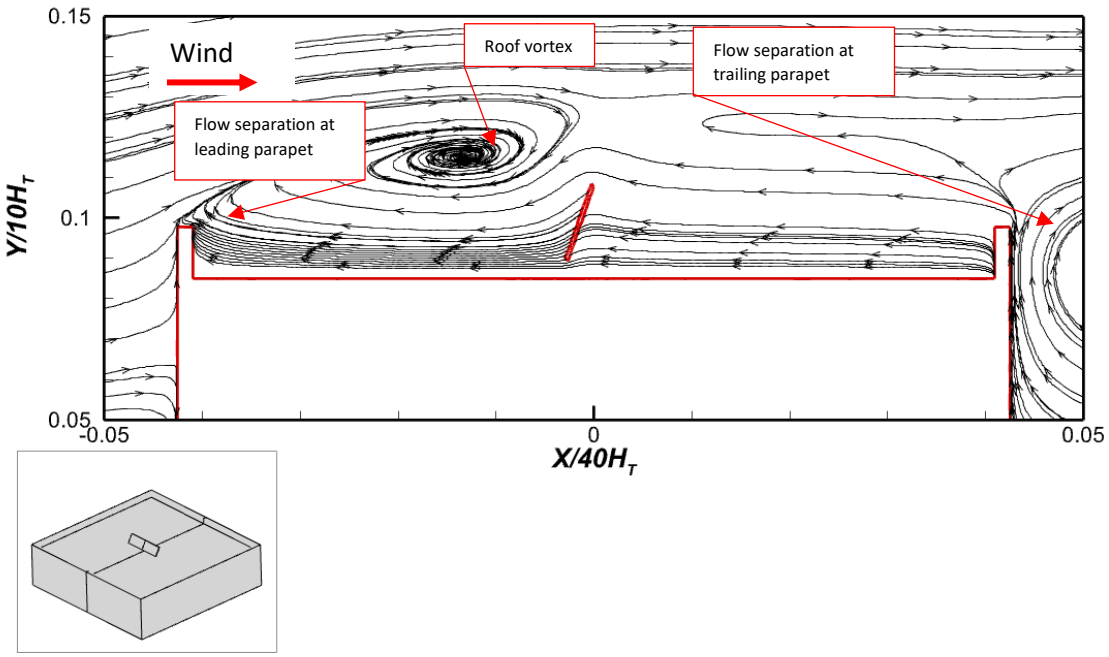

Figure 100: Mean velocity flow stream traces on the center plane for flow behavior with low parapet present (Operational condition v = 10 m/s, β= 60°, Collector location 50 percent of roof)

Upon close examination, as depicted in Figure 102, it becomes evident that there exists a greater velocity at the leading edge of the collector. This phenomenon is attributed to the flow path that is formed between the surface of the roof and the edge of the collector. The observed higher velocity in this case provides basis for the increased heat loss of the unglazed collector when a lower perimetric parapet is present, as depicted in Figure 96.

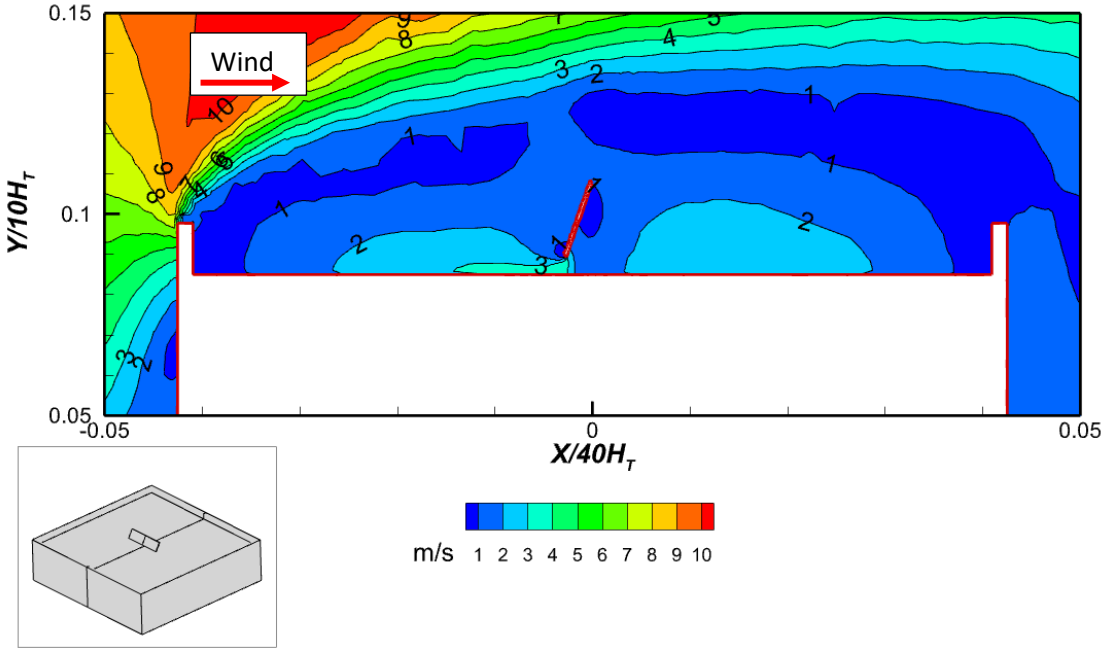

Figure 101: Mean velocity contours on the center plane for flow behavior with high perimetric parapet present (Operational condition v = 10 m/s, β = 60°, Collector location 50 percent of roof's length)

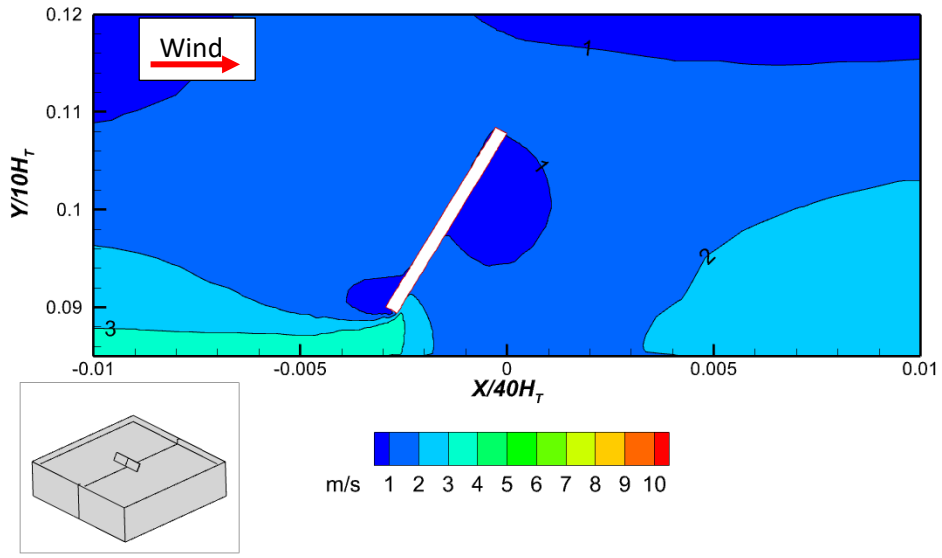

Figure 102: Local velocity (V_l) around collector for collectors located at 50 percent of roof's length with no parapet present.

Figure 103 illustrates the aerodynamic properties of a roof featuring an increased parapet. With the collector tilted to 60°, in conjunction with the increase parapet height, this results in the

generation of two vortices positioned above the roof. A flow separation is observed at the trailing edge of the collector which does not result in a downwash at the collectors rear or front but a resulting decrease in velocity at its front, as illustrated in Figure 104. As a result, the heat loss at the front of the collector is lower when compared to its rear.

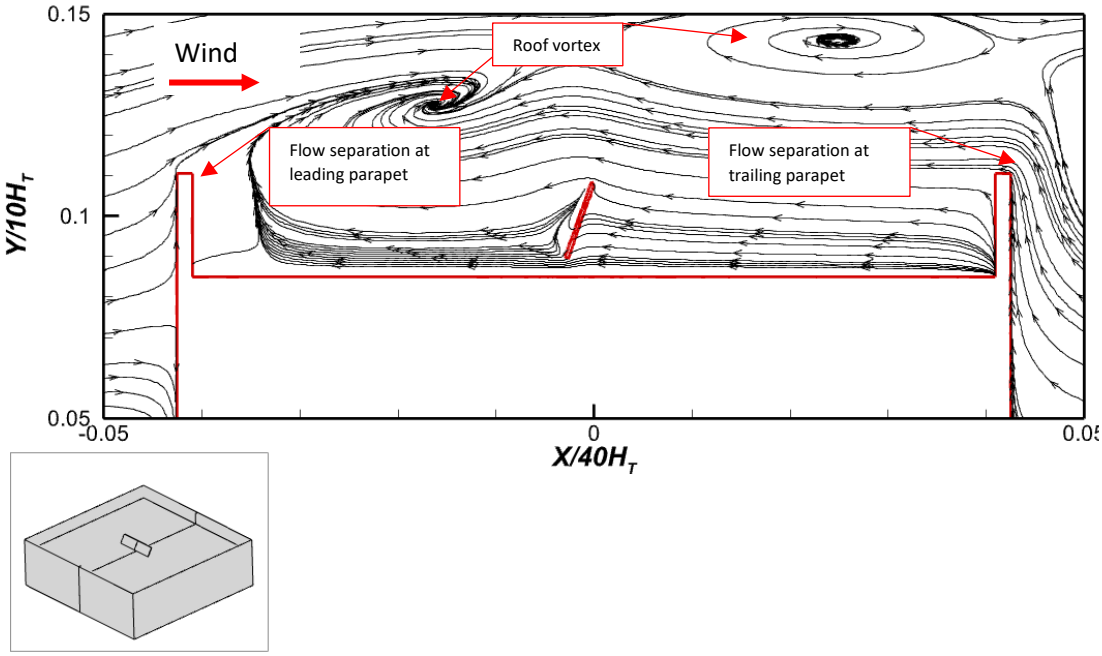

Figure 103: Mean velocity flow stream traces on the center plane for flow behavior with high parapet present (Operational condition V = 10 m/s, B = 60°, Collector location 50 percent of roof)

On the other hand, the gap between the leading edge of the collector and the roof surface leads to a notable increase in velocity at the leading edge of the collector, as illustrated in Figure 105. Therefore, in comparison to the low parapet scenario illustrated in Figure 101, it can be deduced that a low perimetric parapet will result in greater heat loss of the collector at the same tilt angle, as opposed to the case involving a high perimetric parapet.

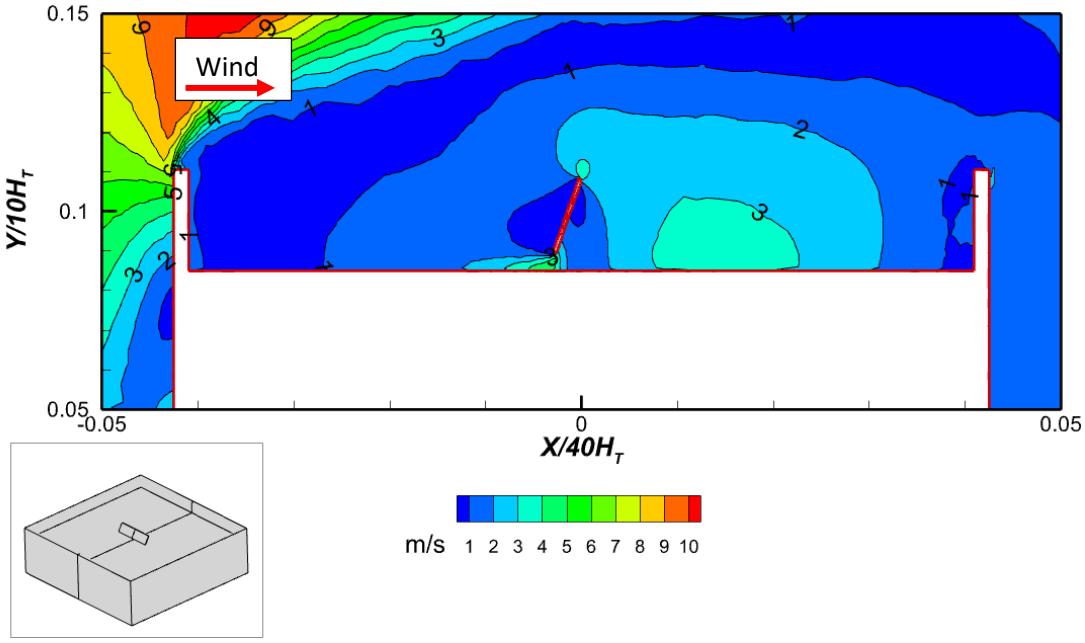

Figure 104: Mean velocity contours on the center plane for flow behavior with high perimetric parapet present (Operational condition v = 10 m/s, β = 60°, Collector location 50 percent of roof's length)

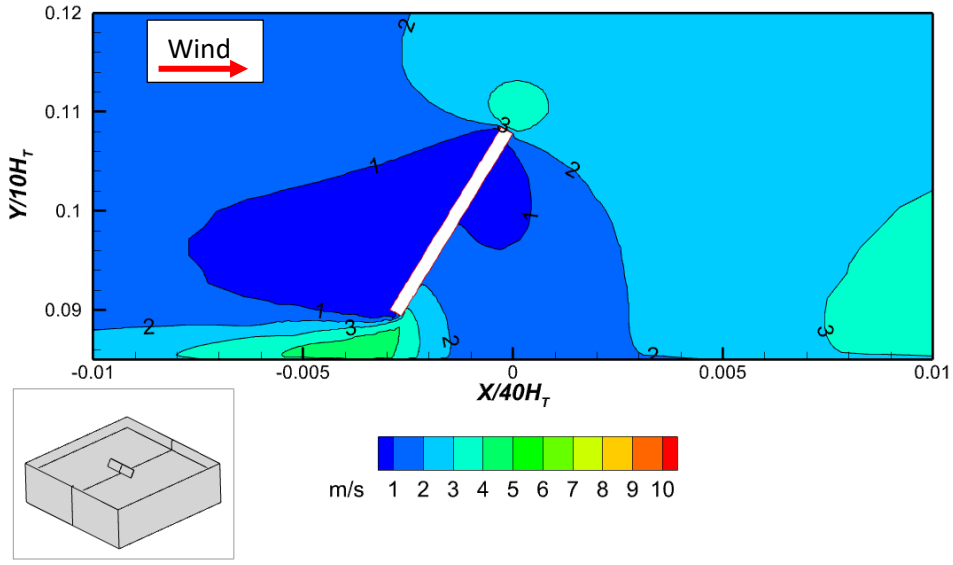

Figure 105: Local velocity (V_l) around collector for collectors located at 50 percent of roof's length with no parapet present

To better understand how the collector tilt angle affects heat loss at different parapet heights, Figure 106 compares the Nu_{avg} for all cases. Clearly it can be seen that increasing the collector tilt angle causes an increase in collector heat loss. The primary reason for this is that high inclination angles expose the collector's surface to the inevitable oncoming flow separation.

As a result, because the velocity on the roof is greater when low parapets are present, the results explain why heat loss is greater for low parapets in each case. Furthermore, the increasing tilt angles expose both the front and back surfaces of the collectors. The trailing edge of the collector,

especially at higher tilt angles, becomes positioned above the parapet, exposing its surface to high velocity thus the heat loss noticed.

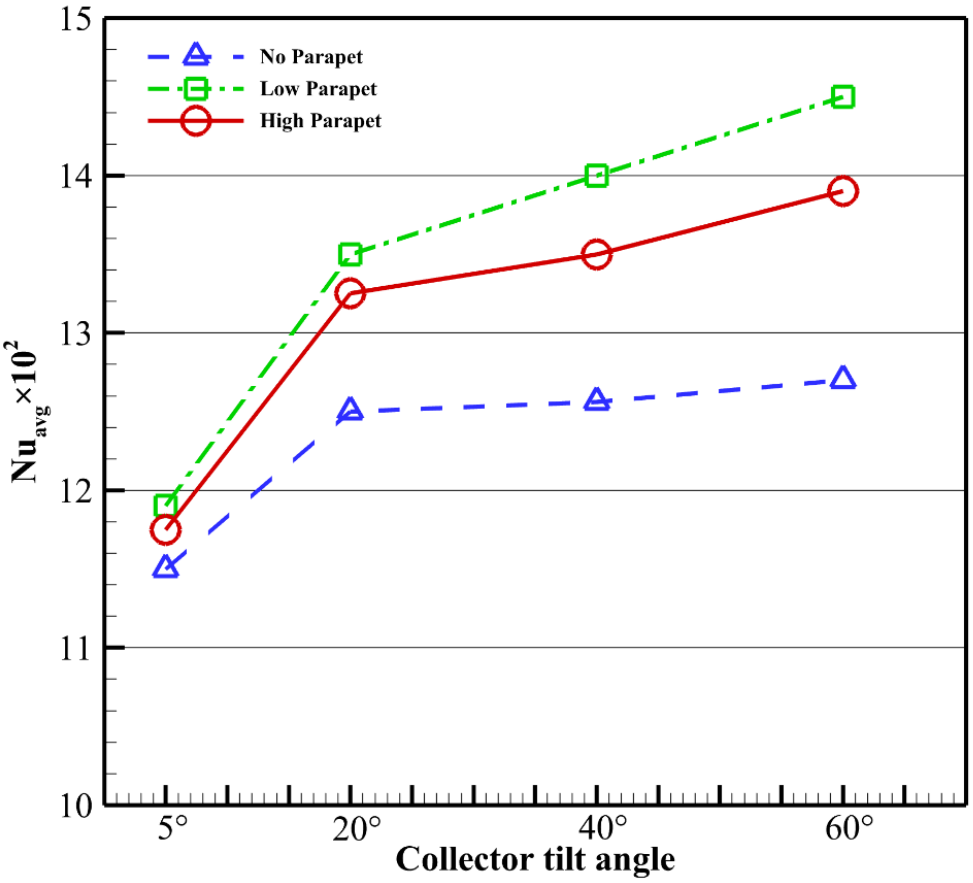

Figure 106: Nu_{avg} for collector at different parapet heights and Reynolds number (Operating conditions of 0° wind incidence, 50 percent location of roof and collector tilt angle of 5°, 20°, 40° and 60°)

3.7 Heat Loss Correlation

The previous section discussed how convective heat loss for a single unglazed solar thermal collector can vary. Depending on the operating conditions, heat loss was found to increase or decrease with perimetric parapets. To better understand the effect of parapets, the independent variables, such as collector tilt angle and wind incidence angle, must be correlated with a dependent variable, such as heat loss at various parapet heights.

Nusselt correlations are used in such cases as a common-dependent dimensionless parameter. Non-linear regression was used to examine the independent relationship between the various operational parameters and convection heat losses (Oosterbaan, 1994, 2002). A correlation was required for no-, low-, and high-parapet configurations under the following conditions: varying

collector mounting location (L_C=0.25,0.5,0.75) representing percentage of roof mounted location. The collector's tilt angle (β=5°,20°,40°,60°) and the wind incidence angle ($\emptyset$ =0°,45°,90°,135°,180°). Three velocities 2.5,5 and 10m/s, corresponding to Reynolds numbers 1.65×10^6, 3.29×10^6 and 6.59×10^6 were chosen for the correlation. The Reynolds number (Re_L) is calculated using equation 6, where the collector's characteristic length used in the Re_L is the length of the collector (1m). An ambient temperature of 298K and a collector temperature of 328 K were used. The fluid properties were taken at mean bulk temperature. L is the characteristic length of the collector, ρ is the density of air (kg/m3), u_∞ is the free stream velocity (m/s) and μ is the dynamic viscosity of air.

$$Re_L = \frac{\rho u_\infty L}{\mu} \qquad 6$$

The simulation results of convective heat transfer coefficients were fitted through multiple nonlinear regression and correlated, as shown in Equation 7, to obtain a correlation of convective heat transfer coefficient applicable to roof-mounted unglazed collectors. Where a, b, c, d, and e are constants. Shown in **Table 2** are the coefficients of best fit for the three cases of no parapet, low parapet, and high parapet. Different coefficients may be required in cases where $1.65 \times 10^6 \leq Re_L \leq 6.59 \times 10^6$, $5° \leq \beta \leq 60°$, $0.25 \leq L_C \leq 0.75$, $0° \leq \emptyset \leq 180°$.

$$N_{U\_avg} = {Re_L}^a {L_C}^b((c\ cos\emptyset + d)(e + (f cos\ \beta))) \qquad 7$$

Table 2 Values of coefficients used in Nusselt Correlation

	Constants					
	a	b	c	d	e	f
No Parapet	1.0E+00	-6.3E-05	2.1E-04	3.3E-03	4.3E-02	1.0E-02
Low Parapet	9.9E-01	5.5E-02	2.3E-04	4.8E-03	5.0E-02	-1.2E-03
High Parapet	1.0E+00	-4.2E-05	2.7E-04	2.1E-03	6.1E-02	2.0E-03

Figure 107 to Figure 109 show the correlation between prediction and numerical results. The correlation indicates that most numerical values derived from forecasted data are within 10 to 30 percent of the numerical values derived from simulations.

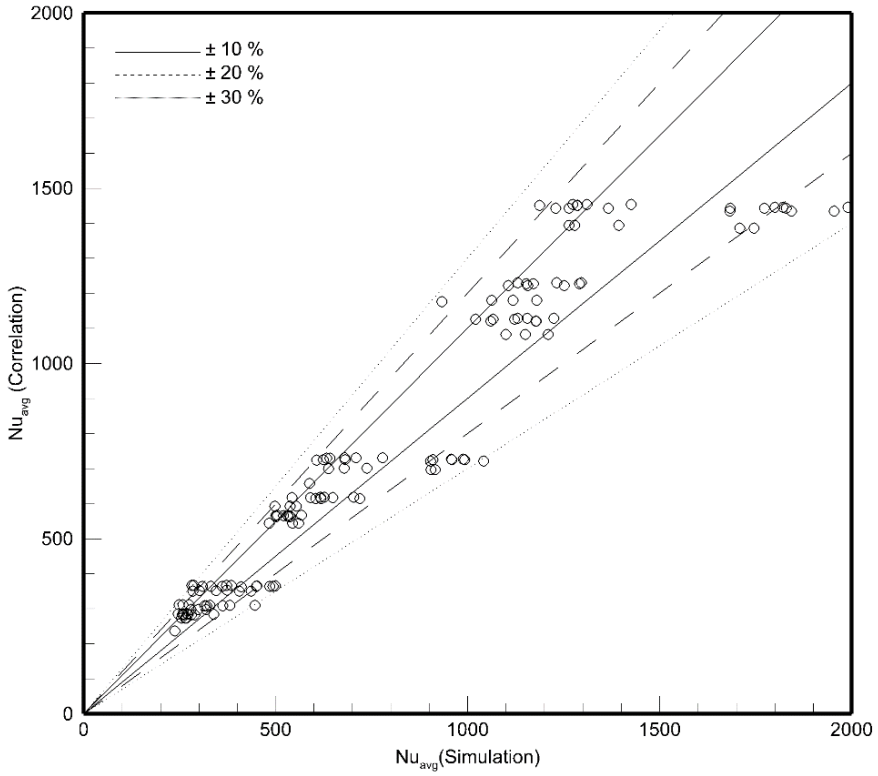

Figure 107: Comparison of Nusselt number obtained from correlation and numerical results — No Parapet

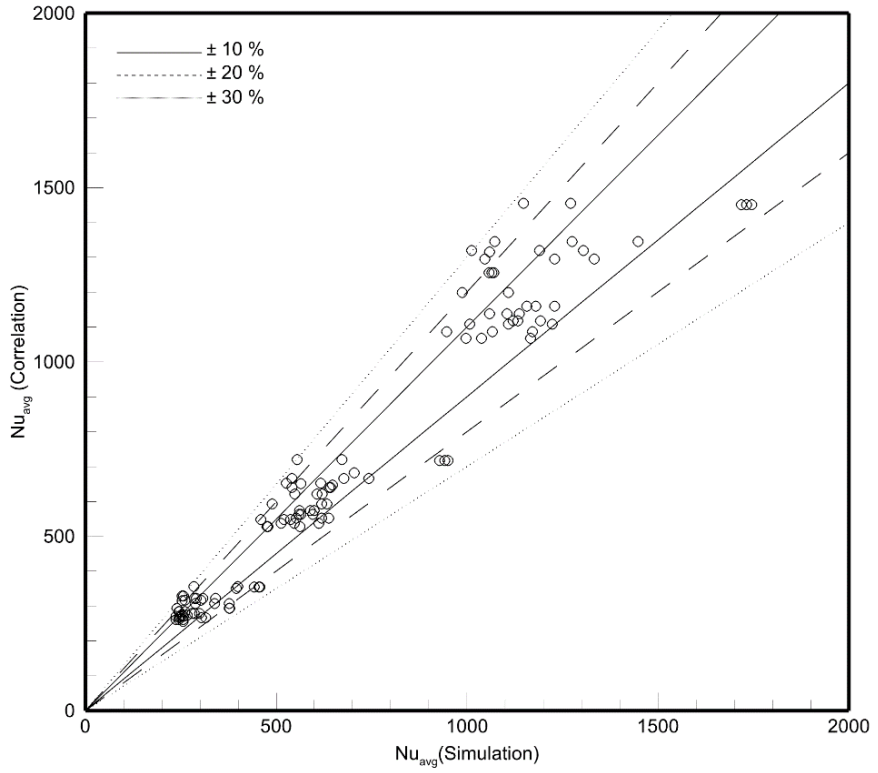

Figure 108: Comparison of Nusselt number obtained from correlation and numerical results — Low Parapet

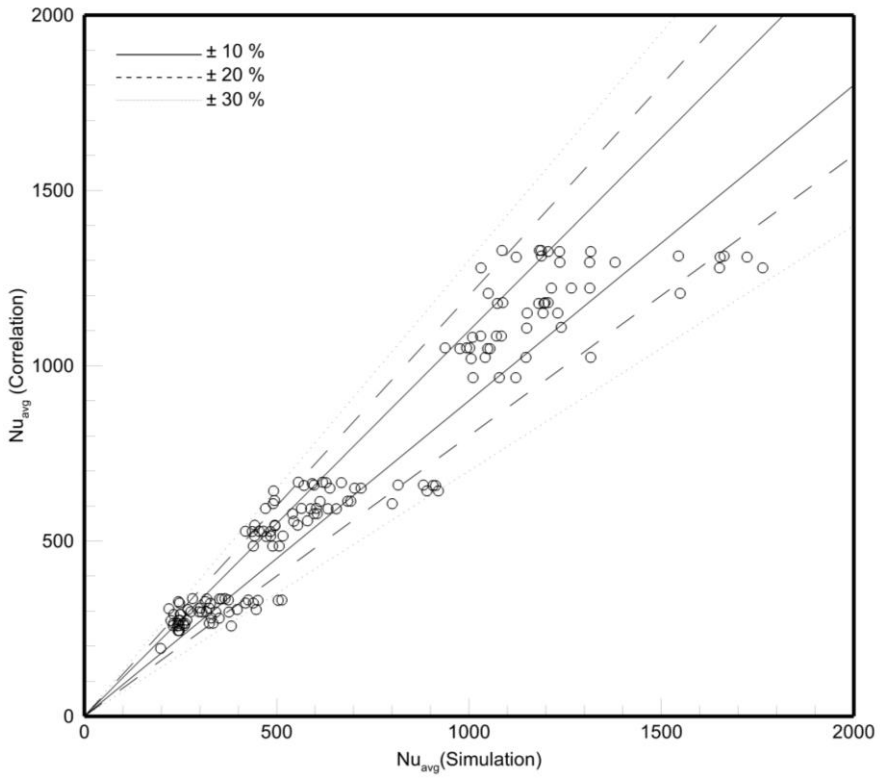

Figure 109: Comparison of Nusselt number obtained from correlation and numerical results —High Parapet

3.8 Thermal performance of unglazed solar collectors with and without roof mounted parapets

In order to understand the impact of a parapet on heat loss, one can utilise the established correlation to forecast the convection heat transfer coefficient for the collector within the specified range of input parameters from equation 7. Subsequently, this enables the estimation of the rate at which heat is lost from the collector. To do this, the simple steady state correlations first reported by Hottel and Whiller (1958); then by Klein, Beckman and Duffie (1976) and Klein (1978), and modified by Duffie and Beckman (2013), was developed in Engineering Equation Solver (EES), inside which the proposed correlation was implemented. This is applied to a simplified unglazed collector shown in

Figure 110.

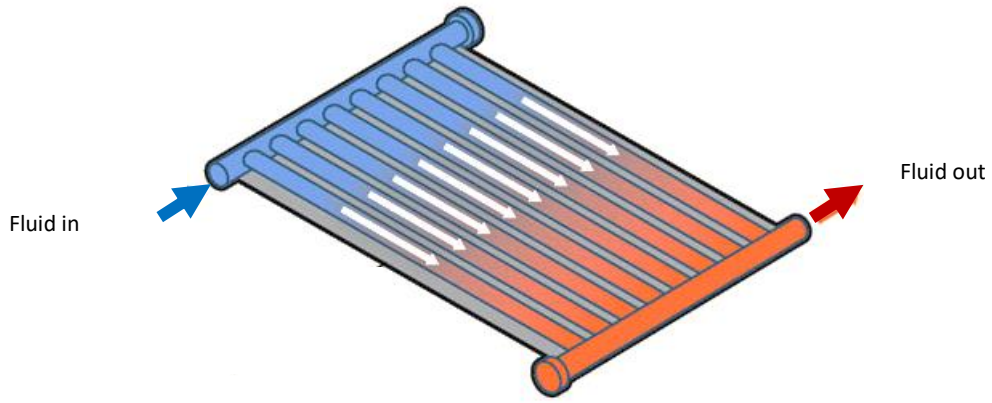

Figure 110: Representation of an unglazed solar collector

The Hottel–Whillier–Bliss equation is used for determining the useful energy yield Q_u, as shown in equation 8 where G is the solar irradiance, A_C is the collector aperture area, F_R is the heat removal factor, τ is the transmittance–absorbance product (for unglazed collectors, this is assumed to be equal to unity as the transmittance component measures the portion of radiation by any layer of glazing present), T_{in} is the fluid inlet temperature and T_a is the ambient temperature.

$$Q_u = F_R A_C [\tau G - U_L (T_{in} - T_a)] \quad (8)$$

The heat removal factor F_R from equation 8 can be determined using equation 9. This accounts for other factors such as mass flow rate ($\dot{m}$), the specific heat capacity (C_P) of the fluid and the corrected fin efficiency F'.

$$F_R = \frac{\dot{m}\, C_P}{A_C U_L}\left[1 - e^{\frac{A_C U_L F'}{\dot{m}\, C_P}}\right] \quad (9)$$

Calculating the corrected fin efficiency (F') is done before determining the heat removal factor F_R. Thus, F' is calculated from equation 10 where (W) is the tube pitch and (d) is the diameter of the tubes. The coefficient (M) accounts for the thermal conductivity of the absorber and is calculated from equation 11.

$$F' = \frac{\tanh\left(M\frac{Wd}{2}\right)}{M\frac{W-d}{2}} \quad (10)$$

$$M = \sqrt{\frac{U_L}{K_{abs}\, L_{abs}}} \quad (11)$$

The corrected fin efficiency, F', is thus calculated from equation 12, where U_L is the overall heat

loss coefficient, made up of the sum of losses from the collector's top, bottom, and edge. d_h is the hydraulic tube diameter.

$$F' = \frac{\frac{1}{U_L}}{W\left[\frac{1}{U_L(d+(W-d)F}\right] + \frac{1}{\pi d_h}} \quad 12$$

As documented by Anderson et al. (2013), in cases where the bottom of the collector is insulated, U_L is determined by the inverse of the insulation R-value which is determined from equation 13 where k and L are the thermal conductivity [W/m ºC] and thickness [m], respectively .

$$U_{bottom}=\frac{k_{bottom}}{L_{bottom}} \quad 13$$

The edge losses (U_{edge}) are determined using equation 14. Here, *p* is the collector perimeter and *t* is the absorber thickness, k_{edge} is the thermal conductivity of the edges whiles L_{edge} is the thickness of the edges.

$$U_{edge} = \frac{k_{edge}\, pt}{L_{edge}\, A_C} \quad 14$$

U_{bottom} and U_{edge} are negligible in the case of unglazed collectors as no insulation is present. Thus, U_L in equation 15 is determined from the combination of the convection and radiation heat losses. This approach has been adopted in existing studies (Bunea et al. 2015; Burch, 2004). Thus, the U_L can be determined from equation 15 below where R_T is the total resistance.

$$U_L = \frac{1}{R_T} \quad 15$$

$$\frac{1}{R_T} = \frac{1}{R_c} + \frac{1}{R_r} \quad 16$$

$$R_T = \frac{1}{h_c + h_r} \quad 17$$

The convective heat transfer coefficient (h_c) is parameterized as shown in equation 18 and determined from the sum of the forced (h_w) and natural convective heat transfer coefficient (h_{nat}) (Eicker, 2003).

$$h_c = \sqrt[3]{{h_w}^3 + {h_{nat}}^3} \quad (18)$$

The forced convection (h_w), is determined from equation 19 (first proposed by Jürges (1924) and cited in McAdams (1954)) where V is the velocity in m/s.

$$h_w = 5.7 + 3.8V \quad (19)$$

However, with parapets present, the simplified equation form of equation 7, as shown in equation 20, may be used to determine the CHTC.

$$h_w = \frac{k(Re^a {L_C}^b((c\,cos\emptyset + d)(e + (f cos\,B))))}{L} \quad (20)$$

The natural convective heat loss (h_{nat}), can be determined from equation 21, where T_a is the ambient temperature and T_pm is the collector mean plate temperature.

$$h_{nat} = 1.78\left[T_\mathrm{pm} - T_\mathrm{a}\right]^{1/3} \quad (21)$$

To determine the heat loss due to radiation h_r, the plate emissivity ε_p, collector mean plate temperature $T_\mathrm{pm}\ (K)$, and the sky temperature $T_\mathrm{s}\ (K)$ are used. This is expressed in equation 22, where $\delta$is the Stefan–Boltzman constant.

$$h_r = \varepsilon_p \delta\left[{T_{pm}}^2 + {T_s}^2\right]\left[T_{pm} - T_s\right] \quad (22)$$

The sky temperature, $T_\mathrm{s}\ (K)$, can be determined from the modified Swinbank equation of Fuentes (Fuentes, 1987) expressed in equation 23 where $T_a(K)$ is the ambient temperature.

$$T_s = 0.037536{T_a}^{1.5} + 0.32T_a \quad (23)$$

Finally, the efficiency of collector, η, can be determined from equation 24, where η is the thermal efficiency of the collector.

$$\eta = \frac{Q_u}{A_C G} \qquad 24$$

Having established the methodology for calculating the performance of a solar thermal collector without glazing, hypothetical design values, as shown in Table 6, were chosen to calculate the collector's performance under varying conditions using the developed correlation within the given range of input parameters.

Table 3 Input parameters for solar collector model

Parameter	Notation	Value	Unit
Ambient Temperature	T_a	301.2	K
Emittance of plate	ε_p	0.95	
Area of collector	A_{col}	4	m^2
Transmittance-Absorptance product	τ	0.8	
Collector mounting location	L_C	0.25, 0.5,0.75	
Heat Removal Efficiency Factor (typical)- Anderson 2010	F_R	~ 0.85	
Wind incidence angle	$\emptyset$	0	Degrees
Reynolds number at 10 m/s wind speed	Re	6.59×10^6	
Characteristic length	L	1	m
Thermal conductivity at mean air temperature of 20°C	k	0.02225	mW/m K
Solar radiation	G	999.8	W/m2
Inlet temperature	T_{in}	300	K
Stefan Boltzman's constant	δ	5.67 x 10^{-8}	W/ $m^{-2} \cdot K^{-4}$
Collector tilt angle	θ	20	Degrees

Figure 111 depicts instantaneous thermal collector efficiency at various collector locations and parapet heights. The findings show that parapets reduce the thermal efficiency of collectors mounted away from the oncoming flow. A decrease in performance can be attributed to an increase in velocity at roof centres caused by flow separation at the parapet edges, which results in the formation of vortices. In contrast, as parapet height increases, collectors mounted closer to the leading edge of the roof perform better in terms of thermal performance. This is due to parapets, which prevent the oncoming flow from passing directly over the roof. This obstruction reduces the velocity closer to the leading edge of the roof, resulting in less heat loss.

When comparing the thermal efficiency of collectors with high and low parapets, it is clear that higher parapets result in higher efficiency than lower parapets. However, when the collector is mounted closer to the trailing parapet, where a downwash is prominent, the case is different. Thus, the collector's thermal efficiency will be lower. From the above, this study demonstrates that the presence of parapets alters the thermal performance of collectors especially with low perimetric parapets present. Furthermore, when the effect of parapet on thermal performance of the collector is analysed, the difference is approximately 12.4% when the collector is mounted near the roof's leading edge, which represents 25% of its length, 3% when the collector is mounted in the centre, and a 7% reduction in performance when it is mounted near the trailing parapet. The above indicates that parapets can improve collector performance in situations where collectors are placed near the leading edge of the roof but are disadvantageous when placed near the trailing parapet.

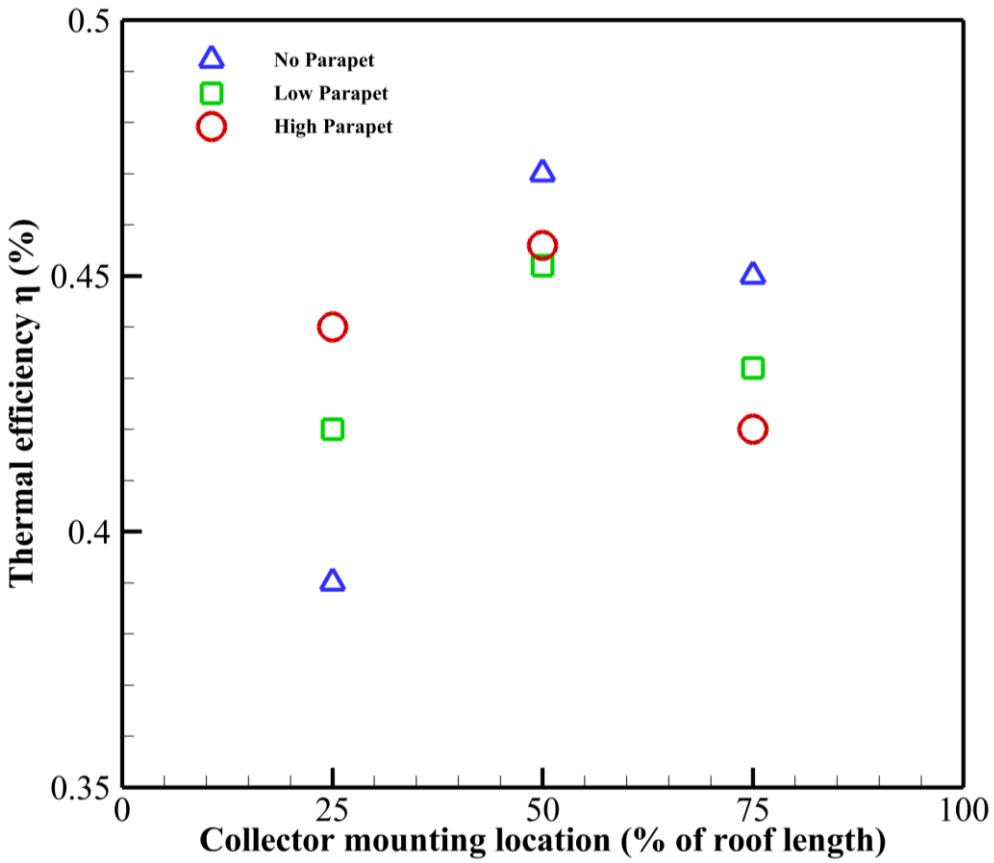

Figure 111: Comparison of collector efficiency at varying roof length and parapet height.

3.9 Chapter Conclusion

This chapter investigates the heat loss in a steady-state condition from a single unglazed solar thermal collector that is installed on a roof featuring different perimetric parapet heights. Perimetric parapets alter the velocity on the roof of a low-rise building in response to variations in wind incidence angle. The high velocity observed at low parapets was particularly conspicuous.

The findings indicate that except for solar collectors positioned near the front edge of a roof without a parapet, heat losses from solar collectors are higher when located near low parapets. The presence of a high velocity in the vicinity of the collector can be attributed to several factors, including the vortex generated on the roof, the downwash effect on the collector's surfaces, and the flow separation occurring at both the leading and trailing edges of the parapet. In higher parapets, the presence of comparable flow structures leads to an increase in velocity surrounding the collector, resulting in a subsequent loss of heat. On the contrary, it can be observed that a high parapet results in reduced heat loss compared to a low parapet due to the displacement of the vortex at a higher elevation above the roof.

Furthermore, it has been shown that the loss of heat from the collector is dependent on the location at which it is mounted. In addition to collectors positioned nearer to the leading edge of the roof where parapets are absent, collectors situated in the middle of the roof exhibit a greater susceptibility to heat loss compared to those mounted in close proximity to the leading and trailing edges. This is attributed to the presence of higher velocity at the central regions of the roof. As hypothesised in the second chapter areas situated nearer to the periphery of the roof, specifically those at lower and higher parapets, would exhibit reduced velocity zones. Furthermore, it was observed that altering the tilt angle of the collector resulted in an elevation of heat loss in all cases. The reason for this phenomenon is that as the tilt angle increases, the collector surface becomes more exposed to the oncoming flow and vortex.

The findings led to the development of a new generalised correlation for predicting the heat loss of unglazed solar thermal collectors. At various parapet heights, the correlation takes into account operational factors like wind incidence angle, collector tilt angle, and collector mounting location. The analysis presented above holds significant value for architects and manufacturers involved in

decision-making processes pertaining to the integration of renewable energy technologies, such as photovoltaics and solar thermal collectors, within buildings. This is particularly relevant due to the acknowledged significance of the parapet and the growing utilisation of unglazed collectors, which are not only cost-effective but also gaining popularity.

Chapter 4

Effect of parapet on roof mounted array unglazed solar thermal collector

4.1 Introduction

The previous chapters demonstrated that parapets influence the local velocity on roofs and, as a result, the heat loss of roof-mounted unglazed collectors. Aside from parapets, other parameters such as collector tilt angle, collector mounting location, and wind incidence angle, all affect aerodynamics and thus the local velocity around the collector. This aerodynamics is primarily shaped by vortices on the roof that vary with parapet height due to flow separation at the parapet's leading and trailing edges. However, the preceding chapters only addressed the variation in heat loss for a single roof-mounted unglazed solar thermal collector.

For many low-rise buildings, flat-plate solar collectors are arranged in arrays to provide heating and hot water as shown in Figure 112. This is because besides satisfying load demand, the assumption that a single collector is tilted at an optimum angle is unrealistic as the collector's height can sometimes be limited by its optimal height or other roof characteristics. The tilt angle, for example, has been shown to cause more turbulent mixing, resulting in higher convection transfer when certain angles of tilt are used; while at other angles the flow is redirected, thus enhancing, or reducing convection heat loss for ground- or roof-mounted arrays (Glick *et al.*, 2020). In addition, there has been evidence that spacing, layout and wind speed may influence heat transfer through solar collectors or PV panels in an array (Armstrong and Hurley, 2010). Consequently, it is necessary to study the aerodynamics and local velocity of a roof with parapets in order to better understand the effect it has on heat loss on roof mounted collector arrays.

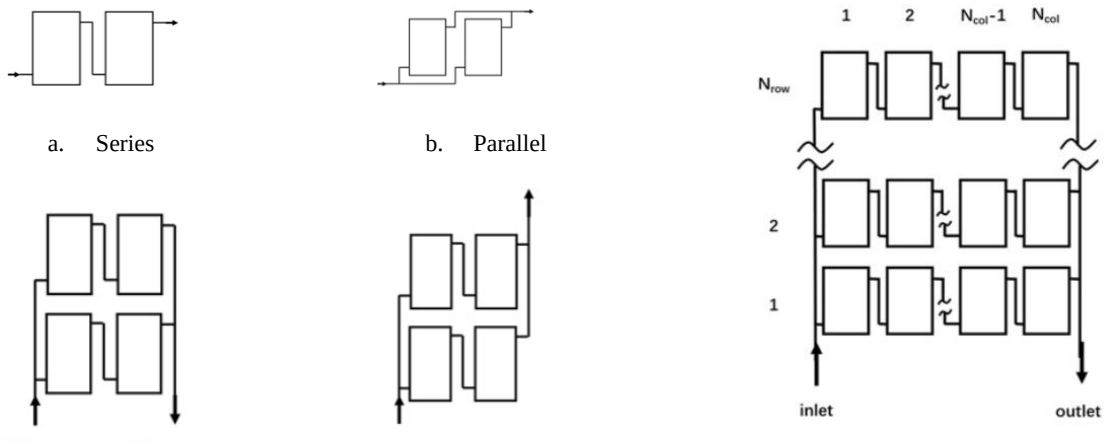

a. Series b. Parallel

c. Series parallel C-Type d. Series parallel Z-Type e. Configuration solar collector field

Figure 112: Different connection type of flat plate solar collectors (Zhu, 2009)

4.2 Method

To address the issues outlined above, a 3D square building of dimension 16 m (length) x 16 m (width) x 4 m (height) was modelled using the commercial software Ansys-Space Claim vR3. Six rows of solar collectors each unit with dimension 2 m (length) x 1m (width) x 0.07m (thickness) were mounted on the building and labelled as R1 to R6 accordingly. For each row, three collectors were mounted side by side with no spacing in between. The individual collectors were labelled as a to c on each row as shown in Figure 113.

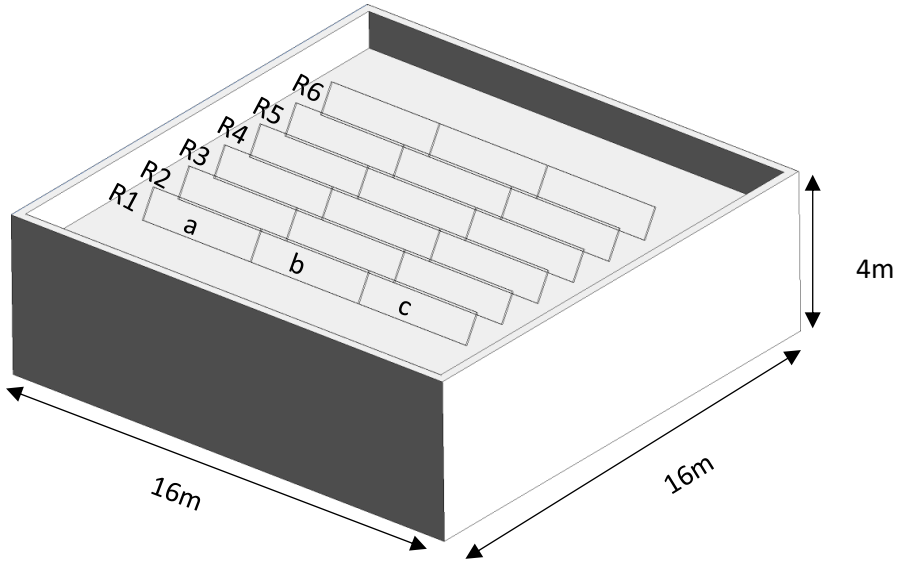

Figure 113: Schematic view of roof mounted solar arrays with parapets (Not drawn scale)

Between each row, a spacing was maintained based on equations 25 per the guidance documented in (Kalogirou and Kalogirou, 2009). Adherence to the guidance is critical to avoid shading the rows of collectors at low shade angles.

$$\frac{b}{a} = \frac{\sin(\beta)}{\tan(\theta_s)} + \cos(\beta) \qquad 25$$

$$b_s = a\left[\frac{\sin(\beta)\cos(z)}{\tan(\theta_s)} + \cos(\beta)\right] \qquad 26$$

The symbols in the above equation are b/a which is the ratio of the row spacing and collector height for a south facing array without a consideration of the collector thickness. θ_s is the shading angle and β the collector inclination. In instances where, the solar azimuth angle z is not zero, equation 26 can be used where b_s is the shading distance, a is the solar altitude angle. In this chapter, two collector tilt angles ($\beta = 5°, 60°$) representing the minimum and a maximum collector tilt angle from the previous chapter was considered. A distance of 1.6m was maintained between the leading edges of the collectors in line with industry best practise as shown in Figure 114. A minimum annual noon elevation was assumed for θ_s, where θ_s is 38.2° for collector tilt angle of 60° and 7.99º for 5°.

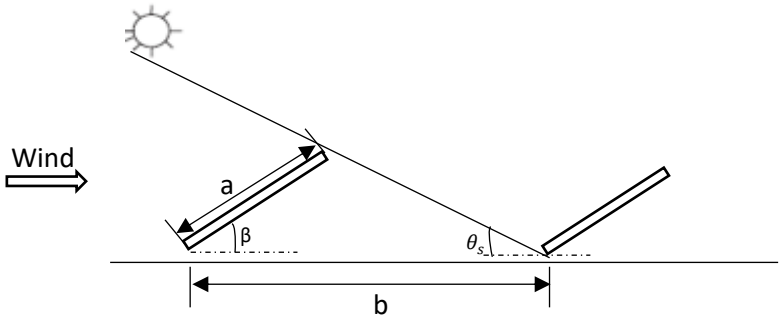

Figure 114: Schematic view of row-to-row collector shading layout.

Following the above, a variation in perimetric parapet height for no parapet, low parapet and high parapet configuration were considered based on the parapet height classification reported in the chapter 2 of this study. A spacing of 3.5m was specified from the collectors to the front and back roof edges, with 1.6 m on the sides of the roof. A gap of 0.2m was maintained between the roof

surface and the leading edge of each collector row. Operational conditions of wind speed: 2.5m/s, 5m/s and 10m/s and wind incidence angles of 0º and 90º were considered accordingly.

After completing the geometry modelling, the computational domain discussed in Chapter 3 was applied. Similarly, an O-H type meshing was performed for the entire domain, with hexahedral cells applied to the domain in the outside region and tetrahedral cells applied to the domain in the interior. Appendix A contains information on the mesh sensitivity that followed. The numerical method discussed in chapter 3 was also applied. Thus, the $k-\varepsilon$ turbulence model-realizable was used for the closure of the transport equation, SIMPLE algorithm scheme for pressure velocity coupling and a second-order discretization scheme and pressure interpolation for both convection and viscous equations were applied. Subsequently, the temperature of each collector was specified as 328 K with ambient temperature specified as 298 K. Figure 115 depicts the computational domain and meshing applied.

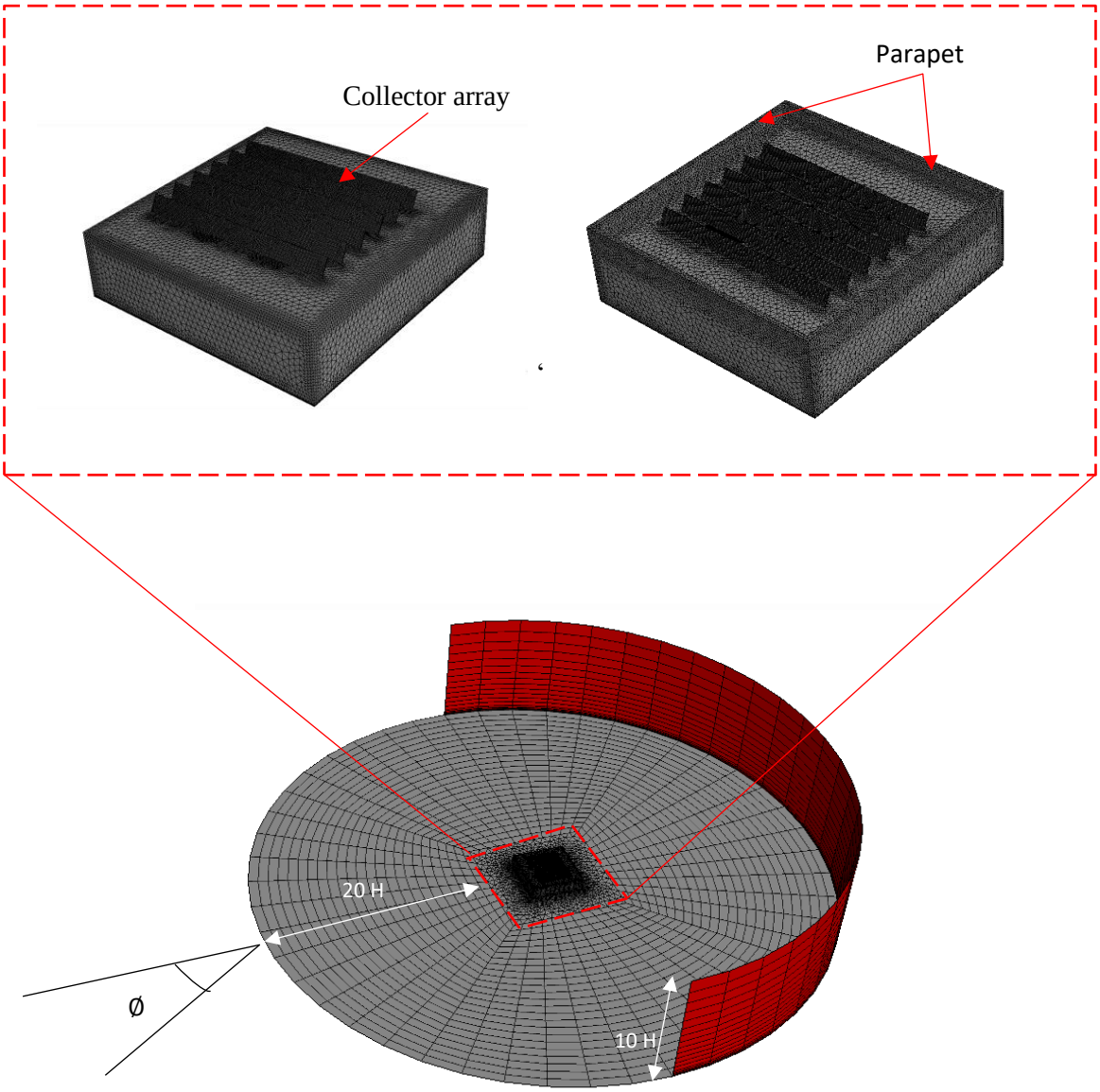

Figure 115: Computational domain and mesh for building and near flat-roof building with and without parapet

4.3 Validation

The numerical method was validated using the lift and drag coefficients, as these coefficients are dependent on velocity, which has been shown to influence the amount of heat lost from the collector. To do this, the lift and drag coefficients of the collector arrays in this study were compared to previously published experimental data from Wang *et al.*, (2018). In Wang *et al.*, (2018), seven rows of solar panels were installed on the roof, each row consisting of 3 separate panels, each 1 m by 2 m in size. A tilt angle of 15° was applied to each row of panels. Pressure

taps were mounted to the upper and lower surfaces of the panel to measure the local wind pressure characteristics. To determine the approaching wind characteristics, an open terrain with a wind speed of 10 m/s was used. Figure 116 shows the comparison of Drag (C_D) and Lift (C_L) lift coefficient between (Wang *et al.*, 2018) and the current study. Here, F_L is the lift force, F_D is the drag force and A_c is the area of the collector. The results show a good agreement in terms of drag and lift over the panels.

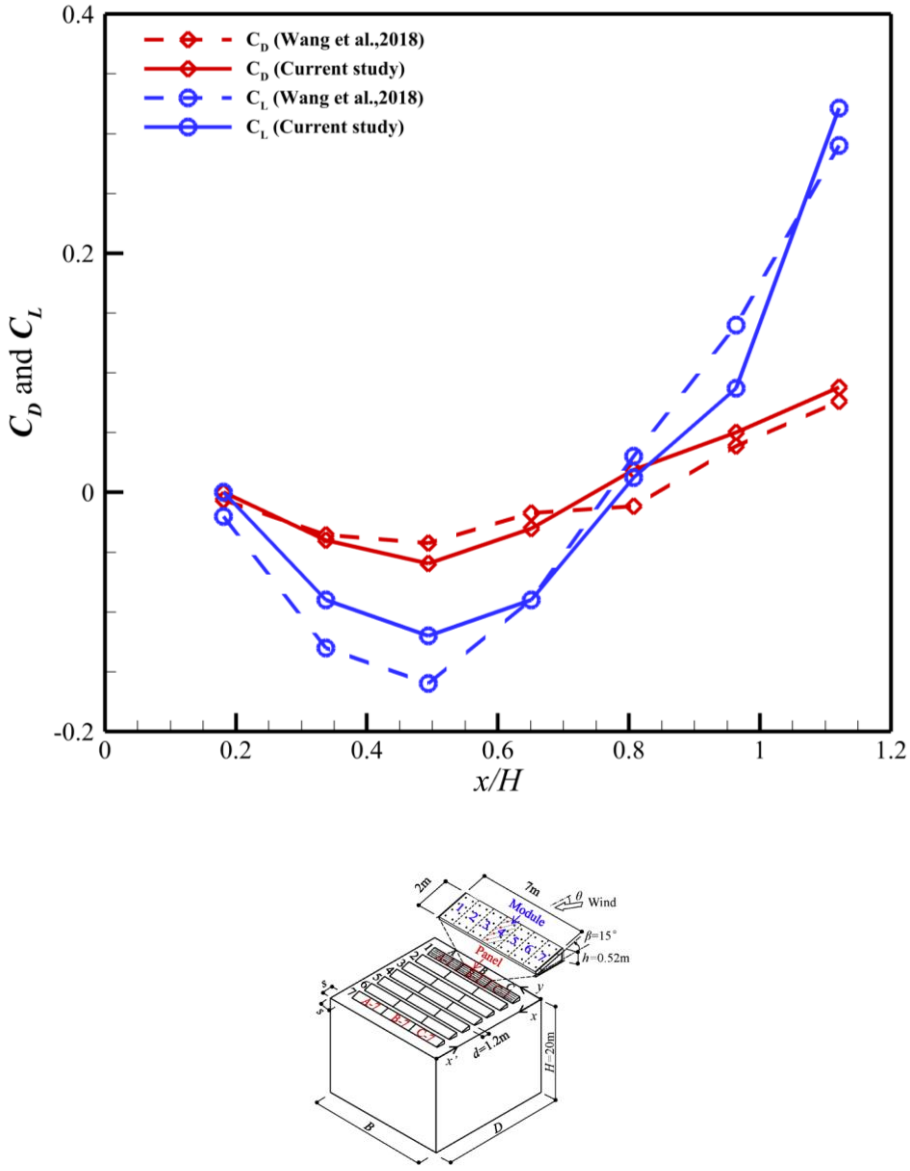

Figure 116: Comparison of Mean drag and lift coefficients of solar panels of (Wang et al., 2018 experimental work) and current study at 0° wind incidence.

4.4 Results and Discussion

The previous chapter demonstrated that the wind incidence angle can influence roof wind velocity, which in turn influences collector heat loss. Similarly, the presence of parapets and varying mounting locations of a stand-alone roof mounted collector were shown to affect velocity and impact heat loss variably. Based on this, it was determined that the initial course of action would involve investigating the impact of parapets and collector array layouts on roof velocity under different wind incidence angles. This preliminary analysis aims to shed light on the manner in which these factors influence the velocity of the roof, thus affecting its heat loss. Following this, a comprehensive analysis was carried out to evaluate the influence of the parapet on the thermal energy dissipation of each individual solar collectors in the array. Subsequently, an investigation was conducted to explore the nexus between the height of the parapet and the inclination angle of the collectors.

4.5 Effect of wind incidence angle on velocity for roof top arrays with parapets

To investigate the effect of wind incidence angle at varying parapet height for a collector array, an assessment of wind incidence angles 0° and 90° was conducted at a reference plane of Y=4.3. These angles were chosen for two reasons. In view of the possibility that the first row of collectors within the array could obstruct the oncoming flow, it was important to examine how wind incidence normal to the building would affect the roof wind velocity with and without parapets. Secondly, a 90 °of incidence means that the collectors align with the path of the oncoming flow, so the effect of the parapet could then be examined. Moreover, the reference plane of 4.3 was also selected because, due to the varying heights of the parapets, it was necessary to examine the entire roof to get a clearer picture of the velocity map. Y=4.3 represents the centre of the collectors, equidistant from the trailing and leading edges. The plane of reference for this assessment is shown in Figure 117.

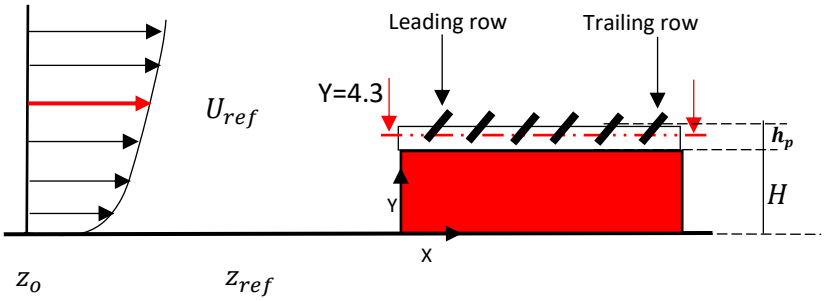

Figure 117: Reference coordinates and plane of assessment for wind incidence angle for roof top array (Not drawn to scale)

4.5.1 Wind incidence angle 0° on roof with collector array

In the absence of parapets, the wind incident at an angle of 0° leads to a significant increase in velocity in close proximity to the leading edge of the roof and in front of the initial row of solar collectors. Nevertheless, the velocity exhibits a gradual decline beyond the initial row of collectors, as depicted in Figure 118. This phenomenon arises because of the obstructive impact generated by the consecutive arrangement of collectors, resulting in a decrease in the velocity of the airflow along the roof. The influence of velocity on heat loss implies that in the absence of parapets, the heat loss of the collectors would diminish as the distance from the incoming flow increases. This observation also implies that collectors situated downstream of the flow path would experience minimal heat loss, unless there are nearby structures or obstructions that modify the aerodynamics of the roof.

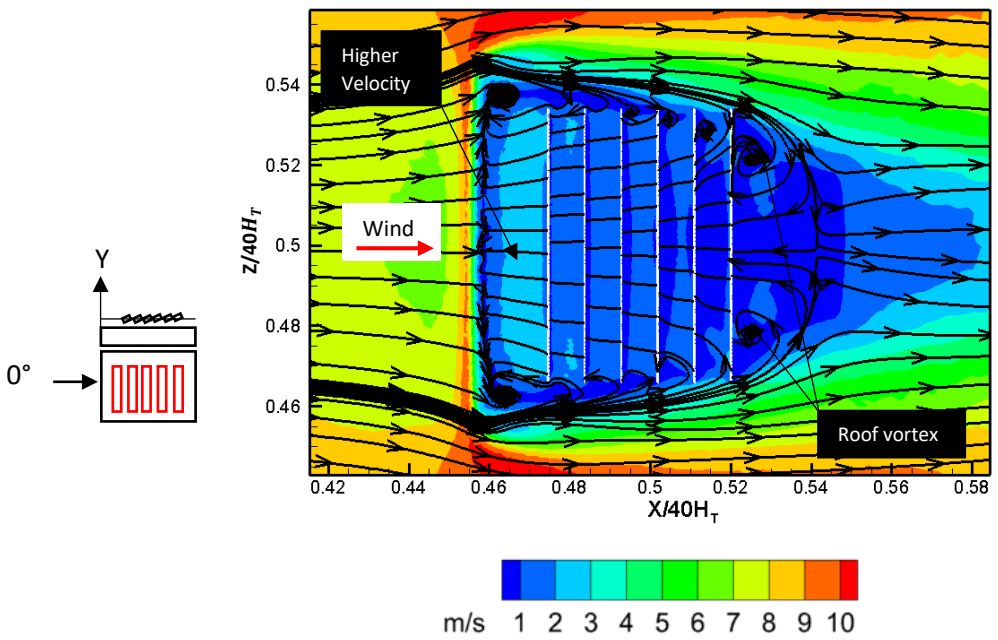

Figure 118: Mean streamlines and velocity contours on plane Y= 4.3 at collector tilt angle of 60 ° at varying wind incidence angle with no parapet

Figure 119 illustrates the velocity distribution on the roof and in the vicinity of the array in the presence of a low perimetric parapet. It is evident that the presence of a low parapet results in the formation of regions characterised by elevated velocity in the vicinity of the initial rows of collectors. In the given array, the velocity exhibits a decreasing trend away from the leading row of collectors. Nevertheless, it is worth noting that the corners of the roof exhibit higher velocity zones, indicating a potentially greater heat loss from the collectors located in those areas of the array. Based on the observed velocity, it appears that the heat loss for the final row of collectors would also be minimal, similar to the scenario without a parapet.

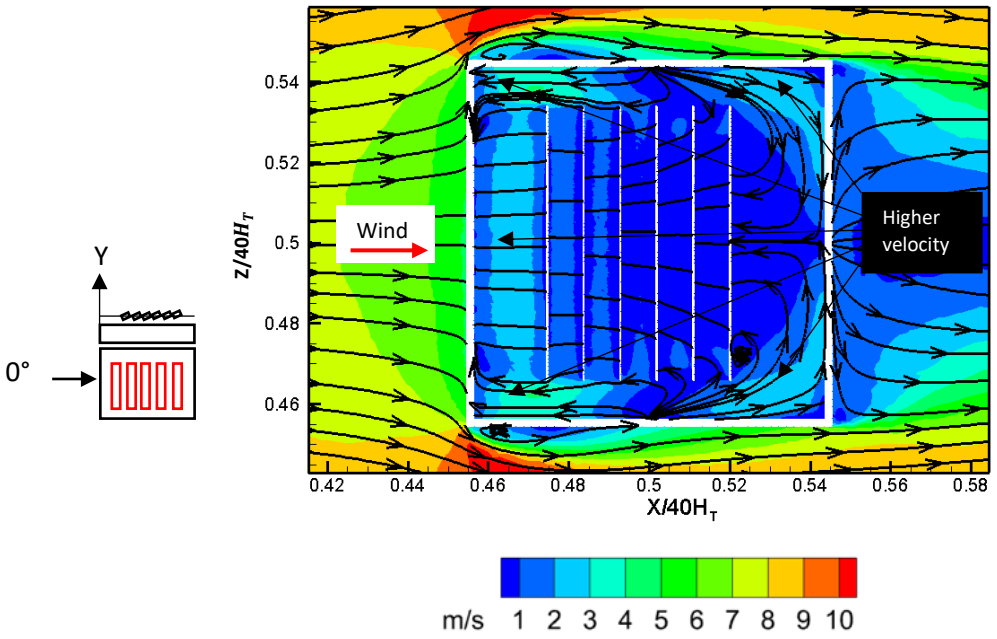

Figure 119: Mean streamlines and velocity contours on plane Y= 4.3 at collector tilt angle of 60 ° at varying wind incidence angle with low parapet

In Figure 120, it is observed that higher velocities are also present at the corners of the roof in higher parapets. However, this value is lower compared to the occurrence observed when lower parapets are present. The velocity zone located at the central region of the roof exhibits a low velocity, indicating minimal heat losses in this specific area. Additionally, it is evident that there is a discernible decrease in velocity at the forefront of the roof, indicating a minimal amount of heat loss for the initial row of collectors in comparison to alternative scenarios. As a result, it can be observed that the absence of parapets on a roof, in comparison to roofs with low and high parapets, leads to a greater velocity when a collector array is present at wind incidence angle is normal to the building.

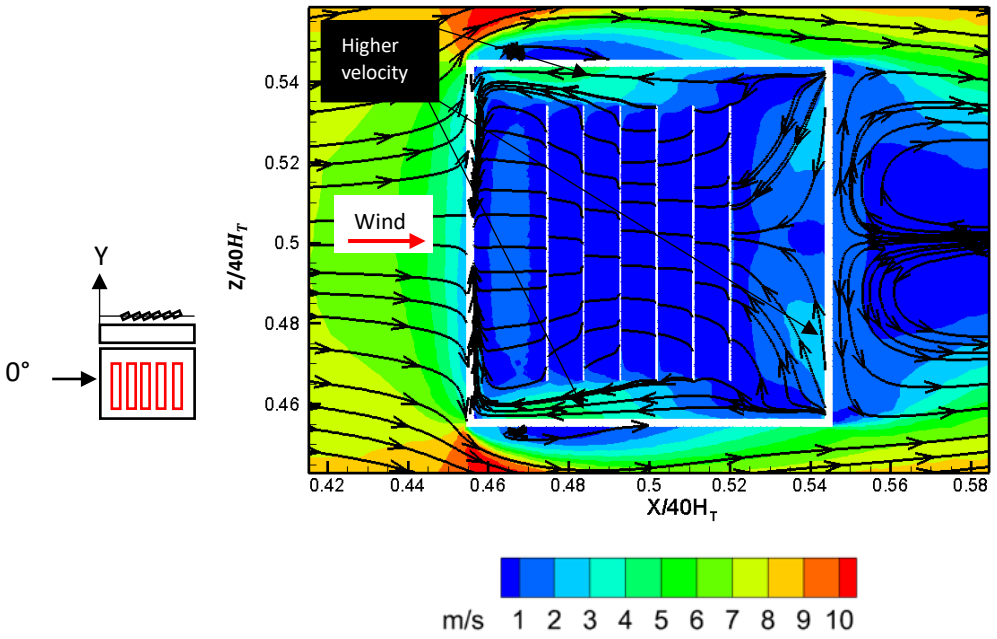

Figure 120: Mean streamlines and velocity contours on plane Y= 4.3 at collector tilt angle of 60 ° at varying wind incidence angle with high parapet

4.5.2 Wind incidence angle 90° on roof with collector array

Figure 121 illustrate that vortices are generated in the vicinity of the collectors on the roof's edges when the wind incidence angle is 90°. The lack of parapets, as depicted in Figure 121, results in the presence of a discernible area of increased velocity on the roof along the path of the flow. Based on the preceding analysis, it is probable that collectors positioned in closer proximity to the oncoming flow will experience a higher degree of heat loss compared to collectors situated at a greater distance. Furthermore, it should be noted that while the collectors are indeed positioned in alignment with the direction of the oncoming flow, the above finding can be attributed to the occurrence of flow separation at the roof edge adjacent to the approaching flow, as previously examined in the preceding chapter. Furthermore, it is evident that the vortices generated on the roof give rise to regions of reduced velocity in the vicinity of the vortex core. This observation implies that collectors positioned within these regions would experience a lower heat loss.

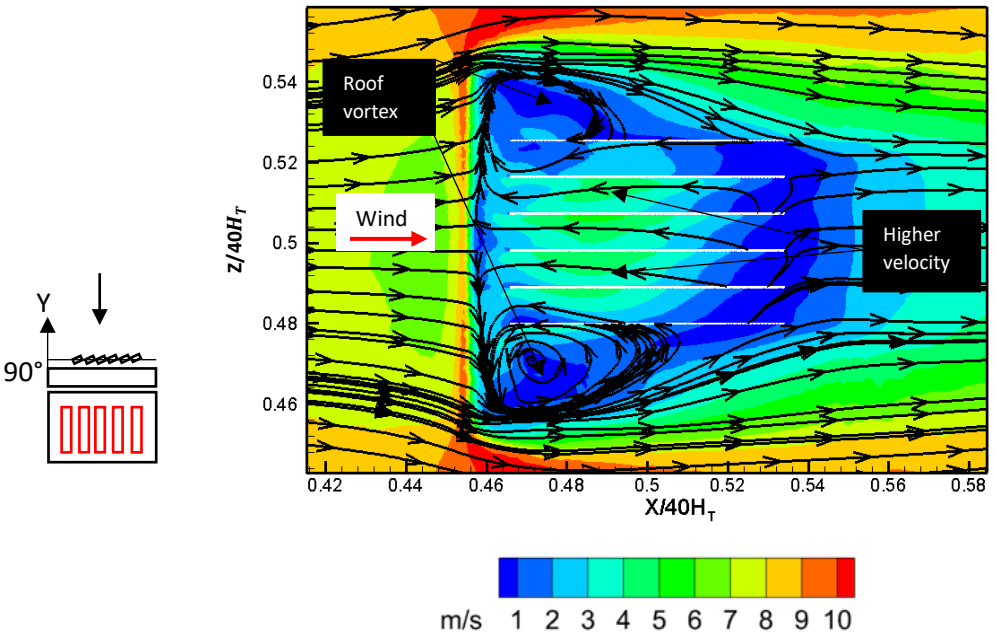

Figure 121: Mean streamlines and velocity contours on plane Y= 4.3 at collector tilt angle of 60 ° at varying wind incidence angle with no parapet

In Figure 122, it can be observed that the low perimetric parapet exhibits a phenomenon wherein the higher velocity extends to a greater distance from the oncoming flow. Likewise, a pair of vortices emerge in proximity to the roof's periphery, in close proximity to the incoming flow. Based on the above, it can be inferred that the heat loss experienced by the collector situated at the central position of the roof would exceed that of the collectors positioned along the edges. Additionally, it is worth noting that there are observable clusters of high velocity located at the corners of the roof, positioned away from the incoming flow. This suggests that collectors situated in closer proximity to these regions may experience a notable influence on their heat loss. Therefore, in the scenario where collectors are oriented in the same direction as the flow, the presence of low parapets on a roof would result in greater heat loss for the collector, as compared to a roof without any parapets.

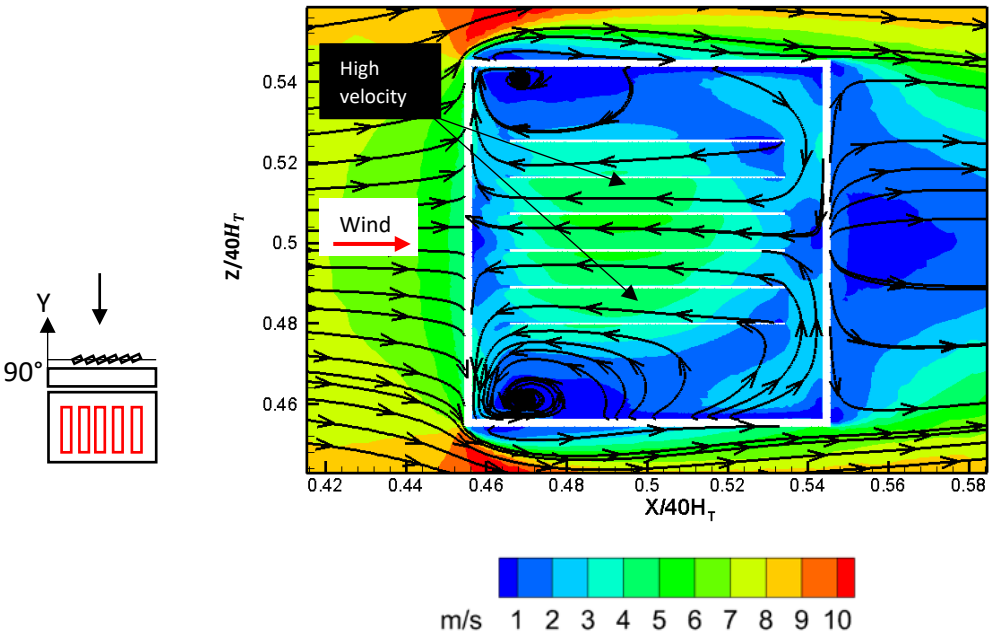

Figure 122: Mean streamlines and velocity contours on plane Y= 4.3 at collector tilt angle of 60 ° at varying wind incidence angle with low parapet

Figure 123 depicts the aerodynamics and velocity of the roof in the presence of a high parapet. It is evident that the aerodynamics of the roof bears resemblance to that of a low parapet. The presence of a low parapet on the roof is observed to result in a visibly higher velocity and vortex, particularly in the central region of the roof. The observation implies that the heat loss from collectors is more pronounced in the case of low parapets compared to high parapets. In general, when the wind incidence angles of 0° and 90° are analysed, the findings indicate that the leading row of collectors serves as obstacles to the incoming airflow at a wind incidence angle of 0°. The outcome suggests there would be the reduction of heat loss in the following row of collectors in the array. However, when the wind angle is 90°, the findings indicate that the collectors positioning will have very little impact on the heat loss in the direction of flow. Nevertheless, it is worth noting that the velocity on the roof exhibits a noticeable increase when the parapets are low, followed by higher parapets, and finally, in the absence of parapets.

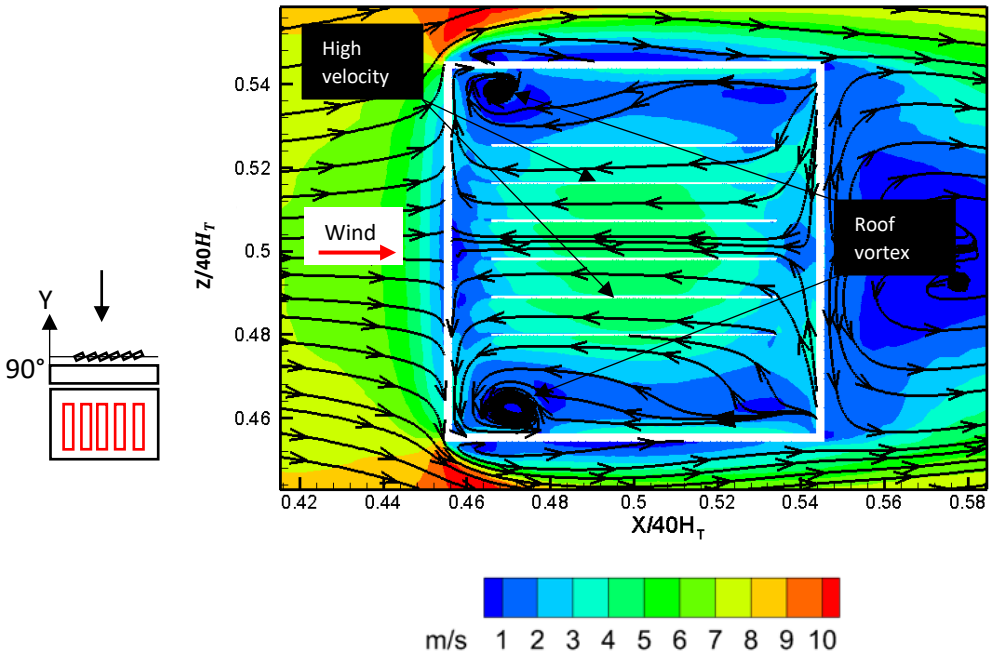

Figure 123: Mean streamlines and velocity contours on plane Y= 4.3 at collector tilt angle of 60 ° at varying wind incidence angle with high parapet

4.6 Effect of parapet on collector array heat loss

The previous section demonstrated the correlation between roof velocity, parapet height, and wind incidence angle. The subsequent step involved investigating the impact of parapet height on collector heat loss for a fixed wind incidence angle of 0°, with a predominant focus on parapets. Moreover, based on the findings presented in the preceding chapter which indicated a positive correlation between collector tilt angles and heat loss, it was determined that the assessment described above would be carried out at a collector tilt angle of 60°. This decision was made considering the potential shielding effect of the first row of collectors on the subsequent rows. Furthermore, given the identification of roof corner velocity zones in the preceding section, a separate assessment was undertaken for each collector in this case. This approach was taken due to the expectation that collectors situated at the edges would encounter distinct heat loss rates. The layout and labelling of the array are depicted in Figure 124. The diagram illustrates collectors, with each collector being distinguished by its corresponding row and location, specifically labelled as a, b, and c.

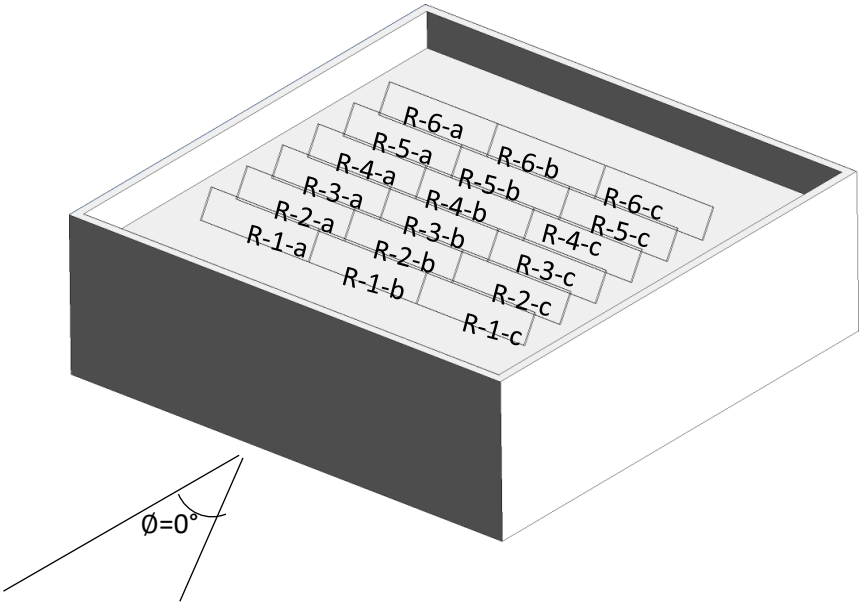

Figure 124: Layout and labelling of collector array.

Figure 125 depicts the average Nusselt number Nu_{avg} corresponding to each collector present in the array, under the conditions of a wind incidence angle of 0° and a collector tilt angle of 60°. It is evident that the heat loss of the collectors decreases away from the incoming flow path, irrespective of the parapet height. When there is no parapet on the roof, it is observed that the first row of collectors experiences a higher level of heat loss compared to situations where there are low or higher parapets present. Also noticeable is the fact that the collectors positioned at the trailing edge of the roof exhibit a decrease in heat loss, regardless of the parapet's height.

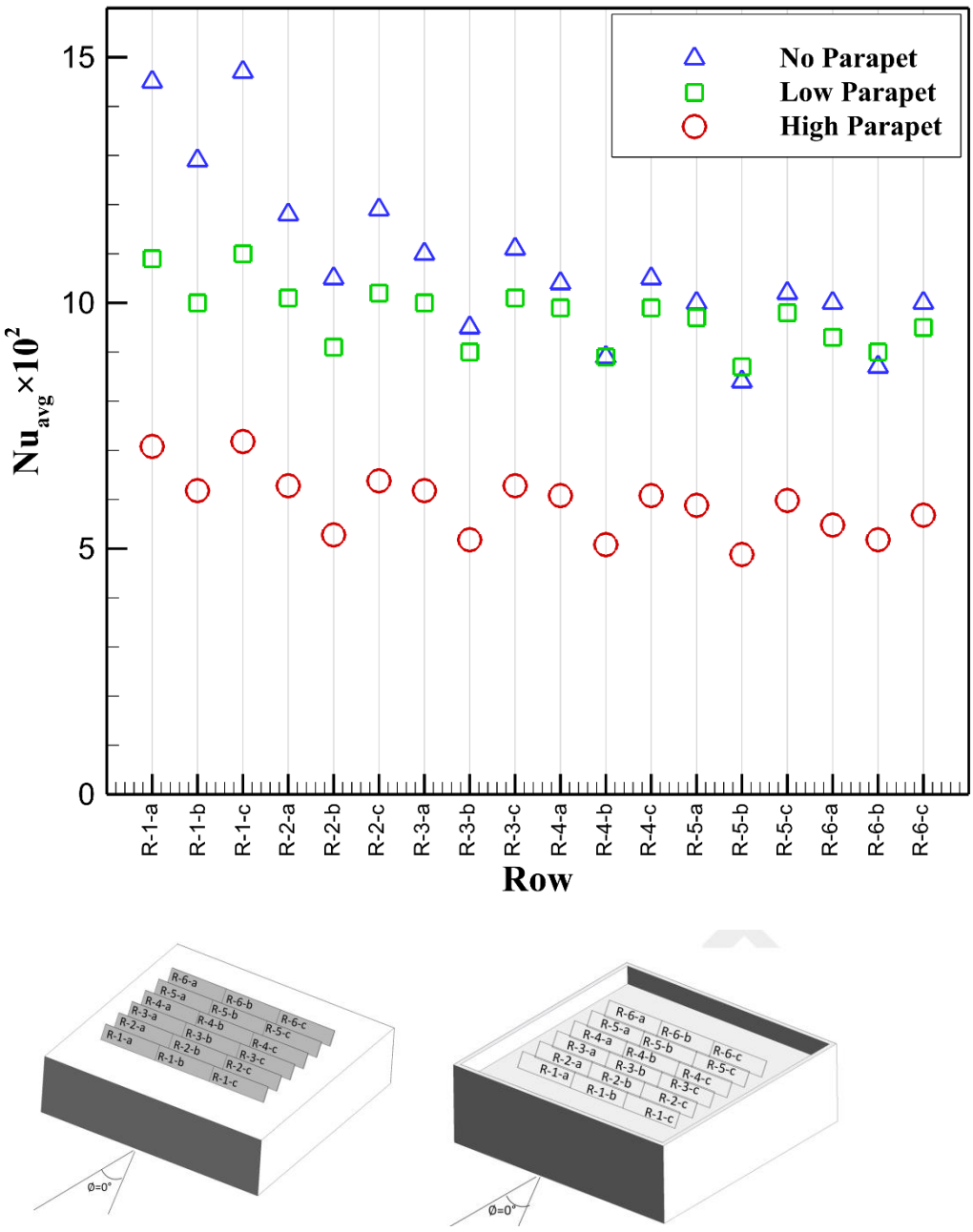

Figure 125: Nu_{avg} for collector array at different parapet heights and Reynolds number

In order to provide a further understanding of the findings presented in Figure 125, Figure 126 illustrates the aerodynamic characteristics and velocity patterns surrounding an array of solar collectors situated on a roof lacking any parapets. The occurrence of flow separation at the leading edge of the roof induces the formation of a vortex in front of the leading row of collectors. The presence of this vortex induces downwash at the surface of the collector, leading to an increased velocity at the front surface of the collector. As depicted in the plot of average Nu_{avg} values, this

results in an increase in velocity which explains the higher rate of heat loss for the first row of collectors (R-1-a to R-1-c).

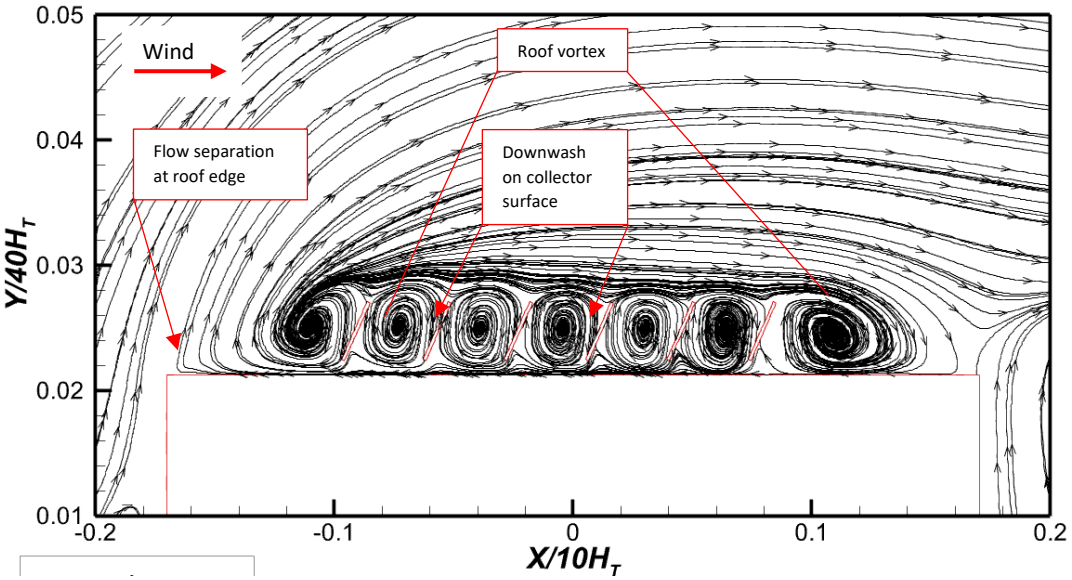

a. Mean velocity streamlines

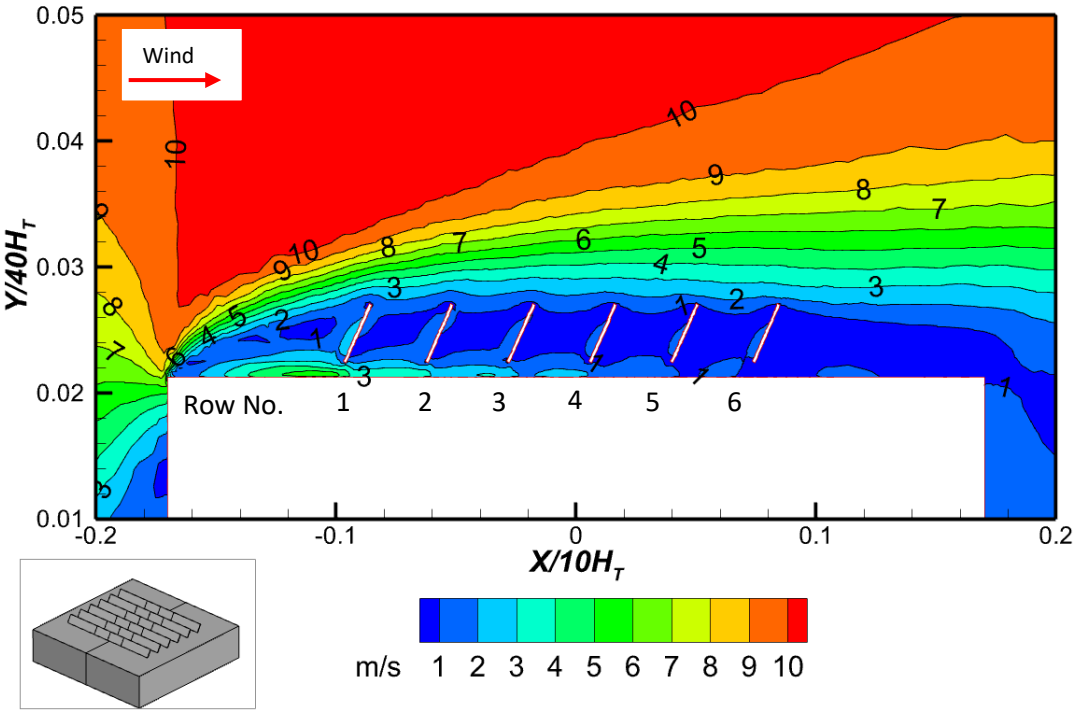

b. *Mean Velocity contours*

Figure 126: Mean streamlines and velocity contours on centre plane, β= 60 °, wind incidence angle 0 ° for no parapet present.

Based on the observations depicted in Figure 126 and Figure 127, it is evident that two phenomena manifest themselves in the row of collectors under consideration. Firstly, there is the occurrence of flow separation at the trailing edge of the initial row of collectors. Secondly, vortices are generated in front of the subsequent row of collectors. Collectors positioned further

from the approaching flow exhibit a reduced velocity in their vicinity compared to those in closer proximity to the leading edge of the roof. The velocity decreases as one moves away from the leading edge of the roof due to the obstructive influence of the collectors in the flow pathway. This phenomenon provides an explanation for the uniform reduction in heat loss of the collectors away from the leading edge of the roof.

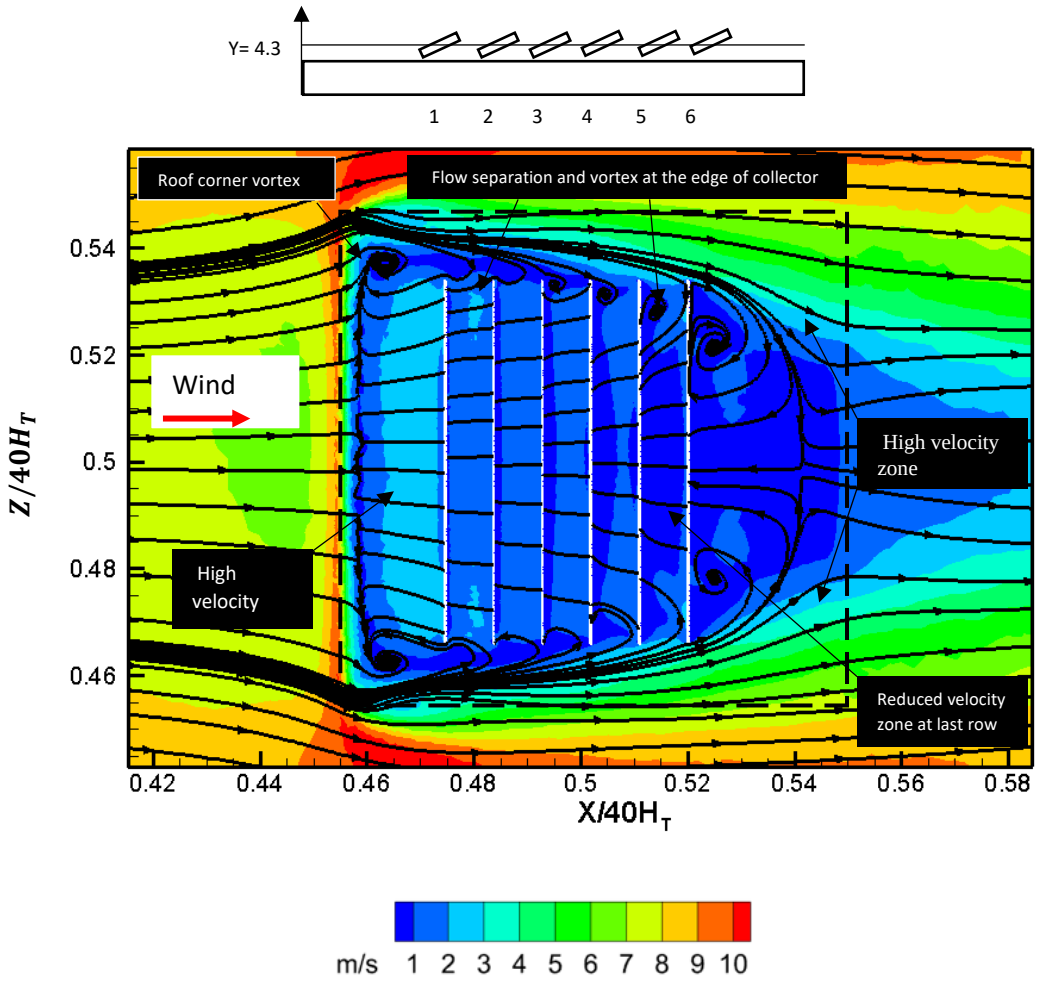

Figure 127: Mean streamlines and velocity contours on plane y= 4.3, β= 60 °, wind incidence angle 0 ° for no parapet configuration.

Furthermore, the vortices that are generated in front of each row of the subsequent collector have an equal impact on the rear surface of the preceding row of collectors. Therefore, considering the unglazed nature of the collectors, the total heat loss of each collector is influenced by the heat loss occurring at its rear surface, which also diminishes away from the incoming flow. The explanation clarifies the underlying reasons for the diminished heat loss in the collectors away from the oncoming flow in the absence of a perimetric parapet.

Figure 128 and Figure 129, illustrates the aerodynamics and velocity distribution around the collector in the presence of a low perimetric parapet. The presence of flow separation at the leading edge of the roof gives rise to the formation of a vortex in the vicinity of the first row of collectors. The separation of flow at the roof parapet leads to a downwash effect on the initial row of collectors. The phenomenon of downwash is associated with high velocity, which can account for the greater heat loss experienced by the initial row of collectors compared to subsequent rows. This observation is supported by the plot of average Nusselt numbers (Nu_{avg})in Figure 125.

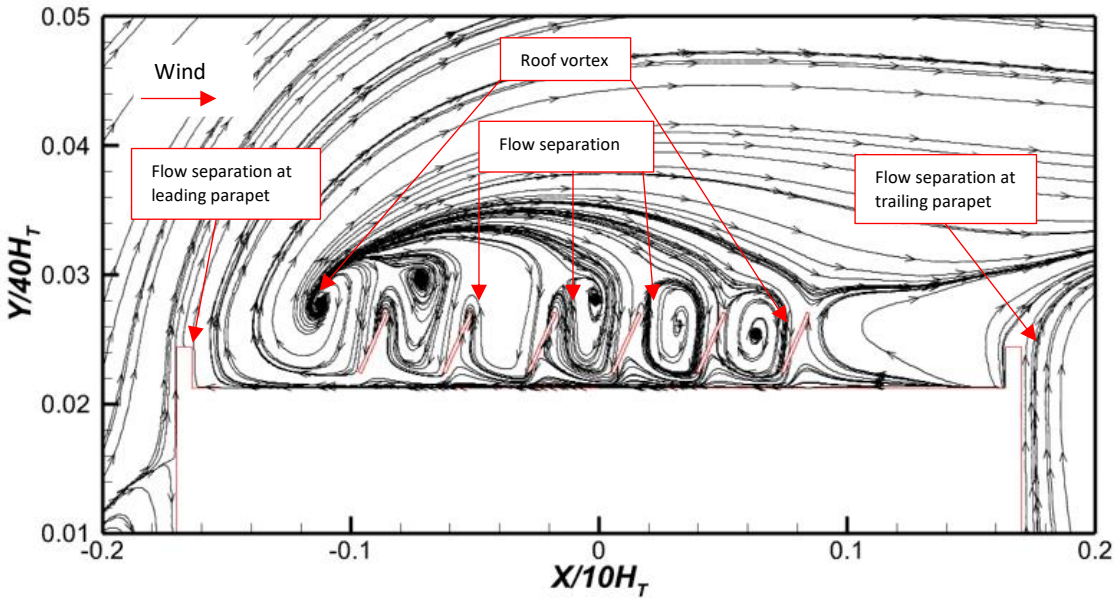

a. Mean velocity streamlines

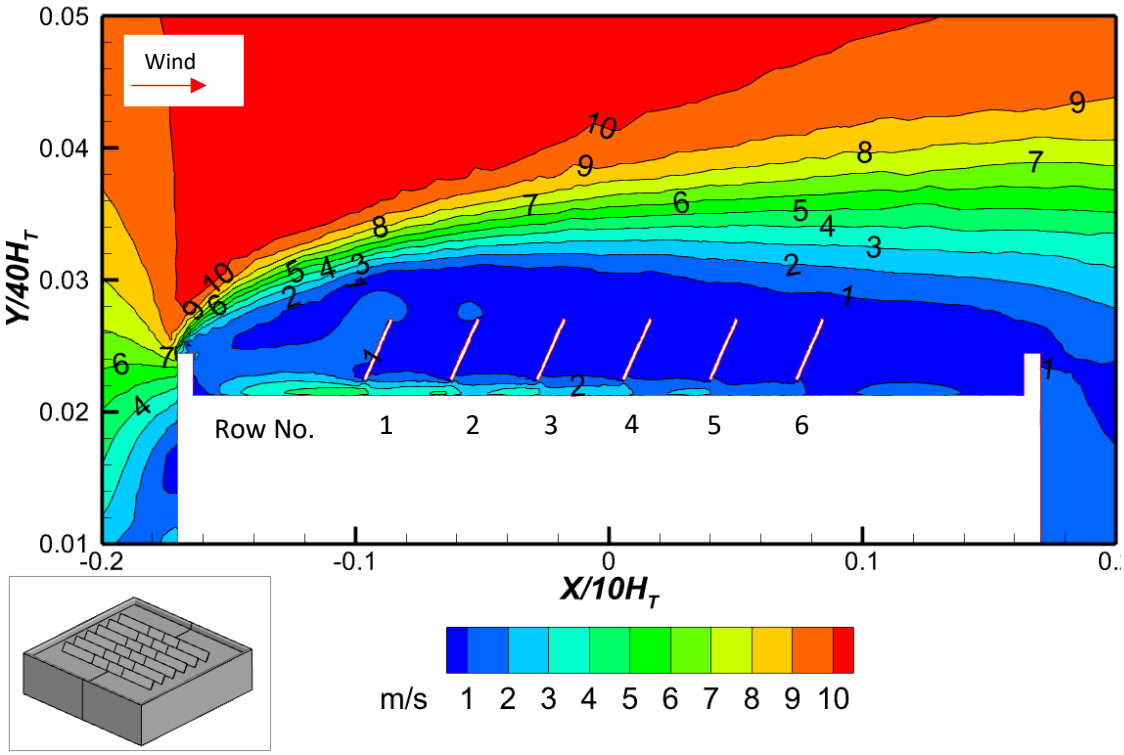

b. Mean Velocity contours

Figure 128: Mean streamlines and velocity contours on centre plane, β= 60 °, wind incidence angle 0 ° for low parapet configuration.

Upon conducting a more thorough analysis of the following series of collectors, it becomes apparent that each row displays a flow separation at its trailing edge because of the separation originating from the leading parapet. As a consequence of this phenomenon, the downwash effect experienced on the surface of the collector in subsequent rows is reduced, resulting in a decline in both velocity and heat loss away from the incoming flow. When comparing the present case with a case without parapets, it becomes apparent that in the latter scenario, flow separation occurs at both the lowest point of the roof and the leading edge of the collector. Consequently, this leads to higher velocity and increased heat loss, particularly for the collectors situated in close proximity to the leading edge of the roof.

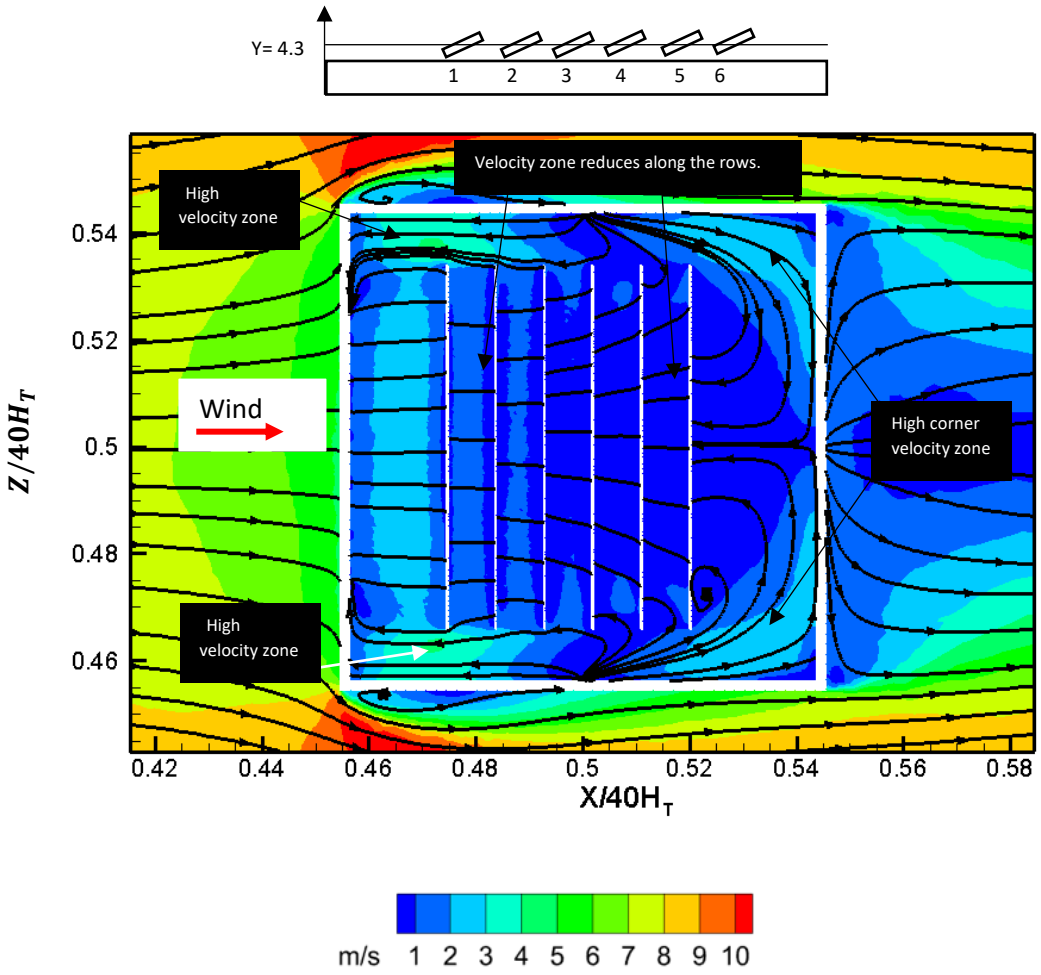

Figure 129: Mean streamlines and velocity contours on plane y= 4.3 at collector tilt angle of 60 ° at wind incidence angle 0 ° for low parapet configuration.

Figure 130 illustrates the aerodynamic characteristics and velocity distribution on the roof of a building featuring a high parapet along its perimeter. It can be observed that a vortex is generated at a higher altitude above the array due to the occurrence of flow separation at the leading edge of the parapet. The presence of a recirculation bubble surrounding the array, as indicated by the parapet height and point of flow separation, leads to the formation of regions with low velocity around the collectors. Consequently, the collectors exhibit reduced heat losses at higher parapets, as depicted in Figure 125.

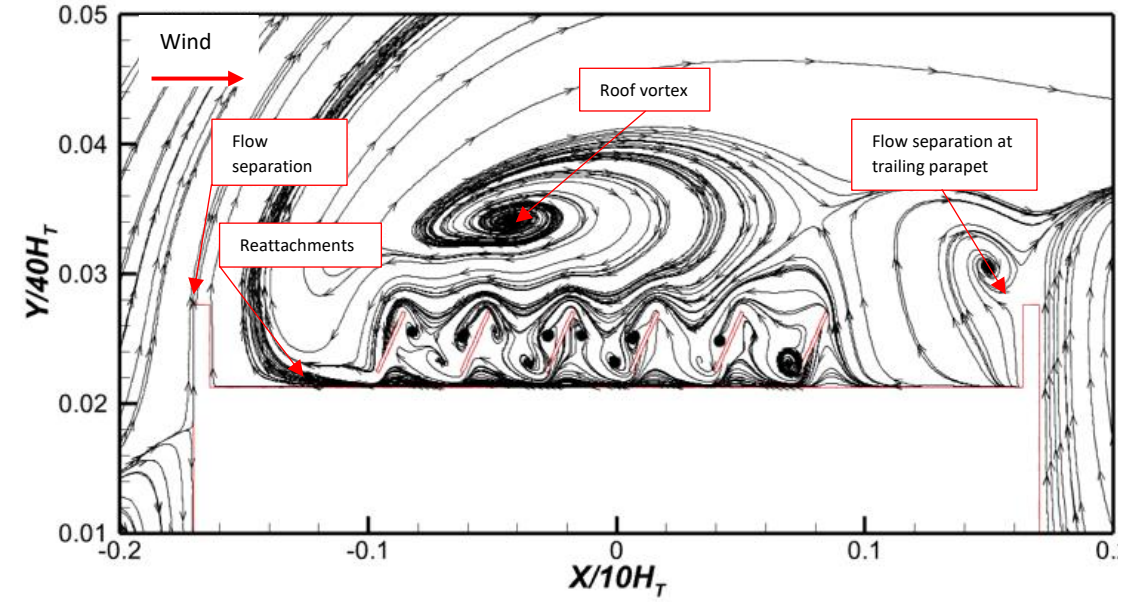

a. Mean Velocity streamlines

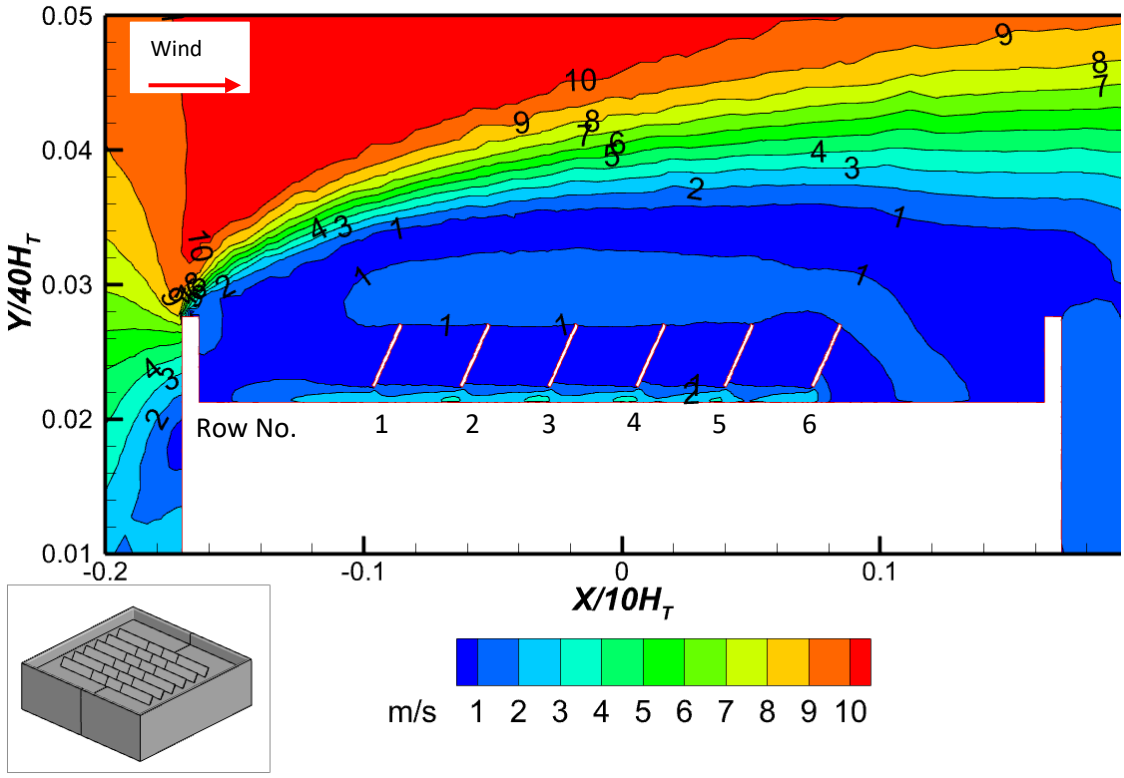

b Mean Velocity contours

Figure 130: Mean streamlines and velocity contours on centre plane, β= 60 °, wind incidence angle 0 ° for high parapet configuration.

Additionally, it is evident that (Figure 131), there is a minimal presence of downward washing observed on the surface of the collector. This phenomenon occurs due to the limited interaction between the approaching flow and the surface of the collector. This stands in contrast to situations where a low or absent parapet is present. Also, the aerodynamic characteristics of this case exhibit

a distinct vortex formation on the roof, as depicted in Figure 131 which signifies that a considerable section of the roof and the surrounding area of the collector experiences a notable decrease in velocity, thereby leading to relatively low heat loss.

Similar to the case of low and high parapets, the initial row of collectors exhibits a greater amount of heat loss, which can be attributed to the presence of a higher velocity zone, as illustrated in Figure 125. Overall, it can be inferred that the heat loss patterns along the flow path exhibit a near-identical nature for each collector. In the scenario involving high parapets, it is observed that the parapet functions as a barrier that hinders the escape of heat by obstructing the collectors due to their elevated position. Consequently, this leads to a decrease in heat loss observed in Figure 125.

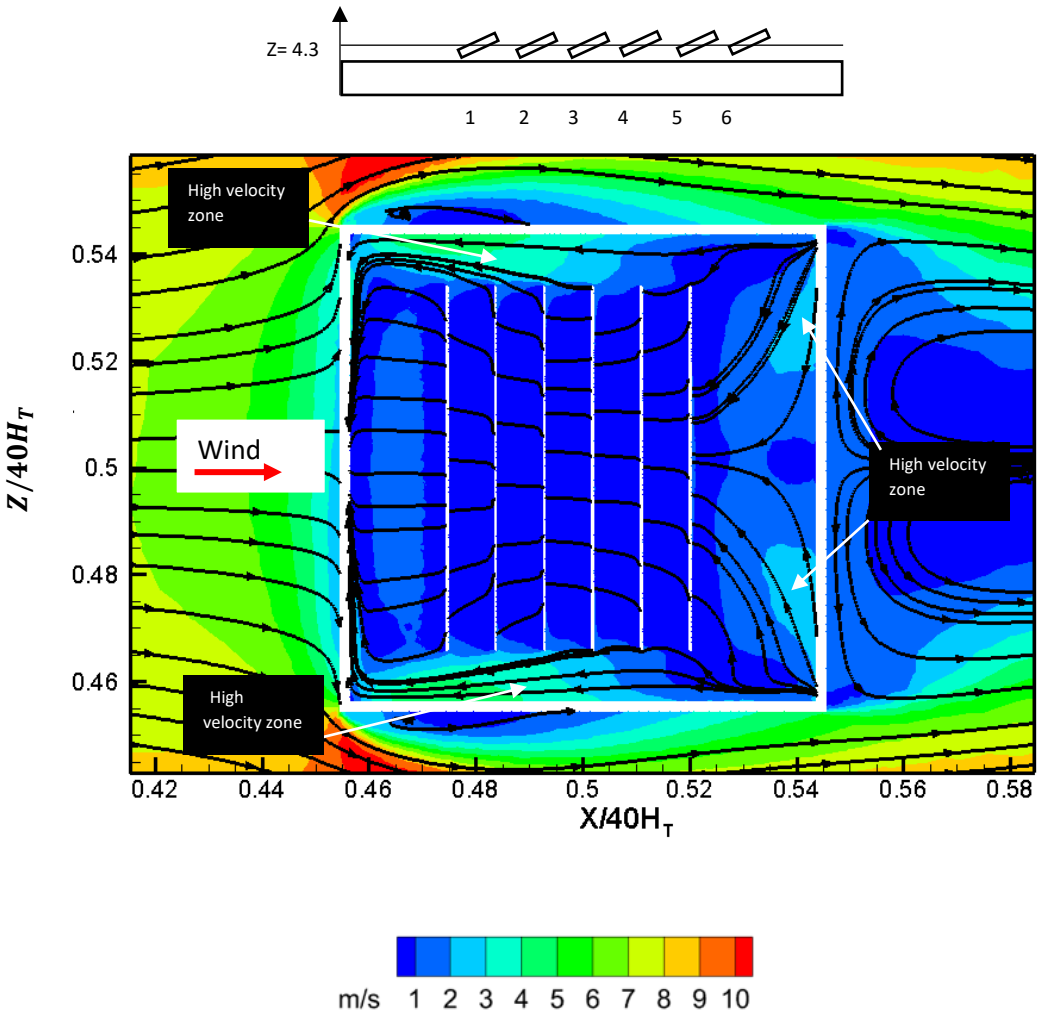

Figure 131: Mean streamlines and velocity contours on plane y=4.3, β=60 °, wind incidence angle 0 ° for high parapet configuration

4.7 Effect of parapets on individual heat loss of solar arrays at varying tilt angles

The previous section demonstrated that parapets on roofs with collector arrays can affect heat loss varyingly. It should be noted, however, the above analysis was conducted at a tilt angle of 60°, which can be deemed a worst-case scenario with the collector's almost upright and exposed to the oncoming flow. Since collector arrays can be mounted at low tilt angles, the next step was to compare the heat loss between low and high tilt angles. This was performed to determine the effect of parapets on roofs when collectors are directly in the path of the incoming flow at high tilt angles and when they are blocked by parapets at lower tilt angles. The analysis was also intended to compare the shielding effects of collectors at higher tilt angles, where they are in the flow path, to those at lower tilt angles, where the shielding effect of the collectors is almost absent.

Figure 132 shows the Nu_{avg} values for the different tilt angles without perimetric parapets. It can be seen that the heat loss for the first row of collectors is higher in both cases and even more pronounced at higher tilt angles. The collector surface experiences increased exposure to the oncoming flow as a result of higher tilt angles, in comparison to lower tilt angles. Figure 133 and Figure 134 provides the visual evidence supporting the notion that the velocity at the surface of the first row of the collectors is more prominent when the tilt angles are increased, thereby suggesting a higher degree of heat loss. Also, the first row of collectors shield the subsequent collectors surfaces from the impact of the oncoming flow velocity, thus resulting in a reduced heat loss observed.

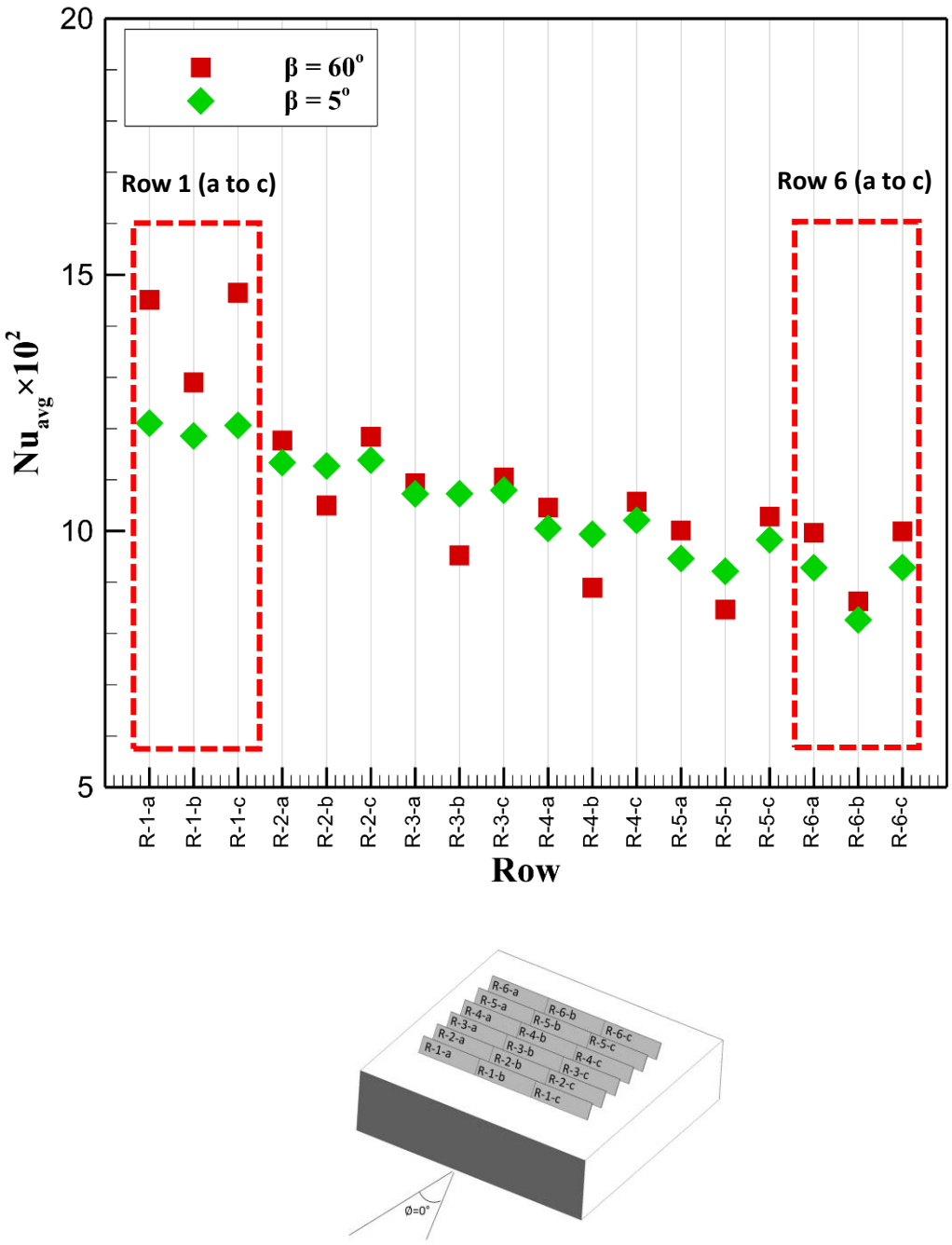

Figure 132: Nu_{avg} for collector array at different parapet heights and Reynolds number with no parapet present.

Furthermore, the heat loss for collectors situated at the central position of each row (denoted as "b" in each instance) exhibits a slight reduction in comparison to the remaining collectors within the identical row. The rationale behind this observation stems from the differential exposure of the collectors on the sides of each row to the incoming wind, in contrast to the complete shielding of the centrally located collector from all sides.

Based on the above, it can be deduced that the absence of perimetric parapets may result in higher heat losses for collectors with higher tilt angles, particularly for the first row of collectors. However, the extent of this heat loss is relatively small compared to collectors with lower tilt angles. Moreover, it should be noted that collectors positioned near the periphery of an array will experience greater heat dissipation compared to collectors situated in the central region of the array.

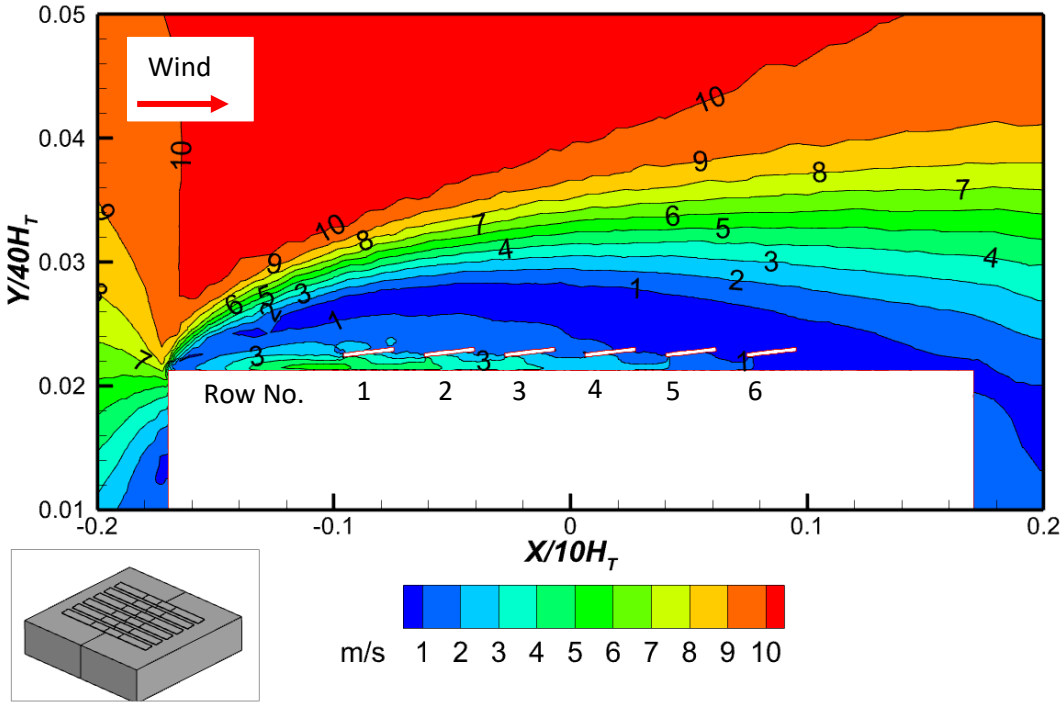

Figure 133: Velocity contours on centre plane, β=5° at wind incidence angle 0 ° for no parapet configuration.

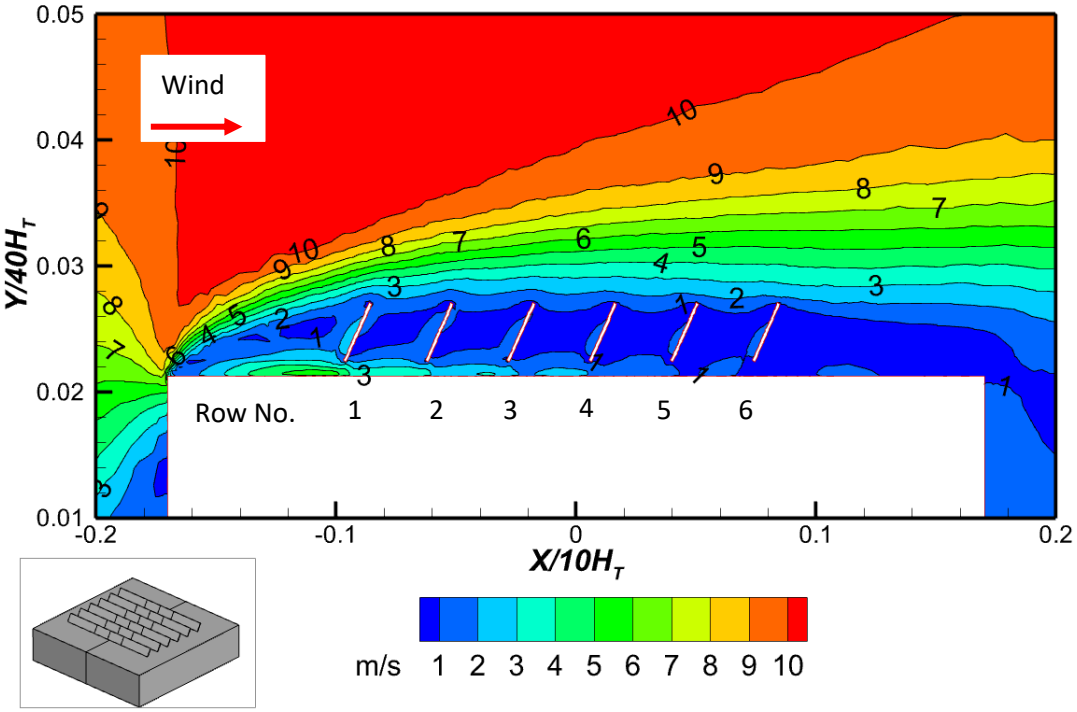

Figure 134: Velocity contours on centre plane, β=60° at wind incidence angle 0 ° for no parapet configuration.

Figure 135 depicts the heat loss when low perimetric parapets are installed. As shown, when the collectors are tilted at 60°, the first row of collectors (R-1-a to R-1-c) experience greater heat loss than collectors inclined at 5°. This is because the trailing edge of the collectors inclined at 60° project above the parapet, while the trailing edge of the collectors at 5° are hidden. Also, when analysed independently, it can be seen that there is an increase in heat loss for the last row of collectors (R-6-a to R-6-c) for collectors inclined at 5° compared to collectors inclined at 60°. This can be explained through a comparative observation of flow behaviours in both cases, depicted in Figure 136 and Figure 137. As shown, between the two tilt angles, there is a formation of higher velocity zones at the rear of the last row of collectors at 5° which is characterised by the flow at the space beneath the collector and the roof surface. The resulting effect of this is a downwash of the collectors' rear surface, which results in a higher velocity and consequently heat loss.

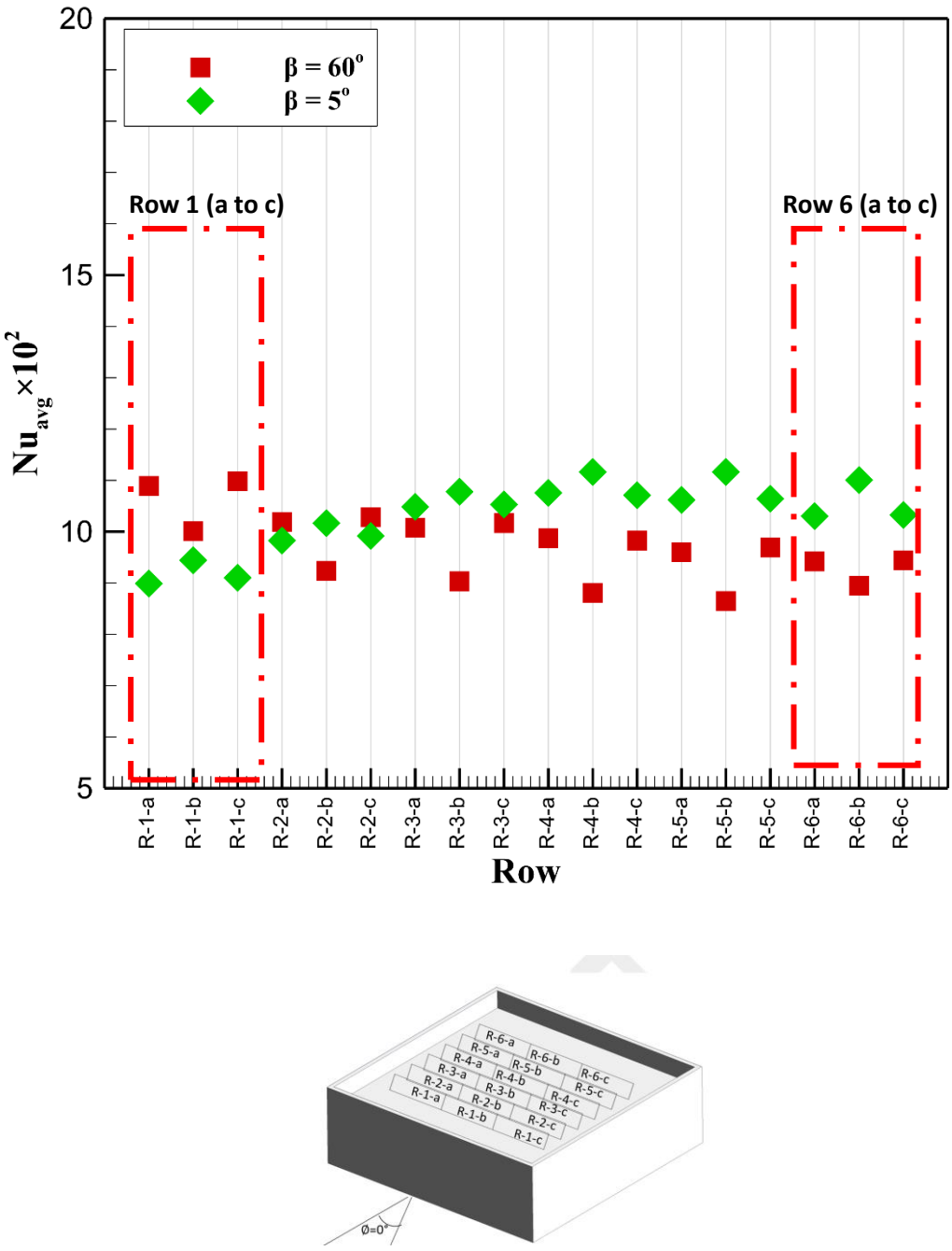

Figure 135: Nu_{avg} **for collector array at different parapet heights and Reynolds number with low parapet present.**

Furthermore, it is evident that the heat loss becomes more prominent in the second to fifth rows of collectors (R-2 to R-5) when considering collectors with a tilt angle of 5°. The underlying cause of this phenomenon can be attributed to the development of regions with elevated velocities on the surface of the collector. It is apparent that when the collector tilt angle is set at 5°, the foremost edge of the collectors becomes fully submerged behind the parapets. As a consequence, this configuration allows for optimal exposure to the high velocity flow present on the surface of the

roof. Therefore, it can be deduced that collectors with lower tilt angles would experience greater heat loss at lower perimetric parapets than collectors with higher tilt angles.

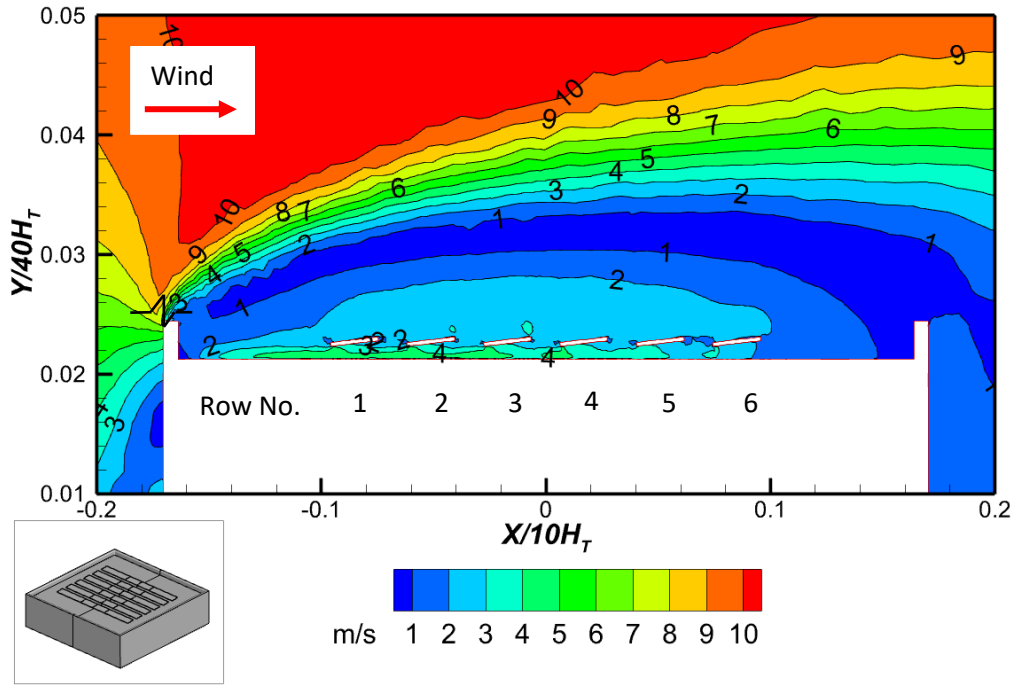

Figure 136: Velocity contours on centre plane, β=5 ° at wind incidence angle 0 ° for low parapet configuration

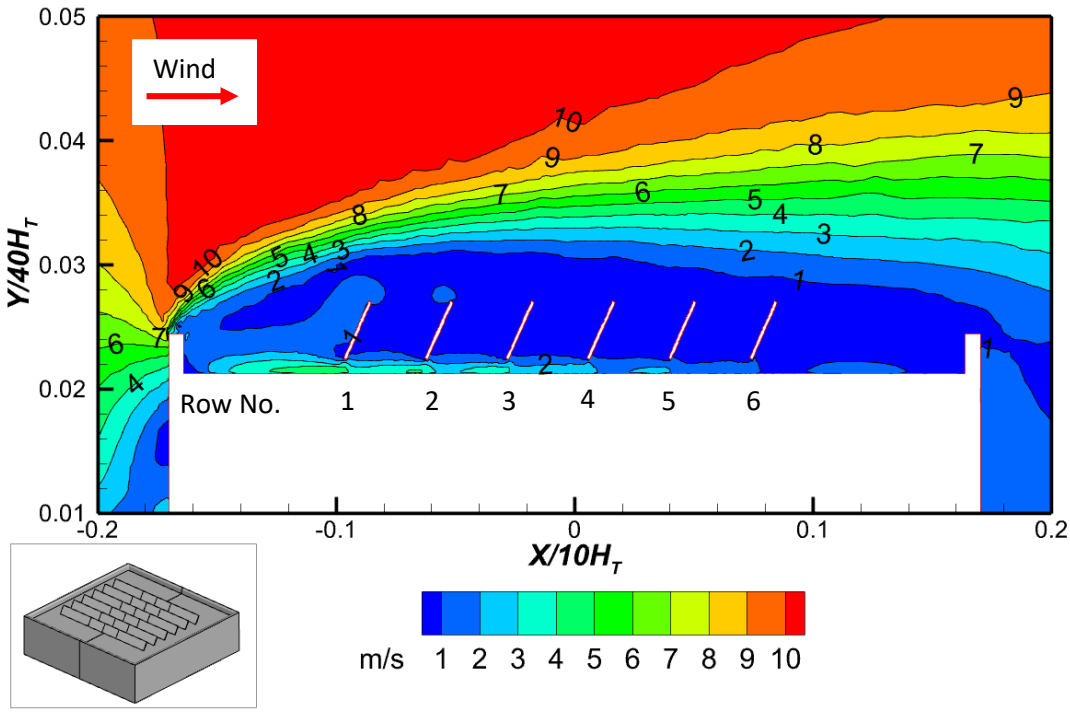

Figure 137: Velocity contours on centre plane, β=60 ° at wind incidence angle 0 ° for low parapet configuration

Moving on from this, Figure 138 shows the Nu_{avg} values at high perimetric parapets for the tilt angles considered. The figure illustrates that collector with a lower tilt angle of 5° experience a greater heat loss compared to collectors with a higher tilt angle of 60°.

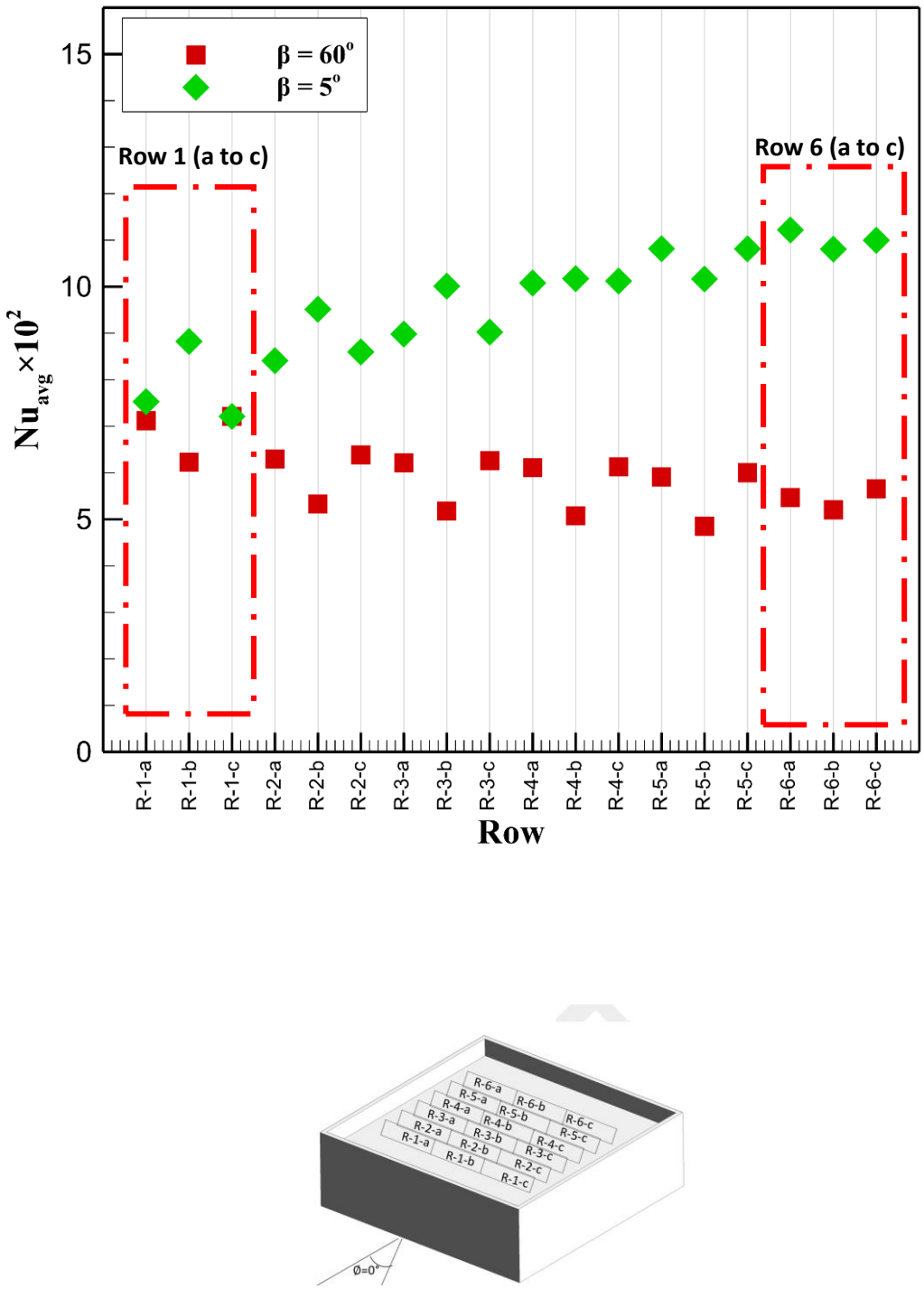

Figure 138: Nu_{avg} for collector array at different parapet heights and Reynolds number with high parapet present.

The restriction of the approaching flow path is evident in Figure 139 and Figure 140 due to the presence of a high parapet. As shown in Figure 140 the vortex is shifted above the roof by the

collectors positioned at a tilt angle of 60°. The outcome of this is a reduced velocity in the vicinity of the collector, resulting in a reduction in heat loss. In contrast, when the collectors are tilted at an angle of 5°, Figure 139, the resulting effect on the vortex present on the roof is minimal. This adjustment leads to the vortex being positioned in closer proximity to the surface, consequently resulting in an increase in velocity at the collector surface. Collectors positioned at low tilt angles experience greater heat loss compared to collectors with high tilt angles in the presence of high perimetric parapets, resulting in this outcome.

Similarly it can be observed in Figure 139 and Figure **140** that the array experiences a greater heat loss away from the oncoming flow at low tilt angles of 5° compared to high tilt angles of 60°. In the case of 5° the observed heat loss can be attributed to the flow interaction occurring between the leading and trailing parapets, leading to an increased velocity in proximity to the trailing parapet. Based on the above observation, it can be deduced that the heat loss of collectors arranged in an array with a low tilt angle will be particularly significant, particularly in the presence of high perimetric parapets.

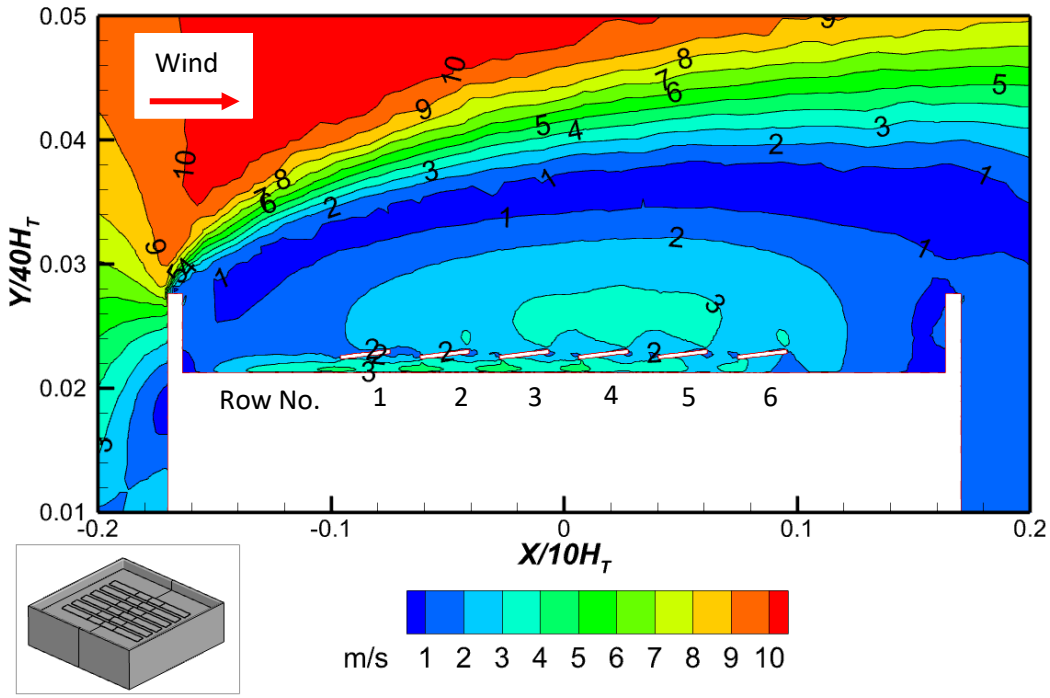

Figure 139: Velocity contours on centre plane, β=5 ° at wind incidence angle 0 ° for high parapet configuration

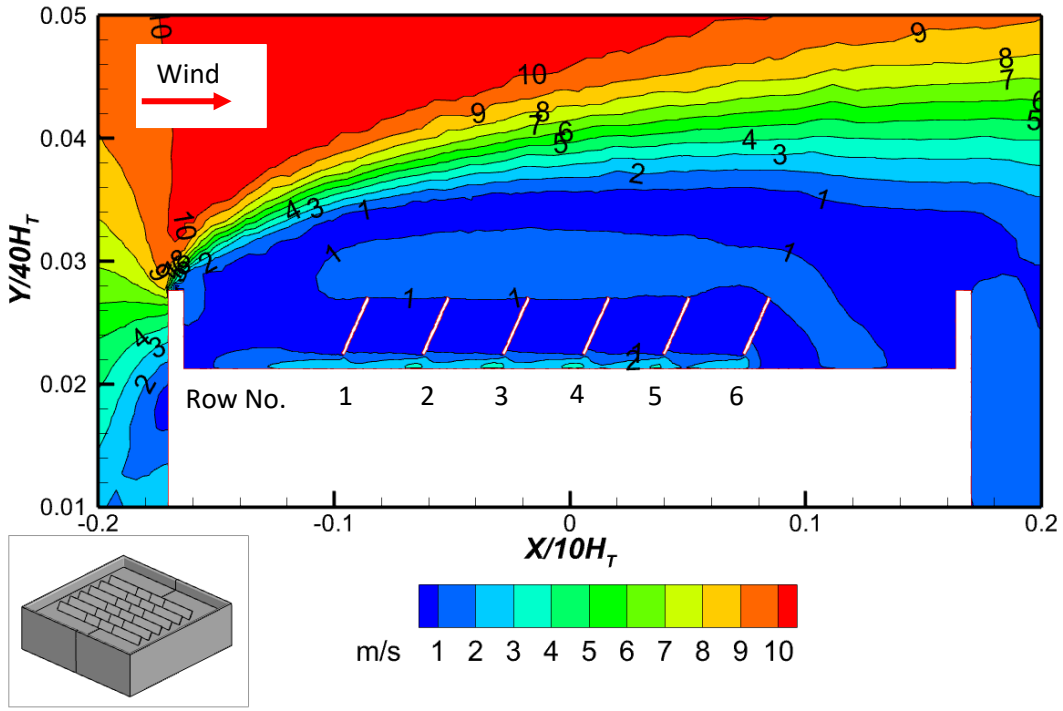

Figure 140: Velocity contours on centre plane, β=60° at wind incidence angle 0 ° for high parapet configuration

4.8 Chapter Conclusion

The convection heat losses from rooftop array collectors were numerically evaluated in this chapter at 10 m/s wind velocity, variable collector tilt angles of 5° and 60°, wind incidence of 0° and varying parapet heights. First the effect of the wind incidence angle on the velocity zone around solar arrays at varying parapet height was investigated. The study initially examined the impact of wind incidence angle on the velocity distribution in the vicinity of solar arrays, considering different parapet heights. The findings of the study indicate that the presence of higher parapets is associated with a reduction in velocity around the first row of collectors, in contrast to situations where no or low parapets are present.

In addition, it has been observed that in roof top arrays where the wind incidence is at a 90° angle, the wind velocity at the central region of the array is greater in comparison to that at a 0° angle. In order to enhance comprehension of the impact on heat loss, a comprehensive examination of the heat loss pertaining to each individual collector was conducted. The findings exhibited two overarching similarities regardless of the height of the parapet. Initially, it is observed that the

heat loss experienced by the first row of collectors is comparatively greater in magnitude when compared to the heat losses encountered by the remaining collectors in the array.

Additionally, the heat loss of the collector is diminished when situated within the array, distant from the incoming flow. Therefore, it is plausible to install dummy collectors in collector arrays in order to mitigate the influence of wind on the adjacent row of collectors. The results of the study also suggest that the absence of a parapet leads to a higher level of heat loss in comparison to scenarios where both low and high perimetric parapets are present. The investigation focused on the analysis of the effect of varying collector inclination arrays on heat loss. The study's findings indicate that in the absence of perimetric parapets, collectors with lower tilt angles (5°) experience a lesser heat loss than collectors with higher tilt angles (60°) for roofs without parapets. On the other hand, roofs with high parapets exhibit the opposite behavior. Moreover, the findings indicate that collectors positioned in proximity to the borders of the array exhibit higher levels of heat loss compared to collectors situated at the centre of the array.

Based on the analysis, the research reveals that the height of parapets has a significant influence on the heat loss of rooftop solar arrays, taking into account both the parapet height and the angle at which the collectors are tilted. Consequently, the aforementioned underscores the significance of taking into account the parapet height, collector tilt angle, and collector position during the installation of collector arrays on rooftops, specifically by professionals in the fields of engineering, design, and architecture.

Chapter 5

Conclusions, recommendations, and future work

5.1 Conclusions

Unglazed solar thermal collectors have been marginalised in comparison to other types of flat plate collectors due to their reported significant heat loss. Perimetric parapets, on the other hand, have been shown to significantly alter wind loads on roof tops of low-rise buildings, by changing the roof aerodynamics thereby the local air velocity. The present study aimed to examine the impact of parapets on the convection heat loss of unglazed solar thermal collectors installed on rooftops.

To do this, simulations of computational fluid dynamics (CFD) were used. The numerical method of the CFD was validated against existing experimental results at each step of the process. For the stand-alone collector, a separate wind tunnel experiment was also undertaken as part of the validation. The research was divided into three sections. To begin, the effect of parapets on the aerodynamics of low-rise buildings was undertaken. This was caried out to determine the effect of parapets on aerodynamic features such as roof vortex, height of stagnation point and the length of recirculation.

Subsequently, the heat loss of an unglazed standalone roof mounted collector was carried out. The roof aerodynamics were compared at various wind incidence angles, and the Nu_{avg} was calculated for varying parapet height, collector mounting location, and collector tilt angle. This led to the development of a generalised convective heat transfer correlation that considered all operational factors. The correlation's applicability was also tested.

Next, the impact of the parapet on the heat loss of solar collector arrays was investigated. In addition to perimetric parapet height, different tilt angles of collector arrays were investigated to determine how these factors influence variations in heat loss for independent collectors within the array.

The study found that when mounted on roofs without parapets, solar thermal collectors should not be placed within 25 percent of the roof length when no perimetric parapets are present. A

collector located closer to the roof leading edge would have its surface in the direct path of the oncoming flow separation emanating from the leading edge of the roof. In contrast, mounting the collector closer to the leading parapet in a region less than 25 percent of the roof had the opposite effect in cases where low or high perimetric parapets are present. According to the findings, the parapet would act as an obstruction to the flow, resulting in flow separation above the roof surfaces and at the leading parapet.

The study also found that when collectors are mounted in the centre of roofs with parapets, the heat loss of the collector increased. Clearly at lower parapets, the flow separates slightly higher above the roof surface, thus resulting in increased velocity on the roof and the collector heat loss. When collectors were mounted farther down the roof (from the oncoming flow), which represents more than 75 percent of the roof's length, the presence of parapets were found to result in a greater heat loss of the collector. This is due to several factors, including backward stepping flow from the trailing parapet and roof vortex displacement, all of which influence the velocity at the collector's rear surface. In contrast, for roofs without parapets, mounting the collector father away from the oncoming wind resulted in less heat loss.

The study also found that in the presence of parapets, standalone collectors with higher tilt angles lose more heat than standalone collectors with lower tilt angles. High tilt angles, according to the numerical simulation, expose the collector's surface above the parapet, resulting in a higher velocity at its surface and, as a result, a higher heat loss. Also, the results showed that low perimetric parapets resulted in significant heat loss in all situations except for cases where the collector was mounted closer to the leading edge of the roof.

An analysis of a roof mounted collector array revealed that the first row of collectors lost the most heat compared to the subsequent rows. The exposure of the first row of collectors, as well as the effect of the roof array on the roof vortex, are two reasons for this. Moreover, as the arrays' tilt angle increased, the heat loss of the subsequent row of collectors decreased away from the oncoming flow. As a result, architects and designers may consider including dummy collectors on roofs to reduce local velocity and heat loss in collector arrays.

The study also looked at the heat loss of collector arrays at different tilt angles. Heat loss was found to be greater for collector arrays with a lower tilt angle than for those with a higher tilt angle. This is because at low tilt angles, the trailing edge of collectors do not disrupt the flow from the roof's leading edge, resulting in higher velocity zones at the roof centre. Finally, based on the foregoing, the presence of parapets may benefit roof-mounted unglazed collectors to some extent by determining the mounting location of standalone collectors and arrays, as well as adding to the factors required to determine an optimal tilt angle for the array of collectors. Also, because unglazed collectors are less expensive than glazed collectors, designers could use the understanding of the effect of parapet shown in this study to offer unglazed collectors as a compelling alternative for hot water and other low grade heating applications.

5.2 Recommendations for future work

The present study, while contributing valuable insights into the impact of parapets on heat loss and the performance of unglazed solar thermal collectors, acknowledges certain limitations arising from simplified assumptions and idealized conditions that may not fully capture real-world scenarios. Consequently, this recommendation outlines avenues for future research to enhance the depth and breadth of knowledge in this domain.

Firstly, the use of Reynolds-averaged Navier-Stokes (RANS) modeling in both stand-alone and array configurations could be supplemented by employing large eddy simulation (LES) and detached eddy simulation (DES) techniques. This approach would allow for a more comprehensive numerical analysis of the unsteady flow properties around the collector and on the roof, particularly when considering varying parametric parapet heights for both stand-alone collectors and collector arrays.

Moreover, an expanded wind tunnel study is suggested, encompassing all operational parameters considered in the current study and exploring values beyond the utilized range. This extended investigation could employ tracer or other conventional flow visualization techniques, synchronized with pressure and velocity metrics, to dissect the aerodynamic mechanisms influencing heat loss of unglazed collectors on roofs with different perimetric heights for both stand-alone and collector arrays.

Given that the study focused on the Tokyo Polytechnic geometry, further exploration into alternative geometric configurations is proposed. Investigating the effect of roof length, building height, and parapet height at varying aspect ratios—representative of different building use such as residential and industrial—could yield insights into the optimal placement of solar thermal collectors or photovoltaic panels.

Additionally, the potential influence of different parapet configurations on wind loads is reported in Huang *et al.,* (2012). Therefore, it is recommended to delve into understanding how various parapet configurations impact the heat loss of solar arrays, either through wind tunnel experiments or computational fluid dynamics (CFD) simulations.

Finally, future studies could explore the effect of shading resulting from diverse parapet configurations and heights. The study indicates that regions close to parapets exhibit lower velocity, especially with higher parapets. Investigating the implications of this shading on solar array heat loss could provide valuable insights into optimizing the design and placement of solar energy systems.

References

AIAA. 1998. Guide for the verification and validation of computational fluid dynamics simulations. American Institute of Aeronautics and Astronautics, Reston, VA

Abohela, I., Hamza, N., Dudek, S., 2013. Effect of roof shape, wind direction, building height and urban configuration on the energy yield and positioning of roof mounted wind turbines. Renew Ener. 50, 1106-1118.

Akhtar, N., Mullick, S.C., 2007. Computation of glass-cover temperatures and top heat loss coefficient of flat-plate solar collectors with double glazing. Energy. 32(7), 1067-1074.

Akon, A.F., Kopp, G.A., 2016a. Mean pressure distributions and reattachment lengths for roof-separation bubbles on low-rise buildings. J. Wind Eng. Ind. Aerodyn. 155, 115-125.

Akon, A.F., Kopp, G.A., 2016b. Pressure fluctuations on the roofs of low-rise buildings in turbulent boundary layers, in: Proceedings of the annual conference. Canadian Society for Civil Engineering.

Aly, A.M., Bitsuamlak, G., 2013. Aerodynamics of ground-mounted solar panels: test model scale effects. J. Wind Eng. Ind. Aerodyn. 123, 250-260.

Anderson, B.N., 1977. Solar energy: fundamentals in building design, in: McGraw-Hill Book Co., New York, p. 380.

Anderson TN, Duke M, Carson JK. Performance of an unglazed solar collector for radiant cooling. In: Proceedngs of Australian Solar Cooling 2013 Conference. Sydney

Anderson, T., Duke, M., Carson, J., 2013. Performance of an unglazed solar collector for radiant cooling. Australian solar cooling.

Appelbaum, J., Bany, J., 1979. Shadow effect of adjacent solar collectors in large scale systems. Sol. Energy. 23(6), 497-507.

Armstrong, S., Hurley, W.G., 2010. A thermal model for photovoltaic panels under varying atmospheric conditions. Appl. Therm. Eng. 30(11-12), 1488-1495.

Aronescu, A., Appelbaum, J., 2020. Shading on photovoltaic collectors on rooftops. Appl. Sci. 10(8).

Asghari Mooneghi, M., Kargarmoakhar, R., 2016. Aerodynamic mitigation and shape optimization of buildings: review. J. Build. Eng. 6, 225-235.

Aziz, W., Chaturvedi, S.K., Kheireddine, A., 1999. Thermodynamic analysis of two-component, two-phase flow in solar collectors with application to a direct-expansion solar-assisted heat pump. Energy. 24(3), 247-259.

Baeder, D. et al., 2011. Comparison of numerical simulations with experiments of bluff bodies including under-hood flow, in: SAE 2011 world congress and exhibition.

Banks, D., 2013. The role of corner vortices in dictating peak wind loads on tilted flat solar panels mounted on large, flat roofs. J. Wind Eng. Ind. Aerodynamics. 123, 192-201.

Bany, J., Appelbaum, J., 1987. The effect of shading on the design of a field of solar collectors. Sol. Cells. 20(3), 201-228.

Bartelsen, B., Rockendorf, G., Vennemann, N., Tepe, R., Lorenz, K., Purkarthofer, G., 1999. Elastomer-metal-absorber: development and application. Sol. Energy. 67(4-6), 215-226.

Basara, B., Krajnović, S., Girimaji, S.S., 2008. PANS vs. LES for Computations of the Flow around a 3D Bluff Body, in: 7th International ERCOFTAC Symposium on “Engineering Turbulence Modelling and Measurements.

Baskaran, A., Stathopoulos, T., 1988. Roof corner wind loads and parapet configurations. J. Wind Eng. Ind. Aerodyn. 29(1-3), 79-88.

Beck, F., Martinot, E., 2004. Renewable Energy Policies and Barriers. Encyclopedia Energy 365-383.

Becker, S., Lienhart, H., Durst, F., 2002. Flow around three-dimensional obstacles in boundary layers. J. Wind Eng. Ind. Aerodyn. 90(4-5), 265-279.

Beyers, J.H.M., Sundsbø, P.A., Harms, T.M., 2004. Numerical simulation of three-dimensional, transient snow drifting around a cube. J. Wind Eng. Ind. Aerodyn. 92(9), 725-747.

Blazek, J., 2005. Principles and Applications (Second Edition). Elsevier Science. https://doi.org/10.1016/B978-008044506-9/50000-X

Bonhôte, P., Eperon, Y., Renaud, P., 2009. Unglazed coloured solar absorbers on façade: modelling and performance evaluation. Sol. Energy. 83(6), 799-811.

Browne, M.T.L., Gibbons, M.P.M., Gamble, S., Galsworthy, J., 2013. Wind loading on tilted roof-top solar arrays: the parapet effect. J. Wind Eng. Ind. Aerodyn. 123, 202-213.

Buonomano, A., De Luca, G., Figaj, R.D., Vanoli, L., 2015. Dynamic simulation and thermo-economic analysis of a PhotoVoltaic/Thermal collector heating system for an indoor-outdoor swimming pool. Energy Convers. Manag. 99, 176-192.

Burch, J., Christensen, C., Salasovich, J., Thornton, J., 2004. Simulation of an unglazed collector system for domestic hot water and space heating and cooling, in: Sol. Energy. 77(4), 399-406.

Burch, J., Salasovich, J., 2005. An assessment of unglazed solar domestic water heaters. Water. NREL/CP-550-37759.

Cao, J., Yoshida, A., Saha, P.K., Tamura, Y., 2013. Wind loading characteristics of solar arrays mounted on flat roofs. J. Wind Eng. Ind. Aerodyn. 123, 214-225.

Cebeci, T., & Bradshaw, P. (1977). Momentum transfer in boundary layers. New York, McGraw-Hill Book Co. Hemisphere Publishing Corp, Washington, DC.

Celik, I.B., Ghia, U., & Roache, P.J. 2008. Procedure for estimation and reporting of uncertainty due to discretization in CFD applications. Journal of fluids Engineering-Transactions of the ASME 130.

Chang, Y.P., 2010. Optimal the tilt angles for photovoltaic modules in Taiwan. International Journal of Electrical Power & Energy Systems, 32(9), pp.956-964.

Chaturvedi, S.K., Gagrani, V.D., Abdel-Salam, T.M., 2014. Solar-assisted heat pump – A sustainable system for low-temperature water heating applications. Energy Convers. Manag. 77, 550-557.

Chopra, K., Pathak, P.K., Samykano, M., Tyagi, V.V., Pandey, A.K., 2021. Recent advancements in design of flat plate solar collectors. IOP Conf. S. Mater. Sci. Eng. 1127(1).

Chyu, M.K., Natarajan, V., 1991. Local heat/iass transfer distributions on the surface of a wall-mounted cube. J. Heat Transf. 113(4), 851-857.

Dagnew, A.K., Bitsuamlak, G.T., 2013. Computational evaluation of wind loads on buildings: a review. Wind Struct. 16(6), 629-660.

Dean, J., McNutt, P., Lisell, L., Burch, J., Jones, D., & Heinicke, D. (2015). Photovoltaic-thermal new technology demonstration. National Renewable Energy Lab. (NREL), Golden, CO (United States).

Decker, B., Jahn, U., 1997. Performance of 170 grid connected PV plants in northern Germany – Analysis of yields and optimization potentials, in: Sol. Energy. 59(4-6), 127-133.

Defraeye, T., Blocken, B., Carmeliet, J., 2011. Convective heat transfer coefficients for exterior building surfaces: existing correlations and CFD modelling. Energy Convers. Manag. 52(1), 512-522.

Deploying renewables: principles for effective policies, 2011. Deploying Renew. Princ. Effect. Pol.

Duffie, J.A., Beckman, W.A., 2013. Solar engineering of thermal processes. 4th ed., Solar Engineering of Thermal Processes.

Eicker, U., Dalibard, A., 2011. Photovoltaic-thermal collectors for night radiative cooling of buildings. Sol. Energy. 85(7), 1322-1335.

Erge, T. et al., 1998. The German 1000-roofs-PV programme – a résumé of the 5 years pioneer project for small grid-connected PV systems, in: »Reliability« - Final Report.

Ferziger, J.H., & Perić, M. 1996. Computational methods for fluid dynamics. Springer Berlin.

Fleiter, T., Worrell, E., Eichhammer, W., 2011. Barriers to energy efficiency in industrial bottom-up energy demand models – a review. Renew. Sustain. Energy Rev. 15(6), 3099-3111.

Fluent Inc. 2009. Fluent 12.0 User's Guide. Lebabon.

Franke, J., Hellsten, A., Schlünzen, H., & Carissimo, B. 2007. Best practice guideline for the CFD simulation of flows in the urban environment. In COST action.

FSEC. Solar water and pool heating manual. Cocoa, Florida. Available at: http://www.nabcep.org/wp-content/uploads/2013/08/FSEC_Solar_Water_and_Pool_Heating_Manual.pdf, 2006.

Gimenez, J.M., Bre, F., 2019. Optimization of RANS turbulence models using genetic algorithms to improve the prediction of wind pressure coefficients on low-rise buildings. J. Wind Eng. Ind. Aerodyn. 193, 103978.

Gimenez, J.M., Bre, F., Nigro, N.M., Fachinotti, V., 2018. Computational modeling of natural ventilation in low-rise non-rectangular floor-plan buildings. Build. Simul. 11(6), 1255-1271.

Glick, A., Ali, N., Bossuyt, J., Calaf, M., Cal, R.B., 2020. Utility-scale solar PV performance enhancements through system-level modifications. Sci. Rep. 10(1), 10505.

Hagishima, A., Tanimoto, J., 2003. Field measurements for estimating the convective heat transfer coefficient at building surfaces. Build. Environ. 38(7), 873-881.

Hale, S.J.B., 1986. Methods of testing to determine the thermal performance of solar collectors. Ashrae.

Harrison, S.J., McClenahan, D., Nielsen, V.H., 1989. Testing unglazed solar collector thermal performance, in: Proceedings of the ISES solar world congress. Kobe, Japan, pp. 736-741.

Hawlader, M.N.A., Chou, S.K., Ullah, M.Z., 2001. The performance of a solar assisted heat pump water heating system. Appl. Therm. Eng. 21(10), 1049-1065.

Hu, C.-H., 2003. Proposed guidelines of using CFD and the validity of the CFD models in the numerical simulations of wind environments around buildings. Heriot-Watt University.

IRENA. OECD/IEA and REN21. Renewable energy policies in a time of transition:heating and cooling. Available at: https://www.irena.org/publications/2020/Nov/Renewable-Energy-Policies-in-a-Time-of-Transition-Heating-and-Cooling, 2020.

Ito, S., Miura, N., Wang, K., 1999. Performance of a heat pump using direct expansion solar collectors1Paper presented at the ISES Solar World Congress, Taejon, South Korea, 24–29 August 1997. Sol. Energy. 65(3), 189-196.

Jayamaha, S.E.G., Wijeysundera, N.E., Chou, S.K., 1996. Measurement of the heat transfer coefficient for walls. Build. Environ. 31(5), 399-407.

Jubayer, C.M., 2014. Wind and thermal effects on ground mounted photovoltaic (PV) panels. University of Western Ontario.

Jubayer, C.M., Hangan, H., 2014. Numerical simulation of wind effects on a stand-alone ground mounted Photovoltaic (PV) system. J. Wind Eng. Ind. Aerodyn. 134, 56-64.

Jürges, W., 1924. Der Wärmeübergang an einer ebenen Wand Beih. Zum Gesundh.−Ing, pp. 1227-1249.

Kahsay, M.T., Bitsuamlak, G., Tariku, F., 2017: Resilience of the Integrated Building - Proceedings of the Architectural Engineering National Conference. Numerical simulation of forced convective heat transfer coefficients on the facade of low- and high-rise buildings, in: AEI, p. 2017.

Kalogirou, S.A., 2004. Solar thermal collectors and applications. Prog. Energy Combust. Sci. 30(3), 231-295.

Kalogirou, S.A., Kalogirou, S.A., 2009. Chapter five – solar water Heating Systems, in: Solar energy engineering.

Karava, P., Jubayer, C.M., Savory, E., 2011. Numerical modelling of forced convective heat transfer from the inclined windward roof of an isolated low-rise building with application to photovoltaic/thermal systems. Appl. Therm. Eng. 31(11-12), 1950-1963.

Karava, P., Mohammad Jubayer, C., Savory, E., Li, S., 2012. Effect of incident flow conditions on convective heat transfer from the inclined windward roof of a low-rise building with application to photovoltaic-thermal systems. J. Wind Eng. Ind. Aerodyn. 104-106, 428-438.

Keller, J., 1985. Characterization of the thermal performance of uncovered solar collectors by parameters including the dependence on wind velocity, humidity and infrared sky radiation as well as on solar irradiance, in: Conference: 2. workshop on solar assisted heat pumps with ground coupled storage, Vienna, Austria, 8 May 1985. Switzerland, p. 34.

Kind, R.J., Gladstone, D.H., Moizer, A.D., 1983. Convective heat losses from flat-plate solar collectors in turbulent winds. J. Sol. Energy Eng. Trans. ASME. 105(1), 80-85.

Klevinskis, A., Bučinskas, V., 2012. Analysis Of A Flat-Plate Solar Collector / Plokščiojo Saulės Kolektoriaus Tyrimas ‘Analysis of a Flat-Plate Solar Collector’, Mokslas - Lietuvos ateitis. 3(6), 39-43.

Kondjoyan, A., Péneau, F., Boisson, H.C., 2002. Effect of high free stream turbulence on heat transfer between plates and air flows: a review of existing experimental results. Int. J. Therm. Sci. 41(1), 1-16.

Kopp, G.A., 2013. Wind loads on low profile, tilted, solar arrays placed on low-rise building roofs, in: Advances in Hurricane Engineering: learning from our past. Proceedings of the 2012 ATC and SEI conference on advances in Hurricane Engineering.

Kopp, G., Maffei, J., Tilley, C., 2011. Rooftop solar arrays and wind loading: A primer on using wind tunnel testing as a basis for code compliant design per ASCE; 7. Ontario, Canada. (No, N. 6A 5B9).

Kopp, G.A., Mans, C., Surry, D., 2005. Wind effects of parapets on low buildings: Part 2. Structural loads. J. Wind Eng. Ind. Aerodyn. 93(11), 843-855.

Kopp, G.A., Surry, D., Mans, C., 2005. Wind effects of parapets on low buildings: Part 1. Basic aerodynamics and local loads. J. Wind Eng. Ind. Aerodyn. 93(11), 817-841.

Kotu, V., Deshpande, B., 2019. Classification. Data Sci., 65-163.

Kramer, C., Gerhardt, H.J., Scherer, S., 1978. Wind pressure on block-type buildings, in: Proceedings, 4th Colloquium on Ind. Aerodynamic. West, Aachen Germany.

Kumar, S., Mullick, S.C., 2010. Wind heat transfer coefficient in solar collectors in outdoor conditions. Sol. Energy. 84(6), 956-963.

Kurokawa, K. et al., 1997. Extended performance analysis of 70 PV systems in Japanese field test program, in: Conf. Rec. IEEE Photovolt. Spec. Conf.

Ladas, D.I., Stathopoulos, T., Rounis, E.D., 2017. Wind effects on the performance of solar collectors on rectangular flat roofs: A wind tunnel study. J. Wind Eng. Ind. Aerodyn. 161, 27-41.

Launder, B. E., & Spalding, D. B. (1974). The numerical computation of turbulent flows. Computer Methods in Applied Mechanics and Engineering, 3, 269–289.

Leon, M.A., Kumar, S., 2007. Mathematical modeling and thermal performance analysis of unglazed transpired solar collectors. Sol. Energy. 81(1), 62-75.

Li, S., Karava, P., Savory, E., Lin, W.E., 2013. Airflow and thermal analysis of flat and corrugated unglazed transpired solar collectors. Sol. Energy. 91, 297-315.

Liu, Y., Harris, D.J., 2007. Full-scale measurements of convective coefficient on external surface of a low-rise building in sheltered conditions. Build. Environ. 42(7), 2718-2736.

Liu, Z., Yu, Z., Chen, X., Cao, R., Zhu, F., 2020. An investigation on external airflow around low-rise building with various roof types: PIV measurements and les simulations. Build. Environ. 169, 106583.

Loveday, D.L., Taki, A.H., 1996. Convective heat transfer coefficients at a plane surface on a full-scale building facade. Int. J. Heat Mass Transf. 39(8), 1729-1742.

Lu, Y., Gurgenci, H., Guan, Z., He, S., 2014. The influence of windbreak wall orientation on the cooling performance of small natural draft dry cooling towers. Int. J. Heat Mass Transf. 79, 1059-1069.

Lübcke, H., Schmidt, S., Rung, T., Thiele, F., 2001. Comparison of les and RANS in bluff-body flows. J. Wind Eng. Ind. Aerodyn. 89(14-15), 1471-1485.

Lund, P.D., 2009. Effects of energy policies on industry expansion in renewable energy. Renew. Energy. 34(1), 53-64.

Luthra, S., Kumar, S., Garg, D., Haleem, A., 2015. Barriers to renewable/sustainable energy technologies adoption: Indian perspective. Renew. Sustain. Energy Rev. 41, 762-776.

Lythe, G., Surry, D., 1983. Wind loading of flat roofs with and without parapets. J. Wind Eng. Ind. Aerodyn. 11(1-3), 75-94.

Mahesh, A., 2017. Solar collectors and adsorption materials aspects of cooling system. Renewable and Sustainable Energy Reviews, 73, pp.1300-1312.

Mans, C., Kopp, G.A., Surry, D., 2005. Wind effects of parapets on low buildings: Part 3. Parapet loads. J. Wind Eng. Ind. Aerodyn. 93(11), 857-872.

Manual, U. D. F. (2009). ANSYS FLUENT 12.0. Theory Guide, 67.

Martinez, R.G., Goikolea, B.A., Paya, I.G., Bonnamy, P., Raji, S., Lopez, J., 2017. Performance assessment of an unglazed solar thermal collector for envelope retrofitting, in: Energy Procedia. 115, 361-368.

Martinuzzi, R., Tropea, C., 1993. The flow around surface-mounted, prismatic obstacles placed in a fully developed channel flow: (Data bank contribution). J. Fluids Eng. Trans. ASME. 115(1), 85-92.

Matuška, T., Pokorný, N., Shemelin, V., 2019. Performance of unglazed photovoltaic-thermal collectors for cooling purpose, In IOP Conference Series. IOP Conf. Ser.: Earth Environ. Sci. 290(1).

Mathews, E.H., 1987, Prediction of the wind-generated pressure distribution around buildings, J. Wind Eng. Ind. Aerodyn., 25, 219-228.

McAdams, W.H., 1954. Heat transmission. 3rd ed. 3rd ed. Kogakusha, Tokyo, Japan. McGraw-Hill.

Medved, S., Arkar, C., Černe, B., 2003. A large-panel unglazed roof-integrated liquid solar collector-energy and economic evaluation. Sol. Energy. 75(6), 455-467.

Meinders, E.R., Hanjalic, K., Martinuzzi, R.J., 1999. Experimental study of the local convection heat transfer from a wall-mounted cube in turbulent channel flow. J. Heat Transf. 121(3), 564-573.

Menanteau, P., Finon, D., Lamy, M.L., 2003. Prices versus quantities: choosing policies for promoting the development of renewable energy. Energy Policy. 31(8), 799-812.

Mesalhy, O.M., Abdel Aziz, S.S., El-Sayed, M.M., 2010. Flow and heat transfer over shallow cavities. Int. J. Therm. Sci. 49(3), 514-521.

Mier-Torrecilla, M., Herrera, E., Doblaré, M., 2014. Numerical calculation of wind loads over solar collectors, in: Energy Procedia. 49, 163-173.

Mohtasham, J., 2015. Review article-renewable energies, in: Energy Procedia. 74, 1289-1297.

Molineaux, B., Lachal, B., Guisan, O., 1994. Thermal analysis of five outdoor swimming pools heated by unglazed solar collectors. Sol. Energy. 53(1), 21-26.

Mullick, S.C., Samdarshi, S.K., 1988. An improved technique for computing the top heat loss factor of a flat-plate collector with a single glazing. J. Sol. Energy Eng. Trans. ASME. 110(4), 262-267.

Nakamura, H., Igarashi, T., Tsutsui, T., 1999a. Local heat transfer around a wall-mounted cube. Trans.JSME B. 65(637), 3105-3110.

Nakamura, H., Igarashi, T., Tsutsui, T., 1999b. Local heat transfer around a wall-mounted cube (The case of the attack angle of 45 deg.). Trans.JSME B. 65(639), 3771-3776.

Nakamura, H., Igarashi, T., Tsutsui, T., 2001. Local heat transfer around a wall-mounted cube in the turbulent boundary layer. Int. J. Heat Mass Transf. 44(18), 3385-3395.

Nakamura, H., Igarashi, T., Tsutsui, T., 2003. Local heat transfer around a wall-mounted cube at 45° to flow in a turbulent boundary layer. Int. J. Heat Fluid Flow. 24(6), 807-815.

Natarajan, V., Chyu, M.K., 1993. Surface heat transfer of two cubes in tandem arrangement, in: American Society of Mechanical Engineers. Heat Transfer Division (Publication) HTD.

O'Hegarty, R., Kinnane, O., McCormack, S.J., 2016. Review and analysis of solar thermal facades. Sol. Energy. 135, 408-422.

Onur, N., 1993. Forced convection heat transfer from a flat-plate model collector on roof of a model house. Wärme Stoffübertragung. 28(3), 141-145.

Oosthuizen, P.H., Naylor, D., 1999. Introduction to convective heat transfer analysis. McGraw-Hill, New York.

Palyvos, J.A., 2008a. "A survey of wind convection coefficient correlations for building envelope energy systems" modeling. Appl. Therm. Eng. 28(8-9), 801-808.

Pandey, K.M., Chaurasiya, R., 2017. A review on analysis and development of solar flat plate collector. Renew. Sustain. Energy Rev. 67, 641-650.

Ragheb, M. Solar thermal power, and energy storage. Available at: http://www.solarthermalworld.org/sites/gstec/files/story/2015-04-18/solar_thermal_power_and_energy_storage_historical_perspective.pdf, 2014.

Ramponi, R., & Blocken, B. 2012a. CFD simulation of cross-ventilation for a generic isolated building: impact of computational parameters. Building and Environment 53, 34–48.

Ramponi, R., & Blocken, B. 2012b. CFD simulation of cross-ventilation flow for different isolated building configurations: validation with wind tunnel measurements and analysis of physical and numerical diffusion effects. Journal of Wind Engineering and Industrial Aerodynamics 104, 408–418.

Ratner, B., 2009. The correlation coefficient: its values range between 1/1, or do they. J. Target. Meas. Anal. Mark. 17(2), 139-142.

REN21, 2021 Renewables 2021 global status report. Paris.

Reiter, S. (2010). Assessing wind comfort in urban planning. Environment and Planning B: Planning and Design, 37(5), 857-873.

Richards, P.J., Fong, S., Hoxey, R.P., 1997. Anisotropic turbulence in the atmospheric surface layer. J. Wind Eng. Ind. Aerodyn. 69-71, 903-913.

Richards, P.J., Hoxey, R.P., 1992. Computational and wind tunnel modelling of mean wind loads on the Silsoe structures building. J. Wind Eng. Ind. Aerodyn. 43(1-3), 1641-1652.

Richards, P.J., Hoxey, R.P., 1993. Appropriate boundary conditions for computational wind engineering models using the k-ϵ turbulence model. J. Wind Eng. Ind. Aerodyn. 46-47, 145-153.

Richards, P.J., Hoxey, R.P., Connell, B.D., Lander, D.P., 2007. Wind-tunnel modelling of the Silsoe Cube. J. Wind Eng. Ind. Aerodyn. 95(9-11), 1384-1399.

Richards, P. J., & Norris, S. E. (2015). Appropriate boundary conditions for a pressure driven boundary layer. Journal of Wind Engineering and Industrial Aerodynamics, 142, 43-52. doi:10.1016/j.jweia.2015.03.003

Rodi, W., 1997. Comparison of les and RANS calculations of the flow around bluff bodies. J. Wind Eng. Ind. Aerodyn. 69-71, 55-75.

Roache, P.J. 1994. Perspective: a method for uniform reporting of grid refinement studies. Journal of fluids Engineering-Transactions of the ASME 116, 405–405.

Roache, P.J. 1997. Quantification of uncertainty in computational fluid dynamics. Annual Review of Fluid Mechanics 29, 123–160.

Roache, P.J., Ghia, K.N., & White, F.M. 1986. Editorial policy statement on the control of numerical accuracy. Journal of Fluids Engineering 108, 2.

Sartori, E., 2006. Convection coefficient equations for forced air flow over flat surfaces. Sol. Energy. 80(9), 1063-1071.

Sau, A., Hwang, R.R., Sheu, T.W., Yang, W.C., 2003. Interaction of trailing vortices in the wake of a wall-mounted rectangular cylinder. Phys. Rev. E Stat. Nonlin. Soft Matter Phys. 68(5 Pt 2), 056303.

Schlipf, M., Tismer, A., Riedelbauch, S., 2016. On the application of hybrid meshes in hydraulic machinery CFD simulations, In IOP Conference Series. IOP Conf. Ser.: Earth Environ. Sci. 49(6).

Seeta Ratnam, G., Vengadesan, S., 2008. Performance of two equation turbulence models for prediction of flow and heat transfer over a wall mounted cube. Int. J. Heat Mass Transf. 51(11-12), 2834-2846.

Sen, S., Ganguly, S., 2017. Opportunities, barriers and issues with renewable energy development – A discussion. Renew. Sustain. Energy Rev. 69, 1170-1181.

Sharples, S., Charlesworth, P.S., 1998. Full-scale measurements of wind-induced: convective heat transfer from a roof mounted flat plate solar collector. Sol. Energy. 62(2), 69-77.

Shih, T.H., Liou, W.W., Shabbir, A., Yang, Z., Zhu, J., 1995. A new k-ϵ eddy viscosity model for high Reynolds number turbulent flows. Comput. Fluids. 24(3), 227-238.

Simiu, E., 2011. Design of Buildings for Wind: A Guide for ASCE 7–10 Standard Users and Designers of Special Structures (2nd ed.). Wiley. https://doi.org/10.1002/9781118086131

Smith, B.L., 2017. The difference between traditional experiments and CFD validation benchmark experiments. Nucl. Eng. Des. 312, 42-47.

Soltau, H., 1992a. Testing the thermal performance of uncovered solar collectors. Sol. Energy. 49(4), 263-272.

Sopian, K., Syahri, M., Abdullah, S., Othman, M.Y., Yatim, B., 2004. Performance of a non-metallic unglazed solar water heater with integrated storage system. Renew. Energy. 29(9), 1421-1430.

Sparrow, E.M., Niethammer, J.E., Chaboki, A., 1982. Heat transfer and pressure drop characteristics of arrays of rectangular modules encountered in electronic equipment. Int. J. Heat Mass Transf. 25(7), 961-973.

Sparrow, E.M., Ramsey, J.W., Mass, E.A., 1979. Effect of finite width on heat transfer and fluid flow about an inclined rectangular plate. J. Heat Transf. 101(2), 199-204.

Sparrow, E.M., Tien, K.K., 1977. Forced convection heat transfer at an inclined and yawed square plate—application to solar collectors. J. Heat Transf. 99(4), 507-512.

Stankovic, S., Campbell, N., Harries, A., 2009. Urban wind energy. Routledge, London.

Stathopoulos, T., Baskaran, A., 1988. Turbulent wind loading of roofs with parapet configurations. Can. J. Civ. Eng. 15(4), 570-578.

Standard, A.S.H.R.A.E., 1987. Methods of testing to determine the thermal performance of solar collectors. ANSI/ASHRAE, pp.93-1986.

Stathopoulos, T., Marathe, R., Wu, H., 1999. Mean wind pressures on flat roof corners affected by parapets: field and wind tunnel studies. Eng. Struct. 21(7), 629-638.

Stathopoulos, T., Saathoff, P., Du, X., 2002. Wind loads on parapets. J. Wind Eng. Ind. Aerodyn. 90(4-5), 503-514.

Stathopoulos, T., Zisis, I., Xypnitou, E., 2014. Local and overall wind pressure and force coefficients for solar panels. J. Wind Eng. Ind. Aerodyn. 125, 195-206.

Tamura, Y. Aerodynamic database for low-rise buildings. Japan. Available at: http://www.wind.arch.t-kougei.ac.jp/system/contents/code/tpu, 2012.

Test, F.L., Lessmann, R.C., Johary, A., 1981. Heat transfer during wind flow over rectangular bodies in the natural environment. J. Heat Transf. 103(2), 262-267.

Tian, Y., Zhao, C.Y., 2013. A review of solar collectors and thermal energy storage in solar thermal applications. Appl. Energy. 104, 538-553.

Tickoo, S. (2021). ANSYS Workbench 2021 R1: A Tutorial Approach.

Tien, K.K., Sparrow, E.M., 1979. Local heat transfer and fluid flow characteristics for airflow oblique or normal to a square plate. Int. J. Heat Mass Transf. 22(3), 349-360.

Tyagi, H., Phelan, P., Prasher, R., 2009. Predicted efficiency of a low-temperature nanofluid-based direct absorption solar collector. J. Sol. Energy Eng. 131(4).

Van Helden, W.G.J., Van Zolingen, R.J.C., Zondag, H.A., 2004. PV Thermal systems: PV panels supplying renewable electricity and heat. Prog. Photovolt. Res. Appl. 12(6), 415-426.

Vidal, O., Goffé, B., & Arndt, N., 2013. Metals for a low-carbon society. Nature Geoscience, 6, 894–896. https://doi.org/10.1038/ngeo1993

Wang, J., Van Phuc, P., Yang, Q., Tamura, Y., 2020. LES study of wind pressure and flow characteristics of flat-roof-mounted solar arrays. J. Wind Eng. Ind. Aerodyn. 198.

Wang, J., Yang, Q., Hui, Y., 2021. Comparisons of design wind pressures on roof-mounted solar arrays between wind tunnel tests and codes and standards. Adv. Struct. Eng. 24(4), 653-666.

Wang, J., Yang, Q., Tamura, Y., 2018. Effects of building parameters on wind loads on flat-roof-mounted solar arrays. J. Wind Eng. Ind. Aerodyn. 174, 210-224.

Wattmuff, J.H., E.a., 1977. Solar and wind induced external coefficient for solar collectors. Cooperation Mediterraneenne pour I'Energue Solaire, Revue Internationale d'Heliotechnique, 2nd Quarter.

Willemsen, E., Wisse, J.A., 2002. Accuracy of assessment of wind speed in the built environment. J. Wind Eng. Ind. Aerodyn. 90(10), 1183-1190.

Wright, N. G., & Hargreaves, D. M. (2006). Unsteady CFD Simulations for natural ventilation. International Journal of Ventilation, 5, 13–20.

Xu, H., Deng, Y., 2017. Dependent evidence combination based on Shearman coefficient and Pearson coefficient. IEEE Access. 6, 11634-11640.

Xypnitou, E., 2012. Wind Loads on Solar Panels attached to Builing Roofs. Concordia University.

Yaqoot, M., Diwan, P., Kandpal, T.C., 2016. Review of barriers to the dissemination of decentralized renewable energy systems. Renew. Sustain. Energy Rev. 58, 477-490.

Yazdanian, M., Klems, J.H., 1994. Measurement of the exterior convective film coefficient for windows in low-rise buildings, in: ASHRAE Trans.

Zhang, L., Zhang, N., Zhao, F., Chen, Y., 2004. A genetic-algorithm-based experimental technique for determining heat transfer coefficient of exterior wall surface. Appl. Therm. Eng. 24(2-3), 339-349.

Zhang, Z., Xu, F., 2020. Spanwise length and mesh resolution effects on simulated flow around a 5:1 rectangular cylinder. J. Wind Eng. Ind. Aerodyn. 202.

Zhou, H., Deng, Z., Xia, Y., Fu, M., 2016. A new sampling method in particle filter based on Pearson correlation coefficient. Neurocomputing. 216, 208-215.

Zhu, H., 2009. Technical handbook for solar heat supply & space heating. Beijing (Chinese).

Zomer, C., Custódio, I., Goulart, S., Mantelli, S., Martins, G., Campos, R., Pinto, G. and Rüther, R., 2020. Energy balance and performance assessment of PV systems installed at a positive-energy building (PEB) solar energy research centre. Solar Energy, 212, pp.258-274.

Appendices

Appendix A: Mesh independence study

To ensure the accuracy of modeled mesh and obtained results, mesh independence study is done based on Roche grid independence approach.

Modeling and boundary conditions

Overall circular grid is generated with building model in the center. Upfront half of far-field domain serving as fluid inlet and rear half given outlet boundary condition. Boundary conditions for inlet are defined using **user defined function**. Here, the Inlet x_velocity, turbulent kinetic energy and turbulent dissipation rate parameter defined via UDF are calculated based on logarithmic boundary layer function, turbulence kinetic energy and dissipations rate characteristic equations respectively. Outlet boundary condition is defined as constant gauge pressure of $0Pa$. All the collector plates are maintained at 328K (55ºC) with an ambient temperature of 298K (25ºC)

Subsequently a total of nine meshes are made for main case studies. Details pertaining to each case are provided in the later sections. Overall cases differences in grid modeling are listed as follows.

Case 01 – Three building models without any collector plate placed on roof.

Case 02 – Three building models with single collector plate on roof.

Case 03 – Three building models with array of 06 collector plates placed on roof.

Results of the area average pressure at building front, area weighted average wall shear at the building roof including parapet and heat flux from the collector plates (in cases where collector plates are employed) are used as the simulation output parameters. Pertaining to flow visualization, contours of pressure and wall shear around the building are presented. Flow orientation is demonstrated with the help of 3-D streamlines. Further explanation along with quantitative differences are outlined as follows.

Roofs with no collector present

Baseline case setup is generated without any collector plate over building roof, a total of three case variants with different mesh density are made. Details for the respective cases are in Table 4.

Table 4 Element cell counts for meshes made for mesh independence study of case-01.

Mesh Setting	***Mesh count***
Coarse	199373
Medium	412844
Fine	748506

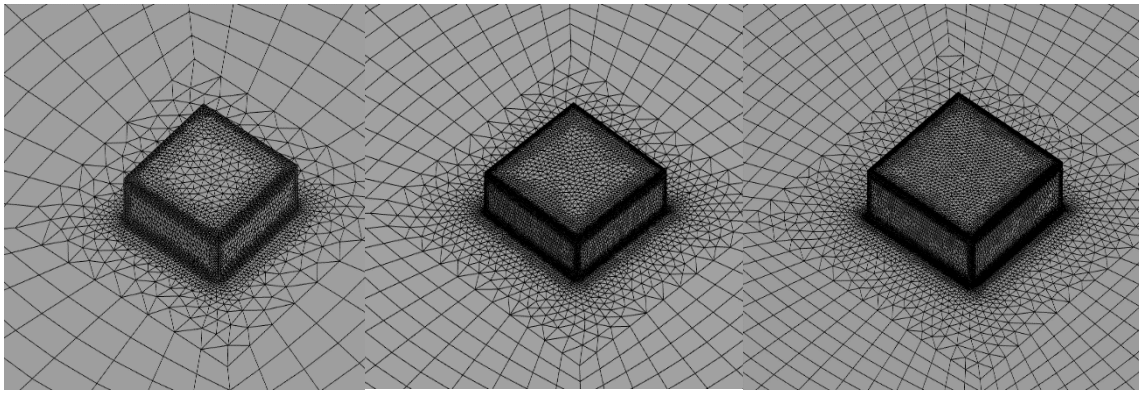

(a) Coarse Mesh *(b) Medium Mesh* *(c) Fine mesh*

Figure 141: Mesh density variations for No collector plate over building roof

Steady state simulations done using the above derivatives of case-01 meshes provide the following results. Area average pressure at building front and area averaged wall shear at building roof are the parameters under focus and listed in Table 5.

Table 5 Simulation results for No collector plate simulation results

Output Parameter	*Coarse mesh*	*Medium mesh*	*Fine mesh*
Area average pressure at building windward surface (Pa)	28.8589	29.0869	29.2001
Area average wall shear at building roof surface (Pa)	0.0550	0.0536	0.05413

Table 6 Percentage difference between different mesh density results

Output parameter	***% Diff. b/w coarse and medium mesh***	***% Diff. b/w medium and fine mesh***
Area average pressure at building windward surface	0.7906 %	0.3887 %

Area average wall shear at building roof surface	2.4380 %	0.8487 %

A comparative analysis of the results reveals that the percentage difference in front wall static pressure between the coarse, medium, and fine mesh is not statistically significant. However, a significantly larger disparity is observed in the building roof wall shear value, approximately 2.5%, between the results obtained using coarse and medium mesh sizes. Therefore, in accordance with the spatial convergence criteria proposed by Roache (1997) and the Richardson extrapolation method described by Williams and Umeel (2002), it can be concluded that the Medium Mesh density grid, consisting of 0.41 million cells, which yields a percent difference of less than or equal to 1%, is the most optimised configuration for simulating the building without a collector or parapet present.

Visual depiction of the focused output parameters is undertaken using contour plots, and flow orientation is depicted using 3-D streamline. The following figure shows the simulation results with medium mesh density setting.

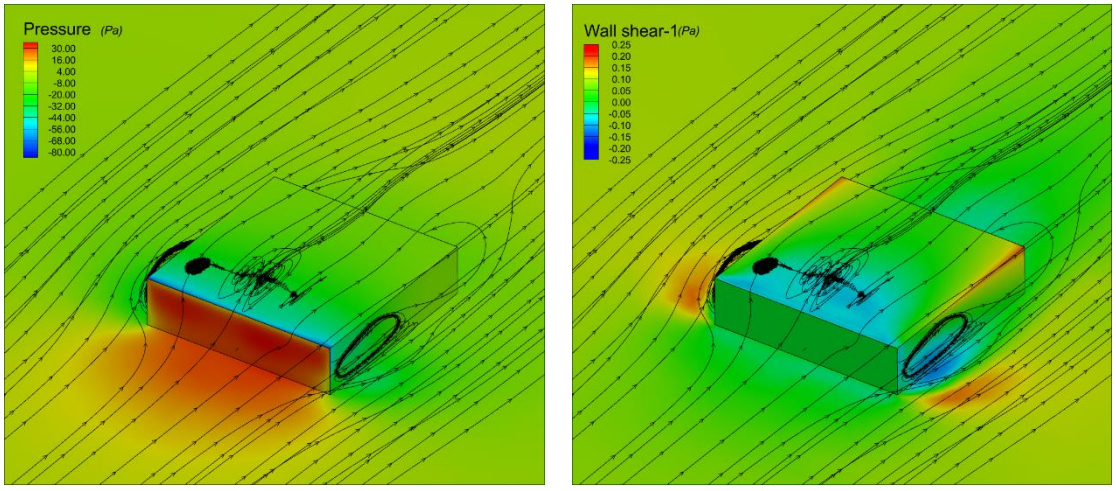

(a) *(b)*

Figure 142: (a)Pressure and (b) wall shear contours along with streamlines for no collector plate case

Roofs with standalone collector

Similar to the above case, three grids with different mesh densities were created for Case-02, which involves a standalone collector positioned on the roof of a building. Similarly, the Energy equations were used to conduct a comprehensive analysis of the thermal parameters. In relation

to the boundary conditions, the collector plate is subjected to a constant temperature of 328K (55°C). This analysis considers the result parameters of the total area weighted average of pressure at the building's windward surface, roof surface , including the parapet, and the surface heat flux over the collector plates.

Details regarding the different meshes for mesh independence study for single collector plate case are provided in Table 7. Subsequently the visual demonstration of different mesh densities is as shown in Figure 143.

Table 7 Element cell counts for meshes made for mesh independence study of case-02

Mesh Setting	***Mesh count***
Coarse	335181
Medium	965024
Fine	2205054

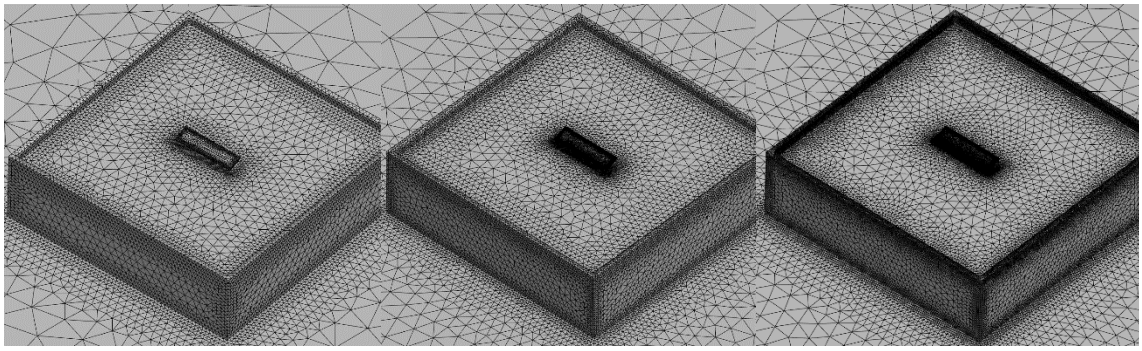

(a) Coarse Mesh *(b) Medium Mesh* *(c) Fine Mesh*

Figure 143: Single collector plate various mesh densities for grid independence study

Steady state simulations using k-ε realizable turbulence model, including active energy model yields the results shown Table 8.

Table 8 Simulation results for Single collector plate over building roof

Output parameter	***Coarse mesh***	***Medium mesh***	***Fine mesh***
Area avg pressure at building windward surface (Pa)	31.0529	30.6641	30.7703
Area avg wall shear at parapet and building roof (Pa)	0.0492	0.0476	0.0478
Heat flux at collector plate (W/m2)	9291.5	9395.67	9476.6

The percentage difference between the Coarse, Medium and fine mesh results are as shown in Table 9.

Table 9 Percentage difference between different mesh density results

Output parameter	***% Diff. b/w coarse and medium mesh***	***% Diff. b/w medium and fine mesh***
Area avg pressure at building windward surface (Pa)	1.25 %	0.35 %
Area avg wall shear at parapet and building roof (Pa)	3.35%	0.44 %
Heat flux at collector plate (W/m2)	1.12 %	0.86%

Following Roache's grid independence study criteria outlined in Roache (1997) and employing the Richardson extrapolation method as described by Williams and Umeel (2002), the optimal mesh count for the current scenario is determined to be 0.96M mesh elements for the scenario with the standalone collector. This mesh count yields an overall percentage difference of ≤1% in output results (including pressure, wall shear, and heat rate) when compared to a grid with 2.29 times finer resolution, consisting of 2.2M mesh elements. Figure 144 presents the flow visualization for this optimized case.

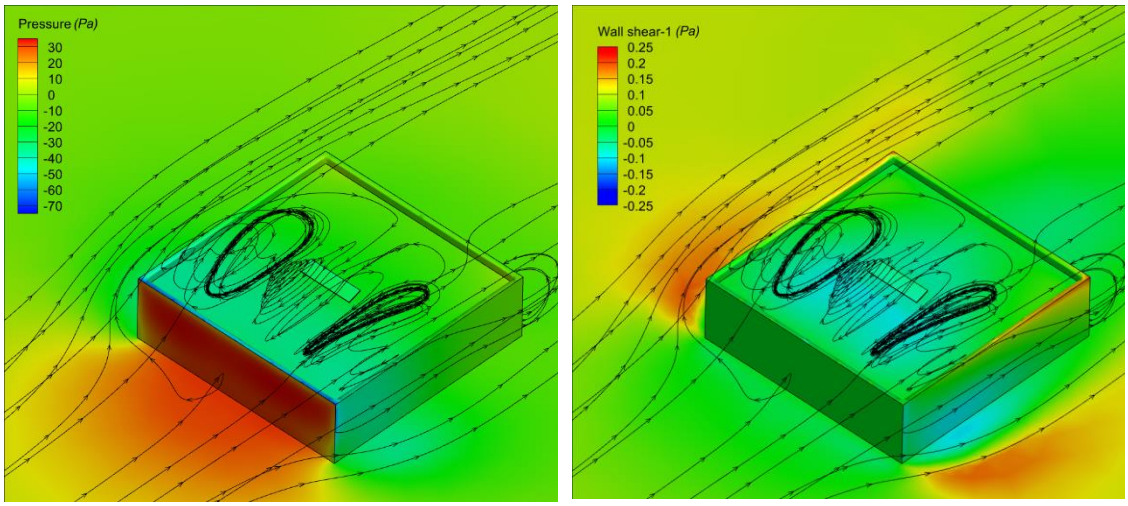

(a) *(b)*

Figure 144 (a) Pressure and (b) Wall shear along with streamlines for single collector plate case medium density mesh

Analysis for collector array

A set of six rows of collector plates are positioned atop the roof of the building, where they are subjected to a consistent temperature of 328 Kelvin. Three distinct meshes are created in a

sequential manner, with each mesh having a higher density than the previous one. Table 10 provides the specific mesh count details, while Figure 145 offers a visual representation of the aforementioned information.

Table 10 Mesh counts for Case - 03 grid independence study.

Mesh Setting	***Mesh Count***
Coarse	742535
Medium	1542657
Fine	2632897

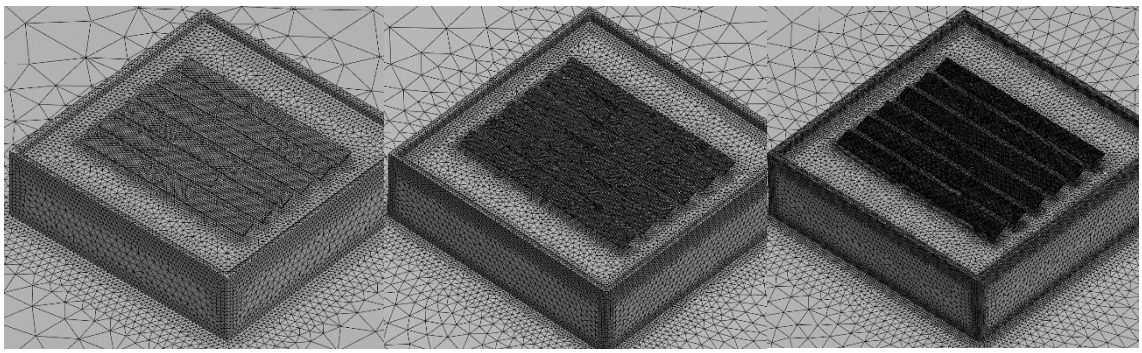

(a) Coarse Mesh *(b) Medium Mesh* *(c) Fine Mesh*

Figure 145: Different mesh densities made array arrangement of 06 collector plates.

Steady simulations with collector plates assigned constant temperature of 328K (55ºC), provides the following results in Table 11.

Table 11 Simulation results for array arrangement of collector plates

Output Parameters	***Coarse mesh***	***Medium mesh***	***Fine mesh***
Area avg pressure at the windward surface of the building front (Pa)	30.4	30.8	30.8
Area avg wall shear on parapet and building roof (Pa)	0.0558	0.0426	0.0420
Heat transfer of last collector plate (W/m2)	18741.9	18804.3	19124.8

The quantitative analysis of results is done to compute the difference between the result of different mesh density cases. Respective percentage differences are provided in the Table 12. Detailed examination shows very profound difference between the area average wall shear results between the coarse and medium mesh density results.

Table 12 Percentage difference between different mesh density results

Output parameter	*% Diff. b/w coarse and medium mesh*	*% Diff. b/w medium and fine mesh*
Area avg pressure @ building front	1.5%	0.6 %
Area avg wall shear @ building roof	23.5 %	1.5 %
Heat Transfer @ last collector plate	0.3 %	1.7 %

In the case of collector plates array, a very profound difference in wall shear value at building roof is seen between coarse and medium density meshes. In conformity with Roache's mesh independence criteria Roache (1997) and the Richardson extrapolation method described by Williams and Umeel (2002), medium mesh density case setup of 1.54M cell count provides percentage difference of ≤ 1.8% comparing to 1.7-time denser mesh density setup, proves to be most effective mesh density configurations.

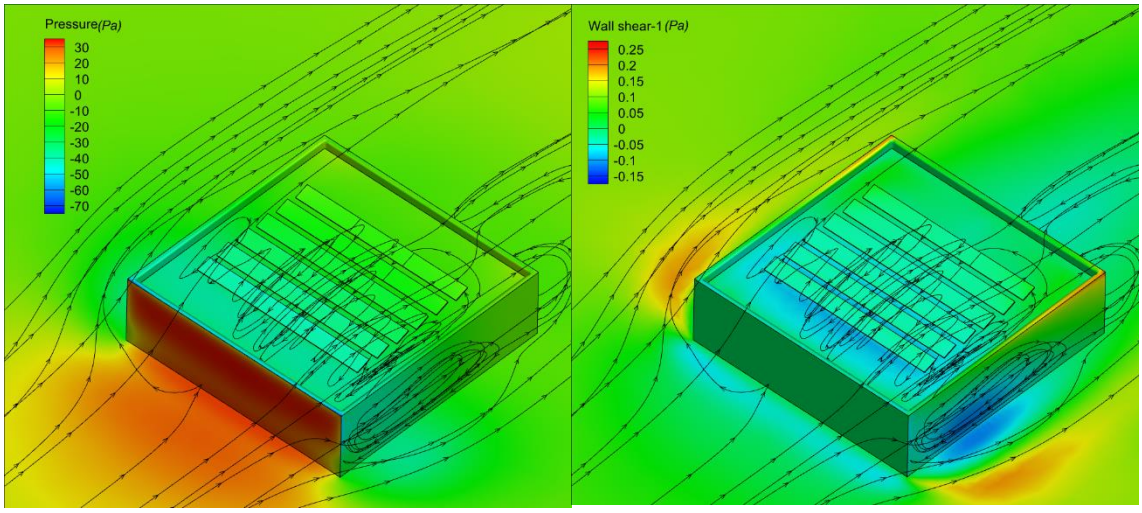

(d) (a) *(e) (b)*

Figure 146 (a) Pressure and (b) Wall shear contours along with streamlines of Collector Plates in array case

Based on the findings of the mesh independence study, it can be inferred that the medium mesh density scenarios, specifically Case-01 (lacking a collector plate), Case-02 (featuring a solitary collector plate on the building roof), and Case-03 (comprising an array of six collector plates on the building surface), demonstrate more advantageous results in terms of optimisation. Moreover, the discrepancy observed in the simulation results between the scenarios with medium and fine mesh densities does not demonstrate a significant magnitude that warrants the computational resources required for fine mesh density simulations.

Appendix B Boundary Conditions and User Defined Function

B1. Boundary Condition

The placement of the inflow and outflow boundary conditions is recommended to be at a distance of 20H from the building, as suggested by Franke *et al.*, in 2007. In order to achieve a more uniform and realistic simulation, fully developed profiles should be implemented at the inlet. In order to accomplish this, two commonly employed techniques in computational fluid dynamics (CFD) are utilised. One approach is to conduct a precursor simulation within a periodic domain in order to generate fully developed profiles for the main simulation, ensuring that the coordinates align appropriately, as depicted in Figure 147. The second approach involves the utilisation of theoretical equations, such as the parabolic profile equation or power law equation, for the purpose of interpolating at the inlet.

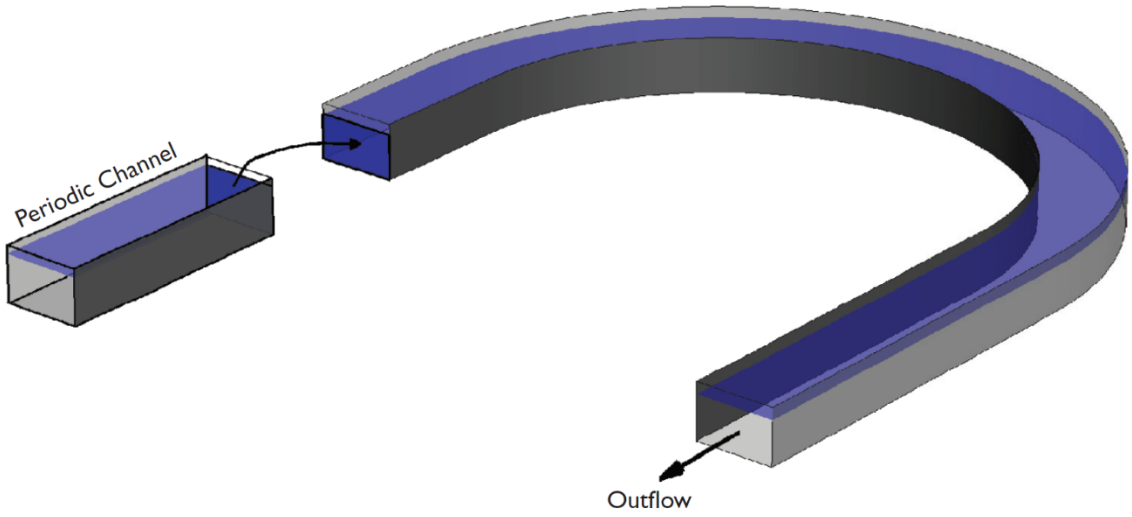

Figure 147: Pre-cursor simulation performed in an upstream periodic channel to generate realistic inflow velocities for the flow in an open-channel through a 180° bend, by (Rodi, 1997)

In this study, it is necessary to have the values of U, T, k, and epsilon at the inlet, as determined by the solutions to the governing equations. Nevertheless, the initial approach is rendered impractical as a result of the semicircular configuration of the inlet. This is due to the requirement for the periodic profiles obtained during the precursor simulation to possess corresponding coordinates with the inlet of the main simulation. Consequently, theoretical equations are utilised. It is assumed that temperature profiles exhibit uniformity and are equivalent to the ambient air temperature. The equations formulated by Richards and Hoxey (1993) for the representation of

the atmospheric boundary layer (ABL) in k-models have been selected for the remaining variables and incorporated into the ANSYS Fluent solver through the utilisation of User-Defined Functions (UDF). The equations can be expressed as follows:

$$U = \frac{u_\tau}{\mathrm{K}} \ln\left(\frac{Y + Y_0}{Y_0}\right) \quad 27$$

$$k = \frac{{u_\tau}^2}{\sqrt{C_\mu}} \quad 18$$

$$\epsilon = \frac{{u_\tau}^3}{K(Y + Y_0)} \quad 29$$

Y is the direction normal to the wall and Y_0 is the surface roughness length. The von Karman constant κ is equal to 0.41 and C_μ is equal to 0.09. The friction velocity is calculated from a reference velocity U_{ref}=2.5,5,10 m/s at a reference location Y_{ref} =3.5.

$$u_\tau = \mathrm{K}\frac{U_{ref}}{\ln((Y_{ref} + Y_0)/Y_0))} \quad 30$$

There is a need to ensure homogeneity of the approaching flow. To accomplish this, a modified velocity and turbulence profile associated with a $k - \varepsilon$ turbulence model proposed by Richards and Hoxey (1993), and later Richard and Norris (2015) to represent the Atmospheric Boundary Layer (ABL) were applied on the ANSYS Fluent solver via User-Defined Functions (UDF). Richards and Hoxey (1993) proposed that the inflow profile must be expressed in terms of velocity profile (U), turbulent kinetic energy (k), and its dissipation rate (ϵ) as shown in equations 27 to 30.

To make the simulations more homogeneous, the equations are adjusted based on numerical values obtained from a precursor simulation in a cyclic domain Figure 147 with dimensions H x 9H x H and 4 x 160 x 4 cells in the streamwise, normal to the wall, and spawnwise directions, respectively. For a mean wind speed of 10 m/s, the first cell centroid from the wall was placed at y+ <1, ensuring numerical integration of the viscous sublayer even at lower analysed wind speeds. The top boundary condition is symmetrical, and the streamwise and spawnwise normal planes have periodic boundary conditions. A constant mean wind speed value drives the flow.

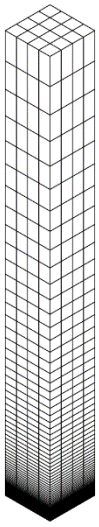

Figure 148 : Periodic domain used to obtain fully developed numerical profiles.

The mean wind speed of 10 m/s was selected as U_{ref} value, and through linear interpolation the corresponding Y_{ref} was obtained, equal to 3.5 m. The roughness length value Y_0 is obtained by trial and error, guessing values close to 0, once smooth walls are assumed, and finding Y_0= 0.0001 a good fit, as shown in Figure 149.

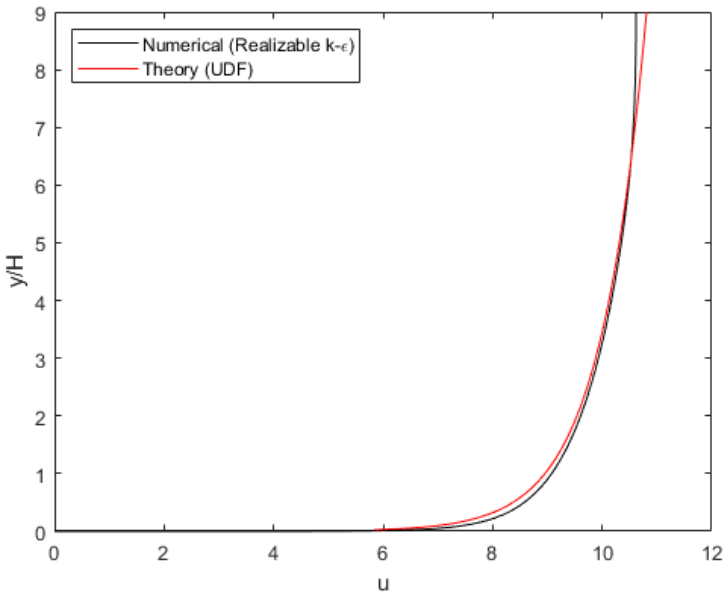

Figure 149: Comparison between fully developed velocity profiles obtained with a numerical simulation and theory for mean wind speed of 10 m/s.

The turbulent kinetic energy profile does not depend on Y and returns a constant value. For values of U_{ref}, Y_{ref} and Y_0 proposed, Equation 28 returns k = 0.4 m2/s2, which is close to the maximum

value of the periodic profiles, of k = 0.28 m2/s2. The eddy dissipation ε profiles in equation 29 for the selected values are shown in Figure 150, also showing good agreement with the numerical values.

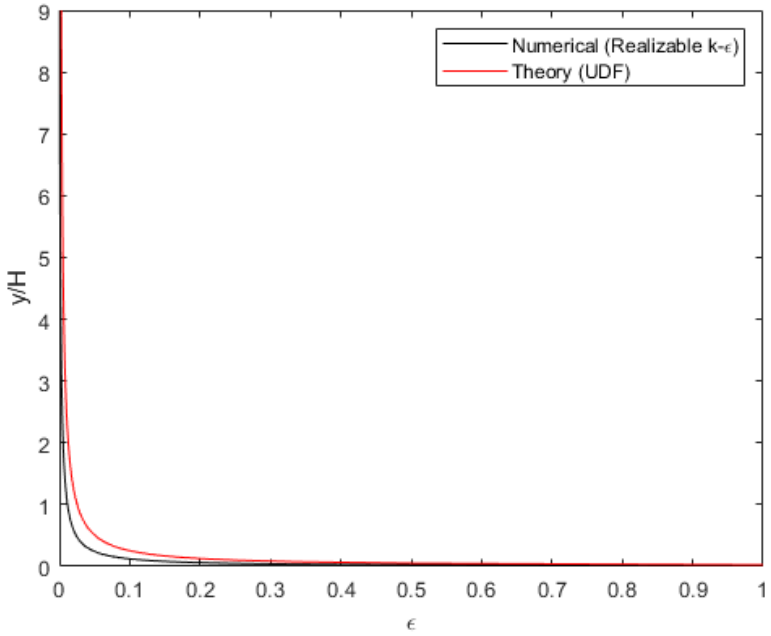

Figure 150: Comparison between fully developed ε profiles obtained with a numerical simulation and theory for mean wind speed of 10 m/s.

For wind speeds of 2.5 and 5 m/s, the use of the values Y_{ref} = 3.5 and Yo = 0.0001 in the theoretical equations also showed good agreement with the corresponding U, k and ε numerical profiles. The velocity theoretical and numerical velocity profiles for 2.5 and 5 m/s are Compared to the numerical values Figure 151 and Figure 152.

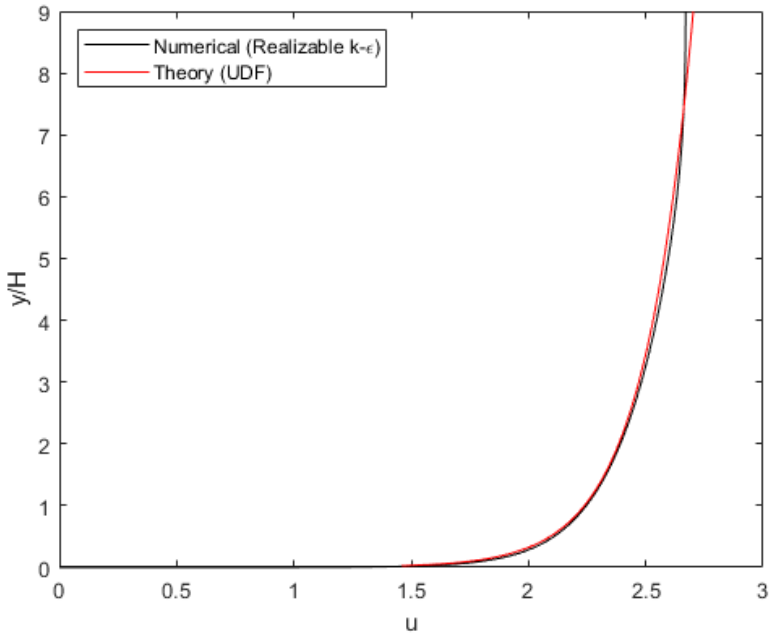

Figure 151: Comparison between fully developed velocity profiles obtained with a numerical simulation and theory for mean wind speed of 2.5 m/s.

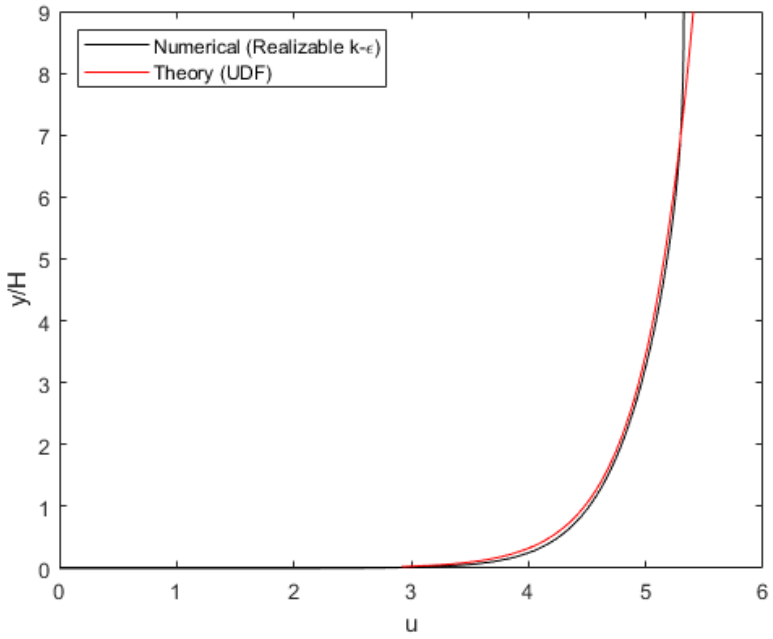

Figure 152: Comparison between fully developed velocity profiles obtained with a numerical simulation and theory for mean wind speed of 5 m/s.

The SIMPLE method is used to solve the pressure-velocity coupling and the pressure is interpolated from the cell centroid to the cell faces through a central differencing scheme (second order). A second order (linear) upwind scheme is used to interpolate the convective terms of momentum, pressure correction, turbulence and energy equations and a central differencing is

used to calculate the diffusive terms. The gradients are computed through the least squares method. The default under-relaxation factors of the SIMPLE algorithm for each equation are: 0.3 for pressure correction, 0.7 for momentum, 0.8 for turbulence and 0.9 for energy. In this work, a value of 0.2 was used for pressure and 0.5 for density, momentum, turbulence and energy to guarantee solution stability and convergence in extreme cases, with high angle of attack, high blowing and Mach equal to 0.8. In most cases, solution stability is only achieved by obtaining a previous converged solution through the use of an upwind scheme for density (pressure correction equation). Flow derived quantities, such as drag and lift, were monitored throughout the iterative process to identify solution convergence.

B.2: User Defined Function Based On Equation in Appendix B1

```
#include "udf.h"
#define kappa 0.41
#define C_mu 0.09
#define y_0 0.0001
#define y_ref 3.5
#define u_ref 2.5,5,10
DEFINE_PROFILE(x_velocity,t,i)
{
        face_t f;
        real u_tau, x[ND_ND], y;
        u_tau = kappa*u_ref/log((y_ref+y_0)/y_0);
        begin_f_loop(f,t)
 {
                F_CENTROID(x,f,t);
                y = x[1];
                F_PROFILE(f,t,i) = u_tau/kappa*log((y+y_0)/y_0);
 }
        end_f_loop(f,t)
}
DEFINE_PROFILE(k_profile,t,i)
{
        face_t f;
        real u_tau, x[ND_ND], y;

        u_tau = kappa*u_ref/log((y_ref+y_0)/y_0);
        begin_f_loop(f,t)
 {
                F_CENTROID(x,f,t);
                y=x[1];
                F_PROFILE(f,t,i) = pow(u_tau,2.0)/sqrt(C_mu);
 }
        end_f_loop(f,t)
}
DEFINE_PROFILE(dissip_profile,t,i)
{
        face_t f;
        real u_tau, x[ND_ND], y;
        u_tau = kappa*u_ref/log((y_ref+y_0)/y_0);
        begin_f_loop(f,t)
 {
                F_CENTROID(x,f,t);
                y=x[1];
                F_PROFILE(f,t,i) = pow(u_tau,3.0)/(kappa*(y+y_0));
 }
        end_f_loop(f,t)
}
```

Appendix C: Validation

C.1 Validation of pressure coefficient on flat roof

Validation of the simulation results were carried out against results from the Wind Engineering Information Center of Tokyo Polytechnic University (TPU) (Tamura, 2012) for a flat-roofed low-rise building. This was carried out at a wind speed of 22m/s at a height of 10m, and wind incidences of 0° and 45°. No information about air temperature was provided from the TPU database, so air properties at 25°C were assumed. Simulations were carried out based on grid sensitivity approach outlined in Appendix A.

All the three meshes created for the sensitivity analyses were based on a (wind speed of 10m/s at a height of 3.5 m), where the distance of first cell centroids from the wall was controlled in order to match the wall treatment requirements. The maximum values of y+ resulting from these simulations was around 500. The pressure coefficient values from the simulation were compared against the results from the TPU database. To match the TPU results, reference values of freestream density, pressure and velocity were obtained on the inlet boundary at a height of 4m (building height).

Since the flow in this study was simulated under a steady state approach, the results were compared against TPU mean results only. Contours and area averaged values for each one of the five building surfaces, numbered as shown in Figure 153 and Figure 154 were compared. Contours from TPU and the current work validation are shown below. To allow for an accurate comparison between the results, the same rainbow color map was used, ranging from blue to red, and having 11 different colours of contours. The area averaged pressure coefficient values for each of the surfaces for 0° and 45° are shown in Table 13 and Table 14, respectively.

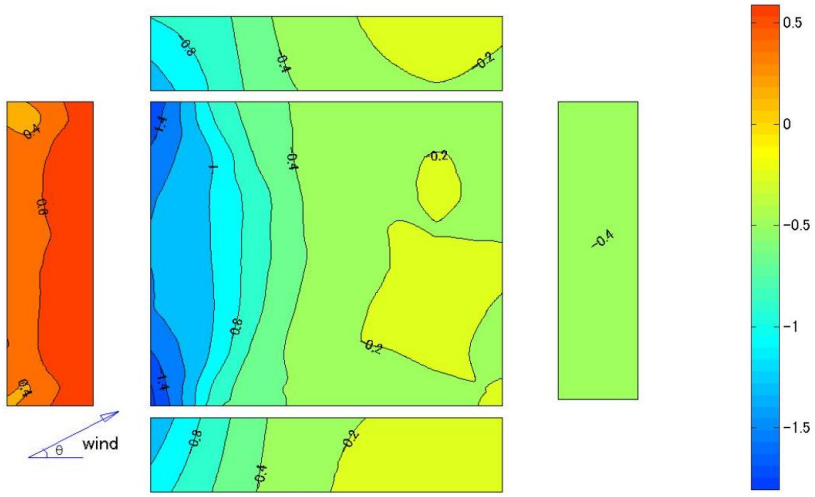

Mean wind pressure coefficients on a flat roof of a low-rise building (TPU). θ=45°

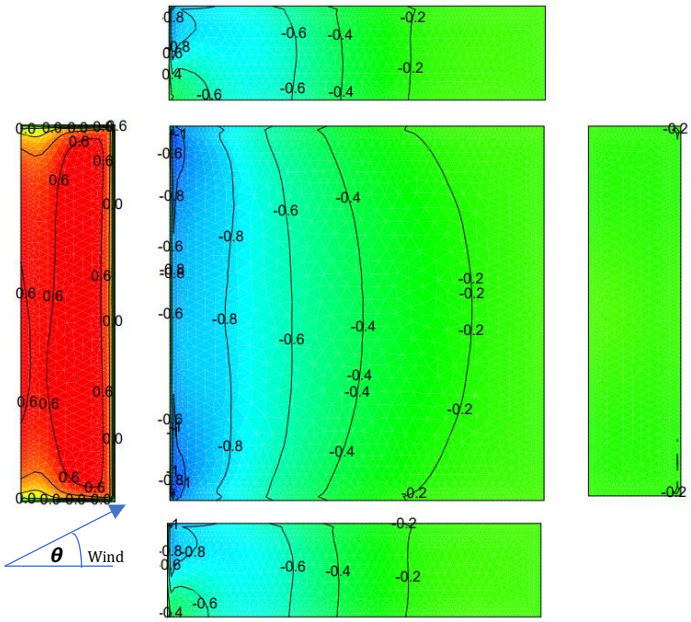

Mean wind pressure coefficients on a flat roof of a low-rise building (CFD simulation). θ=45°

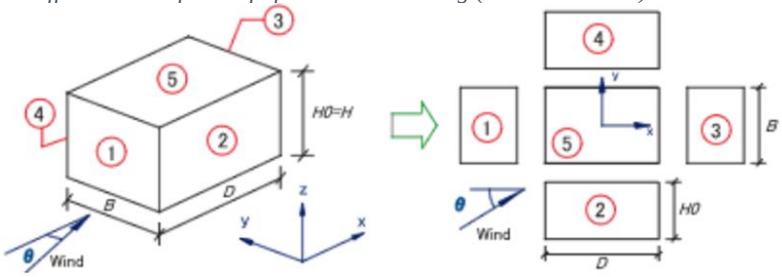

Figure 153: Results of mean pressure contour plots at wind angle of 45 a. TPU Experimental data b. CFD Simulation

Table 13 Comparison between this work and Tokyo area averaged pressure coefficient for wind incidence of 0° on the five building regions.

Region	Tokyo Cp	Simulation Cp	Difference percent
1	0.586	0.572	2.4
2	-0.371	-0.400	7.5
3	-0.262	-0.169	43
4	-0.397	-0.401	1
5	-0.495	-0.451	9.3

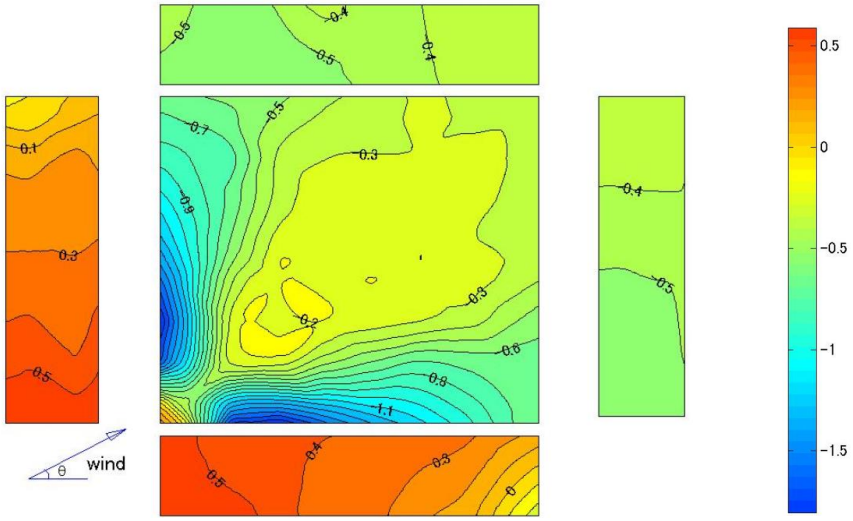

Mean wind pressure coefficients on a flat roof of a low-rise building (TPU). θ=45°

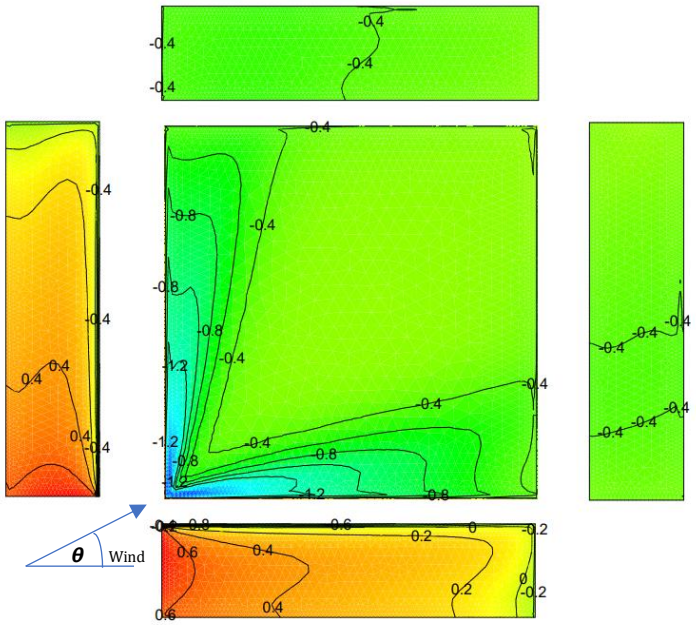

Mean wind pressure coefficients on a flat roof of a low-rise building (CFD simulation). θ=45°

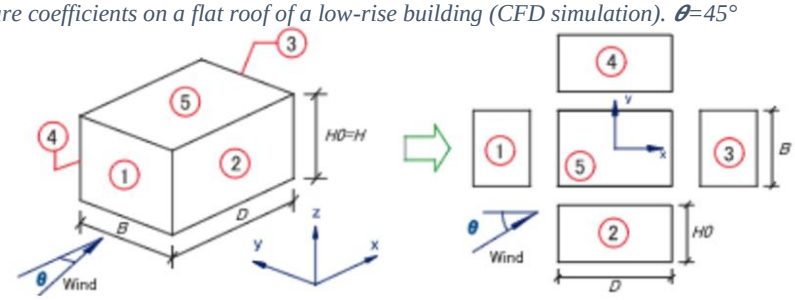

Figure 154: Results of mean pressure contour plots at wind angle of 45 a. TPU Experimental data b. CFD Simulation

Table 14 Comparison between this work and Tokyo area averaged pressure coefficient for wind incidence of 45° on the five building regions.

Region	Tokyo Cp	Simulation Cp	Difference percent
1	0.306	0.310	1.29
2	0.351	0.290	19
3	-0.471	-0.407	14
4	-0.453	-0.349	25
5	-0.508	-0.461	9.7

C.2 Validation of numerical method for single roof mounted collector on low rise building

This section of the appendix describes the numerical method's validation for the case of a single roof-mounted collector with no parapets. In this case, the simulation data was compared to the previously published experimental results from (Xypnitou, 2012; Stathopoulos *et al.*, 2014). Stathopoulos *et al.,* (2014) work, which is a follow-up to Xypnitou, (2012) work, was primarily taken into account because most studies of aerodynamic loads on roofs are conducted using arrays of panels rather than stand-alone collectors.

Stathopoulos *et al.,* (2014) constructed a 1:200 geometric scale model capable of accommodating solar panels at various locations and inclinations. Following that, the various configurations were tested in an Atmospheric Boundary Layer (ABL) wind tunnel to investigate the impact of factors such as building height, panel inclination, location, and direction under various wind conditions. For wind incidences between 120° and 165°, higher force coefficients were recorded on the panel surface if located on the front end of the roof.

As a result, the force coefficient results were validated against published results for various wind incidences ranging from 0° to 180°. In addition, for this validation, the collector was placed at 25 present of the roof, which is representative of the collector being placed close to the leading edge of the roof in the study Stathopoulos *et al.,* (2014). The values of the force coefficient C_L in both studies were then compared, where A_c is the collector area and F_L is the lift force.

$$C_L = \frac{F_L}{0.5\rho {U_{ref}}^2 A_c} \qquad 2$$

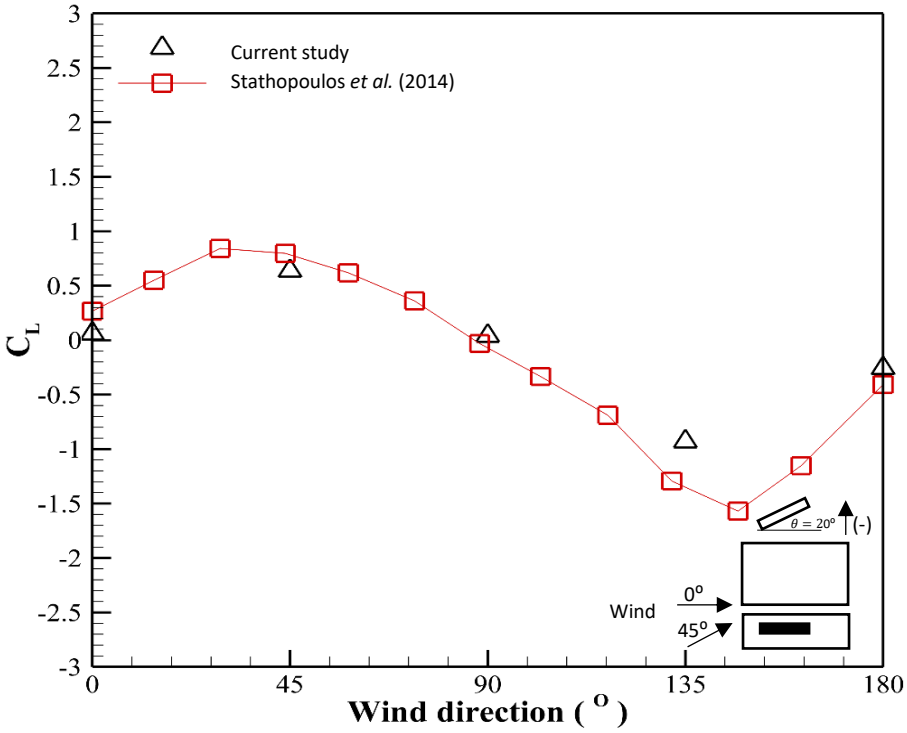

Figure 155: Comparison of Lift coefficeint for panels inclined at 20° at varying wind incidence located at 25percent of roof surface.

Figure 155 shows that the lift coefficient increases as wind incidence increases from 120° to 165°, which is consistent with the results of (Xypnitou, 2012; Stathopoulos *et al.*, 2014). A pronounced close trend can also be seen for wind incidence angles ranging from 0° to 120°. While the simulation data is similar to the experimental data, it should be noted that the current study did not include wind incident angles at 15° intervals, as is the case in the previous study (Xypnitou, 2012; Stathopoulos *et al.*, 2014). This could explain why, despite similar trends, there are some minor differences between the current study and the work of (Xypnitou, 2012; Stathopoulos *et al.*, 2014).

C.3 Experimental Investigation for standalone collector on roof with high perimetric parapet

As part of the validation process, wind tunnel testing was conducted on the stand-alone roof-mounted solar collector, which featured a high perimetric parapet. In order to accomplish this, measurements were conducted within the boundary-layer wind tunnel located at the University of Auckland, employing a nominal scale of 1:20. The experimental setup involved a three-dimensional model positioned perpendicular to the direction of airflow. The boundary-layer wind tunnel operates on a closed-circuit system. It is equipped with two fans and has a maximum wind speed capability of 20 m s-1. The cross-section of the wind tunnel measures 3.6 m in width and 2.5 m in height. Figure 156 displays a schematic diagram illustrating the wind tunnel configuration. The wind tunnel devoid of any obstructions exhibits a remarkably low level of turbulence intensity, estimated to be approximately 1 – 1.5%. The reference wind-tunnel speed at a height of 20 mm (10 m in full-scale) above the floor was 6.2 m/s. In this experiment U=5m/s

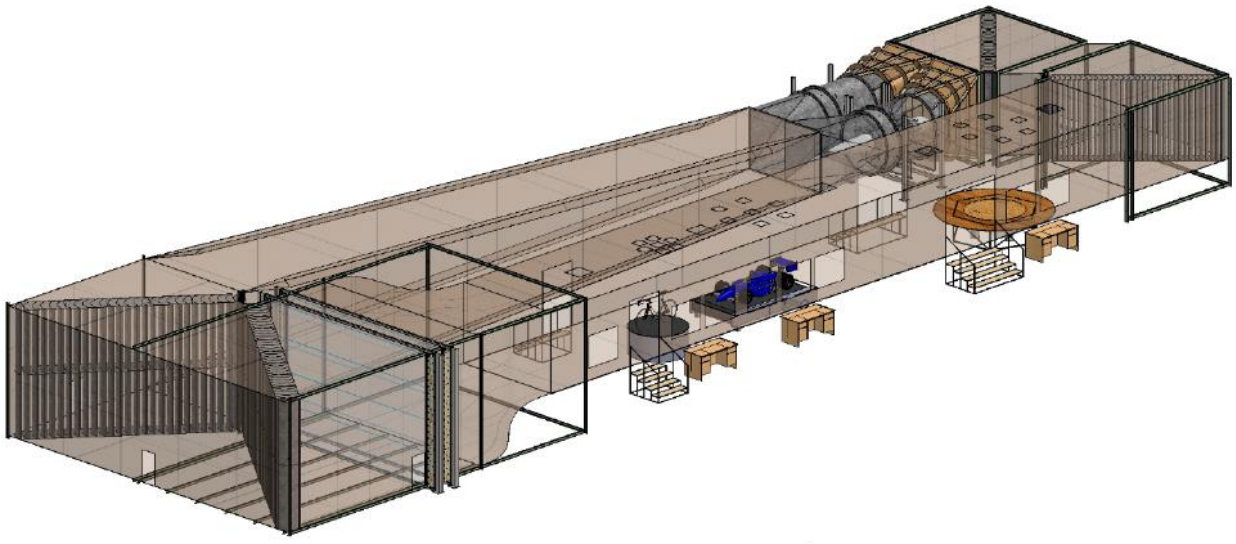

Figure 156: A schematic of the boundary-layer wind tunnel at the University of Auckland

The terrain category 2 for ground roughness, as defined in AS/NZS1170.2 (2011), with a roughness length Yo of 0.02m and representing open grassland, was reproduced in the wind tunnel experiment at a scale ratio of 1:20. This terrain category closely corresponds to surface roughness category C as outlined in ASCE-7 (2016). In order to produce the necessary wind

profile, the tunnel is outfitted with a pair of fans, as well as a collection of roughness elements including spires and trips as depicted in Figure 157.

In order to conduct the investigation, a scaled-down model composed of polymethyl methacrylate (PMMA) sheet material was fabricated at a scale of 1:20. The dimensions of the model were 0.8 m (D) by 0.8 m (B) by 0.2 m (H), with a height-to-breadth ratio (H:B) of 1:4 and a breadth-to-depth ratio (B:D) of 1:1. The consideration of these dimensions was based on their close resemblance to the models utilised in the Aerodynamic database of low-rise buildings at Tokyo Polytechnic University (Tamura, 2012). A rectangular aluminium plate with dimensions of 0.4 m (height) by 0.2 m (base) and a thickness of 0.03 m was affixed onto the level surface of the roof. In this particular case, a collector size larger than the 1:20 scale (specifically, the 1:10 scale) was deemed appropriate in order to accommodate a broader arrangement of pressure taps. Subsequently, two sets of non-slip wedges, fabricated from PMMA sheet material, were affixed to the collector, ensuring that the leading edge of the collector was elevated above the surface of the roof. For the purpose of this validation phase, only the high perimetric parapet configuration of 0.06 m, equivalent to 1.2 m in full scale, was taken into account. The tests-maintained blockage ratios below 3%.

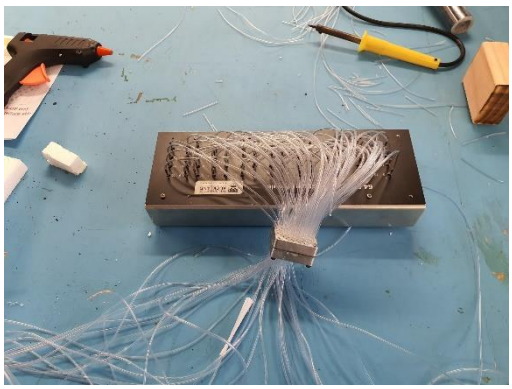

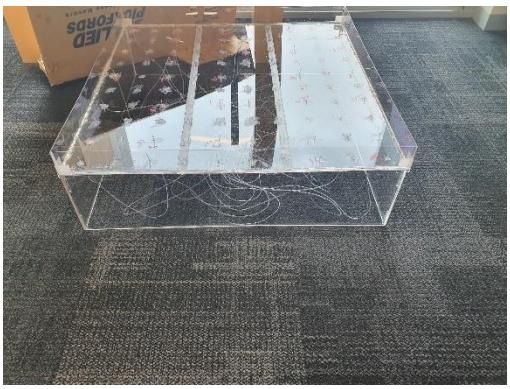

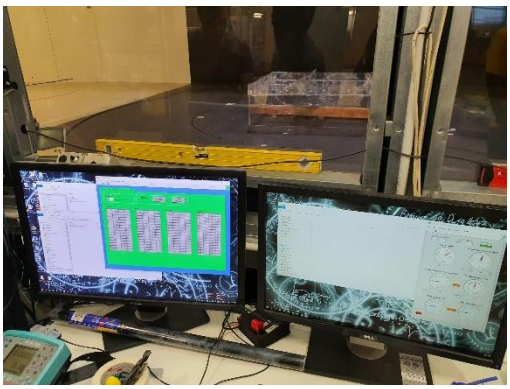

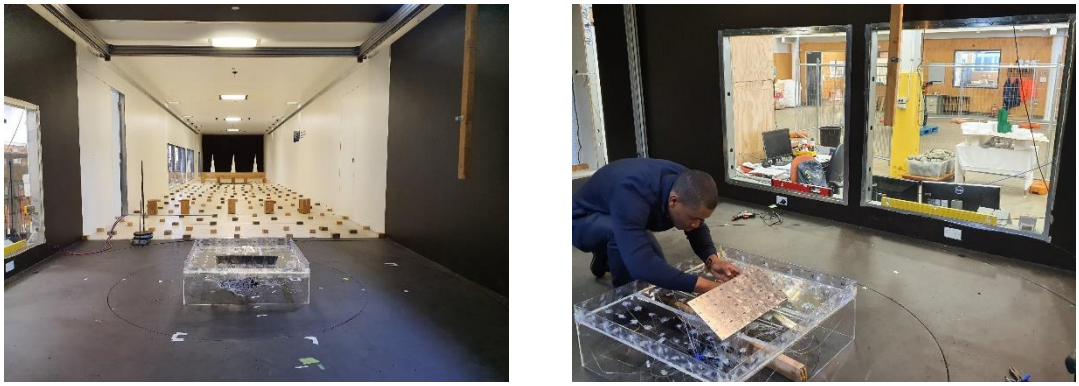

Figure 157: Photos of wind-tunnel set-up.

A range of different pressure tap layouts were used, based on the scale of the model and the size of the standalone solar collector. On the roof, collector, and parapet surfaces, 86 pressure taps were mounted: 5 on each parapet, 36 on the roof, and 30 on the collector surface. A diagram of the model's tap distribution is shown in Figure 158

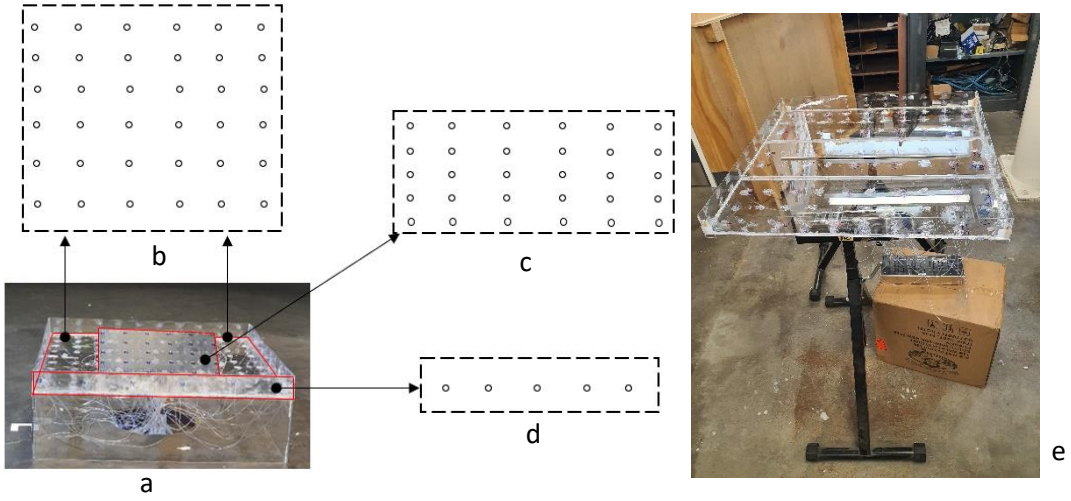

Figure 158: (a) 1:20 wind tunnel test model (b) building plan view (c) collector plan view (d) parapet Plan view with respective tap layout (e) Setting out of pressure tap layout.

The pressures were concurrently sampled at all taps, with frequencies of either 250 Hz or 500 Hz, over periods ranging from 30 seconds to 2 minutes. To compensate for the frequency response of the tubing-transducer system, a correction in the frequency domain was implemented. Pressure measurements were recorded under the operational condition of a wind incidence angle of 0°. The terrain was verified to generate the desired velocity and turbulence intensity profiles, denoted as Iu. This was achieved by measuring vertical profiles in the absence of the model and comparing them with the recommended values outlined in AS/NZS1170.2 (2011). The value of Iu in this

instance is 0.192. Also equation 31 defines the logarithmic velocity profile, where the value of u_* is 0.360 m/s.

$$\frac{U}{u_*} = \frac{1}{\mathrm{K}} \ln\left(\frac{Y}{Y_0}\right) \qquad 31$$

Appendix D: Richardson Number

When forced convection is present, the Nusselt number is influenced by the Reynolds number (Re_L), the Prandtl number (P_r), and the Rayleigh number (R_a). In natural convection, the Nusselt number is influenced by the Rayleigh number, (R_a). The Richardson number for thermal convection, (R_i), a nondimensional parameter, is used to estimate the relative contribution of forced and natural convection in each scenario (see equation 32). Here, Gr_L and Re_L are the Grashof and Reynold numbers respectively.

$$R_i = \frac{Gr_L}{{Re_L}^2} \quad 32$$

When the Richardson number (Ri) is less than 0.1, natural convection becomes negligible, whereas forced convection becomes negligible when Ri exceeds 10. Nevertheless, in the event that the Richardson number lies between 0.1 and 10, it is imperative to acknowledge that both natural and forced convection cannot be deemed insignificant. The Reynolds number Re_L , the Prandtl number (P_r), and Grashof number Gr_L and the Rayleigh number (R_a) can be evaluated from the following expressions:

$$Re_L = \frac{\rho u_\infty L}{\mu} \quad 33$$

$$P_r = \frac{\mu C_p}{k_{air}} \quad 34$$

$$Gr_L = \frac{g\beta(T_C - T_\infty){L_C}^3}{v^2} \quad 35$$

$$R_a = G_R * P_r \quad 36$$

In the above equations 32 to 36, C_p is the specific heat of air at constant pressure (J/kg-K), g is the gravitational acceleration (m/s2), β is the thermal expansion coefficient (1/K), v is the kinematic viscosity (m2/s), ρ is the density of air (kg/m3), u_∞ is the free stream velocity (m/s) and μ is the dynamic viscosity of air (Pa). In present study three velocities were chosen: 2.5, 5 and 10 m/s, representative of Re_L : 1.65×10^6, 3.29×10^6 and 6.59×10^6 respectively.

Accordingly, the Richardson number for thermal convection (R_i) has been deduced at these velocities to establish that forced convection is dominant where $Gr_L/Re_L{}^2 < 1$ in all cases.

Appendix E: Effect of varying wind incidence angle and parapet on roof velocity

This section of the appendix demonstrates the effect of varying wind incidence angles on the roof surface.

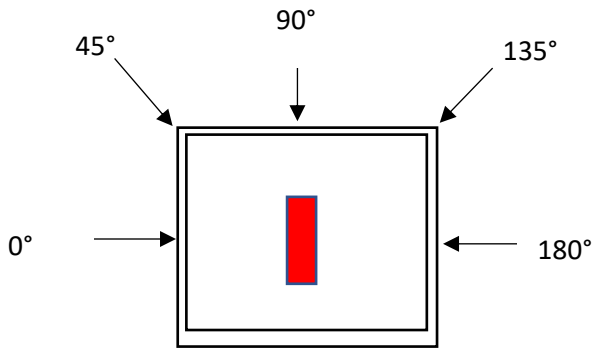

Figure 159: Wind incidence angle to building with standalone roof mounted solar thermal collector.

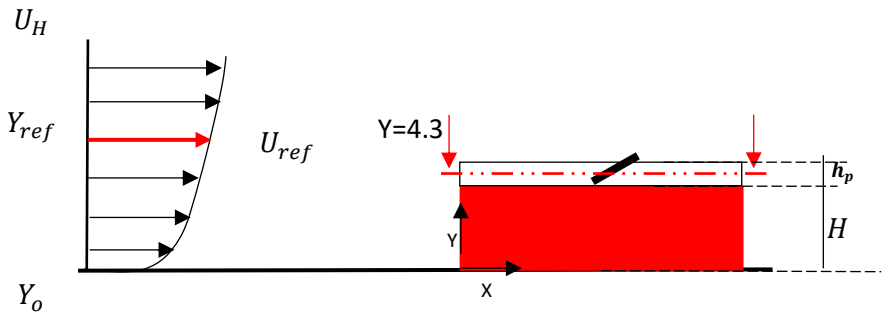

Figure 160: Reference coordinates and plane of assessment (Not drawn to scale)

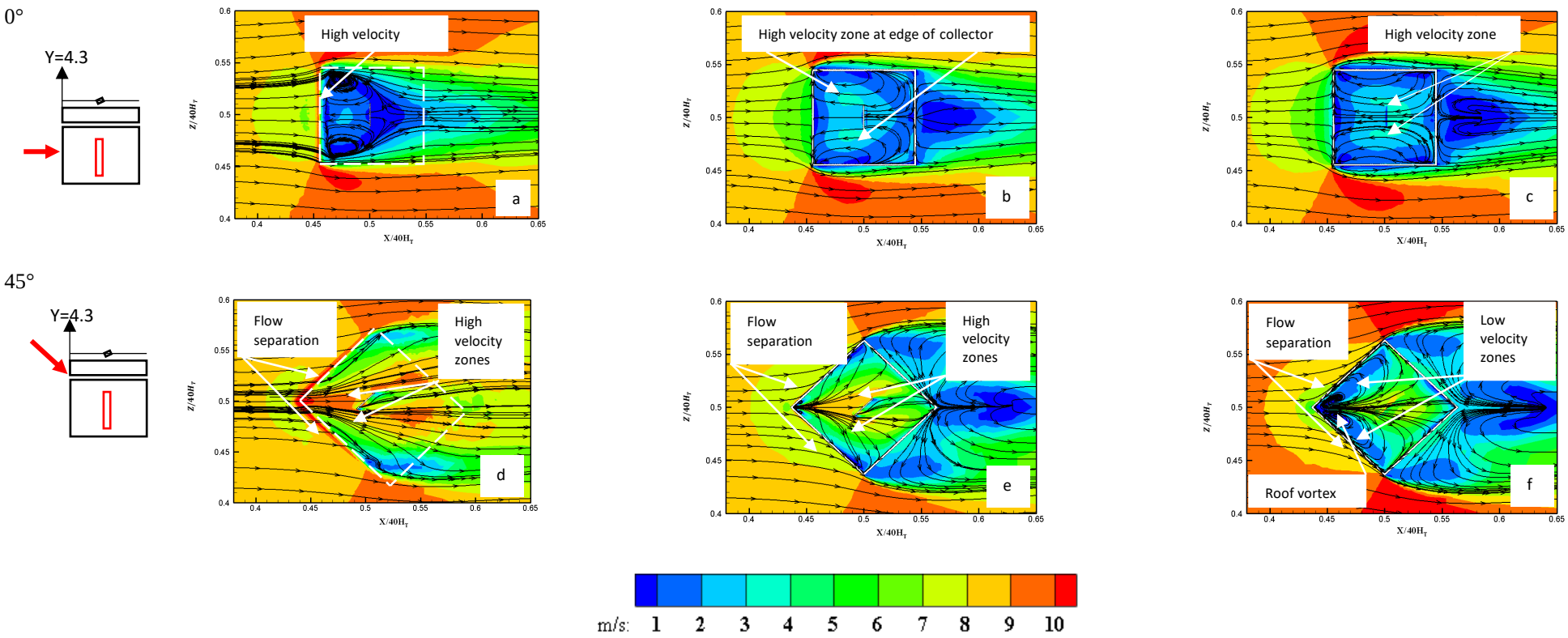

Figure 161: Flow behavior on roof surface at wind incidence angle of 0° and 45° (Operational conditions of V = 10 m/s, β = 20°, Lc = 50 percent of the roof's length)

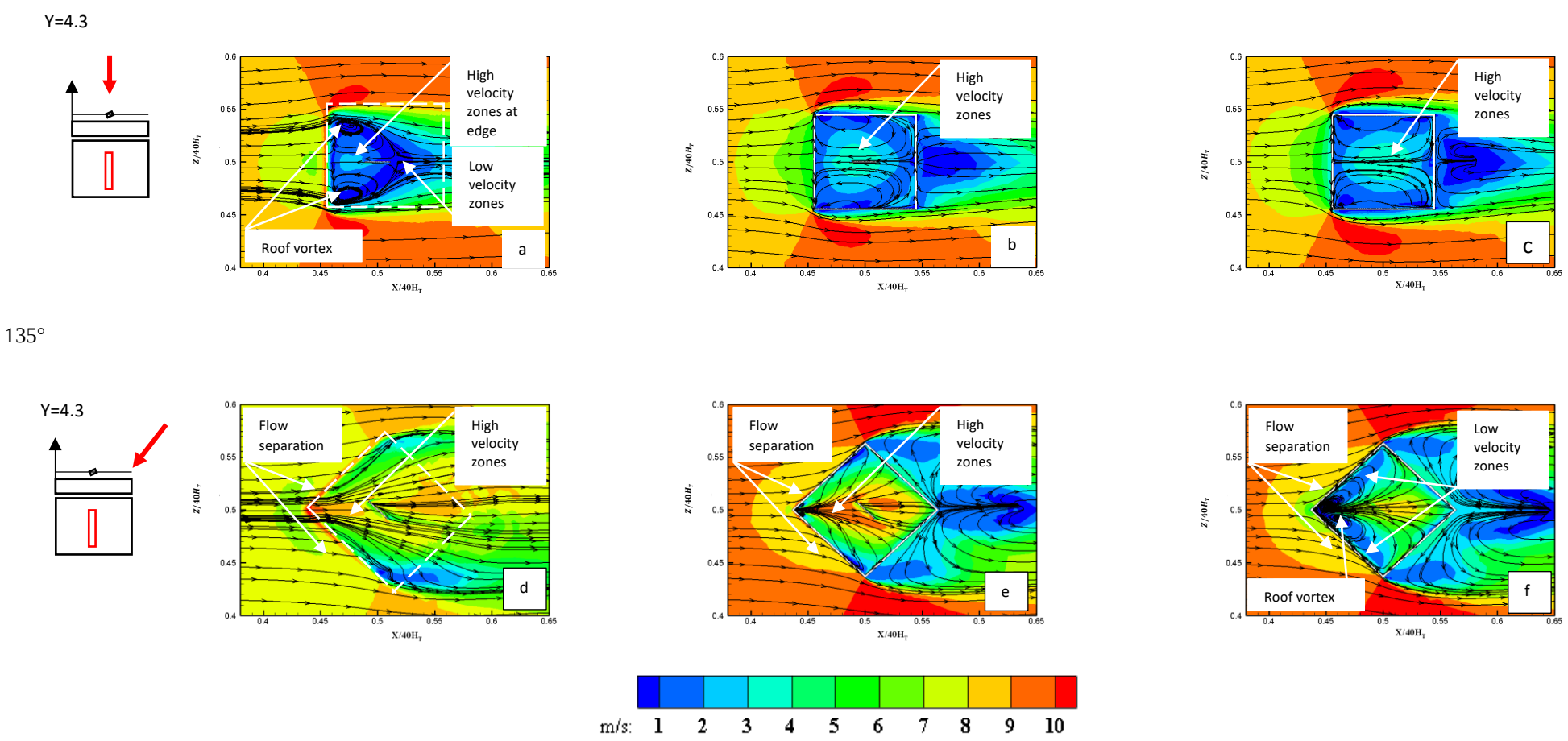

Figure 162: Flow behavior on roof surface at wind incidence angle of 90° and 135° (Operational conditions of V = 10 m/s, β = 20°, Lc = 50 percent of the roof's length)

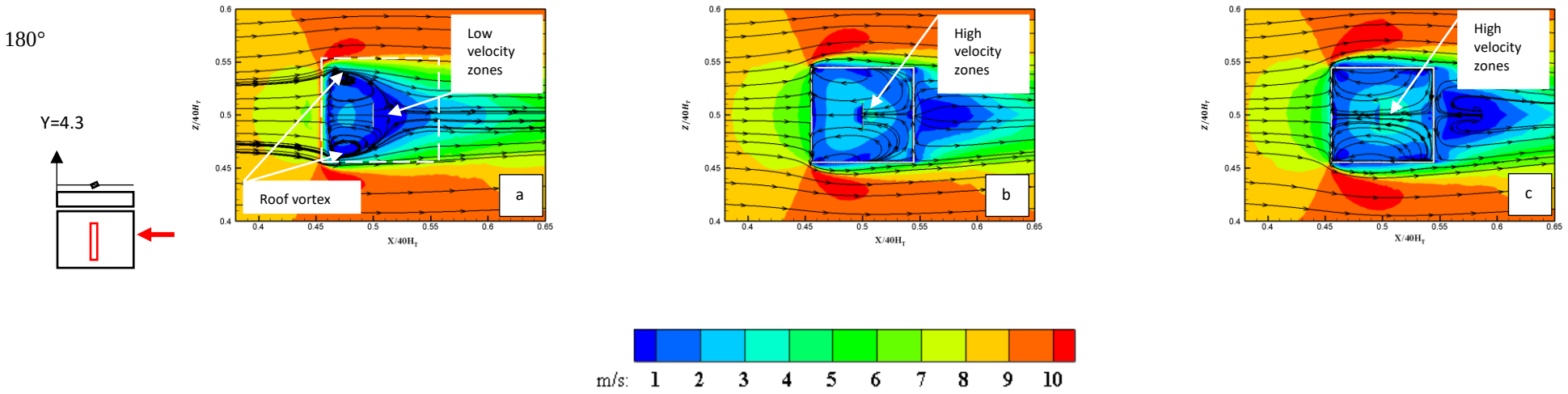

Figure 163: Flow behavior on roof surface at wind incidence angle of 180 ° (Operational conditions of V = 5 m/s, β = 20°, Lc = 50 percent of the roof's length)